

AD-A046 169

NORTHROP RESEARCH AND TECHNOLOGY CENTER HAWTHORNE CALIF

F/G 18/6

IONIZING RADIATION EFFECTS ON SILICON-ON-SAPPHIRE DEVICES AND S--ETC(U)

AUG 77 J R SROUR, S OTHMER, O L CURTIS

DAA639-76-C-0090

UNCLASSIFIED

NRTC-77-28R

HDL-CR-77-090-1

NL

1 OF 3

AD
A046169



HDL-CR-77-090-1

AD A 046169

AUGUST 1977

IONIZING RADIATION EFFECTS ON
SILICON-ON-SAPPHIRE DEVICES AND
SILICON DIOXIDE FILMS

DDC
RECEIVED
NOV 2 1977
B

Prepared by

Northrop Corporation
Northrop Research and Technology Center
3401 West Broadway
Hawthorne, California 90250

Under Contract

DAAG-39-76-C-0090

U.S. Army Materiel Development
and Readiness Command
HARRY DIAMOND LABORATORIES
Adelphi, Maryland 20783

This work was sponsored by the Defense Nuclear Agency under
Nuclear Weapons Effects Research Subtask Z99DAXTA097
(Transient Radiation Effects Physics), Work Unit 61 (Surface
Effects and Interface State Investigations).

Approved for Public Release; Distribution Unlimited

HDL-CR-77-090-1 - Ionizing Radiation Effects on Silicon-on-Sapphire Devices and Silicon Dioxide
Films, by J.R. Strout, S. Ohmer, O.L. Curtis, Jr., K.Y. Chiu, and S.C. Chen

AD No

DDC FILE COPY



The findings in this report are not to be construed as an official Department of the Army position unless so designated by other authorized documents.

Citation of manufacturers' or trade names does not constitute an official endorsement or approval of the use thereof.

Destroy this report when it is no longer needed. Do not return it to the originator.

UNCLASSIFIED

SECURITY CLASSIFICATION OF THIS PAGE (When Data Entered)

19 REPORT DOCUMENTATION PAGE		READ INSTRUCTIONS BEFORE COMPLETING FORM
18 REPORT NUMBER HDL CR-77-090-1	2. GOVT ACCESSION NO.	3. RECIPIENT'S CATALOG NUMBER
4. TITLE (and Subtitle) IONIZING RADIATION EFFECTS ON SILICON- ON-SAPPHIRE DEVICES AND SILICON DIOXIDE FILMS		5. TYPE OF REPORT & PERIOD COVERED Final Report May 1976 to April 1977
6. AUTHOR Joseph R. Srour, Siegfried Othmer, Orlie L. Curtis, Jr., Kuang Y. Chiu, and Susan C. C. Chen		7. PERFORMING ORGANIZATION REPORT NUMBER NRTC-77-28R
8. PERFORMING ORGANIZATION NAME AND ADDRESS Northrop Corporation Northrop Research and Technology Center 3401 West Broadway, Hawthorne, CA 90250		9. CONTRACT OR GRANT NUMBER (if applicable) DAAG-39-76-C-0090 DRCMS Code: 36AA-7100 67204; MIPR 76-654
11. CONTROLLING OFFICE NAME AND ADDRESS Defense Nuclear Agency Washington, D.C. 20305		10. PROGRAM ELEMENT, PROJECT, TASK Prog. Element: 6.27.04H Subtask: Z99QAXTA007 HDL Project: 236628
14. MONITORING AGENCY NAME & ADDRESS (if different from Controlling Office) Harry Diamond Laboratories 2800 Powder Mill Road Adelphi, MD 20783		12. REPORT DATE August 1977
16. DISTRIBUTION STATEMENT (of this Report) Approved for public release; distribution unlimited		13. NUMBER OF PAGES 207
17. DISTRIBUTION STATEMENT (of the abstract entered in Block 20, if different from Report)		15. SECURITY CLASS. (of this report) UNCLASSIFIED
18. SUPPLEMENTARY NOTES This work was sponsored by the Defense Nuclear Agency under Nuclear Weapons Effects Research Subtask Z99QAXTA007 (Transient Radiation Effects Physics), Work Unit 61 (Surface Effects and Interface State Investigations).		15a. DECLASSIFICATION DOWNGRADING SCHEDULE
19. KEY WORDS (Continue on reverse side if necessary and identify by block number) Silicon-on-sapphire devices; SOS devices; MOS devices; ionizing radiation ef- fects; low-energy electron irradiation; gamma irradiation; silicon dioxide; charge transport; charge buildup; threshold voltage; channel mobility; low- temperature radiation effects; aluminum-implanted silicon dioxide; radiation hardening; leakage current; back-channel leakage current.		
20. ABSTRACT (Continue on reverse side if necessary and identify by block number) This report describes results of several related studies of ionizing radia- tion effects on silicon-on-sapphire devices and on silicon dioxide films. In the SOS investigation, emphasis was placed on the study of radiation-induced back-channel leakage current and on a comparison of devices with wet and dry gate oxides. Differing behavior for wet and dry devices is accounted for in terms of a larger density of hole traps in the sapphire for dry transistors as		

DD FORM 1 JAN 73 1473 EDITION OF 1 NOV 65 IS OBSOLETE

UNCLASSIFIED

SECURITY CLASSIFICATION OF THIS PAGE (When Data Entered)

407696.

J/B

UNCLASSIFIED

SECURITY CLASSIFICATION OF THIS PAGE(When Data Entered)

20. ABSTRACT (Continued)

compared to wet units. SEM studies reveal that energy must be deposited in the sapphire before significant increases in leakage current will occur. In addition, such studies indicate that energy deposition deep in the sapphire bulk is relatively unimportant in producing leakage current. A process of radiation-induced reduction of leakage current was observed in which this current can be dramatically reduced to near its pre-irradiation value by simply reducing the applied drain bias to zero and continuing the irradiation. Models for radiations effects on SOS devices are presented. Measurements of the temporal, temperature, and electric-field dependences of radiation-induced charge transport have been performed for radiation-hardened SiO_2 films. It is demonstrated that oxides exhibiting radiation tolerance at room temperature display severe radiation-induced changes at 77°K . A model based on multiple trapping at a continuum of trapping levels is present which accounts for hole transport in SiO_2 films. Experiments and analyses have been performed which relate to ionizing radiation effects on MOS devices at low temperatures, and hardening approaches appropriate for device operation at such temperatures are considered.

ACCESSION for	
NTIS	WFO Section <input checked="" type="checkbox"/>
ODC	WFO Section <input type="checkbox"/>
UNANNOUNCED	<input type="checkbox"/>
AUTHENTICATION	
BY	
DISTRIBUTION/AVAILABILITY CODES	
Dist.	AVAIL. or SPEC.
A	

UNCLASSIFIED

SECURITY CLASSIFICATION OF THIS PAGE(When Data Entered)

TABLE OF CONTENTS

<u>Section</u>	<u>Page</u>
1.0 INTRODUCTION AND SUMMARY - - - - -	13
2.0 RADIATION-INDUCED CHARGE TRANSPORT AND CHARGE BUILDUP IN SiO ₂ FILMS AT LOW TEMPERATURES - - - - -	17
2.1 Introduction - - - - -	17
2.2 Experimental Considerations - - - - -	18
2.3 Experimental Results - - - - -	20
2.3.1 Charge Transport - - - - -	20
2.3.2 Charge Buildup - - - - -	26
2.4 Discussion - - - - -	32
3.0 THE MULTIPLE-TRAPPING MODEL AND HOLE TRANSPORT IN SiO ₂ - - - - -	39
3.1 Introduction - - - - -	39
3.2 Formulation of the Model - - - - -	41
3.3 Results - - - - -	45
3.3.1 Dependence of Hole Collection on Time - - - - -	45
3.3.2 Variation of Hole Collection and Current with Temperature - - - - -	48
3.3.3 Variation of Hole Collection with Field - - - - -	51
3.4 Discussion - - - - -	55
3.5 Conclusion - - - - -	68
4.0 LOW-TEMPERATURE PHENOMENA IN IRRADIATED MOS DEVICES - - - - -	71
4.1 Introduction - - - - -	71
4.2 MOS Hardening Approaches at Low Temperatures - - - - -	71
4.3 Analysis of Ion Implantation Effects - - - - -	73

TABLE OF CONTENTS (Continued)

<u>Section</u>	<u>Page</u>
4.4 Analysis of Applied Field Effects - - - - -	79
4.5 Experimental Results - - - - -	88
4.6 Improved Model - - - - -	97
4.7 Discussion - - - - -	107
4.8 Summary - - - - -	114
5.0 IONIZING RADIATION EFFECTS ON SILICON- ON-SAPPHIRE DEVICES - - - - -	115
5.1 Introduction - - - - -	115
5.2 Experimental Considerations - - - - -	116
5.3 Threshold Voltage Shift in SOS Transistors -	119
5.4 Channel Mobility Degradation in SOS Transistors - - - - -	121
5.5 Back-Channel Leakage Current Studies on SOS Transistors - - - - -	133
5.5.1 Introduction and Experimental Techniques - - - - -	133
5.5.2 Experimental Results for Wet- and Dry-Oxide Devices - - - - -	133
5.5.3 Leakage Current Analysis and Discussion - - - - -	142
5.5.4 Radiation-Induced Reduction of Back- Channel Leakage Current - - - - -	160
5.5.5 Scanning Electron Microscope Studies - - - - -	163
5.5.6 Non-Ohmic Contact Effects on Leak- age Current Measurements - - - - -	180
5.6 Back-Channel Leakage Current Studies on CMOS/SOS Inverters - - - - -	182
5.7 Studies of the Silicon-Sapphire Interface using Capacitance-Voltage Measurements - -	184

TABLE OF CONTENTS (Continued)

<u>Section</u>	<u>Page</u>
5.8 Studies of the Silicon-Sapphire Interface using Transient Current Measurements - - -	189
5.9 Summary - - - - -	196
LITERATURE CITED - - - - -	198
DISTRIBUTION LIST - - - - -	203

LIST OF ILLUSTRATIONS

<u>Figure</u>		<u>Page</u>
1	Gain at 303°K vs. time following pulsed bombardment for an MOS capacitor with various values of applied voltage -----	21
2	Gain at 173°K vs. time following pulsed bombardment with applied voltage as a parameter for an MOS capacitor -----	23
3	Gain at 90°K vs. time following pulsed bombardment with applied voltage as a parameter for an MOS capacitor -----	23
4	Gain at 90°K vs. applied field for three integration times -----	24
5	Gain at 21V vs. temperature for four integration times -----	27
6	Gain at 21V vs. time following pulsed bombardment for four temperatures -----	27
7	Flatband voltage shift vs. Co ⁶⁰ -gamma dose for radiation-hardened MOS capacitors at 77 and 300°K -----	28
8	Time to reach particular values of gain vs. reciprocal temperature -----	33
9	A simplified representation of the multiple-trapping model -----	42
10	Relative trap occupancies for a specific choice of model parameters -----	46
11	An illustration of the variation in model predictions with model parameters -----	47
12	The variation of hole collection with time and temperature: a comparison of experimental results and predictions of the multiple-trapping model -----	49
13	The variation of relative hole current with time and temperature: experimental and analytical results -----	52

LIST OF ILLUSTRATIONS (Continued)

<u>Figure</u>		<u>Page</u>
14	Time dependence of gain as a function of applied voltage - - - - -	53
15	A fit of experimental data using the multiple-trapping model including the Poole-Frenkel effect - - - - -	56
16	Time to reach a particular value of gain vs. reciprocal temperature for an applied voltage of 21V - - - - -	58
17	Analytical prediction of the data of Figure 16 - - -	60
	Measured hole mobility as a function of reciprocal temperature - - - - -	63
19	Measured hole mobility at 90°K as a function of applied field - - - - -	67
20	Schematic of an MOS structure with an ion-implanted oxide - - - - -	74
21	The calculated ratio of $\Delta V_{fb}(\text{implanted})$ to $\Delta V_{fb}(\text{unimplanted})$ vs. implantation depth for three values of electron schubweg - - - - -	77
22	The calculated ratio of $\Delta V_{fb}(\text{implanted})$ to $\Delta V_{fb}(\text{unimplanted})$ vs. implantation depth for several values of applied field - - - - -	78
23	Schematic of an MOS structure showing an incremental oxide thickness containing a positive charge density - - - - -	80
24	Illustration of a simple low-field model for charge buildup in MOS structures at low temperature - - -	82
25	Illustration of a simplified model for high-field behavior of MOS structures irradiated at low temperatures - - - - -	83
26	Calculated flatband voltage shift vs. oxide thickness with transport distance as a parameter for an MOS structure irradiated to 10^5 rads(Si) with positive bias applied to the metal electrode - - - -	85

LIST OF ILLUSTRATIONS (Continued)

<u>Figure</u>		<u>Page</u>
27	Calculated flatband voltage shift vs. oxide thickness with transport distance as a parameter for an MOS structure irradiated to 10^5 rads(Si) with negative bias applied to the metal electrode - - - -	86
28	Calculated flatband voltage shift vs. charge transport distance for a 910 \AA oxide irradiated to 10^5 rads(Si) - - - - -	87
29	Flatband voltage shift at 10^5 rads(Si) vs. applied voltage for MOS capacitors irradiated at 77°K and at room temperature - - - - -	89
30	Flatband voltage shift at 10^6 rads(Si) vs. applied voltage for MOS capacitors irradiated at 77°K and at room temperature - - - - -	90
31	Flatband voltage shift at 77°K after 10^5 rads(Si) vs. oxide field for the case of an applied positive bias during irradiation - - - - -	93
32	Flatband voltage shift at 77°K after 10^5 rads(Si) vs. oxide field for the case of an applied negative bias during irradiation - - - - -	94
33	Calculated transport distance d_t vs. oxide field -	96
34	Overall fit to experimental data based on the fitting procedure illustrated in Figures 31 and 32 - - - -	98
35	Fractional yield vs. oxide field for the present study and for two earlier investigations - - - - -	99
36	Illustration of a more realistic model for the motion of charge at high fields and low temperatures in SiO_2 (positive bias case) - - - - -	101
37	Illustration of a more realistic model for the motion of charge at high fields and low temperatures in SiO_2 (negative bias case) - - - - -	103
38	Transport distance vs. applied field based on calculations using the improved model illustrated in Figure 36 and 37 - - - - -	105

LIST OF ILLUSTRATIONS (Continued)

<u>Figure</u>		<u>Page</u>
39	Flatband voltage shift at 77°K vs. oxide field for the case of an applied positive bias - - - - -	106
40	Flatband voltage shift at 77°K vs. oxide field for the case of an applied negative bias - - - - -	108
41	Fractional yield versus oxide field for the present study (from Figure 39) and for two previous investigations - - - - -	109
42	Illustration of a model for hole transport in SiO ₂ which makes use of a variable "transport angle" θ - - - - -	111
43	Processing sequence for custom n-channel SOS devices fabricated for NRTC by Hughes Aircraft -	117
44	Schematic illustration of custom n-channel SOS transistors with a thin gate metallization - - - - -	118
45	Threshold voltage vs. dose for wet- and dry-oxide n-channel SOS transistors irradiated with $V_{gs} = 0$ -	120
46	Threshold voltage vs. dose for wet- and dry-oxide n-channel SOS transistors irradiated with $V_{gs} = 5V$ - - - - -	122
47	Illustration of a Schottky diode characteristic and two hypothetical I_d vs. V_{ds} curves for two values of V_{gs} - - - - -	125
48	Illustration of an I_d vs. V_{ds} curve after correcting the original characteristic (Figure 47) for the effects of the Schottky diode - - - - -	127
49	Illustration of a g_c vs. V_{gs} curve obtained from a family of curves having the form of that shown in Figure 48 - - - - -	127
50	Field-effect mobility vs. dose for wet- and dry-oxide n-channel SOS transistors irradiated with $V_{gs} = 0$ - - - - -	131
51	Field-effect mobility vs. dose for wet- and dry-oxide n-channel SOS transistors irradiated with $V_{gs} = 5V$ - - - - -	132

LIST OF ILLUSTRATIONS (Continued)

<u>Figure</u>		<u>Page</u>
52	Typical drain current vs. gate voltage characteristics with total ionizing dose as a parameter for n-channel wet-gate-oxide SOS transistors - - - - -	134
53	Typical drain current vs. gate voltage characteristics with total ionizing dose as a parameter for n-channel dry-gate-oxide SOS transistors - - - - -	136
54	Back-channel leakage current vs. dose for dry- and wet-oxide n-channel SOS transistors irradiated with $V_{gs} = 0$ and $V_{ds} = 5V$ at a dose rate of 64 rads(Si)/s - - - - -	137
55	Back-channel leakage current vs. dose for dry- and wet-oxide n-channel SOS transistors irradiated with $V_{gs} = 0$ and $V_{ds} = 5V$ at a dose rate of 4.3 rads(Si)/s - - - - -	139
56	Leakage current vs. reciprocal temperature for four n-channel SOS transistors, two with a wet oxide and two with dry - - - - -	140
57	Leakage current vs. $\Delta E/kT$ - - - - -	141
58	Results of fitting a linear charging model to the leakage current vs. dose data of Figure 54 - - - - -	145
59	Illustration of a photocurrent that dominated measured leakage current at low doses for the wet-oxide data of Figure 55 - - - - -	147
60	Radiation-induced leakage current vs. dose for wet- and dry-oxide SOS transistors irradiated to a rate of 4.3 rads(Si)/s - - - - -	148
61	Channel mobility vs. inversion-layer carrier density for the cases of low and high interface charge - - - - -	150
61a	Leakage current vs. reciprocal temperature for an unirradiated wet-oxide n-channel SOS transistor - - - - -	156
62	Leakage current vs. dose for a wet-oxide n-channel SOS transistor - - - - -	161

LIST OF ILLUSTRATIONS (Continued)

<u>Figure</u>		<u>Page</u>
63	Energy deposition profiles for the present SOS structures bombarded by low energy electrons - -	164
64	Back-channel leakage current vs. dose for 6-keV and 15-keV electron bombardment of a wet-oxide n-channel SOS transistor - - - - -	167
65	Radiation-induced leakage current vs. dose for wet-oxide n-channel SOS transistors bombarded by Co ⁶⁰ gamma rays (from Figure 60) and by 15-keV electrons (from Figure 64) - - - - -	169
66	Relative effectiveness in producing leakage current vs. bombarding electron beam energy for dry- and wet-oxide transistors - - - - -	171
67	Absolute production effectiveness vs. electron range in sapphire for a dry-oxide n-channel SOS transistor - - - - -	173
68	Relative recovery (or reduction) effectiveness vs. bombarding electron beam energy for leakage current in dry- and wet-oxide n-channel SOS transistors - - - - -	175
69	Minimum back-channel leakage current in a dry-oxide transistor vs. the bombarding electron beam energy used to reduce leakage current to a particular minimum value by irradiation with $V_{ds} = 0$ - - - - -	177
70	Schematic of experimental technique developed to measure C-V characteristics for SOS structures - - - - -	186
71	Schematic of circuit employed to measure transient currents in SOS capacitors - - - - -	192
72	Current settling waveform for transient recovery circuit incorporating transient compensation - - -	193
73	Transient current following depleting pulse from accumulation to inversion for three final voltages in inversion - - - - -	194

LIST OF ILLUSTRATIONS (Continued)

<u>Figure</u>		<u>Page</u>
74	Current transient before and after irradiation with 10^6 rads(Si) Co^{60} gammas - - - - -	195

LIST OF TABLES

<u>Number</u>		<u>Page</u>
I	Conductance mobility for wet- and dry-oxide n-channel SOS transistors before and after gamma irradiation - - - - -	130
II	Leakage current information for irradiated n-channel transistors in CMOS/SOS inverters from three manufacturers - - - - -	183

SECTION 1.0

INTRODUCTION AND SUMMARY

This report describes results of several related studies of ionizing radiation effects on silicon MOS devices. Emphasis is placed on determining the mechanisms of the interaction of ionizing radiation with MOS structures with a view toward gaining understanding of benefit to developers of radiation-tolerant devices. Section 2.0 describes results of a study of charge transport and charge buildup in SiO_2 films at low temperatures. In Section 3.0, a detailed description of a multiple-trapping model for hole transport in SiO_2 is presented. Section 4.0 deals with low-temperature phenomena in irradiated MOS devices and includes a discussion of hardening approaches for operation at such temperatures. In Section 5.0, results of an extensive study of ionizing radiation effects on silicon-on-sapphire devices are described. The remainder of the present section summarizes major findings reported in this document.

Studies of the temporal, temperature, and electric-field dependences of radiation induced charge transport have been performed for radiation-hardened SiO_2 films. At room temperature for high applied fields, nearly all electrons and holes generated in the oxide by a pulse of ionizing radiation (5-keV electrons) drift to the interfaces, whereas at low temperatures only electrons contribute to observed transport for relatively low fields. Below $\sim 130^\circ\text{K}$ at high fields, field-induced emission of trapped holes occurs, giving rise to collection within seconds of a significant fraction of the total number of holes generated. The present hole transport data are accounted for quite well in terms of a multiple-trapping model with a spread in trap levels ranging from ~ 0.3 to ~ 0.5 eV from the valence band. Comparison with the stochastic hopping transport model is made and that model is found to be less satisfactory in explaining these data. Charge buildup was examined in a Co^{60} environment and it is demonstrated that oxides exhibiting radiation tolerance at room temperature display severe radiation-induced changes at 77°K . It is also demonstrated that low-temperature charge buildup problems can be alleviated either by employing an ion-implanted oxide or by applying a relatively high field to the oxide during irradiation.

An understanding of the charge transport process in SiO_2 is vital to an understanding of radiation effects in MOS effects. To account for hole transport in SiO_2 below room temperature, a stochastic hopping transport (or Continuous Time Random Walk (CTRW)) model has been employed by others with considerable success. We have developed an alternate model which explains many experimental data in an even more satisfactory fashion. This model is based on multiple-trapping at a continuum of trapping levels, the concentrations of which decrease exponentially with energy from the valence band edge. Adjusting rate parameters in the differential equation describing the multiple-trapping process and a parameter describing the width of the exponential trap distribution results in a good fit to the measured dependence of collected charge versus time following pulsed excitation at a single temperature. With no adjustment of parameters with temperature, the following results were obtained: (1) charge collection curves at other temperatures were accurately predicted; (2) the magnitudes and features of the time dependence of hole current extending over five orders of magnitude in current and six orders of magnitude in time were accurately predicted; (3) the magnitude of apparent activation energy and its spread in time were accurately predicted from behavior at a single temperature. It is submitted that the multiple-trapping model is superior to the CTRW model in explaining hole transport in SiO_2 films, at least for the particular material and experimental conditions analyzed.

Experiments and analyses have been performed which relate to ionizing radiation effects on MOS devices at low temperatures. This work is described in detail in Section 4.0 and is an extension of certain aspects of that presented in Section 2.0. In particular, hardening approaches for low-temperature applications of MOS are considered. Analysis of the effects of ion implantation on charge buildup in SiO_2 films at low temperatures is presented. Experimental results for the dependence of flatband voltage shift at 77°K on applied field are described and models for explaining observed behavior are considered. Positive charge buildup in irradiated MOS devices at low temperatures is explained in terms of the dependence of carrier yield on applied field and hole transport at relatively high fields.

A detailed study of ionizing radiation effects on SOS devices has been performed using two radiation sources: Co^{60} and a scanning electron microscope. Most of the experiments were performed

on custom n-channel transistors with both wet and dry radiation-hardened gate oxides. Data were also obtained for hardened CMOS/SOS inverters fabricated by three manufacturers. Emphasis in this investigation was placed on the study of radiation-induced back-channel leakage current, and a comparison of behavior for wet- and dry-oxide devices is made. Threshold voltage shifts and channel mobility degradation were also examined.

Measurements of threshold voltage shift in a ^{60}Co environment demonstrated both wet- and dry-oxide devices to be quite radiation tolerant in terms of changes in that parameter. Under worst-case biasing conditions, the maximum value of threshold shift observed up to 10^7 rads(Si) was 1.3V. Effects of radiation-induced interface states were considerably more significant in wet devices than in their dry counterparts. In studies of channel mobility degradation, changes in this quantity at 10^7 rads were insignificant for dry transistors but for wet units post-irradiation mobilities at that same dose ranged from ~40 to ~70% of initial values. Such reductions are qualitatively consistent with the interface state effects observed for wet-oxide devices in threshold voltage studies.

In back-channel leakage current studies, several significant observations were made. Leakage currents in the dry-oxide transistors investigated are approximately two orders of magnitude larger than in wet devices both before and after irradiation. These findings are interpreted in terms of differing densities of identical traps in the two device types. At room temperature, radiation-induced leakage current varies as (dose)^{1.5} for wet and dry devices at doses less than that for which leakage current saturation is observed. The variation of leakage current with temperature in both irradiated and unirradiated devices is attributed to the dependence of back-channel mobility on both temperature and inversion-layer carrier density. For an unirradiated wet-oxide transistor at room temperature, in addition to this back-channel "mobility mechanism," thermal generation in the drain depletion region also appears to be important in giving rise to leakage current. A process of radiation-induced reduction of back-channel leakage current was observed. This reduction of I_{L} to near its pre-irradiation value is accomplished by irradiating a device with $V_{\text{ds}} = 0$. A cycling experiment showed that this process can be repeated, which suggests that periodic reduction of V_{ds} to zero

to cause a reduction in I_L is a potential remedy for leakage current problems in SOS devices employed in a space radiation environment.

Scanning-electron-microscope studies on SOS devices indicate that injection of electrons from Si into Al_2O_3 where they recombine with trapped holes is the mechanism of radiation-induced recovery. However, if all trapped holes are located at the Al_2O_3 interface and are not distributed spatially into the sapphire, then we cannot rule out radiation-induced hole depopulation as the dominant mechanism. SEM studies as a function of beam energy also demonstrate conclusively that energy must be deposited in the sapphire before significant increases in back-channel leakage current will be observed. The process of radiation-induced reduction of I_L was also observed in measurements on radiation-hardened CMOS inverters. In fact, post-recovery leakage currents were often observed to be less than pre-irradiation values. Studies of the Si- Al_2O_3 interface based on C-V measurements and transient current techniques have also been performed and preliminary findings are described.

SECTION 2.0

RADIATION-INDUCED CHARGE TRANSPORT AND CHARGE BUILDUP IN SiO_2 FILMS AT LOW TEMPERATURES*

2.1 INTRODUCTION

Silicon MOS devices are presently being utilized in applications requiring low temperature operation. For example, extrinsic silicon detector arrays for infrared imaging will typically need to be cooled to temperatures less than 100°K , and these arrays may incorporate charge transfer devices on the same chip as the detector elements.^{1,2} Behavior of an MOS device operated at low temperatures in an ionizing radiation environment is quite different from that at room temperature.³⁻⁷ In an attempt to gain increased understanding of the mechanisms of low-temperature radiation effects in MOS devices and thereby anticipate problems for circuits operated under such conditions, we have performed a detailed study of charge transport in radiation-hardened SiO_2 films as a function of temperature, electric field, and time following a pulse of ionizing radiation. Charge buildup was also examined and it is demonstrated that oxides exhibiting radiation tolerance at room temperature display severe radiation-induced changes at 77°K .

* Published in the IEEE Transactions on Nuclear Science 23, 1513 (1976).

¹A. J. Steckl, R. D. Nelson, B. T. French, R. A. Gudmundsen, and D. Schechter, Proc. IEEE 63, (1975).

²K. Nummedal, J. C. Fraser, S. C. Su, R. Baron, and R. M. Finnila, in "Proceedings of 1975 International Conference on the Application of Charge-Coupled Devices," p. 19.

³R. L. Nielsen and D. K. Nichols, IEEE Trans. Nucl. Sci. 20, 319 (Dec. 1973).

⁴E. Harari, S. Wang, and B. S. H. Royce, J. Appl. Phys. 46, 1310 (1975).

⁵H. H. Sander and B. L. Gregory, IEEE Trans. Nucl. Sci. 22, 2157 (1975).

⁶H. E. Boesch, Jr., F. B. McLean, J. M. McGarrity, and G. A. Ausman, Jr., IEEE Trans. Nucl. Sci. 22, 2163 (1975).

⁷R. C. Hughes, E. P. EerNisse, and H. J. Stein, IEEE Trans. Nucl. Sci. 22, 2227 (1975).

It is of current interest to determine the specific mechanisms of hole transport in SiO_2 films. A frequently postulated model for transport in insulators involves motion of a carrier in the valence band between detrapping and trapping events. In this multiple-trapping description, a range of trap levels may be effective, with the deeper traps dominating behavior at longer times following carrier excitation. An alternative explanation, involving stochastic hopping transport between localized sites,⁸ has been invoked by Boesch et al.⁶⁻⁹ to account for hole conduction in amorphous SiO_2 . The present work provides information of value in deciding upon an appropriate transport model.

2.2 EXPERIMENTAL CONSIDERATIONS

MOS capacitors fabricated at Hughes Aircraft on an n-type silicon wafer (~ 1 ohm-cm with (100) orientation) were used as test vehicles. These units contained a radiation-hardened dry thermal SiO_2 film of the type developed by Aubuchon.¹⁰ The oxide layer was grown at 1000°C to a thickness of $0.135\text{ }\mu\text{m}$ and no N_2 anneal was performed. Following deposition of aluminum ($0.105\text{ }\mu\text{m}$ thickness) from a clean graphite crucible, the wafer was sintered in N_2 for 20 min at 500°C . (Capacitors from this same wafer have been utilized in previous charge transport and charge buildup studies at these laboratories.^{11,12})

Electron-hole pairs were generated in the SiO_2 layer of an MOS capacitor using a pulse of low-energy electrons. The pulse-width was typically on the order of $10\text{ }\mu\text{s}$ and the electron beam energy was typically 5 keV. The amount of energy deposited in the oxide per electron pulse was less than or equal to ~ 80 rads (Si). Charge transport in the oxide was monitored as a function of time following the bombarding pulse using a current integrator.

⁶H. E. Boesch, Jr., F. B. McLean, J. M. McGarrity, and G. A. Ausman, Jr., *IEEE Trans. Nucl. Sci.* **22**, 2163 (1975).

⁸H. Scher and E. W. Montroll, *Phys. Rev.* **B12**, 2455 (1975).

⁹F. B. McLean, G. A. Ausman, Jr., H. E. Boesch, Jr., and J. M. McGarrity, *J. Appl. Phys.* **47**, 1529 (1976).

¹⁰K. G. Aubuchon, *IEEE Trans. Nucl. Sci.* **18**, 117 (Dec. 1971).

¹¹J. R. Srour, O. L. Curtis, Jr., and K. Y. Chiu, *IEEE Trans. Nucl. Sci.* **21**, 73 (Dec. 1974).

¹²O. L. Curtis, Jr., J. R. Srour, and K. Y. Chiu, *IEEE Trans. Nucl. Sci.* **22**, 2174 (1975).

Electron beam current was determined using a Faraday cup. Measurements of charge transport were performed over the temperature range from 90 to 303°K for field strengths up to 4×10^6 V/cm (Al electrode positively biased - silicon surface accumulated). It was desirable to obtain complete characterization of each specimen. Since hundreds of pulses were required, minimization of the cumulative charge buildup necessitated the use of the minimum excitation level permitting accurate measurements. Sample current measurements were made by using a Burr-Brown 3523L electrometer operational amplifier and procelain feedback capacitor in a current-integrating configuration. Measurement sensitivity extended to about 1 fA by virtue of bias current compensation, temperature stabilization of the amplifier, and temperature control of the sample to within 0.04°C. The quiescent sample leakage current under high bias (on the order of 0.1 pA) was also compensated for, so that only the beam-induced signal was observed. (A detailed description of the experimental apparatus is given in Reference 13. This apparatus is a refined version of that used in previous charge transport studies.^{11, 12, 14})

Knowledge of the energy deposition profile and the pair creation energy for SiO₂ allows calculation of the maximum amount of charge transport that can occur in our test specimens. This condition will occur when all electron-hole pairs generated in the SiO₂ are separated and drift to the electrodes (oxide boundaries). Energy deposition profiles were determined based on the work of Everhart and Hoff¹⁵ for both 3.5- and 5-keV electrons impinging on the MOS structure studied here. Using the 5-keV profile¹² and a pair creation energy^{11, 16} of 18 eV we find that the calculated maximum ratio of integrated oxide current to integrated beam

¹¹J. R. Srouf, O. L. Curtis, Jr., and K. Y. Chiu, IEEE Trans. Nucl. Sci. 21, 73 (Dec. 1974).

¹²O. L. Curtis, Jr., J. R. Srouf, and K. Y. Chiu, IEEE Trans. Nucl. Sci. 22, 2174 (1975).

¹³J. R. Srouf, S. Othmer, O. L. Curtis, Jr., and K. Y. Chiu, Harry Diamond Laboratories Report HDL-CR-76-161-1, June 1976.

¹⁴O. L. Curtis, Jr., J. R. Srouf, and K. Y. Chiu, J. Appl. Phys. 45, 4506 (1974).

¹⁵T. E. Everhart and P. H. Hoff, J. Appl. Phys. 42, 5837 (1971).

¹⁶G. A. Ausman and F. B. McLean, Appl. Phys. Lett. 26, 173 (1975).

current is 109. Thus, if the measured charge multiplication factor, or "gain", equals 109, then presumably all carriers excited in the oxide layer reach the electrodes and none recombine in the bulk. By presenting experimental data in terms of gain versus time, temperature, and field, one can readily estimate for a given situation the fraction of generated charge that has been trapped or has recombined and the fraction that has been transported.

Although measurements were performed on several MOS capacitors from the same wafer, most of the charge transport data presented here were obtained on the same sample (#4). These data were representative of those for the wafer studied and constitute a comprehensive, consistent set of measurements which form the basis for interpretations given below regarding the mechanisms of low-temperature charge transport in SiC_2 films.

2.3 EXPERIMENTAL RESULTS

2.3.1 Charge Transport

Charge transport findings at 303°K are presented in Figure 1 where gain is plotted versus time following pulsed bombardment for various values of applied voltage. (Time is referenced to the beginning of the pulse.) Negligible additional charge transport is evident over the time regime examined except at the earliest times for relatively low applied voltages. At 54V (4×10^6 V/cm), the observed gain is 103, as compared to a predicted maximum of 109, and is invariant with time. Apparently all carriers that can be collected at this field are swept out in a time short compared to the bombarding pulsewidth. Since the observed gain at 54V is not yet saturated, a portion of the generated pairs may have undergone geminate and/or columnar recombination^{11,14,16} and this may explain why transport of only ~95% of the excited carriers is observed. We also note that systematic errors in the experiment, such as in the measurement of aluminum and oxide thickness, as well as in the knowledge of energy deposition profile, could affect both the experimental and theoretical values of

¹¹J. R. Srour, O. L. Curtis, Jr., and K. Y. Chiu, IEEE Trans. Nucl. Sci. 21, 73 (Dec. 1974).

¹⁴O. L. Curtis, Jr., J. R. Srour, and K. Y. Chiu, J. Appl. Phys. 45, 4506 (1974).

¹⁶G. A. Ausman and F. B. McLean, Appl. Phys. Lett. 26, 173 (1975).

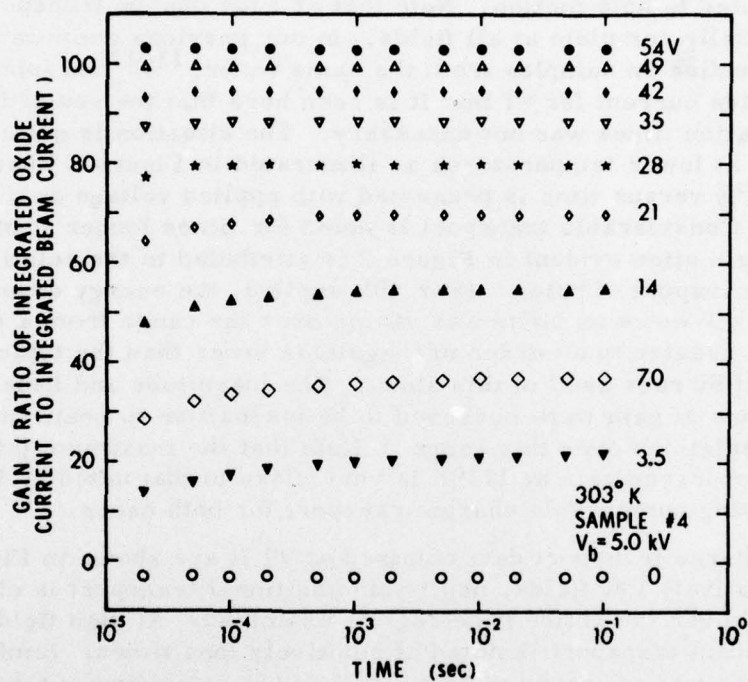


Figure 1. Gain at 303°K vs time following pulsed bombardment for an MOS capacitor with various values of applied voltage. Gain is a quantity proportional to the amount of charge transport in the oxide and is equal to the ratio of integrated oxide current to integrated electron-beam current.

gain, perhaps at the 5% level. Random errors, on the other hand, were kept to typical values of 2-3% by statistical averaging of data.

In keeping with observations at lower temperatures (discussed below) the early-time low-field transport evident in Figure 1 is attributed to hole motion. Note that at 1 ms charge transport is essentially complete at all fields. In our previous room temperature studies on samples from the same wafer,^{11,12} we integrated the oxide current for ~1 ms; it is seen here that the use of longer integration times was not necessary. The situation is quite different at lower temperatures as illustrated in Figure 2 where gain at 173°K versus time is presented with applied voltage as a parameter. Considerable transport is noted for times longer than 1 ms. Charge motion evident in Figure 2 is attributed to the relatively slow transport of holes. (For 49V applied, the energy deposited per 5-keV electron pulse was varied over the range from a factor of five greater to an order of magnitude lower than the typical dose of 80 rads used in this study. The magnitude and time dependence of gain were observed to be insensitive to beam intensity variations over this range.) Note that the maximum (highest-field) observed gain at 173°K is very close to that noted at 303°K, indicating comparable charge transport for both cases.

Charge transport data obtained at 90°K are shown in Figure 3. At relatively low fields, negligible additional transport is observed over the entire time regime examined. At high fields, significant transport is noted at relatively long times. Similar behavior was observed up to ~130°K and is indicative of a temperature-independent field-induced emission process for hole transport below this temperature. (Hole transport in SiO₂ at low temperatures has also been reported by other researchers.^{4,6}) This effect is more clearly illustrated in Figure 4 where the dependence of gain at 90°K on applied field is shown for several integration

⁴E. Harari, S. Wang, and B. S. H. Royce, J. Appl. Phys. 46, 1310 (1975).

⁶H. E. Boesch, Jr., F. B. McLean, J. M. McGarrity, and G. A. Ausman, Jr., IEEE Trans. Nucl. Sci. 22, 2163 (1975).

¹¹J. R. Srour, O. L. Curtis, Jr., and K. Y. Chiu, IEEE Trans. Nucl. Sci. 21, 73 (Dec. 1974).

¹²O. L. Curtis, Jr., J. R. Srour, and K. Y. Chiu, IEEE Trans. Nucl. Sci. 22, 2174 (1975).

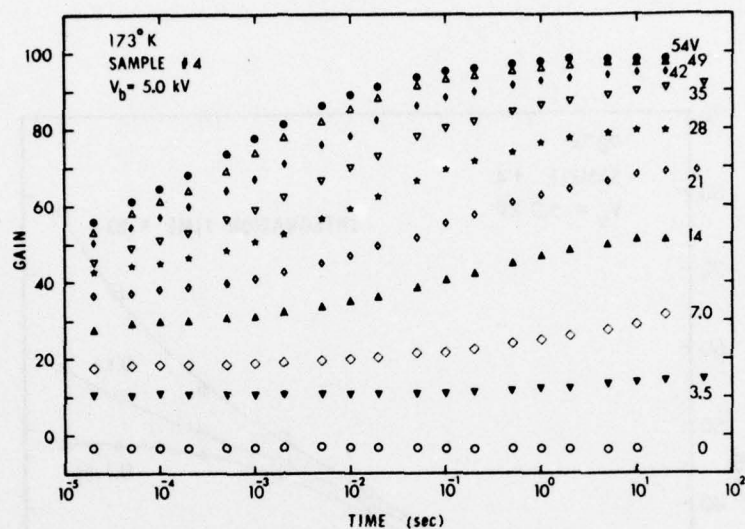


Figure 2. Gain at 173°K vs time following pulsed bombardment with applied voltage as a parameter for an MOS capacitor.

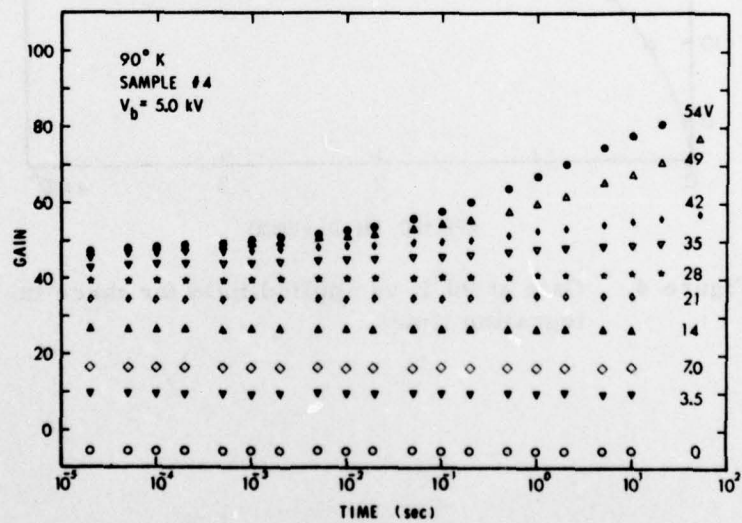


Figure 3. Gain at 90°K vs time following pulsed bombardment with applied voltage as a parameter for an MOS capacitor.

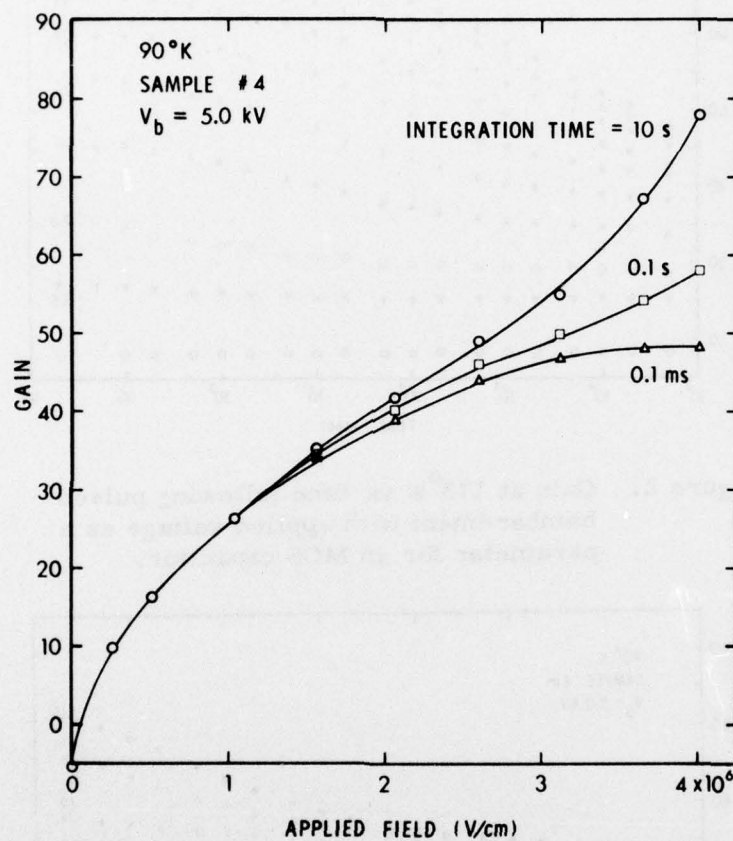


Figure 4. Gain at 90°K vs applied field for three integration times.

times. Below 2×10^6 V/cm, applying a field for relatively long times has a negligible effect on carrier transport. At higher fields, field-induced emission of trapped carriers appears to occur at long times, and this point is discussed below.

Because of the asymmetric 5-keV energy deposition profile in the SiO_2 layer,¹² holes will contribute more to observed charge transport than electrons for an applied positive bias since holes will, on the average, traverse a greater distance in the oxide. If all created electrons are swept out, and no hole motion occurs, then a collected fraction of 0.42 is expected for 5-keV electron bombardment. Upon comparing early-time gains at 90°K (Figure 3) with late-time gains at 303°K (Figure 1), the average ratio for all applied voltages is 0.47. Since these measured ratios are less than 0.5, the data suggest that holes are immobile at 90°K (except for high applied fields). Two possible reasons why the observed ratio (0.47) is larger than the expected value (0.42) for complete electron sweep-out and no hole motion are: (1) Hole transport may occur at low temperatures just following carrier generation before holes are trapped; (2) Trapping of some holes at room temperature may occur at deep levels either in the oxide bulk or near the SiO_2 -Si interface, resulting in incomplete collection of holes escaping recombination.

An additional experiment was performed to verify the conclusion of low-temperature hole immobility. A pulse of 3.5-keV electrons was employed for carrier excitation. Electron-hole pairs will be excited in the oxide only very near the Al- SiO_2 interface for this case. If holes are immobile but electrons are mobile at low temperatures, then observed gain for a relatively nonpenetrating beam should be significantly larger for an applied negative bias than for positive bias. We performed such an experiment and found this indeed to be the case. (Depletion-region relaxation phenomena in the Si substrate were taken into account in the negative-bias measurement.) We also compared the ratio of low-temperature gain to room-temperature gain for impinging 3.5-keV electrons to the same ratio for 5-keV electrons. In this positive-bias comparison, holes, if mobile, will contribute significantly more to observed gain than electrons for a nonpenetrating beam since the holes will travel a significantly greater distance in the

¹²O. L. Curtis, Jr., J. R. Srouer, and K. Y. Chiu, IEEE Trans. Nucl. Sci. 22, 2174 (1975).

oxide. The low-temperature-to-room-temperature gain ratio decreased as the beam energy was decreased from 5- to 3.5-keV, once again demonstrating hole immobility at low temperatures. The same conclusion has been reached by other workers^{5,6} using a different approach, and the present findings serve to substantiate their results.

Transport data are shown versus temperature in Figure 5 where gain at an applied voltage of 21V is plotted for various integration times. At the lowest temperature, observed gain is due to electron transport. Electrons that escape recombination are swept out in a time shorter than 10 μ s. Increasing the temperature or the integration time increases the amount of hole transport observed. At room temperature, all electrons and holes that escape recombination are swept to the electrodes for integration times ≥ 1 ms. The S-shaped form of the data in Figure 5 is also quite evident in Figure 6 where gain at 21V versus time is plotted for four relatively closely spaced intermediate temperatures. Significant hole transport is apparent over six decades in time.

2.3.2 Charge Buildup

Since holes are immobile at low temperatures for all fields except the highest ones examined, it is expected that the effects of positive charge buildup on the electrical properties of MOS devices will be enhanced compared to those at room temperature. This is indeed the case as shown in Figure 7 where flatband voltage shift is plotted versus dose (Co^{60} -- ~ 40 rads/s) for radiation-hardened MOS capacitors from the same wafer for which transport studies were performed (applied field = 10^6 V/cm). At 10^6 rads, the 300°K flatband shift is just over 2V whereas at 77°K the shift for an identical device is close to 40V. These data clearly demonstrate that an SiO_2 layer exhibiting radiation tolerance at or near room temperature will exhibit severe radiation-induced changes at cryogenic temperatures due to the decreased mobility of holes in the oxide.

Also shown in Figure 7 is a calculated curve (dashed) predicting the variation of flatband voltage with dose for pure oxide

⁵H. H. Sander and B. L. Gregory, IEEE Trans. Nuc. Sci. 22, 2157 (1975).

⁶H. E. Boesch, Jr., F. B. McLean, J. M. McGarrity, and G. A. Ausman, Jr., IEEE Trans. Nuc. Sci. 22, 2163 (1975).

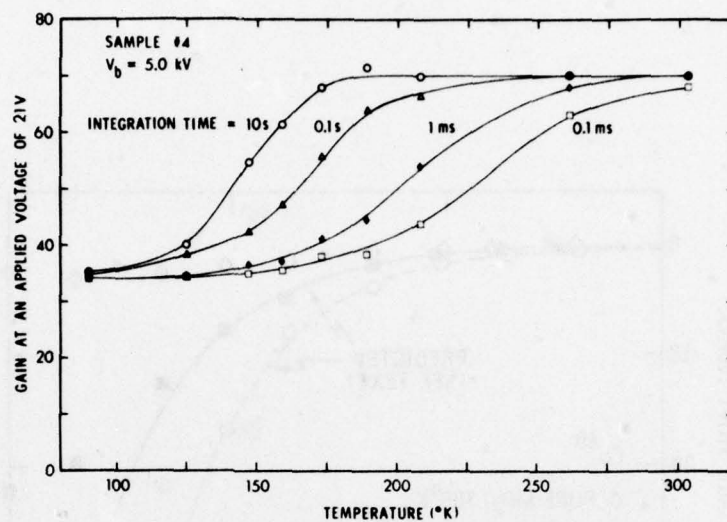


Figure 5. Gain at 21V vs temperature for four integration times.

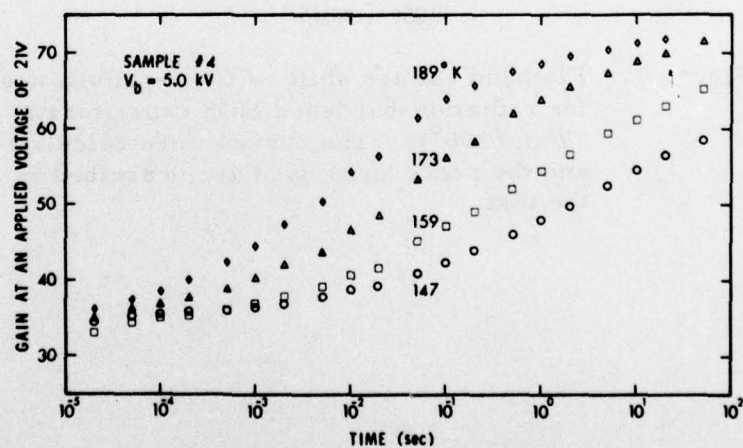


Figure 6. Gain at 21V vs time following pulsed bombardment for four temperatures.

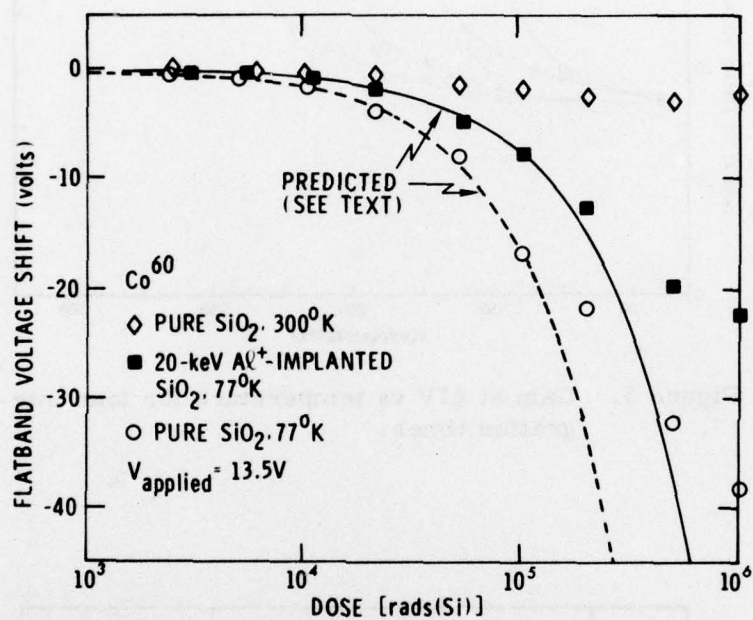


Figure 7. Flatband voltage shift vs Co^{60} -gamma dose for radiation-hardened MOS capacitors at 77 and 300°K . The curves were calculated and the procedures used are described in the text.

at 77°K. We assumed that all electrons escaping recombination are swept out of the oxide and that all holes escaping recombination are frozen in and form a uniform positive charge distribution. Denoting that fraction of generated holes escaping recombination by η and locating this positive charge at a point in the oxide midway between the interfaces, flatband voltage shift can be expressed as $\eta Q_p / 2C_{ox}$, where C_{ox} is oxide capacitance and Q_p is the charge associated with the total number of generated holes at a given dose. We determined Q_p by assuming 18 eV/pair, which yields 7.9×10^{12} pairs/cm³rad. The dashed curve in Figure 7 corresponds to a value for η of 0.5 and an excellent fit to the data is obtained up to a dose of 10^5 rads, with a significant discrepancy occurring at higher doses. At such doses, the field in the oxide will be perturbed due to the significant positive charge buildup, and will increase near the SiO₂-Si interface and decrease near the Al-SiO₂ interface. In the decreased-field region fewer electron-hole pairs will escape initial (and/or track) recombination, and in the increased-field region transport of generated holes will occur. (Figure 4 shows that hole transport does occur below 100°K at fields on the order of 2×10^6 V/cm and larger.) Both of these mechanisms will serve to reduce flatband shifts below expected values at high doses, and thus can qualitatively account for the discrepancy between prediction and experiment in Figure 7.

The present charge transport data at 90°K reveal that approximately one-half of the electrons and holes generated recombine at 10^6 V/cm and the remainder of the electrons are swept out, leaving approximately one-half the generated holes frozen in. Thus, use of $\eta = 0.5$ appears to be justified. However, one must also consider that low-energy electrons were used to obtain yield-versus-field information here whereas flatband-voltage-shift data of Figure 7 were obtained using a Co⁶⁰ gamma-ray source. It is thought that columnar recombination dominates in the former case¹⁶ whereas geminate recombination dominates in the latter situation. Boesch and McGarrity¹⁷ have obtained data for 13-MeV electron-bombarded MOS capacitors, where geminate recombination is expected, which suggest that a larger value of η (~ 0.85) should have been required to account for the data in Figure 7. In

¹⁶ G. A. Ausman and F. B. McLean, Appl. Phys. Lett. 26, 173 (1975).

¹⁷ H. E. Boesch, Jr., and J. M. McGarrity, IEEE Trans. Nucl. Sci. 23, 1520 (1976).

more recent Co^{60} charge buildup experiments (see Section 4.0), we have found that measured flatband shifts at 77°K for devices from a wafer processed in a manner similar to that employed here (oxide thickness $\approx 900 \text{ \AA}$) are consistent with a value for η of ~ 0.7 at 10^6 V/cm . Differences in experimental results are possibly attributable to partial recovery of flatband voltage during the relatively slow Co^{60} irradiations and to specimen differences.

One approach to producing MOS devices which are radiation tolerant at low temperatures is to introduce electron traps in the oxide which, when filled, would serve to compensate for immobile positive charge. Ion implantation is known to produce electron (and hole) traps in SiO_2 films.¹² The wafer employed in the present study also contained regions with Al^+ -implanted oxides.¹² Shown for comparison in Figure 7 are data for a 20-keV implanted device at 77°K, and it is seen that the flatband voltage shift is reduced compared to the pure-oxide unit. The solid curve in the figure corresponds to the predicted variation of flatband voltage with dose for an implanted sample.

The basic assumption made is that results of our previous room-temperature analysis¹² of the trapping properties of an implanted region can be applied to the present low-temperature data. Specifically, the mean distance (schubweg) electrons travel in the implanted zone before being permanently trapped is assumed temperature independent. The main temperature dependence expected is that of capture cross-section, and we neglect this consideration here for simplicity. For 20-keV Al^+ -implanted specimens, the electron schubweg in the implanted zone at room temperature for an applied field of 10^6 V/cm is¹² $\sim 220 \text{ \AA}$ and the ion penetration depth is $\sim 820 \text{ \AA}$. We assume that all electrons generated in the unimplanted zone escaping recombination are swept into the implanted region where they are trapped. The average position for these trapped electrons is thus 600 \AA from the Al-SiO_2 interface. Additionally, we assume that all electrons generated in the implanted zone are trapped there except for that portion which is swept out. The average position for this second contribution to trapped negative charge is thus 300 \AA from the Al-SiO_2 interface. Trapped electrons located at these two average positions in the

¹²O. L. Curtis, Jr., J. R. Srouer, and K. Y. Chiu, IEEE Trans. Nucl. Sci. 22, 2174 (1975).

implanted zone are effective in compensating for 55% of the uniformly trapped positive charge at low temperatures. Thus, the flatband shift for a 20-keV Al^+ -implanted device is expected to be 45% of that for an unimplanted specimen. The resulting curve in Figure 7 fits data for the implanted sample quite well for doses up to 10^5 rads. At higher doses, the discrepancy noted between prediction and experiment can be explained qualitatively in the same manner as above for an unimplanted device, with those considerations now applying primarily to the unimplanted region of an implanted oxide.

If electron traps were introduced in that portion of the oxide nearer the SiO_2 -Si interface, where immobile holes have a significantly larger effect on flatband voltage, then flatband shifts at cryogenic temperatures should be reduced much more significantly than in the present study. A deeper implantation might be an effective means for accomplishing this. If the implanted region extended completely through the oxide and the electron trap density remained the same as in the present 20-keV Al^+ -implanted devices, we expect that the flatband voltage shift would be 30% of that in an unimplanted unit. If twice as many electron traps are introduced by a higher implantation dose, half as many electrons escape the oxide and the average position of trapped electrons is closer to the oxide midpoint, resulting in an expected flatband shift that is 15% of the unimplanted-device value.

Although fabrication of radiation-hardened MOS devices by ion implanting the oxide no longer appears to be necessary (or reliable) for room-temperature applications, implanted devices may be of value for low-temperature hardening. Another possible approach to alleviating charge buildup problems at low temperatures is suggested by the data of Figures 3 and 4. By operating an MOS device at a relatively high field, significant hole transport will occur within seconds following carrier generation, thereby reducing the threshold voltage shift. For example, operating at 4×10^6 V/cm (54V for a 0.135 μm oxide thickness or 20V for 0.05 μm) should result in most of the generated holes being swept to the SiO_2 -Si interface in a few minutes. Some will be trapped there but the voltage shift should be significantly less than for the case of a relatively low applied field. It is interesting to note that threshold shift, after an initial increase, should decrease with increasing bias for a given dose at low temperatures. Such behavior has been confirmed experimentally. (See Section 4.0 of this report.)

2.4 DISCUSSION

The present study demonstrates the dispersive nature of charge transport in SiO_2 films below room temperature. For the purpose of obtaining an understanding of the physical mechanisms underlying this transport process, it is of interest to extract an activation energy from the data. One approach is to examine the temperature dependence of the time required to transport a certain amount of charge. Figure 8 presents a plot of the time required to reach specific values of gain versus reciprocal temperature over a temperature range for which significant hole transport was observed. (Information in Figure 8 was derived from data in Figure 6.) Data shown in Figure 8 are for a moderate applied voltage (21V, 1.6×10^6 V/cm) and an intermediate temperature range (147 to 189°K). Activation energies are given in the figure and it is seen that a monotonic increase in energy occurs with increasing gain (or increasing time). This result suggests a multiple-trapping model of charge transport in which holes undergo a series of trapping and detrapping events over a range of energy levels. Under this description, charge transport occurs in the valence band between these events. With increasing time following excitation, holes settle into deeper trap levels where detrapping is slower. Figure 8 indicates that holes are trapped at early times at levels with a median position ~ 0.3 eV from the band edge and at later times have settled into deeper levels with a median position of ~ 0.5 eV.

The temperature dependence of observed hole transport thus yields a spread in activation energies of ~ 0.2 eV. As a check on the applicability of the multiple-trapping model, we examined the question of whether such a spread in trap level position can account for the observed dispersion in charge transport (or gain) versus time. Our approach was to determine instantaneous charge-collection time constants as a function of time. (Time constants were determined from the local slope at points on a semilogarithmic plot of the relative amount of uncollected hole charge versus time.) To determine the activation energy spread corresponding to the resulting time constant range, we first assumed that all trapping centers are identical except for their energy level, i.e., "frequency-factor" or pre-exponential terms are assumed equal. The time constant τ associated with a hole trap level E_t should be proportional to $\exp(E_t - E_v)/kT$, and the ratio of time constants for two levels can be expressed as

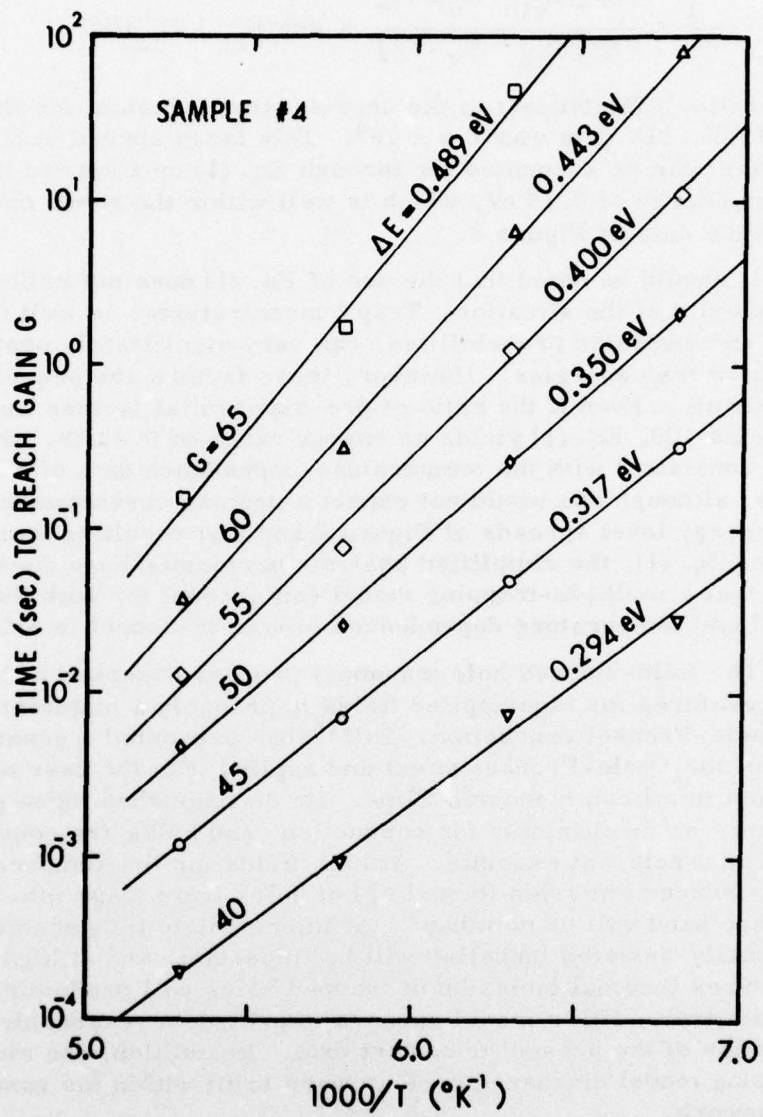


Figure 8. Time to reach particular values of gain vs reciprocal temperature. Activation energies obtained from these data are shown.

$$\frac{\tau_1}{\tau_2} = \frac{\exp[(E_{t1} - E_v)/kT]}{\exp[(E_{t2} - E_v)/kT]} = \exp(E_{t1} - E_{t2})/kT. \quad (1)$$

The ratio of the longest to the shortest time constant for the case of 173°K, 21V data was 1.8×10^4 . This large spread in time constant can be accounted for through Eq. (1) by a spread in activation energy of 0.15 eV, which is well within the range obtained from the data of Figure 8.

It should be noted that the use of Eq. (1) does not reflect the complexity of the situation. Trap concentrations, as well as capture and emission probabilities, can vary significantly over the range of trap energies. However, these factors are pre-exponential terms. Even if the ratio of pre-exponential factors were as large as 100, Eq. (1) yields an energy range of 0.22 eV, which is still consistent with the temperature-dependence data of Figure 8. Thus, although one would not expect a precise correspondence in the energy level spreads of Figure 8 and that resulting from the use of Eq. (1), the simplified analysis performed here does suggest that a multiple-trapping model can account for both the temporal and temperature dependences of hole transport in SiO₂ films.

The field-induced hole transport process observed at low temperatures for high applied fields is probably a manifestation of Poole-Frenkel conduction. Hill¹⁸ has presented a generalization of the Poole-Frenkel effect and applied it to the case of conduction in silicon monoxide films. He distinguishes three general regimes or mechanisms for conduction, and holes are considered here as a relevant example. At high fields for low temperatures, field-induced emission (tunneling) of holes from traps into the valence band will be dominant. At intermediate temperatures, thermally-assisted tunneling will be important, and at high temperatures thermal emission of trapped holes will predominate. Qualitatively, Hill's model appears to provide a reasonable description of the present transport data. In addition, the multiple-trapping model discussed here appears to fit within his generalized framework.

¹⁸ R. H. Hill, Phil. Mag. 23, 59 (1971).

Boesch et al.^{6,9} have used the stochastic hopping transport model of Scher and Montroll⁸ to describe dispersive hole motion in SiO₂ films. In this model, hole transport takes place via hopping between localized sites, with no transition to the valence band occurring. One motivation for invoking the stochastic model instead of a multiple-trapping description was to attempt to explain the discrepancy between optical and thermal activation energies for trapped holes in SiO₂ noted by Harari et al.⁴ Harari observed an optical activation energy of 1.8 eV in photodepopulation measurements and indicated that this should correspond to a thermal activation energy of 0.95 eV based on a relationship between thermal and optical trap depths.¹⁹ This expected thermal energy is ~0.5 eV deeper than that obtained from Figure 8 in the present work, and thus an apparent problem is posed for the multiple-trapping model but not the stochastic model.⁶ There are several possible explanations for this discrepancy. First, the ratio of optical to thermal activation energies may be larger than the value of 1.9 employed by Harari et al. since the relation used is quite approximate.¹⁹ Second, the ionization dose used in their optical experiments was very large compared to the dose used in the present investigation. In fact, irradiation was continued until the flat-band voltage shift saturated, indicating that all traps were filled. Relative occupancy may be quite different under high and low dose conditions. If the shallow levels have larger capture cross sections, they will fill more rapidly than the deeper levels and have a more pronounced effect at low doses, even though they are present in lower concentrations. Large doses will tend to fill all the levels and reflect the total distribution, irrespective of relative cross sections. Furthermore, the optical data of Harari et al. indicate the presence of a substantial number of levels in the lower energy range. Their data do not extend below ~1 eV in photon energy and the population of levels seems to be increasing with

⁴ E. Harari, S. Wang, and B. S. H. Royce, *J. Appl. Phys.* **46**, 1310 (1975).

⁶ H. E. Boesch, Jr., F. B. McLean, J. M. McGarrity, and G. A. Ausman, Jr., *IEEE Trans. Nucl. Sci.* **22**, 2163 (1975).

⁸ H. Scher and E. W. Montroll, *Phys. Rev.* **B12**, 2455 (1975).

⁹ F. B. McLean, G. A. Ausman, Jr., H. E. Boesch, Jr., and J. M. McGarrity, *J. Appl. Phys.* **47**, 1529 (1976).

¹⁹ N. F. Mott and R. W. Gurney, *Electronic Processes in Ionic Crystals*, 2d. Ed. (Dover, New York, 1964), 160.

decreasing energy in this range. Third, their optical measurements were made after long periods of irradiation. As discussed above, the thermal activation energy observed here increases with time as holes (according to the multiple-trapping model) settle into deeper traps. Considering these three factors, the apparent discrepancy between optical and thermal data may not be significant.

Apparent problems exist in accounting for the present data using the stochastic hopping transport model. The basic stochastic transport description predicts universality in charge transport curves, namely, an invariance with respect to field and temperature in the shape of such curves. A single activation energy is associated with the transport process in this model. Data presented here exhibit a spread in activation energy and do not exhibit universality. A problem still appears to occur if we attempt to apply a more general hopping model to the present data. To explain the situation qualitatively, consider first the findings of Boesch et al.⁶ They were able to account for hole transport in their test specimens using the stochastic model with a single activation energy (0.3 eV). Thus, significant dispersion in hole transport, associated with randomly distributed hopping sites (hopping time distribution), can occur in the stochastic description with only a single thermal activation energy. Now consider a spread in thermal activation energies within the stochastic transport framework. We expect two contributions to the dispersive nature of hole transport in this case: (1) dispersion due to the range of trap energies at a given site; (2) dispersion due to the intersite hopping time distribution. Thus, under the stochastic model we expect more dispersion in the temporal dependence of hole transport for the case of a range of thermal activation energies than for the single activation-energy situation. That is, the spread in activation energies obtained from temperature-dependence data is not expected to be as large as the apparent energy spread associated with temporal-dependence data for the stochastic hopping transport model. Data presented above are not in agreement with this expectation.

⁶ H. E. Boesch, Jr., F. B. McLean, J. M. McGarrity, and G. A. Ausman, Jr., IEEE Trans. Nucl. Sci. 22, 2163 (1975).

McLean et al.²⁰ have studied the temporal dependence of flatband voltage shift in MOS capacitors following a pulse of ionizing radiation. They observed a recovery process at low temperatures ($<150^{\circ}\text{K}$) that was not evident in the present investigation. Their activation energy plot (the counterpart of Figure 8 in this report) revealed two regimes: a higher temperature regime characterized by an activation energy on the order of 0.4 eV and a lower temperature regime with a considerably smaller activation energy. They noted the onset of appreciable flatband voltage recovery at 1 sec for a specimen at 87°K , and presumably charge transport was responsible for this recovery. On the other hand, we did not observe transport in our specimens under the same conditions. At 10^6 V/cm, the field employed by McLean et al., no charge transport is evident at 90°K in our samples for times up to 10 sec after bombardment (see 14V data in Figure 3). This same statement applies for applied fields up to twice this value. Regarding our activation energy plot, two data points obtained¹³ at 125°K ($1000/T = 8.0$; data not shown in Figure 8) are in agreement with extrapolated fits to the $G = 40$ and 45 data, once again demonstrating that the lower activation energy behavior noted by McLean et al. below 150°K is not evident in our specimens. This discrepancy suggests that charge transport (or flatband voltage recovery) behavior at low temperatures in SiO_2 films is processing dependent. On the other hand, this discrepancy may reflect differences in experimental conditions and techniques. McLean employed C-V measurements at relatively high doses whereas we employed direct measurements of charge transport at low doses.

At present, in weighing the multiple-trapping model versus the stochastic transport model, it is difficult to state conclusively which is more appropriate for describing the available experimental data. However, it does not appear necessary to invoke hopping transport in the present case since the multiple-trapping description accounts for the data quite well. Indeed, the present data seem inconsistent with the stochastic model. (We have developed an analytical formulation of the multiple-trapping model

¹³ J. R. Srouf, S. Othmer, O. L. Curtis, Jr., and K. Y. Chiu, Harry Diamond Laboratories Report HDL-CR-76-161-1, June 1976.

²⁰ F. B. McLean, H. E. Boesch, Jr., and J. M. McGarrity, IEEE Trans. Nucl. Sci. 23, 1506 (1976).

which yields excellent fits to the present experimental data. This work is described in Section 3.0 of this report.)

The present hole transport data can be interpreted in terms of mobility and a preliminary analysis has been performed. (See Section 3.0 for more details.) Mobility is observed to depend on electric field, time after excitation, and temperature. At 173°K, the trap-limited hole mobility ranges from $\sim 3 \times 10^{-9} \text{ cm}^2/\text{Vsec}$ at 10^{-4} sec to $\sim 1.5 \times 10^{-12} \text{ cm}^2/\text{Vsec}$ at 1 sec following excitation. A strong field dependence ($\mu \propto E^{3.2}$) was noted at intermediate temperatures, with an even stronger dependence ($\mu \propto E^{12.6}$) observed at the lowest temperatures. An Arrhenius plot of mobility, measured at the point where one-half the holes have been collected, yields an activation energy of 0.39 eV.

In summary, we have examined in detail the temporal, temperature, and electric-field dependences of charge transport in SiO_2 films over wide ranges. Below 130°K, temperature-independent transport was noted at high fields and attributed to field-induced emission of trapped holes. Experiments were performed which substantiate the conclusion that holes are immobile at low temperatures for relatively low applied fields. This frozen-in positive charge gives rise to significant flatband voltage shifts and thus creates a potentially severe practical problem for MOS devices operated at low temperatures in an ionizing radiation environment. For such applications, development of a new class of radiation-tolerant devices will be necessary, and the present work demonstrates that either applying a relatively high field to the oxide or utilizing an ion-implanted oxide may be useful approaches to meeting this requirement.

SECTION 3.0

THE MULTIPLE-TRAPPING MODEL AND HOLE TRANSPORT IN SiO_2 *

3.1 INTRODUCTION

Ionizing radiation alters the electrical properties of silicon MOS devices; the primary source of this vulnerability is the trapping inside SiO_2 layers of holes generated therein by radiation. At room temperature a fraction of the holes generated inside the oxide are trapped near the oxide-semiconductor interface, and at low temperatures they are immobilized within the bulk of the SiO_2 . To understand radiation effects on MOS devices and to intelligently approach the problem of reducing device vulnerability, it would be useful to be able to describe the charge transport process in SiO_2 films quantitatively. That is the goal of this section.

Various workers have studied charge transport and charge buildup in SiO_2 films during the past several years. Under a coordinated effort, two groups have collected a large amount of information about hole transport in SiO_2 over a wide range of experimental conditions. These groups are located at Harry Diamond Laboratories and at Northrop Research and Technology Center. A number of papers have been published by these groups and are referenced here in chronological order.^{14, 11, 16, 6, 12, 9, 21, 17, 20}

*Accepted for publication in the Journal of Applied Physics.

⁶H. E. Boesch, Jr., F. B. McLean, J. M. McGarrity, and G. A. Ausman, Jr., IEEE Trans. Nucl. Sci. 22, 2163 (1975).

⁹F. B. McLean, G. A. Ausman, Jr., H. E. Boesch, Jr., and J. M. McGarrity, J. Appl. Phys. 47, 1529 (1976).

¹¹J. R. Srouf, O. L. Curtis, Jr., and K. Y. Chiu, IEEE Trans. Nucl. Sci. 21, 73 (Dec. 1974).

¹²O. L. Curtis, Jr., J. R. Srouf, and K. Y. Chiu, IEEE Trans. Nucl. Sci. 22, 2174 (1975).

¹⁴O. L. Curtis, Jr., J. R. Srouf, and K. Y. Chiu, J. Appl. Phys. 45, 4506 (1974).

¹⁶G. A. Ausman and F. B. McLean, Appl. Phys. Lett. 26, 173 (1975).

¹⁷H. E. Boesch, Jr., and J. M. McGarrity, IEEE Trans. Nucl. Sci. 23, 1520 (1976).

²⁰F. B. McLean, H. E. Boesch, Jr., and J. M. McGarrity, IEEE Trans. Nucl. Sci. 23, 1506 (1976).

Related charge transport studies have also been performed by R. C. Hughes at Sandia Laboratories.^{7, 22-24}

In the course of these previous investigations, an analysis of hole transport has been presented which is predicated on a model involving stochastic hopping transport. This description, based on the work of Scher and Montroll,⁸ accounts for many of the features of hole conduction in SiO_2 and has been termed the Continuous Time Random Walk (CTRW) model. A description of the model and its success in fitting various data are presented in several papers.^{6, 9, 20, 24}

The success of the CTRW model in fitting experimental data is impressive. A wide range of experimental observations can be understood on this basis. However, there has been some reticence to accept the CTRW model completely because of observations that the apparent activation energy for the charge collection process depends on the fraction of charge collected²¹ (see Section 2.0). This observation is at odds with the CTRW model as it has been presented, since that model predicts "universality"; i.e., charge transport curves obtained at different temperatures should superimpose with a simple shift in the time axis.⁶ Although charge collection curves obtained at different temperatures do superimpose approximately, there is some deviation, and this deviation is in the direction predicted by the multiple-trapping model which is described herein. Until the present, objections to the CTRW model have been qualitative in nature and it was not known whether the multiple-trapping model could adequately account for transport

⁶ H. E. Boesch, Jr., F. B. McLean, J. M. McGarrity, and G. A. Ausman, Jr., IEEE Trans. Nucl. Sci. 22, 2163 (1975).

⁷ R. C. Hughes, E. P. EerNisse, and H. J. Stein, IEEE Trans. Nucl. Sci. 22, 2227 (1975).

⁸ H. Scher and E. W. Montroll, Phys. Rev. B12, 2455 (1975).

⁹ F. B. McLean, G. A. Ausman, Jr., H. E. Boesch, Jr., and J. M. McGarrity, J. Appl. Phys. 47, 1529 (1976).

²⁰ F. B. McLean, H. E. Boesch, Jr., and J. M. McGarrity, IEEE Trans. Nucl. Sci. 23, 1506 (1976).

²¹ J. R. Srouf, S. Othmer, O. L. Curtis, Jr., and K. Y. Chiu, IEEE Trans. Nucl. Sci. 23, 1513 (1976).

²² R. C. Hughes, Phys. Rev. Lett. 30, 1333 (1973).

²³ R. C. Hughes, Appl. Phys. Lett. 26, 436 (1976).

²⁴ R. C. Hughes, Phys. Rev. B15, 2012 (1977).

data. This section presents an analysis based on the multiple-trapping model, and it is seen that the agreement between the model and experimental data herein considered is noteworthy. For fitting these data, the multiple-trapping model is significantly more successful than the CTRW model.

3.2 FORMULATION OF THE MODEL

The multiple-trapping model is illustrated schematically in Figure 9. The concept is very simple. Only hole transport need be considered because excess electrons generated simultaneously with the holes are swept out of the oxide in a time short to any considered here. The dominance of holes in the observed transport process has been established elsewhere.^{6,7,21} The aspect of hole transport with which we are concerned is the amount of time it takes a hole generated within the SiO₂ to be transported to either electrode. Consider an insulator containing excess holes and several trapping levels. Upon creation, the holes are subject to capture at all the trapping levels. However, after capture the time spent in a given level will depend strongly on energy position, varying approximately as $\exp(\Delta E/kT)$ if the carriers are thermally re-emitted. (The quantity ΔE is the energy difference between the trap level and the valence band edge.) The result of such a process is intuitively obvious; as time progresses, the holes will settle into deeper traps. This is in keeping with the experimental observation²¹ that the apparent trap level position, determined from an Arrhenius plot, increases with the increasing fraction of generated charge that is collected. To provide a quantitative framework for this intuitive analysis it is necessary to formulate a set of coupled differential equations describing the transport process.

Let p_i represent the concentration of trapped holes at a trap energy level E_i . The rate of change of p_i is given by

$$dp_i/dt = c_p p N_i^0 - e_p N_i^+, \quad (1)$$

⁶ H. E. Boesch, Jr., F. B. McLean, J. M. McGarrity, and G. A. Ausman, Jr., IEEE Trans. Nucl. Sci. 22, 2163 (1975).

⁷ R. C. Hughes, E. P. EerNisse, and H. J. Stein, IEEE Trans. Nucl. Sci. 22, 2227 (1975).

²¹ J. R. Srour, S. Othmer, O. L. Curtis, Jr., and K. Y. Chiu, IEEE Trans. Nucl. Sci. 23, 1513 (1976).

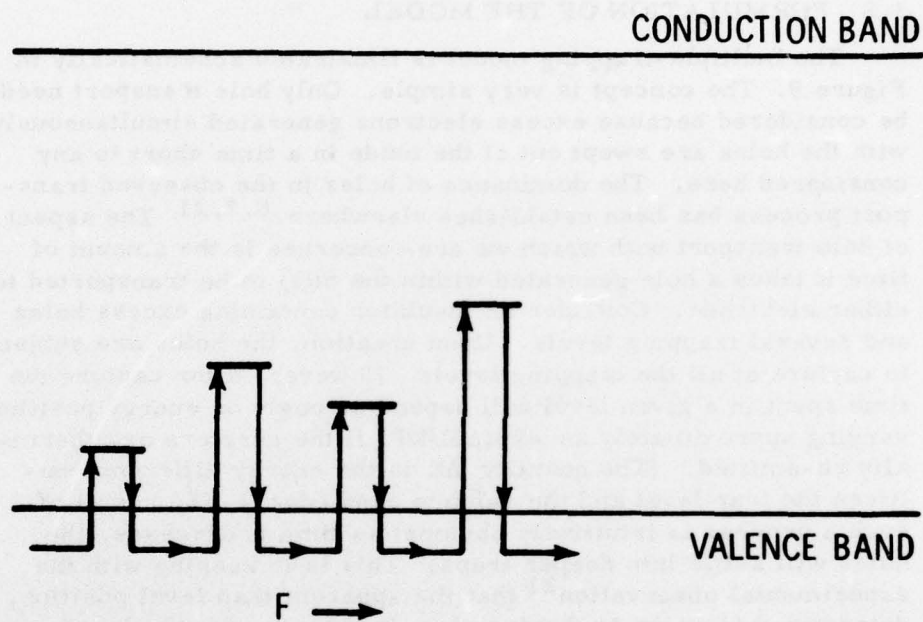


Figure 9. A simplified representation of the multiple-trapping model.

where c_p is the hole capture probability (assumed to be the same for all levels), p is the concentration of holes in the valence band, N_i^0 is the concentration of traps at E_i not already containing a hole, and N_i^+ is the number of traps containing a hole ($N_i^+ = p_i$). Assuming low-injection-level conditions, $N_i^0 = N_i$, the total trap level concentration at E_i . The emission factor e_p is of the form $e_p = e_0 \exp(-E_i/kT)$, where the pre-exponential factor e_0 was assumed in this analysis to be the same for all centers. Thus,

$$dp_i/dt = c_p p N_i - p_i e_0 \exp(-E_i/kT). \quad (2)$$

In addition to one differential equation of this form for each level, there must be a conservation equation. In the absence of hole sweepout the net change in hole concentration would be zero, or

$$dp/dt + \sum_{i=1}^n dp_i/dt = 0, \quad (3)$$

where n is the number of trapping levels considered. Without knowing the details of the transport process a priori, it is not possible to provide exactly for sweepout in the conservation equation. To account for a sweepout term, a simplifying approximation was made. It was assumed that during the sweepout process the hole distribution in the oxide remains uniform. For extremely dispersive transport such as is considered here, this should be a reasonable approach. (The results are not sensitive to this approximation.) Under this assumption, the rate of hole sweepout is proportional to the number of holes in the valence band and the applied electric field F . The net rate of change of hole concentration is then given by

$$dp/dt + \sum_{i=1}^n dp_i/dt = -k_1 p F, \quad (4)$$

where k_1 contains the free-carrier mobility and other factors. Thus, the formulation of the mathematical problem is quite simple and leads to the requirement of solving $n+1$ coupled differential equations. As an initial ($t=0$) condition, a certain concentration of holes in the valence band and no trapped charge was assumed. This condition corresponds to an experimental situation in which

holes are generated by a short pulse of ionizing radiation. Solutions to Eqs. (2) and (4) were obtained using numerical methods in conjunction with a large-scale digital computer.

Measured activation energies (see discussion below) range from 0.29 to 0.49 eV. With the idea that a continuum of energy levels might be involved, a first attempt at modeling was made using ten levels 0.05 eV apart in the range 0.15 eV to 0.6 eV. Equal concentrations of each level were assumed. With such a distribution, no reasonable fit to charge transport data was possible. Considerable structure in the solution was observed, indicating that if the model were to describe the data accurately, closer spacing of the levels would be required and/or the concentration of trap levels would have to decrease with increasing trap depth.

In a disordered solid, it may be reasonable to expect the existence of levels near the valence band with a concentration that decreases with energy separation from the band edge. Such levels would correspond to valence band states perturbed by crystal disorder, where the number of states with a given amount of disorder would vary inversely with the amount of disorder. The degree of physical perturbation may correspond to a Gaussian distribution about zero, so the number of states with a valence state energy position above the edge of the valence band might decrease exponentially with increasing energy. It is not clear whether such a picture would withstand strict scrutiny, but it may receive some support from the fact that many amorphous materials display optical absorption coefficients that vary exponentially with energy near the band edge, e.g., GeTe,²⁵ Se,²⁶ and As₂S₃.²⁷ In any case, it is as simple as any nonuniform distribution that can be imagined. We employed an exponential distribution here with considerable success. The term N_i in Eq. (2) was replaced with

$$N_i(E_i) = N_0 \exp(-E_i/\beta) \quad (5)$$

where N_0 is the trap concentration at the valence band edge, and the parameter β determines the rate of change of concentration

²⁵ S. K. Bahl and K. L. Chopra, *J. Appl. Phys.* **40**, 4940 (1969).

²⁶ K. J. Siemsen and E. W. Fenton, *Phys. Rev.* **161**, 632 (1967).

²⁷ K. Kosek and J. Tauc, *Czech. J. Phys.* **B20**, 94 (1970).

of trap levels with energy. Since Eq. (2) contains the product $c_p N_i$, absolute values of N_i may not be deduced from fitting the model to the experimental data.

The choice of parameters to fit the experimental data is discussed below. It is useful to consider first the physical process in more detail so that the effect of varying parameters will be understood. Of particular value in terms of added insight is the time dependence of occupancy of trap levels at different energy positions following pulsed carrier excitation. Figure 10 shows relative trap occupancies for a quasi-continuous (level spacing = 0.03 eV) trap distribution with $\beta = 0.04$ eV and $k_1 F = 4 \times 10^5 \text{ s}^{-1}$. Assumed values for the quantities $c_p N_0$ and e_0 were $3 \times 10^9 \text{ cm}^3 \text{ s}^{-1}$ and 10^{12} s^{-1} , respectively. The occupancy of each energy level from 0.21 eV to 0.57 eV is shown as a function of time following hole generation. Also shown is the total trap occupancy. Of particular note is the fact that at any given time one level tends to contain the majority of trapped holes. Thus, at a particular time where a given level has a peak in occupancy, that level will tend to dominate the transport behavior. The relative spacing between the peaks depends on the parameter β and decreases with decreasing β . The spacings in the peaks shown in Figure 10 are much closer than if a uniform (as opposed to an exponential) trap distribution were employed. Below, plots of hole current as a function of time will be presented. The analytical results using the parameters of Figure 10 show almost no structure due to the use of discrete levels in the model and thus such a set of discrete levels can be used to represent adequately a continuum of energy levels. However, for identical energy level spacings but equal concentrations of each level, undulations in current versus time curves were quite apparent. Figure 10 illustrates the observation that even if shallower and deeper levels are present, they will not affect behavior in the time range of interest, and can be neglected. For instance, a level at 0.18 eV has negligible impact for times greater than 1 μs , while a level at 0.6 eV would not become significant until after 1000 sec.

3.3 RESULTS

3.3.1 Dependence of Hole Collection on Time

Typical results of the calculations are shown in Figure 11 where fraction of hole charge collection (which corresponds to one

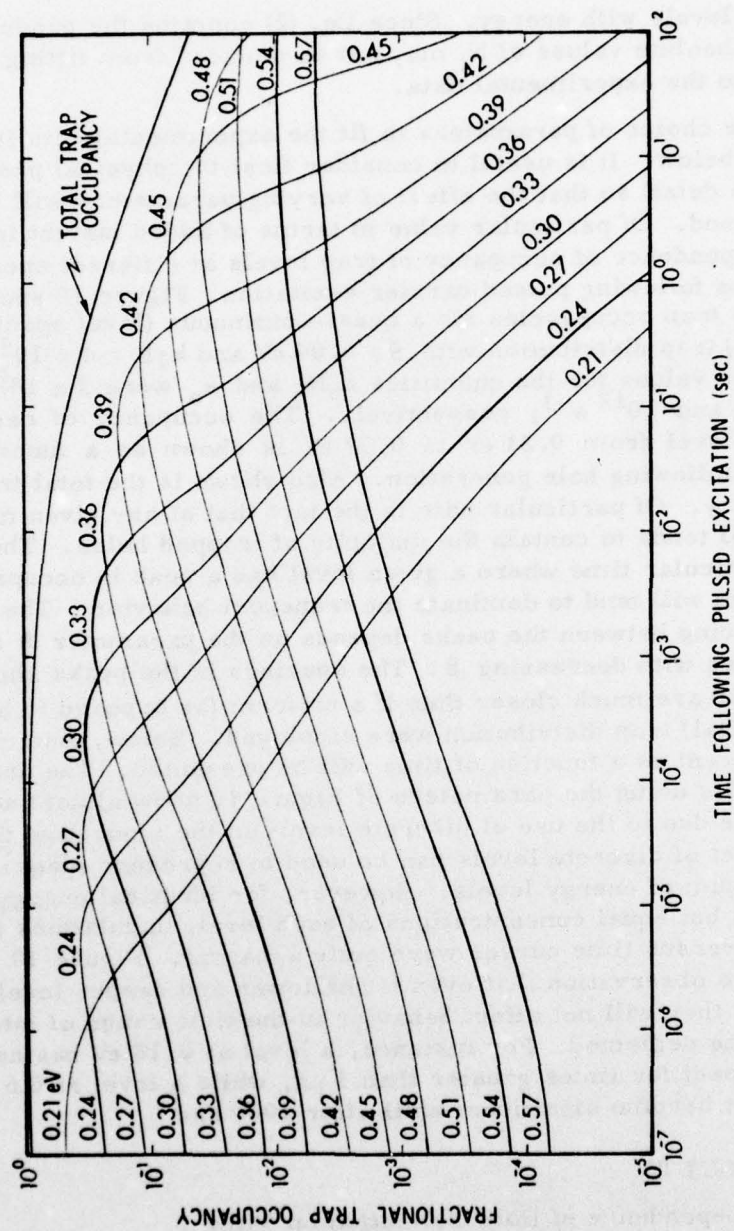


Figure 10. Relative trap occupancies for a specific choice of model parameters.

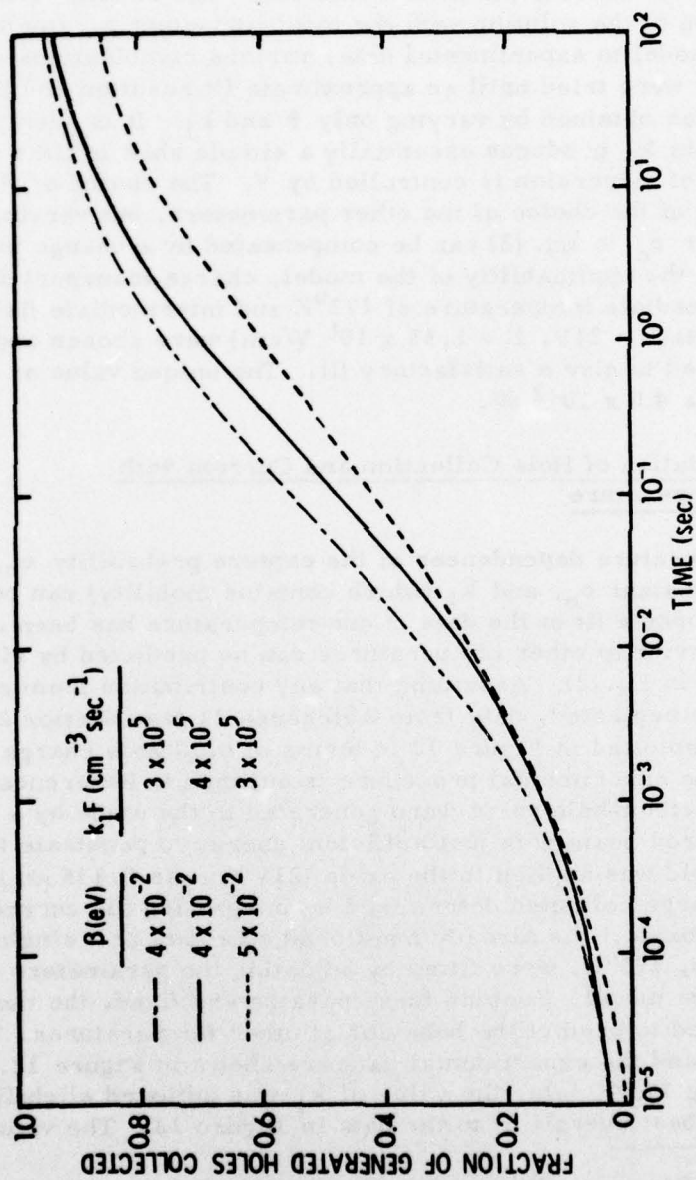


Figure 11. An illustration of the variation in model predictions with model parameters.

minus the total trap occupancy, since the relative number of holes in the valence band at any time is very small) is plotted as a function of time for various parameter choices. The results illustrate the variation of the solution with the most important parameters. To fit the model to experimental data, various combinations of parameters were tried until an approximate fit resulted and then a final fit was obtained by varying only β and k_1 . It is seen that a variation in k_1 produces essentially a simple shift in time while the amount of dispersion is controlled by β . The choice of β is independent of the choice of the other parameters, but varying either c_p or e_o in Eq. (2) can be compensated by a change in k_1 . To examine the applicability of the model, charge transport data²¹ at an intermediate temperature of 173°K and intermediate field (applied voltage = 21V, $F = 1.55 \times 10^6$ V/cm) were chosen and β and k_1 varied to give a satisfactory fit. The unique value of β so obtained was 4.0×10^{-2} eV.

3.3.2 Variation of Hole Collection and Current with Temperature

If temperature dependences of the capture probability c_p , emission constant e_o , and k_1 (which contains mobility) can be neglected, once a fit to the data at one temperature has been obtained, behavior at other temperatures can be predicted by simply changing T in Eq.(2). Assuming that any contribution from electrons can be neglected, data from Reference 21 (see Section 2.0) have been replotted in Figure 12 in terms of total hole charge collected. (The experimental procedure is outlined in Reference 21. Briefly, electron-hole pairs were generated in the oxide by a pulsed electron beam with just sufficient energy to penetrate the oxide. A field was applied to the oxide (21V across 0.135 μ m) and the total charge collected determined by integrating the current through the oxide.) As already mentioned, the data at a single temperature, 173°K, were fitted by adjusting the parameters β and k_1 in the model. Keeping these parameters fixed, the model was then used to predict the behavior at other temperatures. These predictions and the experimental data are shown in Figure 12. (After fitting 173°K data, the value of k_1 was adjusted slightly to provide the best overall fit to the data in Figure 12. The value of

²¹ J. R. Srour, S. Othmer, O. L. Curtis, Jr., and K. Y. Chiu, IEEE Trans. Nucl. Sci. 23, 1513 (1976).

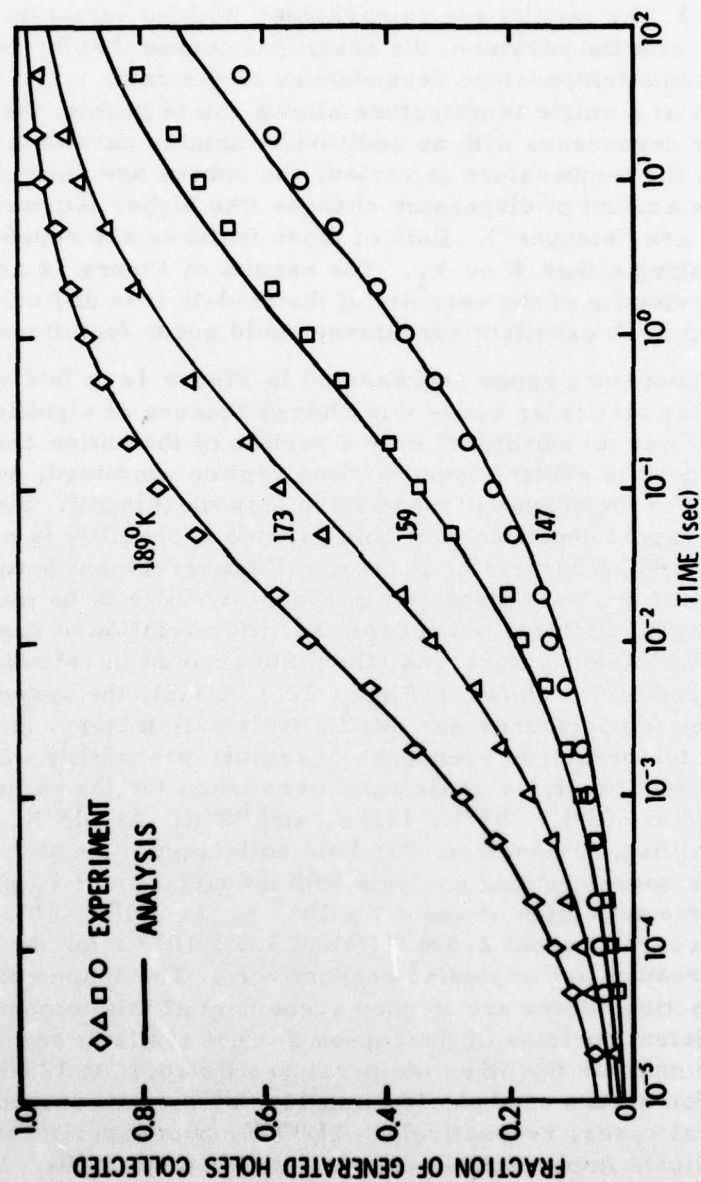


Figure 12. The variation of hole collection with time and temperature: a comparison of experimental results and predictions of the multiple-trapping model. (Data shown are taken from Figure 6 of Reference 21 -- see Section 2.0.)

$k_1 F$ used was $3.1 \times 10^5 \text{ s}^{-1}$; all other parameter values were equal to those employed for the calculations of Figure 10, as given above.) The results are remarkable: With no variation in parameters with temperature, the analytical curves display very nearly the same temperature dependences as the data; i.e., fitting the data at a single temperature allows one to predict the temperature dependence with no additional variable parameters. Note that as the temperature is varied, the curves are shifted with time and the amount of dispersion changes (the higher temperature curves are "steeper"). Both of these features are reproduced without changing either β or k_1 . The results of Figure 12 are convincing evidence of the veracity of the model; it is difficult to conceive that such excellent agreement would occur fortuitously.

The temperature range represented in Figure 12 is fairly narrow. That particular range was chosen because at significantly higher and lower temperatures only a portion of the entire charge collection curve is evident over the time regime examined, and comparisons of the shapes of curves are less meaningful. Since some temperature dependence of hole capture probability is expected, it would be surprising if the excellent agreement between experiment and analysis displayed in Figure 12 were to be manifested at greatly different temperatures. (No variation of capture probability with temperature was taken into account in calculating the model predictions shown in Figure 12.) In fact, the agreement at other temperatures was qualitatively satisfactory, and only a weak temperature dependence of capture probability was indicated. Specifically, comparisons were made for the same electric field at 303°K, 261°K, 125°K, and 90°K. At 303°K, the experimental data demonstrate 90% hole collection at about $3 \times 10^{-5} \text{ s}$. The corresponding analysis with no variation of c_p predicts the same collection at about $7 \times 10^{-5} \text{ s}$. At 261°K, 60% collection occurs at about 2.5×10^{-5} and $3.5 \times 10^{-5} \text{ s}$ for the experimental results and analysis, respectively. The shapes of the charge collection curves are in good agreement at this temperature. (Sufficient portions of the curves are not available to make such a statement for the other temperatures listed.) At 125°K, 20% collection occurs at about 14s and 11s for the experimental and analytical cases, respectively. At 90°K, both experiment and analysis indicate imperceptible charge collection up to 20s. It is clear that by incorporating a weak temperature dependence of hole capture probability into the analysis, the multiple-trapping model

is capable of completely predicting the experimental data over the entire range of 90°K to 303°K.

While the data of Figure 12 were obtained by integrating collected charge, transport data are often obtained in the form of current versus time. To analyze the data of Figure 12 in that form, they were converted by plotting them linearly and determining $I = dQ/dt$ from the local slope. The converted data are plotted in Figure 13 with the analytical results superimposed. Since current varies over about five orders of magnitude, comparisons between theory and experiment in this manner are more critical than the approach of Figure 12; at long or short times large fractional changes in current will have little effect on data presented as in Figure 12. In other words, the fitting process for integrated charge data was dominated by the shape of the curve in the rapidly changing portion near 50% collection. Replotting the data in terms of current allows comparison of the asymptotic behavior at early and late times.

Again, agreement between theory and experiment is excellent. Magnitudes of calculated and measured current agree well over the entire range; calculated and measured initial and final slopes agree (an important point for comparing the CTRW and multiple-trapping models, as discussed below); and crossover points are well predicted. It seems quite significant to observe that the fitting process for integrated charge data, which was relatively insensitive to the asymptotic behavior at early and late times, leads to a solution which satisfactorily predicts the asymptotic behavior of current-versus-time curves. As with the prediction of temperature behavior, it is unlikely that such a prediction capability would occur fortuitously. This fact seems to be compelling evidence for the veracity of the physical model.

3.3.3 Variation of Hole Collection with Field

Assuming that all the parameters of Eqs. (2) and (4) are independent of applied field, it should be possible to predict field dependence simply by varying F in Eq. (4). The results of such a calculation are compared with experiment in Figure 14. A normalization procedure was employed in Figure 14 which should be explained. The mathematical analysis is in terms of fractional charge collected, a quantity that varies from 0 to 1. The experimental data are presented in terms of gain, G , in units of charge

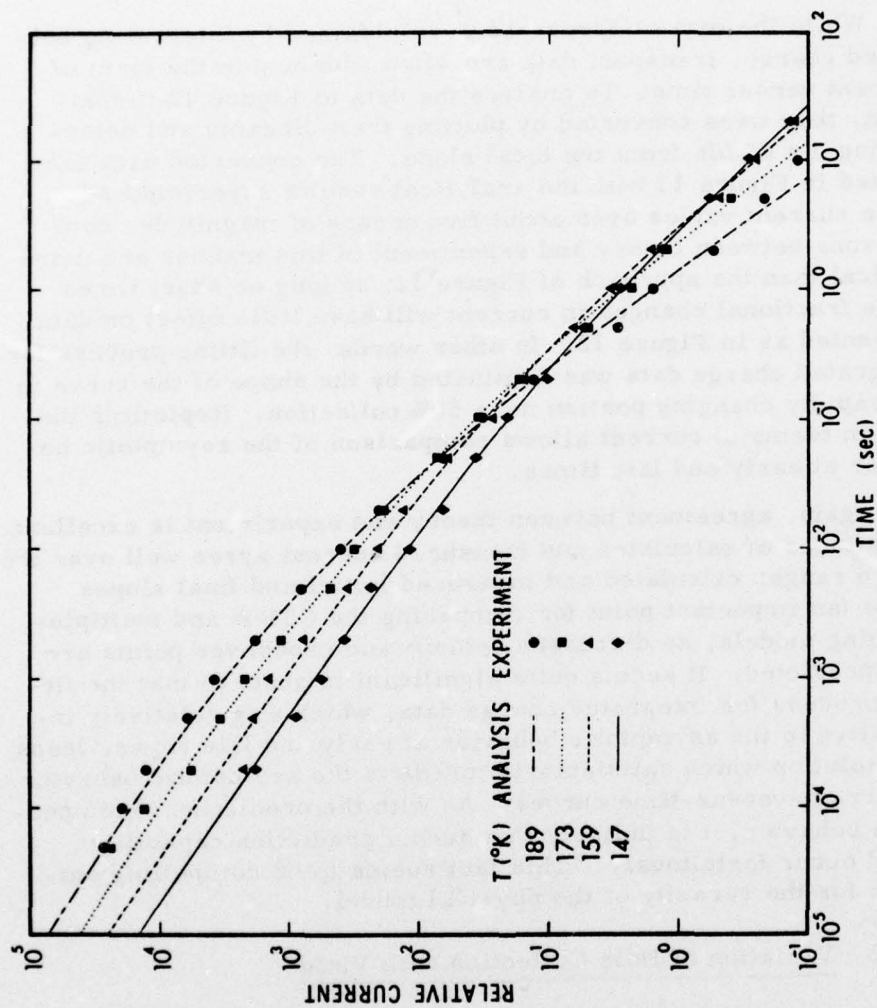


Figure 13. The variation of relative hole current with time and temperature: experimental and analytical results.

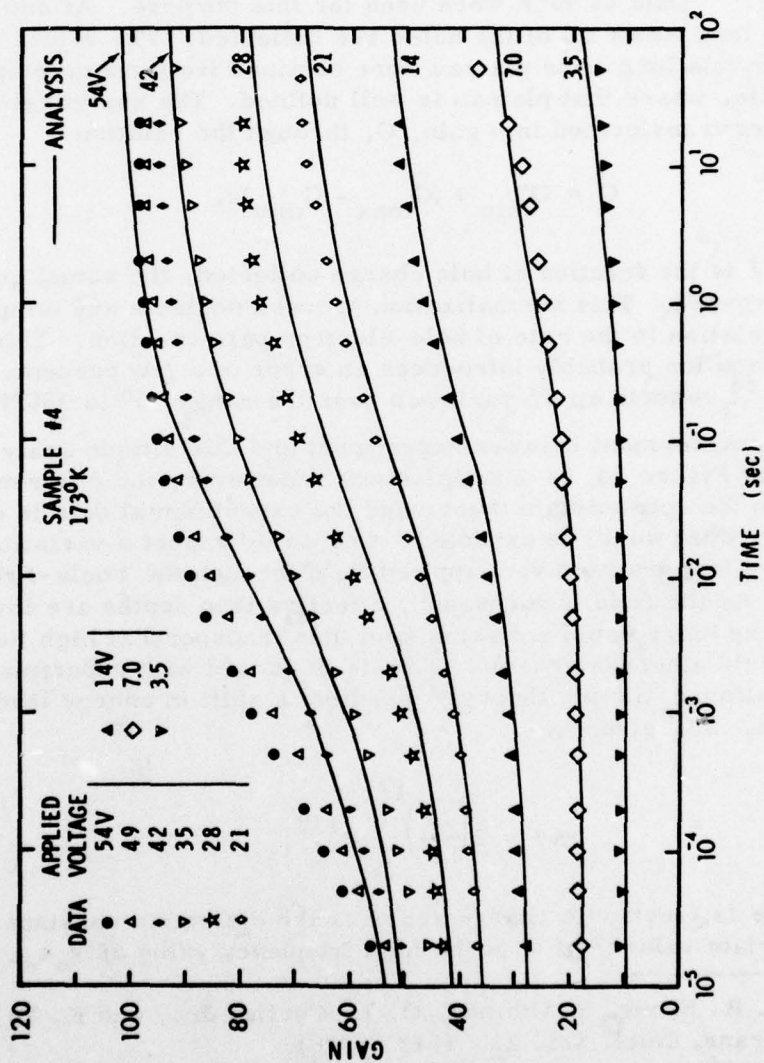


Figure 14. Time dependence of gain as a function of applied voltage. Calculated curves contain no Poole-Frenkel correction.

collected per exciting electron. At short times all of the generated electrons have been collected. The value of the resultant short-time plateau (all electrons but no holes collected) was determined from the value of the plateau at low temperatures where it is well defined.²¹ Data at 90°K were used for this purpose. At sufficiently long times all of the holes are collected. The values of gain for this long-time plateau were obtained from room temperature data, where that plateau is well defined. The analytical results are transformed into gain, G , through the relation

$$G = G_{\min} + (G_{\max} - G_{\min})f, \quad (6)$$

where f is the fraction of hole charge collected, the actual quantity computed. This normalization process neglects any temperature variation in the rate of hole-electron pair creation. This approximation probably introduces an error of a few percent. Hughes²⁴ reports an 8% variation over the range 75° to 300°K.

The agreement between experiment and this simple analysis, shown in Figure 14, is unsatisfactory. However, the difference between the approximate theory and the experimental data is qualitatively what would be expected. One would expect a variation in effective trap position with applied field through the Poole-Frenkel effect. As the field is increased, effective trap depths are lowered producing more rapid emission (and thus transport) at high fields than would otherwise result. This is in accord with experimental observations. Simple theory²⁸ predicts a shift in energy level position, $\Delta\phi$, given by

$$\Delta\phi = 2\left(\frac{e^3}{\epsilon}\right)^{1/2} F^{1/2}, \quad (7)$$

where e is electronic charge and ϵ is the dielectric constant. The appropriate value²⁹ of ϵ is the high frequency value of $\epsilon_0\epsilon_r$,

²¹J. R. Srour, S. Othmer, O. L. Curtis, Jr., and K. Y. Chiu, IEEE Trans. Nucl. Sci. **23**, 1513 (1976).

²⁴R. C. Hughes, Phys. Rev. **B15**, 2012 (1977).

²⁸J. J. O'Dwyer, The Theory of Electrical Conduction and Breakdown in Solid Dielectrics, (Clarendon Press, Oxford, 1973) p. 137

²⁹J. G. Simmons, Phys. Rev. **155**, 657 (1967).

where $\epsilon_r = n^2 = 2.13$. (n is the index of refraction.) With $\Delta\phi$ given in electron volts and F given in V/cm, we obtain (for SiO_2)

$$\Delta\phi = 1.84 \times 10^{-5} F^{1/2}. \quad (8)$$

To determine if the expected Poole-Frenkel shift is consistent with experimental observations, each value of E_i in Eq. (2) was varied in the following manner:

$$E_i = E_{i0} + bF^{1/2}. \quad (9)$$

(E_{i0} is the trap energy level position for zero applied field.) The results are shown in Figure 15. Good agreement is obtained with $b = 3.8 \times 10^{-5}$, approximately twice as large as predicted by Eq. (7). The failure of some of the curves to fit the data exactly is evidently experimental in origin and is attributed to the non-discretionary normalization process of the analysis discussed above and based on experimental measurements at other temperatures. If the values of G_{\min} and G_{\max} in Eq. (6) are adjusted, excellent fits to the data can be obtained. The approach used was chosen to limit the adjustable parameters to those controlled by the Poole-Frenkel effect.

In view of the approximate nature of the theory leading to Eq. (7), the observed agreement is satisfactory when the Poole-Frenkel effect is taken into account. In particular, the bulk dielectric constant for SiO_2 was used in Eq. (8) while on a microscopic basis the effective value might be smaller. Experimentally, Hill¹⁸ obtained $b = 1.4 \times 10^{-4}$ from dark conductivity data in SiO , a value considerably larger than that determined here.

3.4 DISCUSSION

When the data are plotted as in Figure 13, the lack of universality is dramatically exposed. Clearly, a simple shift in log time does not provide superposition of the experimental data. At early times and high currents the time dependence is similar, but at long times it varies with temperature. Recall again that the model contains no parameters that are adjusted with temperature.

¹⁸ R. M. Hill, *Phil. Mag.* 23, 59 (1971).

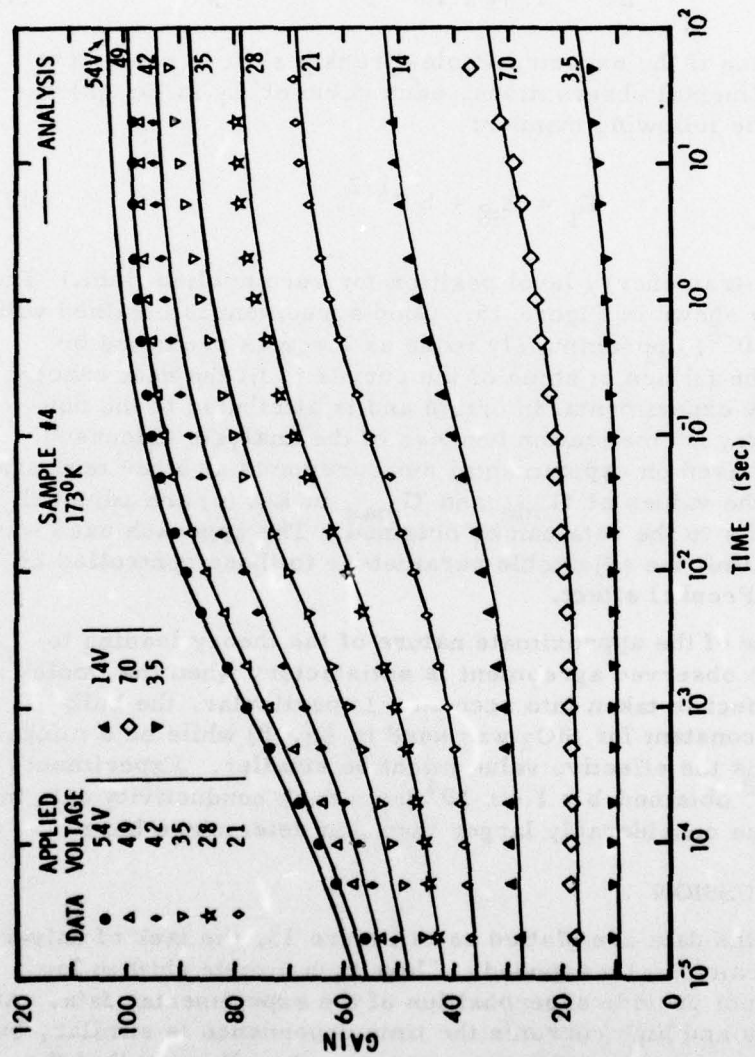


Figure 15. A fit of experimental data using the multiple-trapping model including the Poole-Frenkel effect.

Thus, as a result of what amounts to a single-temperature fit, the analytical and experimental results are in excellent agreement at all temperatures shown. This ability of the multiple-trapping model to predict the dependence of current on time for the present data is some of the most convincing evidence of the superiority of that model over the CTRW model.

By comparison, the CTRW model predicts⁹ that in the short-time limit

$$I \propto t^{(1-\alpha)}, \quad (10)$$

where I is current and α is a parameter in the CTRW model which, like θ used here, varies the amount of time dispersion. The long-time limit is predicted by the CTRW model to be of the form

$$I \propto t^{(1+\alpha)}. \quad (11)$$

Thus, the CTRW model predicts that logarithmic plots of current versus time for different temperatures will have the same initial and final slopes. While the initial slopes of the data in Figure 13 appear equal, this is not true of the final slopes. The multiple-trapping model predicts both the initial and final slopes well.

Another way to put the conflict between the CTRW and multiple-trapping models clearly into perspective is to look at the thermal activation energy as a function of time. Figure 10 predicts that the effective trap level position will change with time. This is not a feature of the basic CTRW model. Figure 16 was obtained from the data of Figure 12 and shows apparent activation energy as a function of fractional amount of hole charge collected.²¹ To obtain these plots, the time required to attain a specific gain (shown on the curves) was plotted as a function of reciprocal temperature. In the original data $G = 35$ corresponded approximately to no holes (but all electrons) collected and $G = 70$ to complete hole collection. Thus the data of Figure 16 cover most of the range of hole collection. The apparent activation energies range from ~ 0.29 eV at $G = 40$ to ~ 0.49 eV at $G = 65$.

⁹ F. B. McLean, G. A. Ausman, Jr., H. E. Boesch, Jr., and J. M. McGarrity, *J. Appl. Phys.* **47**, 1529 (1976).

²¹ J. R. Srour, S. Othmer, O. L. Curtis, Jr., and K. Y. Chiu, *IEEE Trans. Nucl. Sci.* **23**, 1513 (1976).

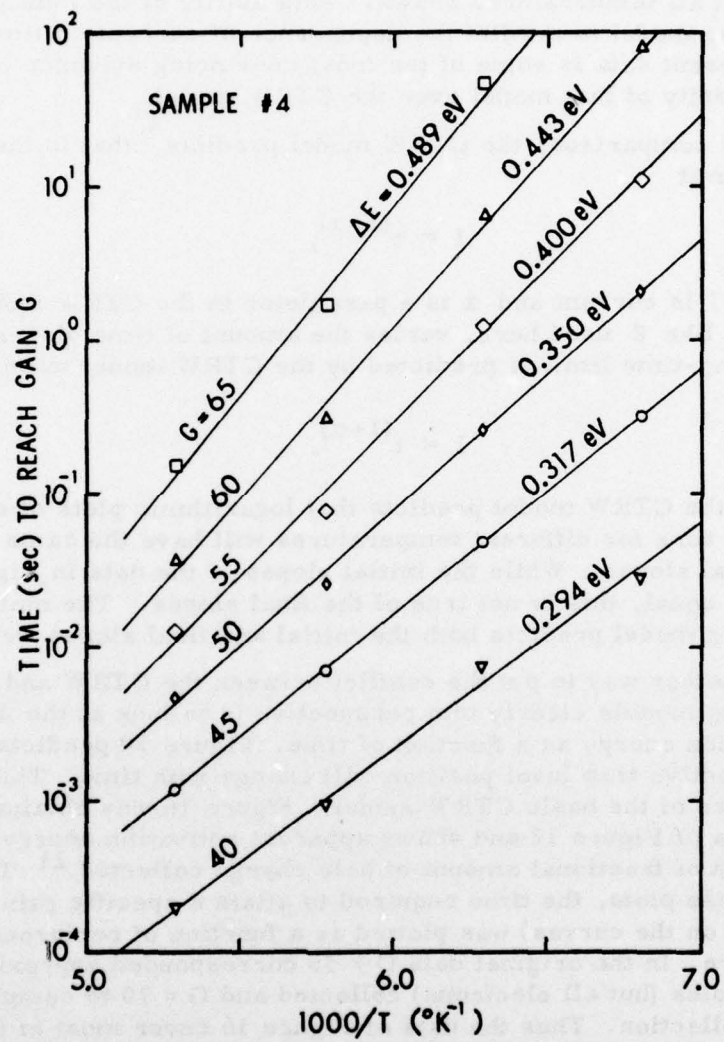


Figure 16. Time to reach a particular value of gain vs. reciprocal temperature for an applied voltage of 21V (from Reference 21).

Figure 17 is the computed version of Figure 16. The behavior is strikingly similar, with the apparent activation energy ranging from 0.27 to 0.43 eV, a range of 0.16 eV compared to the experimental range of 0.20 eV. This agreement is within experimental error. (By comparison, the basic CTRW model predicts no spread.) Interestingly (and perhaps fortuitously), deviations of points from the drawn-in straight lines tend to follow the same pattern in the analytical and experimental cases (note particularly the top and bottom curves). Again, the success of the multiple-trapping model is noteworthy, particularly when it is noted that a single-temperature fit accurately predicts both the magnitude and shift of apparent activation energy.

Comparable shifts in activation energy are observed when data of other investigators are analyzed in a manner comparable to that employed here. For instance, data of Hughes et al. (Figure 2 of Reference 7) also indicate a shift of ~ 0.2 eV, while data of Boesch et al. (Figure 7 of Reference 6) show a shift of ~ 0.1 eV over a smaller fraction of total charge collected than in the present case.

In comparing the results of the CTRW and multiple-trapping models, it should be borne in mind that, in principle, the CTRW model could be modified to include a spread in activation energies.⁸ However, this complicates further a model that already seems more complicated than the multiple-trapping model. Furthermore, it seems that if the dispersion caused by a spread in activation energies plus that due to a spread in hopping distances (a basic feature of the CTRW model) were both to occur, the total dispersion would be greater than actually observed.

If the present model is valid, the "activation energies" obtained from the type of analysis illustrated by Figures 16 and 17 do not correspond to an actual energy level position but to a time dependent effective level position produced by a continuous distribution of energy levels. It is informative to compare the results of Figures 16 and 17 to the analytical results shown in Figure 10. Figure 10 indicates that at a give time a narrow range of energy

⁶ H. E. Boesch, Jr., F. B. McLean, J. M. McGarrity, and G. A. Ausman, Jr., IEEE Trans. Nucl. Sci. 22, 2163 (1975).

⁷ R. C. Hughes, E. P. EerNisse, and H. J. Stein, IEEE Trans. Nucl. Sci. 22, 2227 (1975).

⁸ H. Scher and E.W. Montroll, Phys. Rev. B12, 2455 (1975).

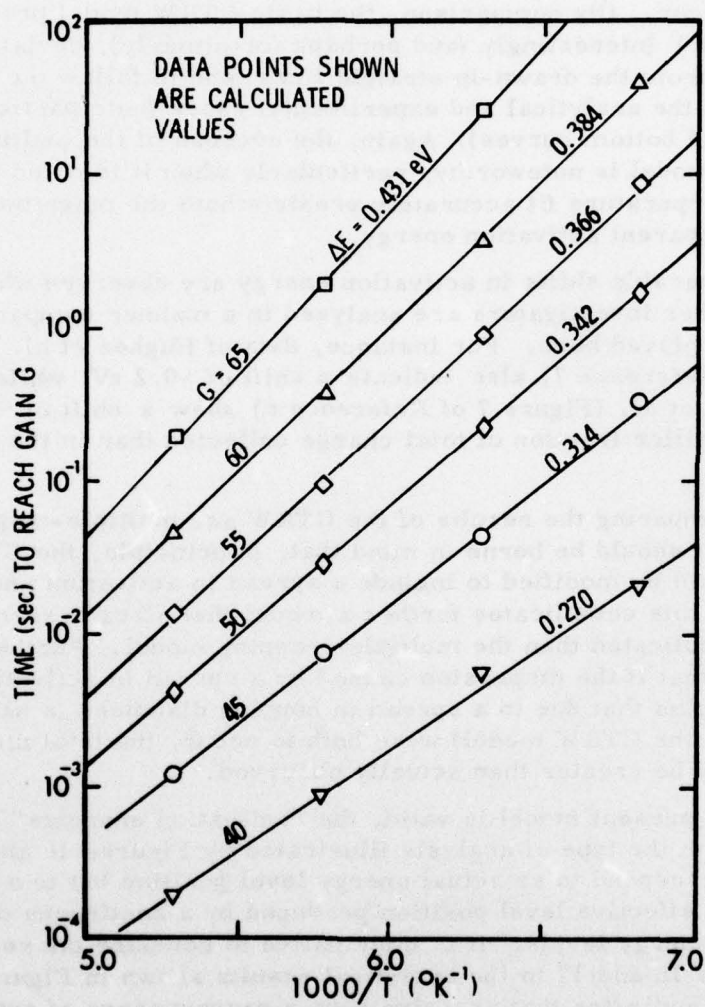


Figure 17. Analytical prediction of the data of Figure 16.

level positions will dominate the trapping process. The middle curves of Figures 16 and 17 ($G = 50$) correspond to a point where about 43% of the holes have been collected. Both Figures 16 and 17 yield activation energies at this point of about 0.35 eV. Figure 10 indicates that for the quasi-continuous mathematical model employed, at the corresponding point (total trap occupancy = 0.57) the 0.36 eV level is still dominant, but very shortly the 0.39 level becomes dominant. Thus, in a continuum the dominant energy level position would be about 0.37 eV. The agreement between the apparent activation energy and the predicted dominant energy level position is another indication of the success of the multiple-trapping model.

An impediment to acceptance of the multiple-trapping model has been the observation by Harari et al.⁴ of an optical activation energy of 1.8 eV through photodepopulation measurements in SiO_2 films at 78°K. The optical measurements were not transient measurements. Rather, holes were first created by ionizing radiation and photodepopulation measurements performed subsequently. A typical time for the entire experiment was ~ 1 h.³⁰ The multiple-trapping model predicts that at 78°K and at 3×10^3 s the dominant trap level will be at ~ 0.3 eV and will vary about 7% over one decade in time. The resultant ratio of optical to electronic transition energies of ~ 6 is considerably larger than the factor of two expected from simple theory.¹⁹ The origin of this discrepancy is not clear. Possibly there is a discrete level deeper in the band in addition to the distribution postulated here. It should be noted that the ionization dose used by Harari et al. was very large compared to the dose used in the present investigation. In fact, irradiation was continued until the flatband voltage shift saturated, indicating that all traps were filled. Relative occupancy may be quite different under high and low dose conditions. If the shallow levels have larger capture cross sections, they will fill more rapidly than the deeper levels and have a more pronounced effect at low doses even though they are present in lower concentrations. Large doses will tend to fill all the levels and reflect the total distribution, irrespective of relative cross sections. Furthermore, the

⁴ E. Harari, S. Wang, and B. S. H. Royce, *J. Appl. Phys.* **46**, 1310 (1975).

¹⁹ N. F. Mott and R. W. Gurney, *Electronic Processes in Ionic Crystals*, 2d Ed. (Dover, New York, 1964), p. 160.

³⁰ E. Harari, personal communication.

optical data of Harari et al. indicate the presence of a substantial number of levels in the lower energy range. Their data do not extend below ~ 1 eV in photon energy and the population of levels seems to be increasing with decreasing energy in this range. Perhaps the 1.8 eV levels represent only a fraction of the total number of hole traps present. Additional optical investigation in the lower photon energy range, with elapsed time from irradiation as a parameter, would be useful to resolve this problem.

It is interesting to examine some of the experimental data in terms of hole mobility. One can determine a mobility through the relationship $\mu = v/F$ where v is the hole velocity. (Mobilities determined here are not those for holes in the valence band, but are trap-modulated mobilities.) Assuming that the total charge in the oxide at a given time is ηp_0 , where p_0 is the initial concentration and η is the fraction of holes not swept out of the sample, and that dp/dt is the rate of change of hole charge determined from current measurements, the hole velocity is given by

$$v = (dp/dt) (L/\eta p_0), \quad (12)$$

where L is the sample thickness. Mobility is then given by

$$\mu = (dp/dt) (L^2/V \eta p_0), \quad (13)$$

where V is the applied voltage.

Data from Reference 21 (see Section 2.0) were used to determine mobility as defined through Eq. (13). Results based on the point where one-half the generated hole charge is collected are plotted in Figure 18. The data show an apparent activation energy of 0.30 eV (almost exactly the dominant energy level position at 50% collection as determined from Figure 10), and a field dependence explained by the Poole-Frenke effect discussed earlier. If the curves of Figure 18 are extrapolated to room temperature, the following values are obtained:

$$\begin{aligned} \mu(T = 300^\circ\text{K}, V = 21 \text{ volts}) &= 3 \times 10^{-6} \text{ cm}^2/\text{volt-sec}, \\ \mu(T = 300^\circ\text{K}, V = 54 \text{ volts}) &= 5 \times 10^{-5} \text{ cm}^2/\text{volt-sec}. \end{aligned}$$

²¹ J. R. Srour, S. Othmer, O. L. Curtis, Jr., and K. Y. Chiu, IEEE Trans. Nucl. Sci. 23, 1513 (1976).

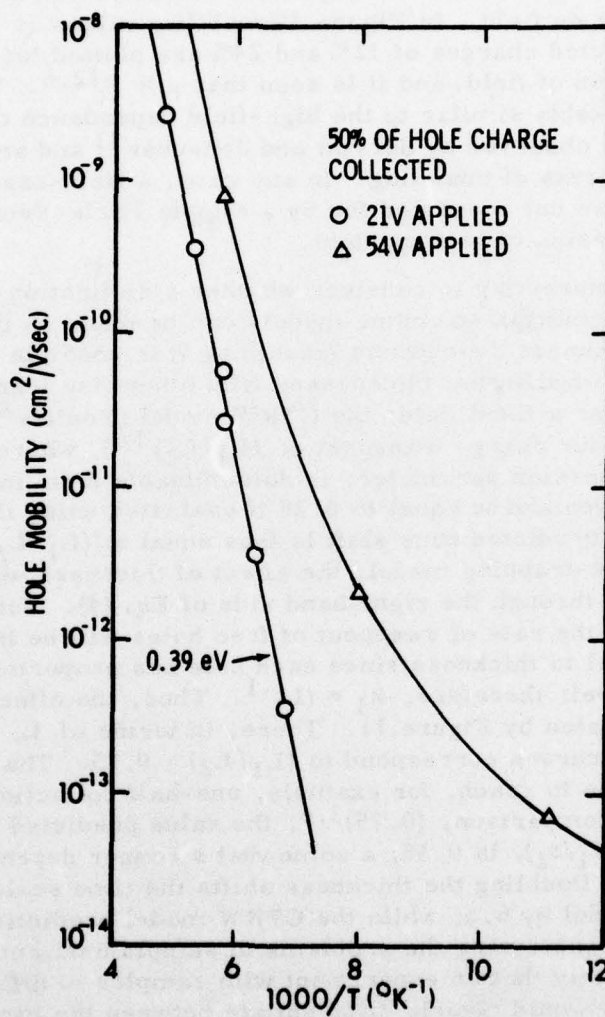


Figure 18. Measured hole mobility as a function of reciprocal temperature.

The high-field data at low temperature demonstrate certain behavior not taken into account in the model presented here and which is unimportant with respect to any of the data presented prior to Figure 18. The "excess" mobility illustrated in Figure 18 is only weakly temperature dependent and shows an extraordinary dependence on field. In Figure 19 mobility values at 90°K and at total collected charges of 12% and 24% are plotted logarithmically as a function of field, and it is seen that $\mu \propto F^{12.6}$. These data are remarkably similar to the high-field dependence of dark current in SiO observed by Servini and Jonscher³¹ and analyzed by Hill¹⁸ in terms of tunneling. In any case, a field-assisted emission process not accounted for by a simple Poole-Frenkel barrier lowering seems to be important.

It is interesting to consider whether a distinction between the CTRW and multiple-trapping models can be made on the basis of sample thickness dependence (assuming it is possible to make SiO₂ films of different thicknesses with otherwise identical properties). For a fixed field, the CTRW model predicts⁸ a time-scale shift for charge transport of $(L_1/L_2)^{1/\alpha}$, where α , the CTRW dispersion parameter, is determinable from initial slopes of $I(t)$ curves and is equal to 0.28 if evaluated using the present data. The predicted time shift is thus equal to $(L_1/L_2)^{3.6}$. In the multiple-trapping model, the effect of thickness would be manifested through the right-hand side of Eq. (4). For uniform excitation, the rate of sweepout of free holes will be inversely proportional to thickness since each hole has proportionately further to travel; therefore, $k_1 \propto (L)^{-1}$. Thus, the effect of varying L is illustrated by Figure 11. There, in terms of L , the two uppermost curves correspond to $(L_1/L_2) = 0.75$. The corresponding time to reach, for example, one-half collection is $(t_1/t_2) = 0.46$. By comparison, $(0.75)^{3.6}$, the value predicted by the CTRW model for (t_1/t_2) , is 0.35, a somewhat stronger dependence on thickness. Doubling the thickness shifts the time scale in the present model by 6.5, while the CTRW model prediction is $2^{3.6}$, or 12.1. Considering the problems of sample uniformity, it seems unlikely that an experiment with samples of different thicknesses would clearly differentiate between the two models.

⁸H. Scher and E. W. Montroll, Phys. Rev. **B12**, 2455 (1975).

¹⁸R. M. Hill, Phil. Mag. **23**, 59 (1971).

³¹A. Servini and A. K. Jonscher, Thin Solid Films **3**, 341 (1969).

The charge transport model presented here explains our experimental data remarkably well. It would be valuable to apply the model to other oxides in order to determine whether the agreement is as good under different material preparation conditions and this has not yet been done quantitatively. However, it is useful to make at least a qualitative comparison between our results and experimental data obtained by others. Figure 7 of Reference 6 (Boesch et al.) shows data roughly equivalent to those in our Figure 12, with the results of the CTRW model superimposed. (Note that the CTRW model only predicts the shape of the charge transport curve, not its absolute shift in time with temperature.) The data from Reference 6 and similar data shown in Figure 2 of Reference 7 and Figure 1 of Reference 24 (Hughes et al.) clearly indicate a steepening of charge collection curves at higher temperatures, as predicted by the multiple-trapping model but not by the basic CTRW model. The data from Reference 6 show somewhat greater time dispersion and the data from Reference 24 somewhat less dispersion than those presented herein, indicating that different defect parameters would be required to obtain a fit. While there appears to be no qualitative problem in fitting the data of Hughes et al.^{7,24} with the multiple-trapping model, the data of Boesch et al.⁶ appear to show somewhat more dispersion relative to the shift in activation energy than would be expected from the formulation of the multiple-trapping model presented here. Later data from the same group²⁰ appear to indicate even less of a spread in activation energy. It is not clear whether the multiple-trapping model could be modified to accommodate those data.

There is another feature present in the data of McLean et al.²⁰ which is not present in our data and which is not predicted by the multiple-trapping model as employed here. Using SiO₂ with different processing histories than those employed here, they observed a low-activation-energy process which dominates low-temperature behavior, in addition to the ~0.4 eV process reported

⁶ H. E. Boesch, Jr., F. B. McLean, J. M. McGarrity, and G. A. Ausman, Jr., IEEE Trans. Nucl. Sci. 22, 2163 (1975).

⁷ R. C. Hughes, E. P. EerNisse, and H. J. Stein, IEEE Trans. Nucl. Sci. 22, 2227 (1975).

²⁰ F. B. McLean, H. E. Boesch, Jr., and J. M. McGarrity, IEEE Trans. Nucl. Sci. 23, 1506 (1976).

²⁴ R. C. Hughes, Phys. Rev. B15, 2012 (1977).

here for higher temperatures. We see a similar effect, but only at higher fields (see Figure 19 and accompanying discussion.) Perhaps the low temperature portions of the data from References 20 and 24 also correspond to a field-assisted tunneling process, or perhaps there is in their samples a hopping type of conduction that dominates at low temperatures. They explain their results in terms of polaron motion.^{20, 24}

The data from Reference 20 show less dispersion and apparently a smaller spread in activation energy than either the data of Reference 6 or the data presented here. In our model less dispersion corresponds to a more rapid decrease in energy level density away from the band edge. This would seem to lead to a narrow spread in activation energy.

One difference between the data employed here and those reported by McLean et al.²⁰ may be of profound significance. The data reported here were obtained under low-level conditions. Changing the excitation conditions by an order of magnitude produced no observable change in the transport characteristics. The total energy deposited during the excitation pulse was on the order of 80 rads, while ~20 krads were used in generating the data of Reference 20. It is, of course, possible that the transport process is different at high doses because of filling of trap levels. (Recent experiments at our laboratory (see Section 4.0) indicate that after large doses, the hole mobility at low temperatures is nearly field independent and does not follow the strong dependence illustrated in Figure 19 for low-dose conditions.) Differences in experimental technique may also be important. Boesch et al.^{6,9,17,20} used flatband voltage shift to investigate the charge collection process. As is well recognized, room-temperature flatband shifts are primarily determined by the trapping of holes transported to the interface. Shallower traps near the interface could affect the

⁶ H. E. Boesch, Jr., F. B. McLean, J. M. McGarrity, and G. A. Ausman, Jr., IEEE Trans. Nucl. Sci. 22, 2163 (1975).

⁹ F. B. McLean, G. A. Ausman, Jr., H. E. Boesch, Jr., and J. M. McGarrity, J. Appl. Phys. 47, 1529 (1976).

¹⁷ H. E. Boesch, Jr., and J. M. McGarrity, IEEE Trans. Nucl. Sci. 23, 1520 (1976).

²⁰ F. B. McLean, H. E. Boesch, Jr., and J. M. McGarrity, IEEE Trans. Nucl. Sci. 23, 1506 (1976).

²⁴ R. C. Hughes, Phys. Rev. B15, 2012 (1977).

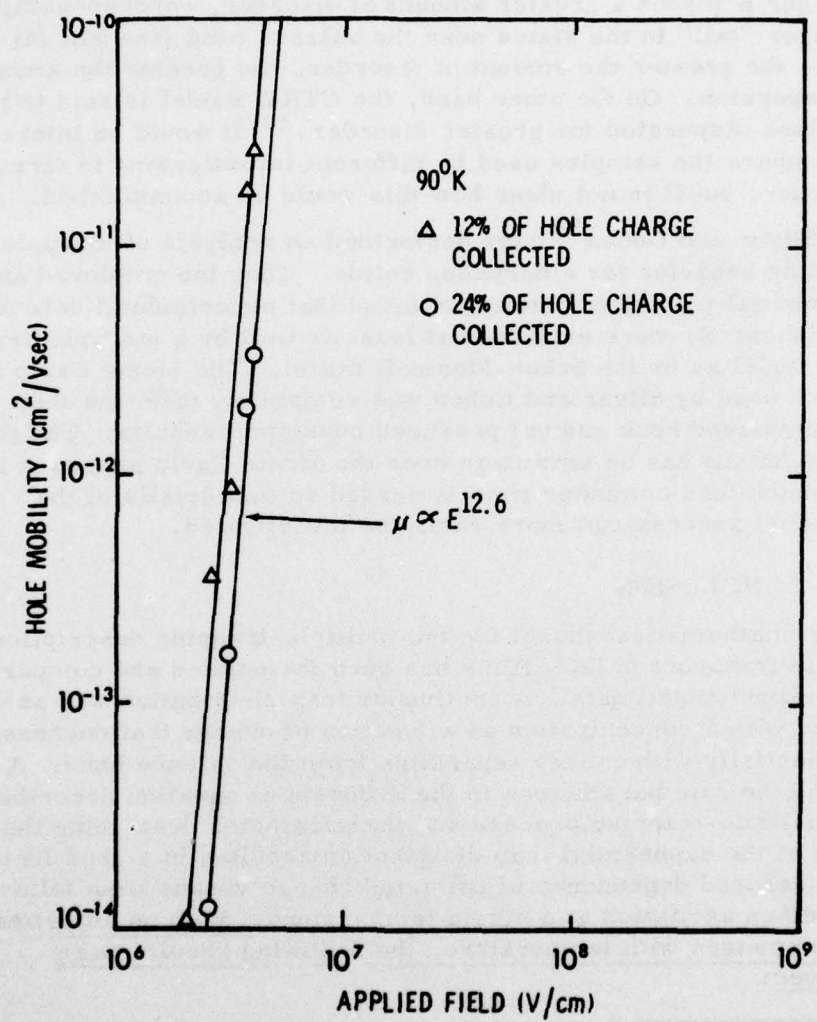


Figure 19. Measured hole mobility at 90°K as a function of applied field.

lower temperature measurements. Any temporary trapping of holes by such traps would tend to make the charge collection process as measured by flatband shift appear more dispersive than it actually is.

The physical significance of β in our model is probably that a larger β means a greater amount of disorder, corresponding to a longer "tail" in the states near the valence band (see Eq. (4)). Thus, the greater the amount of disorder, the greater the amount of dispersion. On the other hand, the CTRW model is said to predict less dispersion for greater disorder.²⁰ It would be interesting to compare the samples used by different investigators in terms of disorder, but it is not clear how this would be accomplished.

Silver and Cohen³² have performed an analysis of multiple trapping behavior for amorphous solids. They too employed an exponential trap distribution and found that experimental data for amorphous Se were explained at least as well by a multiple-trapping model as by the Scher-Montroll model. The Monte Carlo approach used by Silver and Cohen was completely different than that employed here and yet produced consistent results. The present technique has an advantage over the Monte Carlo approach in that much less computer time is needed so that details of the transport process can more easily be investigated.

3.5 CONCLUSION

A mathematical model for the multiple-trapping description of hole transport in SiO_2 films has been formulated and compared with experimental data. A continuous trap distribution was assumed with a concentration as a function of energy that decreases exponentially with energy separation from the valence band. Adjusting the rate parameters in the differential equation describing the multiple-trapping process and the parameter describing the width of the exponential trap distribution resulted in a good fit to the measured dependence of collected charge versus time following pulsed excitation at a single temperature. With no adjustment of parameters with temperature, the following results were obtained:

²⁰ F. B. McLean, H. E. Boesch, Jr., and J. M. McGarrity, IEEE Trans. Nucl. Sci. 23, 1506 (1976).

³² M. Silver and L. Cohen, paper submitted for publication.

- (1) Charge collection curves at other temperatures were accurately predicted.
- (2) The magnitudes and features of the time dependence of hole current extending over five orders of magnitude in current and six orders of magnitude in time were accurately predicted.
- (3) The magnitude of apparent activation energy and its spread in time were accurately predicted from behavior at a single temperature.

This model is proposed as an alternative to the CTRW model. By comparison:

- (1) The CTRW model, as implemented, does not predict the magnitude of the temperature shift of charge collection curves.
- (2) The CTRW model does not predict the change in the shape of charge collection curves with temperature that is experimentally observed here.
- (3) The long-time, low-current portion of the current versus time curves presented here is incorrectly predicted by the CTRW model.
- (4) The CTRW model does not predict from behavior at a single temperature the magnitude of observed activation energies.
- (5) The basic CTRW model does not account for a spread in observed activation energies.

It is submitted that the multiple-trapping model is the superior one for explaining hole transport in SiO_2 films, at least for the particular material and experimental conditions analyzed.

It must be borne in mind that the data utilized here were obtained for one particular type of oxide film. It appears that the multiple-trapping model will adequately describe many of the data obtained by other researchers. However, some of the data show more dispersion than would be expected from the small apparent shift in activation energy displayed. It is not clear whether the multiple-trapping model could accommodate those data. The data least compatible with the multiple-trapping model were obtained using high excitation levels, and flatband voltage shifts were used

to determine indirectly the amount of charge transport.²⁰ Under high excitation conditions the nature of the charge transport process may be different than that observed here, and flatband measurements will be strongly affected by any holes that are transported to and temporarily trapped at the interface. These factors may also influence the observation^{20, 24} of an additional low-activation-energy process at low temperatures, or that process may be caused by field emission or hopping and be observable only when the transport process postulated here has become very slow.

While by comparison the multiple-trapping model seems superior to the CTRW model, the latter approach is quite successful in describing many features of hole transport. This fact raises the question whether data for other materials explained by a stochastic hopping transport model might be explained better by a multiple-trapping description, e.g., α -As₂Se₃ and trinitrofluorenone-polyvinylcarbazole.⁸

⁸ H. Scher and E. W. Montroll, Phys. Rev. B12, 2455 (1975).

²⁰ F. B. McLean, H. E. Boesch, Jr., and J. M. McGarrity, IEEE Trans. Nucl. Sci. 23, 1506 (1976).

²⁴ R. C. Hughes, Phys. Rev. B15, 2012 (1977).

SECTION 4.0

LOW-TEMPERATURE PHENOMENA IN IRRADIATED MOS DEVICES

4.1 INTRODUCTION

Various low-temperature applications of MOS devices have arisen in the past few years, including amplification, signal processing, and infrared imaging. Charge transfer devices (CTDs) and MOS transistors are used in these applications at operating temperatures less than 100°K . If such devices are also employed in a radiation environment, behavior can significantly differ from that for room-temperature operation (see Section 2.0 and references therein). In particular, flatband voltage shifts for MOS capacitors (or threshold voltage shifts for MOS transistors) are considerably larger at low temperatures than at room temperature. The reason for this is that holes generated in the oxide layer by ionizing radiation are relatively immobile at low temperatures except when the field applied during irradiation is high ($>2 \times 10^6 \text{ V/cm}$).²¹ It is significant to note, as discussed in Section 2.0, that devices which are radiation tolerant at room temperature exhibit significant radiation-induced changes at low temperatures.

This section presents analyses and data relating to radiation effects on MOS devices at low temperatures. We first discuss several radiation hardening methods that may find application at such temperatures. That discussion serves as an introduction to the remainder of the present section in which experimental results and analyses pertaining to these suggested hardening approaches are given.

4.2 MOS HARDENING APPROACHES AT LOW TEMPERATURES

The basic effects of total ionizing dose on an MOS device are charge buildup in the oxide layer and interface state production at the $\text{SiO}_2\text{-Si}$ interface. Charge buildup gives rise to flatband and threshold voltage shifts, and interface state creation causes channel mobility reduction in transistors and increases in dark current

²¹ J. R. Srour, S. Othmer, O. L. Curtis, Jr., and K. Y. Chiu, IEEE Trans. Nucl. Sci. 23, 1513 (1976).

and transfer inefficiency in CTDs. As mentioned above, charge buildup in SiO_2 is significantly more severe at low temperatures than at room temperature. An understanding of the basic mechanisms associated with this phenomenon leads us to suggest the following four approaches to alleviating charge buildup problems at low temperatures: (1) carefully select the field applied to the oxide; (2) ion implant the oxide; (3) use a thin oxide; (4) use an insulating film other than SiO_2 . This last item is not pursued here. Such an approach may prove to be impractical, but it should be noted that Boesch has recently found Al_2O_3 films on silicon to be significantly more radiation tolerant at low temperatures than their SiO_2 counterparts.³³

The first potential hardening approach -- selection of applied field -- arose from our observation²¹ that holes are mobile at high fields in SiO_2 films irradiated at low temperatures. Transporting holes out of the oxide reduces the threshold shift in an irradiated transistor. We have explored this concept through experiment and analysis and findings are presented below. Regarding the approach of hardening by ion implanting the oxide, Section 2.0 presented data showing the improved radiation tolerance achieved by this method (see Figure 7 and associated discussion). In the present section, further analysis of ion implantation effects is given, including a treatment of the effect of implantation depth on oxide hardness. The third hardening approach -- use of a thin oxide -- is beneficial for devices operated at room temperature.³⁴ This same procedure is also applicable for low-temperature operation because the total amount of positive charge trapped throughout the oxide decreases with decreasing thickness and therefore threshold voltage shift will also decrease. We do not treat oxide thickness effects as a separate topic in this section but instead consider it within the context of the effects of both ion implantation and applied field.

Section 4.3 presents an analysis of radiation hardening at low temperatures via ion implantation. In Section 4.4, the effects of

²¹J. R. Srour, S. Othmer, O. L. Curtis, Jr., and K. Y. Chiu, IEEE Trans. Nucl. Sci. 23, 1513 (1976).

³³H. E. Boesch, Harry Diamond Laboratories, private communication.

³⁴G. F. Derbenwick and B. L. Gregory, IEEE Trans. Nucl. Sci. 22, 2151 (1975).

applied field on flatband voltage shift are analyzed. Section 4.5 presents experimental results on the field dependence of charge buildup at low temperatures. Included in that subsection is a description of the procedure used to fit experimental data based on the analysis of Section 4.4. Section 4.6 describes an improved model which was also utilized.

4.3 ANALYSIS OF ION IMPLANTATION EFFECTS

Consider the MOS structure of Figure 20. The oxide of thickness t_{ox} is ion implanted and the implantation depth is d_i . The mean electron range (schubweg) w_e in the implanted zone between the metal-SiO₂ interface and d_i is given by $\mu_e \tau_e E$, where μ_e and τ_e are mobility and lifetime, respectively, and E is applied electric field. For the present, it is assumed that at low temperatures all holes generated in the oxide by ionizing radiation in both the implanted and unimplanted zones are immobile. (A portion of the generated holes will initially recombine and we ignore this for now also.) All electrons generated in the unimplanted zone are assumed to be completely swept out of that region, either into the implanted zone or into the silicon depending on the polarity of the applied bias. The case of a positive bias applied to the metal electrode is considered here.

Electrons generated in the implanted region will move an average distance w_e toward the metal electrode before being permanently trapped. Thus, the average position of these trapped electrons is a distance $(d_i - w_e)/2$ from the metal-SiO₂ interface. Electrons generated in the unimplanted region of the oxide will be swept toward the implanted zone and move an average distance w_e into this region before being permanently trapped. The average position of these trapped electrons is a distance $d_i - w_e$ from the metal-SiO₂ interface. Thus, electrons trapped at two average positions in the implanted region will serve to compensate for a portion of the positive charge which, by assumption, is trapped uniformly throughout the implanted and unimplanted zones.

It is of interest to compare expected flatband voltage shifts for implanted and unimplanted MOS capacitors. For an unimplanted unit, the average position of the trapped charge (all positive -- no electrons trapped) is at $t_{ox}/2$. The effectiveness of trapped charge in giving rise to a flatband voltage shift is proportional to its distance from the metal electrode. Thus, the flatband voltage shift is given by

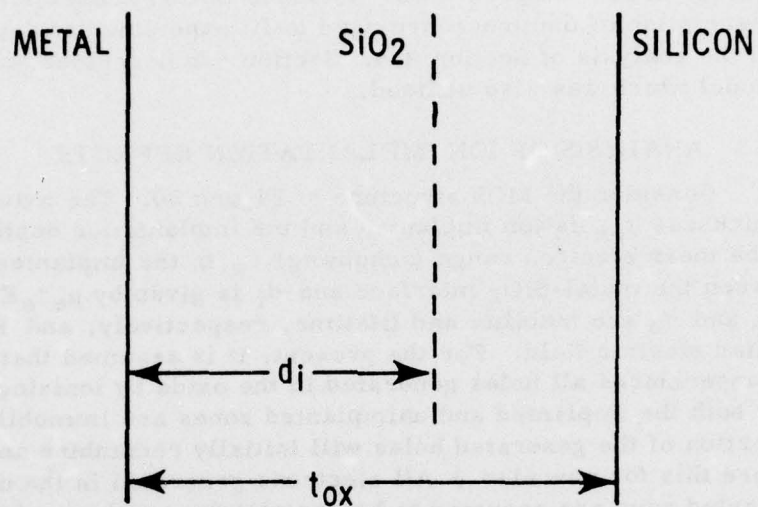


Figure 20. Schematic of an MOS structure with an ion-implanted oxide (implantation depth = d_i , oxide thickness = t_{ox}).

$$\Delta V_{fb} \text{ (unimplanted)} = Q^+ / 2 C_{ox} = t_{ox} Q^+ / 2 \epsilon S, \quad (1)$$

where C_{ox} is oxide capacitance, ϵ is dielectric constant, S is area, and Q^+ is the total amount of positive charge trapped in the oxide. (In Eq. (1), the "effectiveness" factor is $(t_{ox}/2)/t_{ox}$, or $1/2$.) For an implanted sample, the two contributions to ΔV_{fb} from trapped electrons are subtracted from the trapped hole contribution. In addition, different fractions of the total amount of negative charge generated (Q^-) are trapped at the two average positions. The resulting expression is

$$\Delta V_{fb} \text{ (implanted)} = \frac{t_{ox} Q^+}{2 \epsilon S} - \left(\frac{d_i - w_e}{t_{ox}} \right) \left(\frac{t_{ox}}{\epsilon S} \right) \left(\frac{t_{ox} - d_i}{t_{ox}} \right) Q^- - \left(\frac{d_i - w_e}{2 t_{ox}} \right) \left(\frac{t_{ox}}{\epsilon S} \right) \left(\frac{d_i - w_e}{t_{ox}} \right) Q^-. \quad (2)$$

Upon dividing Eq. (2) by Eq. (1) and noting that $Q^+ = Q^-$, we obtain (after rearrangement)

$$\frac{\Delta V_{fb} \text{ (implanted)}}{\Delta V_{fb} \text{ (unimplanted)}} = 1 - \left(\frac{d_i - w_e}{t_{ox}} \right) \left[2 - \left(\frac{d_i + w_e}{t_{ox}} \right) \right]. \quad (3)$$

Equation (3) relates the expected reduction in ΔV_{fb} accomplished by implantation to both the *schubweg* in the implanted zone and the implantation depth. In order to perform example calculations, a value for w_e is needed. Previous work¹² yielded a $\mu_e \tau_e$ value at room temperature of $\sim 2 \times 10^{-12}$ cm²/V for the implanted zone of 20-keV Al⁺-implanted specimens (fluence = 10^{15} cm⁻²). For an applied field of 10^6 V/cm, this value translates to a value for w_e of 200 Å. (Presumably, by implanting to a higher fluence w_e would be reduced.) We assume that w_e is temperature independent and thus that the $\mu_e \tau_e$ value obtained at room temperature can be applied at low temperatures. The primary temperature dependence expected is that of capture cross-section and this

¹² O. L. Curtis, Jr., J. R. Srour, and K. Y. Chiu, IEEE Trans. Nucl. Sci. 22, 2174 (1975).

consideration is neglected here for simplicity. Figure 21 presents results of calculations performed using Eq. (3). The quantity $\Delta V_{fb}(\text{implanted})/\Delta V_{fb}(\text{unimplanted})$ is plotted versus implantation depth for three values of w_e (20, 100, and 200 Å) and an oxide thickness of 1000 Å. The w_e value of 200 Å was chosen to be representative of conditions for a field of 10^6 V/cm and an implantation fluence of 10^{15} cm⁻². The lower values of w_e were selected to examine the expected effects of high fluences (i.e., shorter electron schubweg). The intuitively obvious results are obtained: increasing the ratio of implantation depth to oxide thickness and/or reducing the electron schubweg reduces ΔV_{fb} for an implanted specimen relative to that for an unimplanted unit. For example, implanting ions to a depth of 800 Å at such a fluence to cause w_e to equal 20 Å is predicted to reduce ΔV_{fb} by a factor of 13.

Calculations were also made to illustrate the effect of varying the applied field. Figure 22 shows the calculated ratio of $\Delta V_{fb}(\text{implanted})$ to $\Delta V_{fb}(\text{unimplanted})$ versus implantation depth for various values of applied field. Values of 1000 Å and 2×10^{-12} cm²/V were assumed for t_{ox} and $\mu_e \tau_e$, respectively. (Note that the 10^6 V/cm curve in Figure 22 is identical to the $w_e = 200$ Å curve in Figure 21.) The interpretation of calculations such as these is straightforward. For a given value of $\mu_e \tau_e$ in the implanted zone, increasing the field increases the electron schubweg with the result that a larger fraction of the electrons generated escape being trapped in the implanted zone. Thus, the degree of compensation of trapped positive charge diminishes. For example, Figure 22 shows that for an implantation depth of 800 Å increasing the applied field from 10^6 to 2×10^6 V/cm increases the quantity $\Delta V_{fb}(\text{implanted})/\Delta V_{fb}(\text{unimplanted})$ from 0.40 to 0.68.

As mentioned above, hole transport was neglected in the present treatment of implanted devices. However, previous work²¹ (see Section 2.0 of this report) has shown that holes are mobile in unimplanted SiO₂ films at high fields. Thus, in a more complete analysis of charge compensation and charge buildup in implanted specimens at low temperatures, one should consider motion of holes out of the unimplanted zone into either the silicon substrate or into the implanted region, depending on the polarity of the applied bias. Such additional analysis was not performed

²¹ J. R. Srour, S. Othmer, O. L. Curtis, Jr., and K. Y. Chiu, IEEE Trans. Nucl. Sci. 23, 1513 (1976).

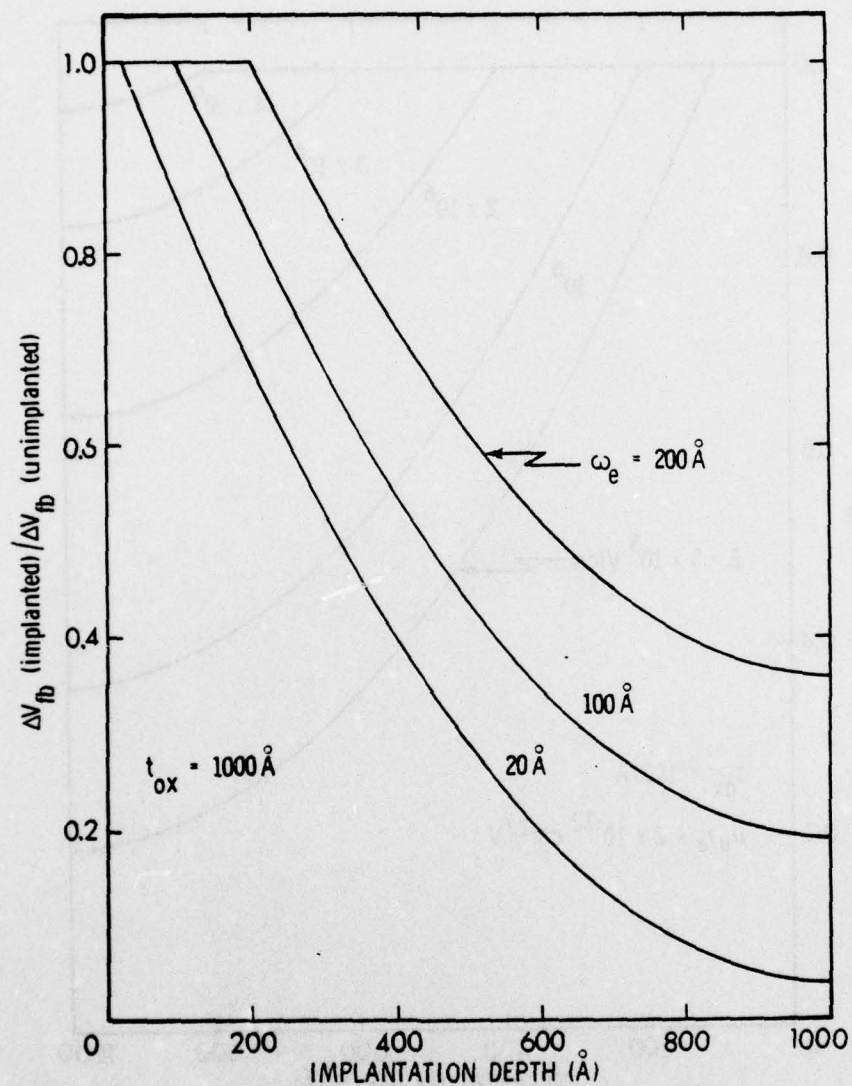


Figure 21. The calculated ratio of $\Delta V_{fb}(\text{implemented})$ to $\Delta V_{fb}(\text{unimplanted})$ versus implantation depth for three values of electron schubweg.

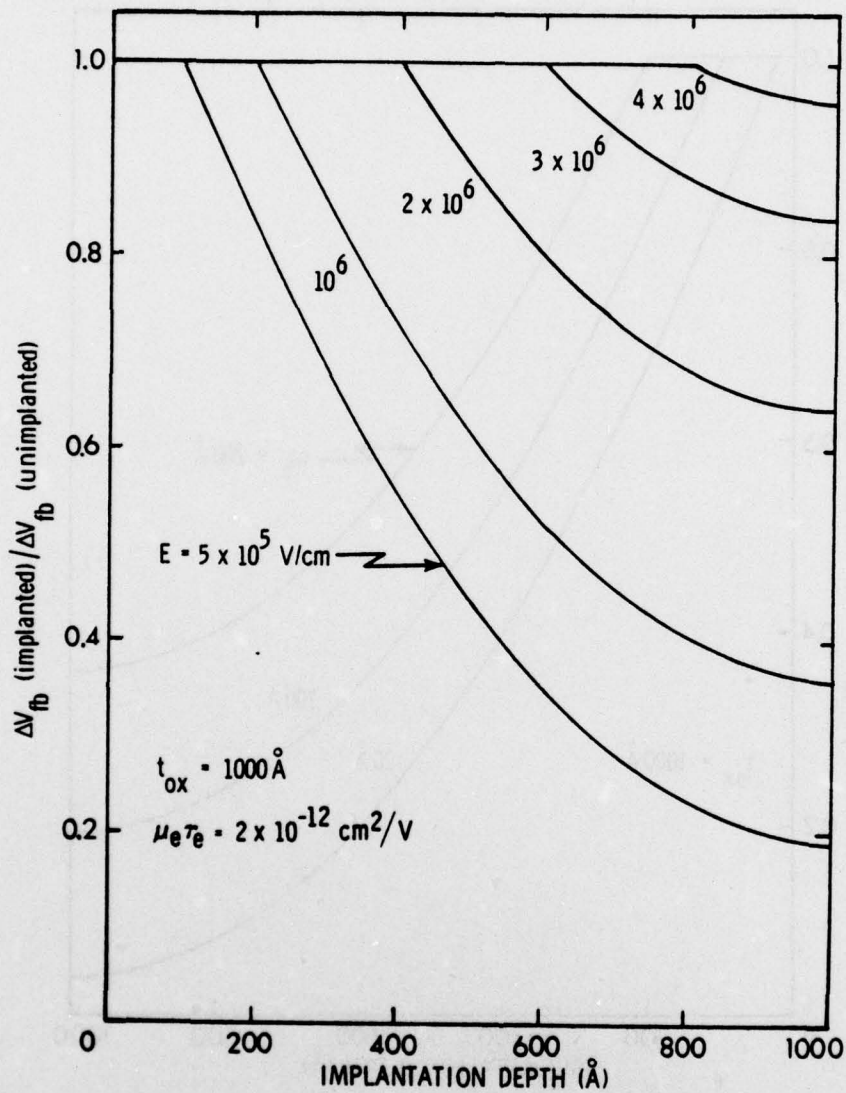


Figure 22. The calculated ratio of $\Delta V_{fb}(\text{implanted})$ to $\Delta V_{fb}(\text{unimplanted})$ versus implantation depth for several values of applied field.

here. In a practical device, it is likely that the applied field would be low enough so that hole transport could be neglected. However, hole transport is treated below for the case of unimplanted specimens irradiated at 77°K and it is demonstrated that, in practice, one should consider utilizing a relatively high applied field to reduce charge buildup effects at low temperatures.

In addition to neglecting hole transport, initial recombination of generated electrons and holes was not considered in the above discussion. The assumption was made in previous work¹² that ion implantation has no effect on the processes of generation and initial recombination of electron-hole pairs, and that same assumption was made here in developing Eq. (3). That is, the same fraction of generated pairs is assumed to initially recombine in both implanted and unimplanted specimens at low temperatures. The validity of this assumption should be examined in future comparisons of theory and experiment.

4.4 ANALYSIS OF APPLIED FIELD EFFECTS

The effects of applied field on charge buildup in unimplanted oxides at low temperatures are treated here. We assume for an unimplanted specimen that all generated electrons escaping initial recombination are swept out of the oxide, leaving behind trapped holes. Figure 23 shows an incremental oxide thickness dx containing a hole density ρ . The contribution to flatband voltage shift by this element can be expressed as

$$d(\Delta V_{fb}) = \frac{\left(\rho S dx\right) \left(\frac{x}{t_{ox}}\right)}{\left(\frac{\epsilon S}{t_{ox}}\right)} = \frac{\rho}{\epsilon} x dx. \quad (4)$$

The quantity ρ is that hole density remaining after initial recombination has taken place. If we assume a uniform trapped hole concentration ρ to exist throughout the entire oxide, the resulting flatband shift is given by

¹² O. L. Curtis, Jr., J. R. Srour, and K. Y. Chiu, IEEE Trans. Nucl. Sci. 22, 2174 (1975).

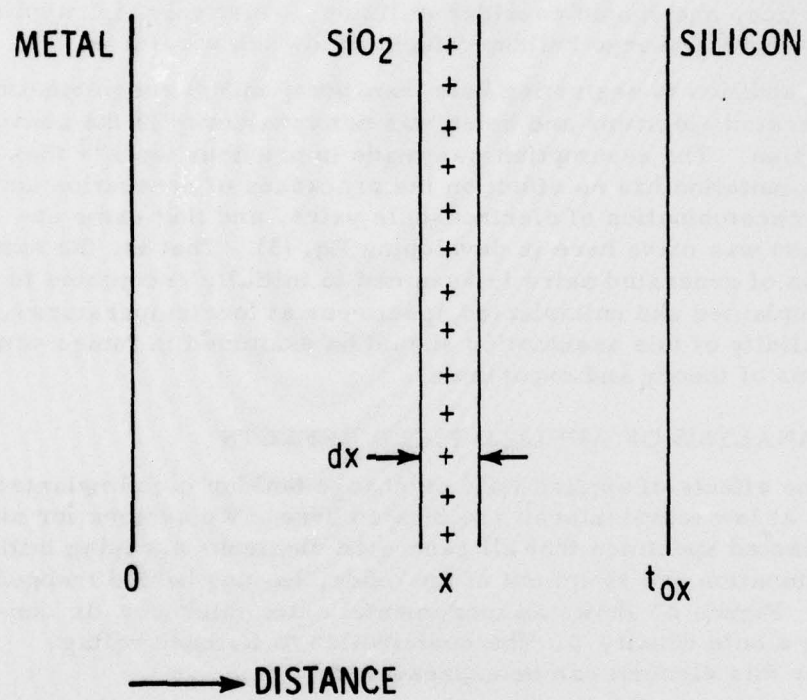


Figure 23. Schematic of an MOS structure showing an incremental oxide thickness containing a positive charge density.

$$\Delta V_{fb} = \frac{\rho}{\epsilon} \int_0^{t_{ox}} x dx = \left(\frac{\rho}{2\epsilon} \right) t_{ox}^2. \quad (5)$$

If initial recombination of holes is neglected, the total positive charge density generated by ionizing radiation can be calculated by assuming 18 eV/pair (translates to 7.9×10^{12} pairs/cm³rad for SiO₂). Then, in terms of ionizing dose γ in rads(Si), the quantity ρ in coul/cm³ can be expressed as

$$\rho = 1.26 \times 10^{-6} \gamma. \quad (6)$$

Flatband voltage shift (Eq. (5)) in volts is then given by

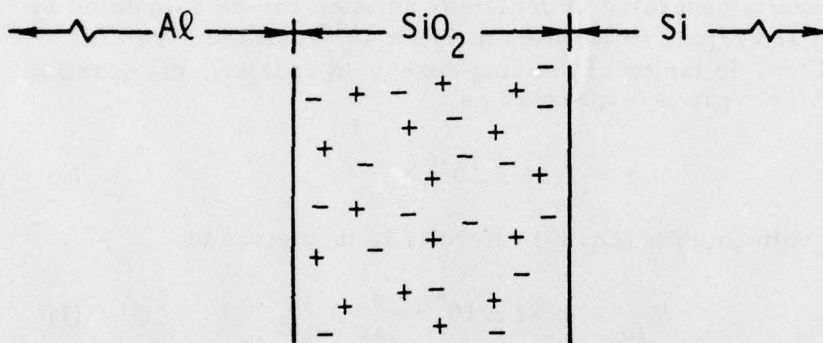
$$\Delta V_{fb} = 1.82 \times 10^6 \gamma t_{ox}^2, \quad (7)$$

where t_{ox} is in cm. Once again, expressions (6) and (7) assume no initial recombination of generated electron-hole pairs. To empirically account for recombination, these two expressions should be multiplied by the fractional electron yield at a given field (assuming no hole motion).

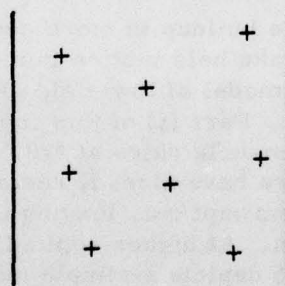
We now consider charge buildup in more detail at low temperatures and specifically take hole motion into account. Figure 24 illustrates a simple model of low-field ($\leq 10^6$ V/cm) behavior at low temperatures. Part (a) of this figure shows uniformly generated electron-hole pairs at $t=0$. At $t=0^+$ (part (b)), a portion of these pairs have already recombined and all of the remaining electrons are swept out, leaving a uniform "frozen-in" trapped hole distribution. At higher applied fields, hole transport occurs²¹ and Figure 25 depicts a simple model for high-field effects. Uniformly generated electron-hole pairs are shown in part (a) at $t=0$. Part (b) shows the situation at $t=0^+$ when electrons have already been swept out. At high fields, initial recombination is negligible and thus essentially all generated holes remain in the oxide at $t=0^+$. Part (c) of Figure 25 illustrates behavior at some later time $t=t_1$. A positive bias on the metal electrode is assumed here and the uniform hole population is shown to have moved a

²¹ J. R. Srour, S. Othmer, O. L. Curtis, Jr., and K. Y. Chiu, IEEE Trans. Nucl. Sci. 23, 1513 (1976).

LOW-FIELD ($\leq 10^6$ V/cm) MODEL



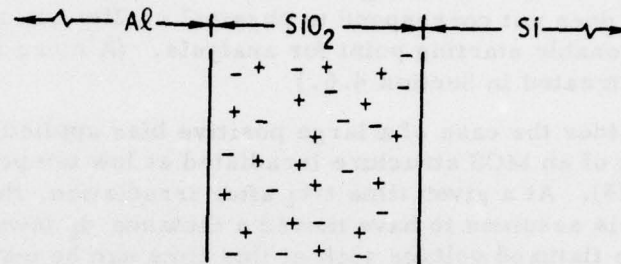
A. AFTER PAIR GENERATION AT $t = 0$



B. AFTER ELECTRON-HOLE RECOMBINATION AND SWEEP-OUT OF THE REMAINING ELECTRONS AT $t = 0^+$

Figure 24. Illustration of a simple low-field model for charge buildup in MOS structures at low temperatures.

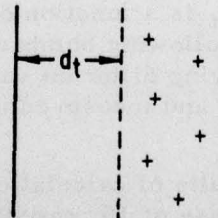
HIGH-FIELD ($>10^6$ V/cm) MODEL



A. AFTER PAIR GENERATION AT $t = 0$



B. AFTER ELECTRON-HOLE RECOMBINATION (NEGLIGIBLE AT HIGHEST FIELDS) AND SWEEPOUT OF THE REMAINING ELECTRONS AT $t = 0^+$



C. AFTER TRANSPORT OF THE HOLE POPULATION A DISTANCE d_t AT $t=t_1$ (POSITIVE BIAS ON Al)

Figure 25. Illustration of a simplified model for high-field behavior of MOS structures irradiated at low temperatures.

"transport distance" d_t in a time t_1 . In the present simplified treatment, the entire distribution of holes is assumed to move uniformly as depicted in Figure 25(c). It is likely that this assumption does not correspond to physical reality but does serve as a reasonable starting point for analysis. (A more realistic model is treated in Section 4.6.)

Consider the case of a large positive bias applied to the metal electrode of an MOS structure irradiated at low temperatures (Figure 25). At a given time $t=t_1$ after irradiation, the hole distribution is assumed to have moved a distance d_t toward the silicon. The flatband voltage shift at this time can be expressed as

$$\Delta V_{fb} = \frac{\rho}{\epsilon} \int_{d_t}^{t_{ox}} x \, dx = \frac{\rho}{2\epsilon} (t_{ox}^2 - d_t^2). \quad (8)$$

For an applied negative bias, the positive charge distribution moves toward the metal electrode and at time t_1 has moved a distance d_t measured from the SiO_2 -Si interface. We obtain for this case

$$\Delta V_{fb} = \frac{\rho}{\epsilon} \int_0^{t_{ox}-d_t} x \, dx = \frac{\rho}{2\epsilon} (t_{ox} - d_t)^2. \quad (9)$$

Equations (8) and (9) can be viewed as yielding the temporal dependence of ΔV_{fb} since d_t is a function of time following bombardment. For a fixed time following bombardment, variations in d_t can be obtained by employing different values of applied field to a set of samples irradiated and measured under otherwise identical conditions.

Figure 26 shows results of calculations using Eq. (8) for the case of irradiation to a dose of 10^5 rads(Si). Shown is flatband voltage shift versus oxide thickness for several values of transport distance d_t with a positive bias applied to the metal electrode. Figure 27 shows results of similar calculations for an applied negative bias (Eq. (9)). Both figures illustrate the decrease in ΔV_{fb} that occurs with increasing hole transport distance and with decreasing oxide thickness (for a given d_t). Figure 28 presents calculated flatband voltage shift versus charge transport distance

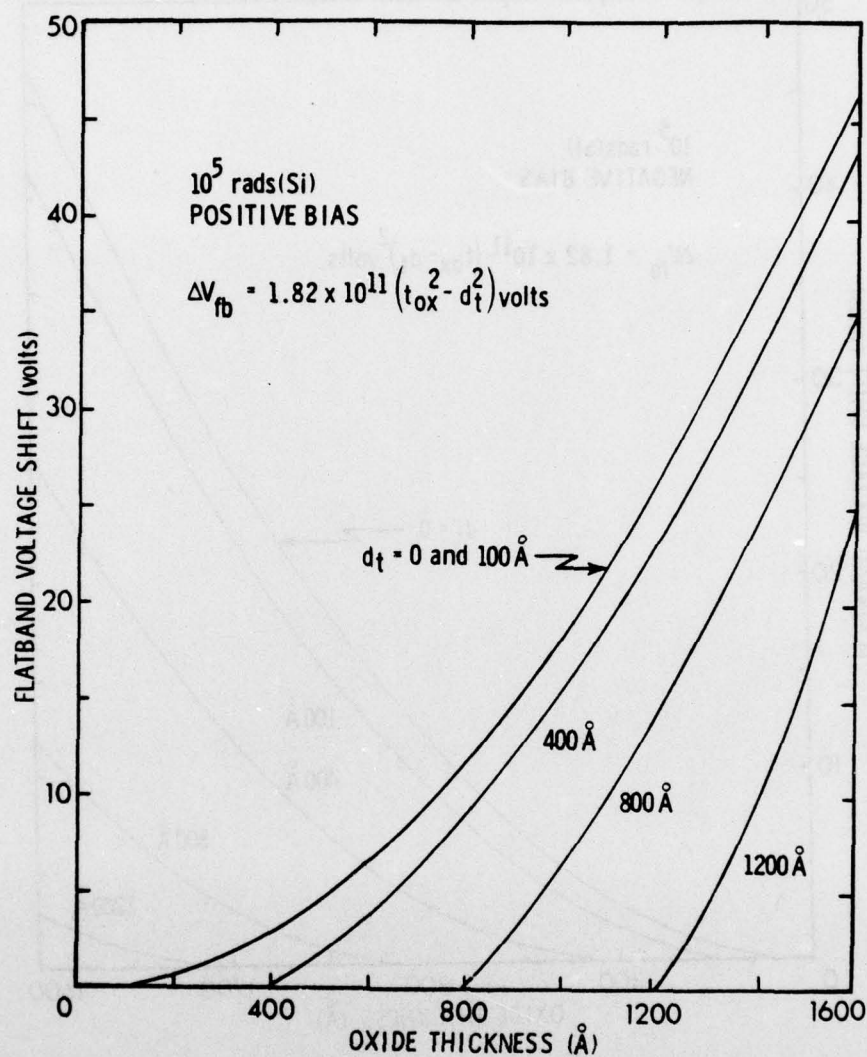


Figure 26. Calculated flatband voltage shift versus oxide thickness with transport distance as a parameter for an MOS structure irradiated to 10^5 rads(Si) with positive bias applied to the metal electrode.

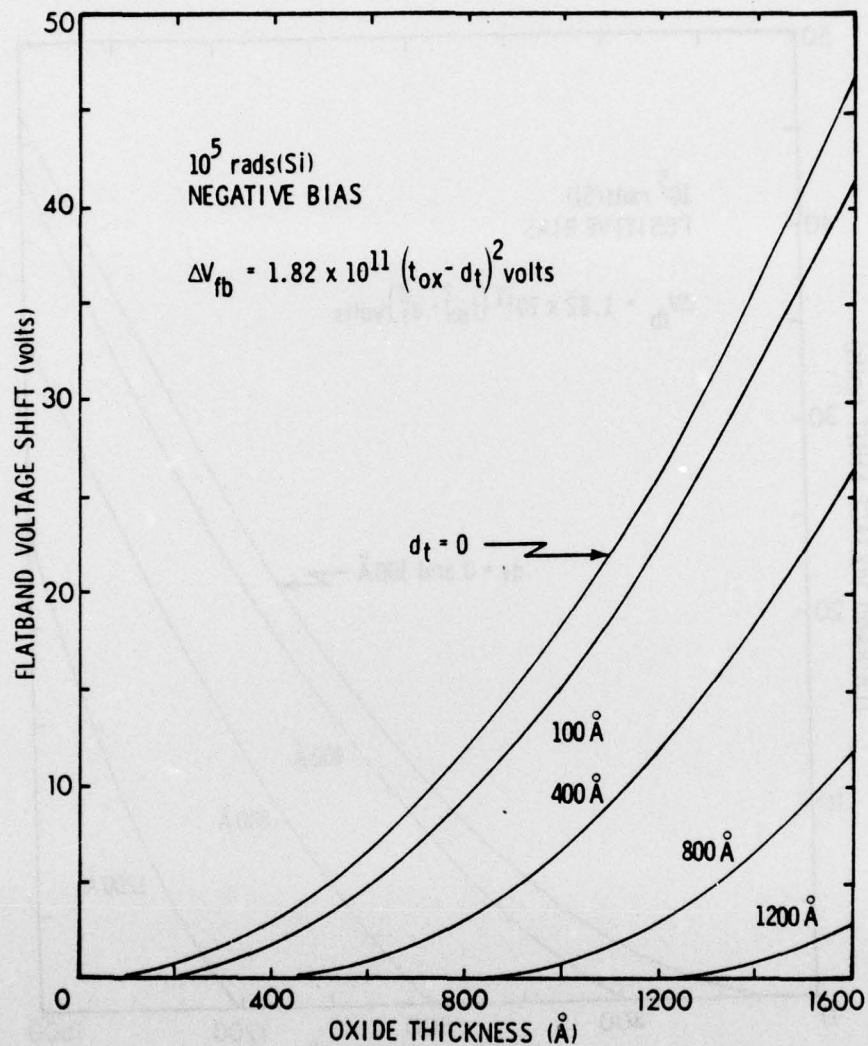


Figure 27. Calculated flatband voltage shift versus oxide thickness with transport distance as a parameter for an MOS structure irradiated to 10⁵ rads(Si) with negative bias applied to the metal electrode.

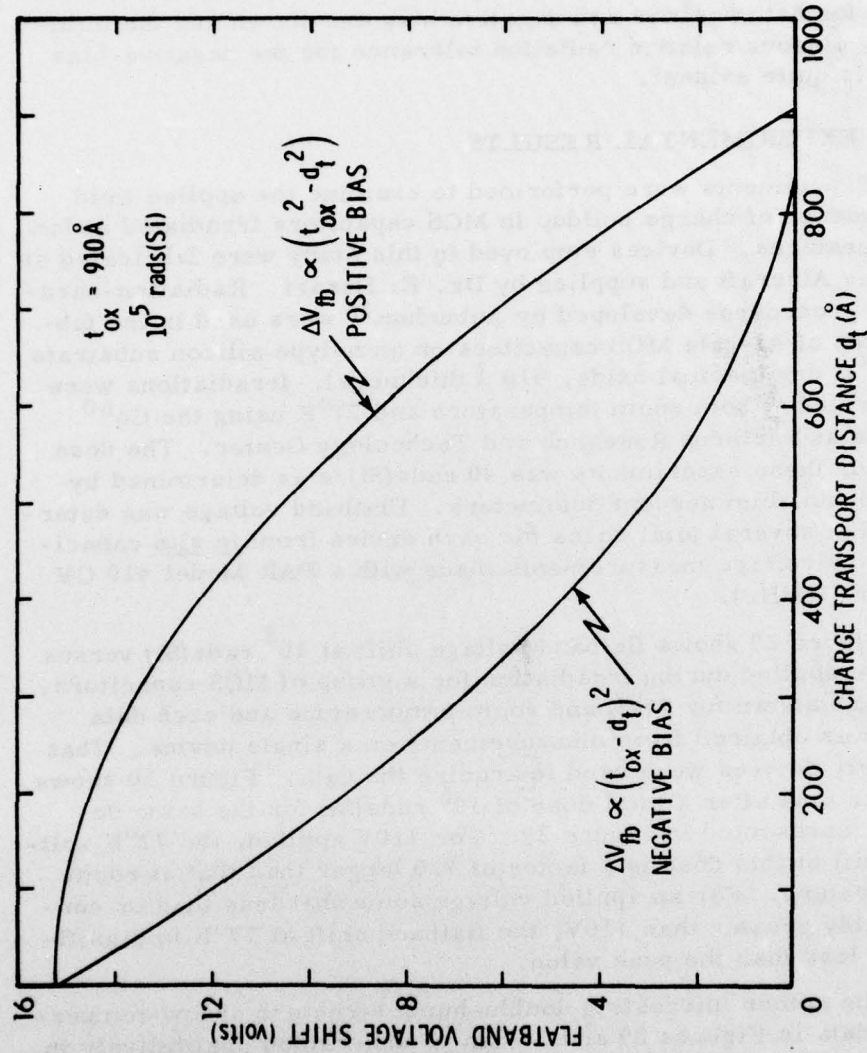


Figure 28. Calculated flatband voltage shift versus charge transport distance for a 910 Å oxide irradiated to 10^5 rads(Si). Results for both positive and negative bias are shown.

for the case of a 910 Å oxide irradiated to 10^5 rads(Si). Calculations for both positive and negative bias are shown and the intuitively obvious relative radiation tolerance for the negative-bias case is quite evident.

4.5 EXPERIMENTAL RESULTS

Experiments were performed to examine the applied field dependence of charge buildup in MOS capacitors irradiated at low temperatures. Devices employed in this study were fabricated at Hughes Aircraft and supplied by Dr. E. Harari. Radiation-hardening procedures developed by Aubuchon¹⁰ were used in the fabrication of Al-gate MOS capacitors on an n-type silicon substrate (1000°C dry thermal oxide, 910 Å thickness). Irradiations were performed at both room temperature and 77°K using the Co⁶⁰ source at Northrop Research and Technology Center. The dose rate for these experiments was 40 rads(Si)/s as determined by CaF thermoluminescent dosimeters. Flatband voltage was determined at several total doses for each device from *in situ* capacitance-vs-voltage measurements made with a PAR Model 410 CV plotter (1 MHz).

Figure 29 shows flatband voltage shift at 10^5 rads(Si) versus voltage applied during irradiation for a group of MOS capacitors. Data are shown for 77°K and room temperature and each data point was obtained from measurements on a single device. That is, forty devices were used to acquire the data. Figure 30 shows similar data after a total dose of 10^6 rads(Si) for the same devices represented in Figure 29. For +10V applied, the 77°K voltage shift at this dose is a factor of 7.5 larger than that at room temperature. For an applied voltage somewhat less than or considerably greater than +10V, the flatband shift at 77°K is significantly less than the peak value.

The rather interesting double-hump structure of low-temperature data in Figures 29 and 30 can be understood qualitatively in terms of the simple model described above and illustrated in Figures 24 and 25. Briefly, at low fields ($< 2 \times 10^6$ V/cm) a portion of the electron-hole pairs generated in the oxide recombine. Electrons escaping recombination are swept out while remaining holes are "frozen in." As the field is increased, a larger fraction of electrons escape recombination leaving a larger amount of

¹⁰ K. G. Aubuchon, IEEE Trans. Nucl. Sci. 18, 117 (Dec. 1971).

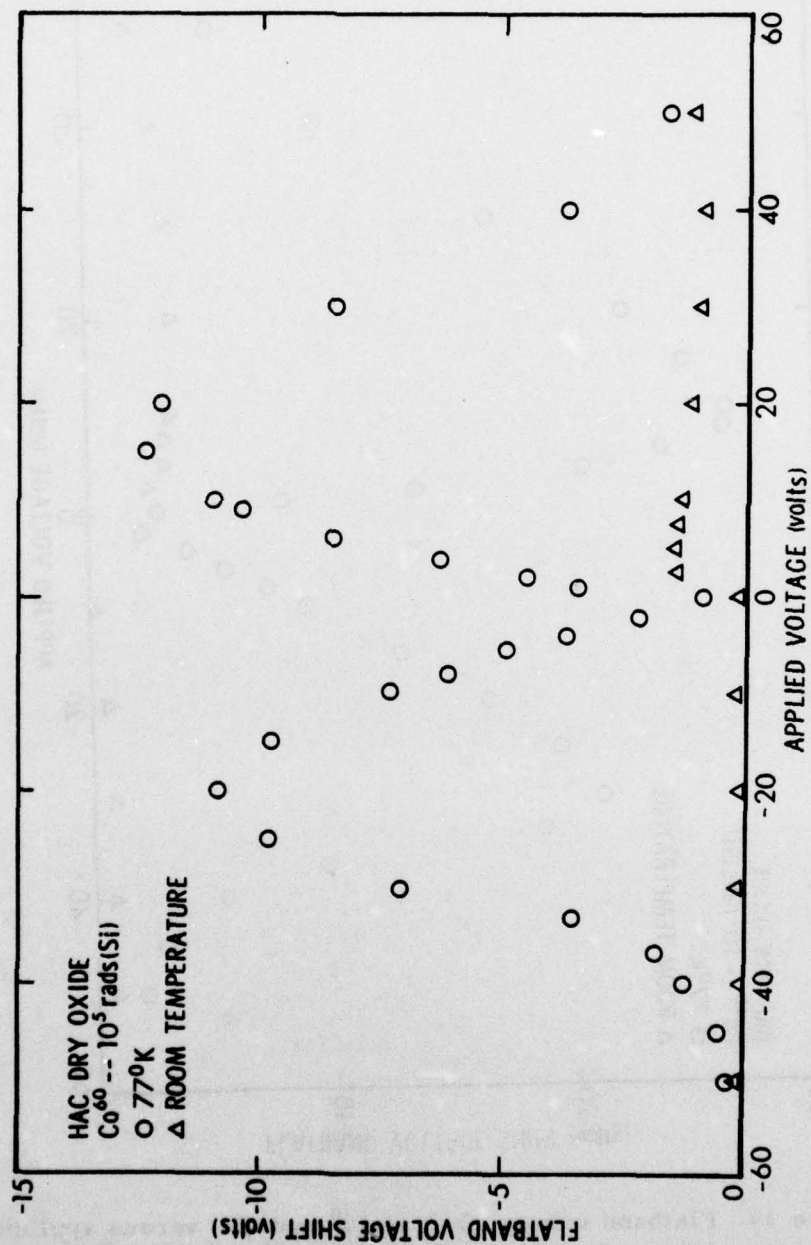


Figure 29. Flatband voltage shift at 10^5 rads(Si) versus applied voltage for MOS capacitors irradiated at 77°K and at room temperature.

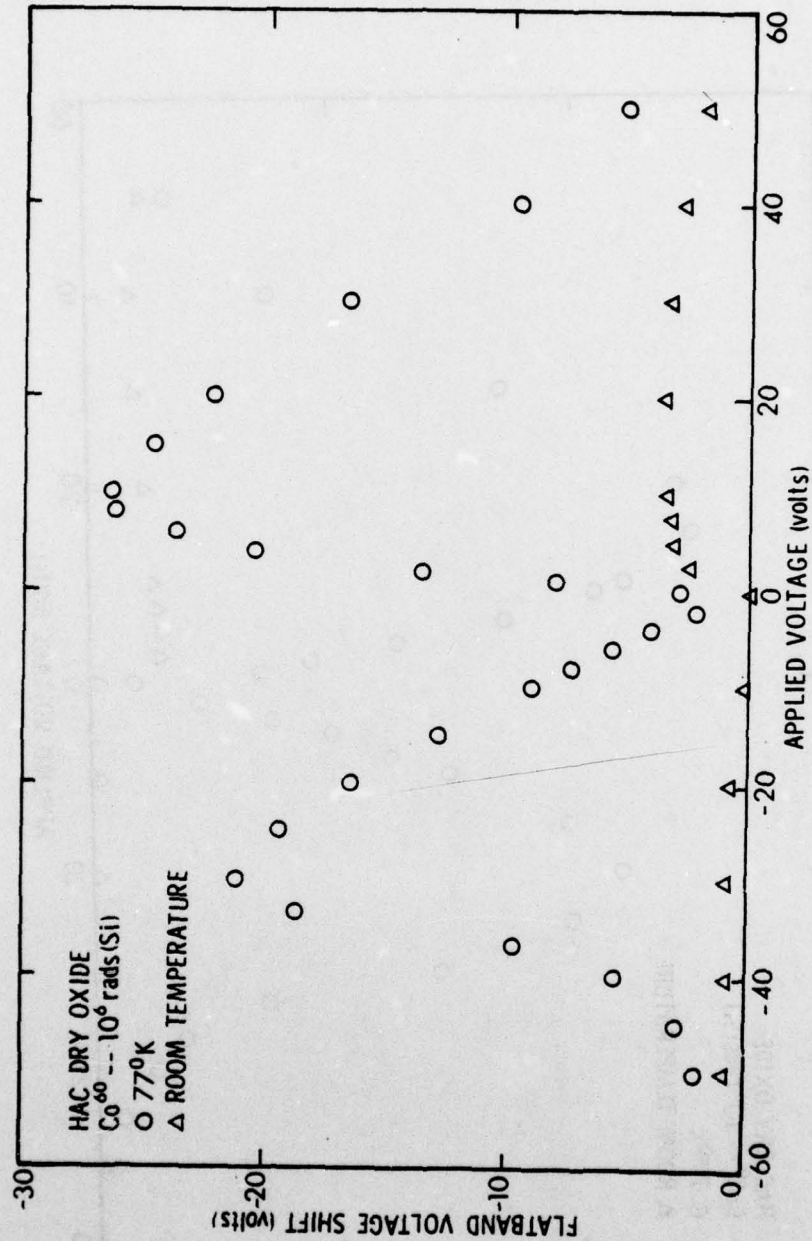


Figure 30. Flatband voltage shift at 10^6 rads(Si) versus applied voltage for MOS capacitors irradiated at 77°K and at room temperature.

uniformly-distributed positive charge. Thus, ΔV_{fb} at a given dose increases with increasing applied voltage. At higher fields, the holes become mobile which results in less positive charge in the oxide and thus gives rise to the observed decrease in ΔV_{fb} with increasing bias.

As discussed in Section 2.0, a complication arises when comparing expected and measured flatband voltage shifts at low temperatures for doses greater than $\sim 10^5$ rads(Si). At such doses, the oxide field will be perturbed due to the substantial charge buildup that exists. This perturbation is manifested as a decrease in field near the metal-SiO₂ interface and an increase in field near the SiO₂-Si interface. In the increased field region, hole transport will occur if the field there is greater than 2×10^6 V/cm. In the decreased field region more initial recombination of generated electron-hole pairs will occur. Flatband voltage shifts will be reduced by both of the above mechanisms relative to values expected on the basis of a uniform field throughout the oxide. Hence, in analysis of the present experimental results we only treat data obtained at 10^5 rads(Si) in an attempt to avoid these complications. (Recent calculations by Boesch and McGarrity¹⁷ for an oxide of thickness similar to that utilized here indicate non-negligible field modification at 10^5 rads(Si) for a device irradiated at 80°K with a 10V bias. Assuming that their calculations apply quantitatively to the present experimental conditions, it still appears likely that the predicted field perturbation for this dose would not significantly alter conclusions made below which are based on data fitting with a simple model and with a more realistic model.)

Analysis of flatband shift versus applied voltage data in Figure 29 was performed with the aid of Eqs. (8) and (9). At 10^5 rads(Si) for an oxide thickness of 910 Å, Eq. (8) can be expressed as

$$\Delta V_{fb} = \frac{\rho t_{ox}^2}{2\epsilon} \left(1 - \frac{d_t^2}{t_{ox}^2} \right) = 15.2 \left(1 - \frac{d_t^2}{t_{ox}^2} \right) \text{volts.} \quad (10)$$

¹⁷ H. E. Boesch, Jr., and J. M. McGarrity, IEEE Trans. Nucl. Sci. 23, 1520 (1976).

The coefficient 15.2 only applies for the case of no initial recombination. That is, the maximum predicted value of ΔV_{fb} is 15.2V and this value should result when all holes generated at 10^5 rads are trapped without being transported and all generated electrons are swept out of the oxide. Similarly, Eq. (9) can be written as

$$\Delta V_{fb} = \frac{\rho t_{ox}^2}{2\epsilon} \left(1 - \frac{d_t}{t_{ox}}\right)^2 = 15.2 \left(1 - \frac{d_t}{t_{ox}}\right)^2 \text{ volts.} \quad (11)$$

Boesch and McGarrity¹⁷ determined the field dependence of carrier yield for MOS capacitors irradiated at 80°K. Discussion of their findings is given below, but for now we note that the yield was nearly saturated for fields $> 2 \times 10^6$ V/cm. As a starting point for analysis, we therefore assume that all generated electrons escape recombination and are swept out of the oxide for fields $> 2 \times 10^6$ V/cm in the present experiments. For this regime, Eqs. (10) and (11) thus apply for positive and negative bias, respectively.

Figure 31 shows the positive bias data of Figure 29 replotted in terms of oxide field. All of the applied voltage appears across the oxide for this case since devices were biased into accumulation. Figure 32 presents the negative bias data of Figure 29 as a function of oxide field. It should be noted that in order to translate applied voltage into oxide field for these data, it was necessary to subtract off that portion of the applied voltage appearing across the depletion region in the semiconductor substrate. For applied voltages greater than the inversion voltage V_{inv} on a given C-V curve, a voltage equal to the difference between V_{fb} and V_{inv} was subtracted from the applied bias. For applied biases in between V_{fb} and V_{inv} , a voltage equal to the difference between V_{fb} and the applied voltage was subtracted from the applied voltage. This procedure is not exact but should be a good approximation, particularly when the applied bias is considerably larger than V_{fb} .

Analysis of the positive bias data of Figure 31 is considered first. Under the assumption of yield saturation for fields greater than 2×10^6 V/cm, Eq. (10) can be employed to calculate values for transport distance d_t at high fields by using measured values of

¹⁷ H. E. Boesch, Jr., and J. M. McGarrity, IEEE Trans. Nucl. Sci. 23, 1520 (1976).

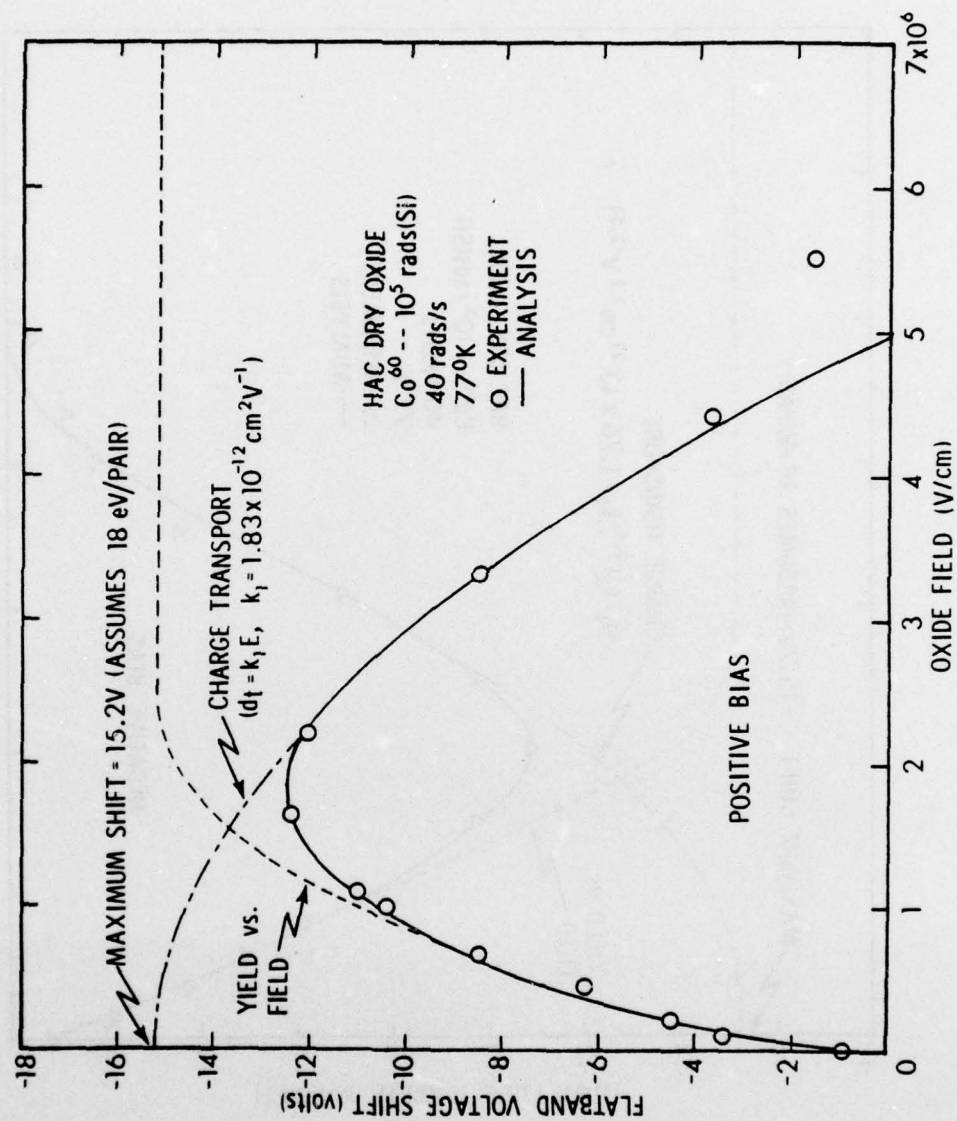


Figure 31. Flatband voltage shift at 77°K after 10⁵ rads(Si) versus oxide field for the case of an applied positive bias during irradiation. Results of data fitting are also shown (see text for discussion).

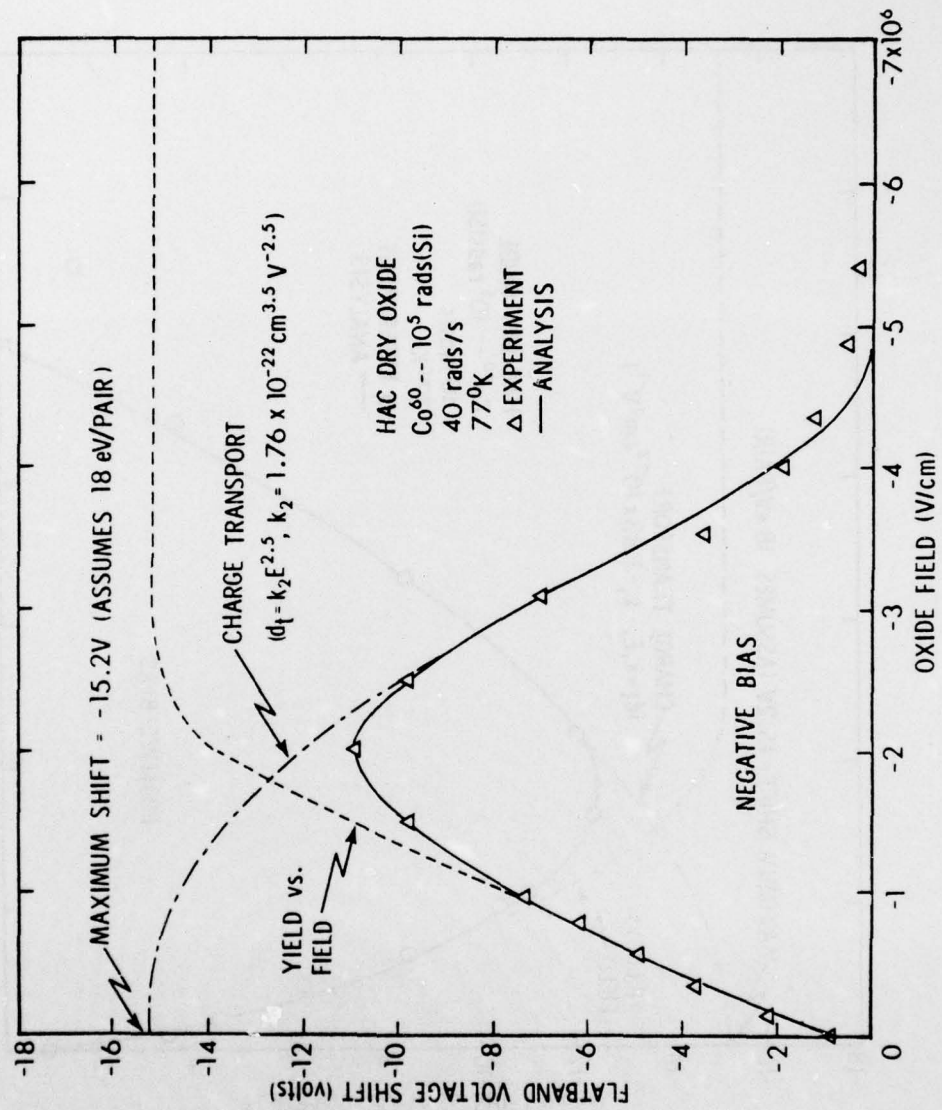


Figure 32. Flatband voltage shift at 77°K after 10^5 rads(Si) versus oxide field for the case of an applied negative bias during irradiation. Results of data fitting are also shown (see text for discussion).

AD-A046 169

NORTHROP RESEARCH AND TECHNOLOGY CENTER HAWTHORNE CALIF F/6 18/6
IONIZING RADIATION EFFECTS ON SILICON-ON-SAPPHIRE DEVICES AND S--ETC(U)
AUG 77 J R SROUR, S OTHMER, O L CURTIS DAA639-76-C-0090

UNCLASSIFIED

NRTC-77-28R

HDL-CR-77-090-1

NL

2 OF 3

AD
A046169



ΔV_{fb} . The values of d_t thus obtained are those required, based on the simple charge transport model being used, to yield the experimental data. Results are shown in Figure 33 (open triangles). For now, the reader's attention is directed to the four highest-field triangular data points. The maximum value of d_t is, by definition, t_{ox} and this saturation level is indicated in the figure. A straight-line fit to three of the four points being considered (the highest field point being excluded since it lies in the saturation regime) has unity slope and suggests a linear dependence of d_t on E . Such a relation was assumed and used to obtain the fit to high-field data in Figure 31 labeled "charge transport." Equation (10) was employed for this purpose.

The next step in the analysis was to empirically fit a "yield-vs-field" curve to the low-field data of Figure 31. At low fields, increasing the field sweeps a larger fraction of the generated electrons out of the oxide, thus causing ΔV_{fb} to increase. The criterion employed was to obtain a yield-vs-field curve that, when considered simultaneously with the charge transport curve, would yield a good composite fit to the experimental data. The resulting yield-vs-field curve is shown in Figure 31 along with the composite fit to the data (solid curve). (To obtain this fit, the charge transport curve is simply multiplied by the yield-vs-field curve normalized to its saturation value.) Having obtained a yield-vs-field curve, one can then use Eq. (10) to calculate d_t at fields $< 2 \times 10^6$ V/cm by simply using the appropriate field-dependent coefficient (i.e., < 15.2) obtained from this curve. Figure 33 shows three corrected triangular points (solid) obtained by this method and it is seen that all values (except the one in the saturation regime) are now fit quite well by a unity-slope line. (This "correction" procedure actually forces those calculated d_t values which deviate from the unity slope line to agree with it.) The three uncorrected open-triangle points at fields $< 2 \times 10^6$ V/cm deviate from this line due to the effect of the yield-vs-field curve on charge transport. That is, the charge transport curve by itself does not take initial recombination into account. We also note that the observation of d_t depending linearly on oxide field is at first surprising, and this feature is discussed below.

The negative bias data of Figure 32 are now considered. The same fitting procedure as described for the positive bias case was employed except that Eq. (11) was used instead of Eq. (10). Use of this equation to calculate d_t at high fields yielded the results

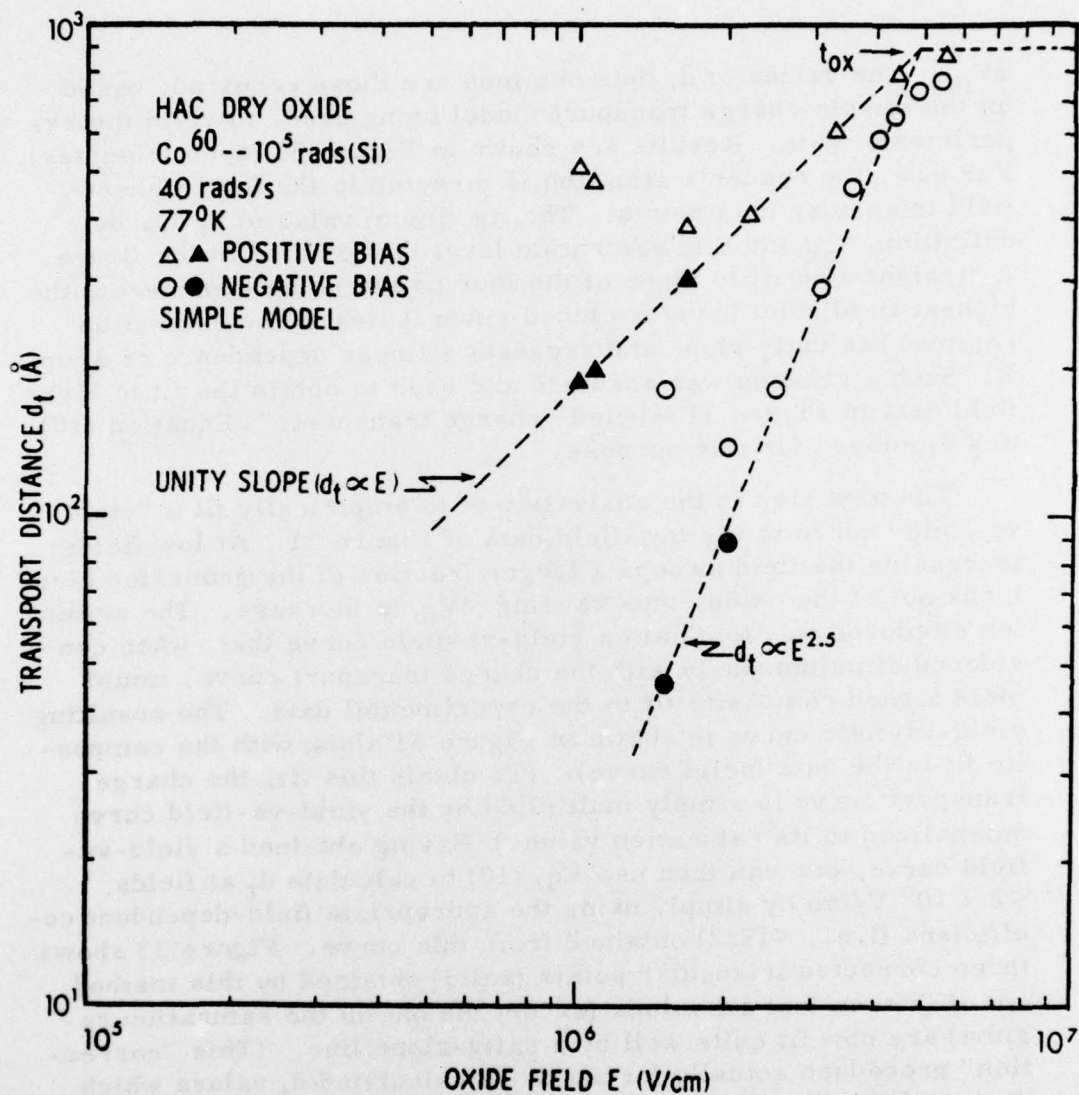


Figure 33. Calculated transport distance d_t versus oxide field. Calculations were performed using Eqs. (10) and (11) in conjunction with measured values of ΔV_{fb} .

shown in Figure 33. The relation $d_t \propto E^{2.5}$ is seen to describe the data well except for the two lowest-field points which are influenced by the variation of yield with field as in the positive bias case. (Corrected values of these two points are shown in the figure also -- solid circles.) The resulting charge transport fit is shown in Figure 32, along with the yield-vs-field curve required to obtain the composite fit to the data. Figure 34 shows fits to both positive and negative bias data taken from Figures 31 and 32.

It is of interest to compare the yield-vs-field fits of Figures 31 and 32 with results of other studies. Figure 35 compares the present yield-vs-field curves with that obtained by Boesch and McGarrity¹⁷ for 13-MeV electron-bombarded specimens at 80°K and with room temperature data (5-keV electrons) obtained at these laboratories.¹¹ Data of Boesch and McGarrity is for positive bias and the present positive bias curve is similar in shape to their curve. The magnitudes are in reasonable agreement also. At 10^6 V/cm we obtain a fractional yield of 0.73 as compared to 0.86 for their data. Differences between results of Boesch and the present findings (Figure 35) may be attributable in part to partial recovery of V_{fb} during the relatively slow Co^{60} irradiations as compared to pulsed 13-MeV electron bombardment where measurements were performed ~ 1 ms after the pulse. Specimen differences may also play a role. Regarding differences between low-energy electron curve in Figure 35 and the other three curves (Co^{60} , 13-MeV electrons), it is thought that geminate recombination dominates in the latter cases whereas columnar recombination is important in the former case,¹⁶ and this may provide the explanation for the discrepancy. (Additional discussion of this point is given in Section 4.6.)

4.6 IMPROVED MODEL

The inadequacy of the simple model described in Section 4.4 in accounting for the experimental results presented above is illustrated in Figure 33. Calculation of transport distance versus

¹¹ J. R. Srour, O. L. Curtis, Jr., and K. Y. Chiu, IEEE Trans. Nucl. Sci. 21, 73 (Dec. 1974).

¹⁶ G. A. Ausman and F. B. McLean, Appl. Phys. Lett. 26, 73 (1975).

¹⁷ H. E. Boesch, Jr., and J. M. McGarrity, IEEE Trans. Nucl. Sci. 23, 1520 (1976).

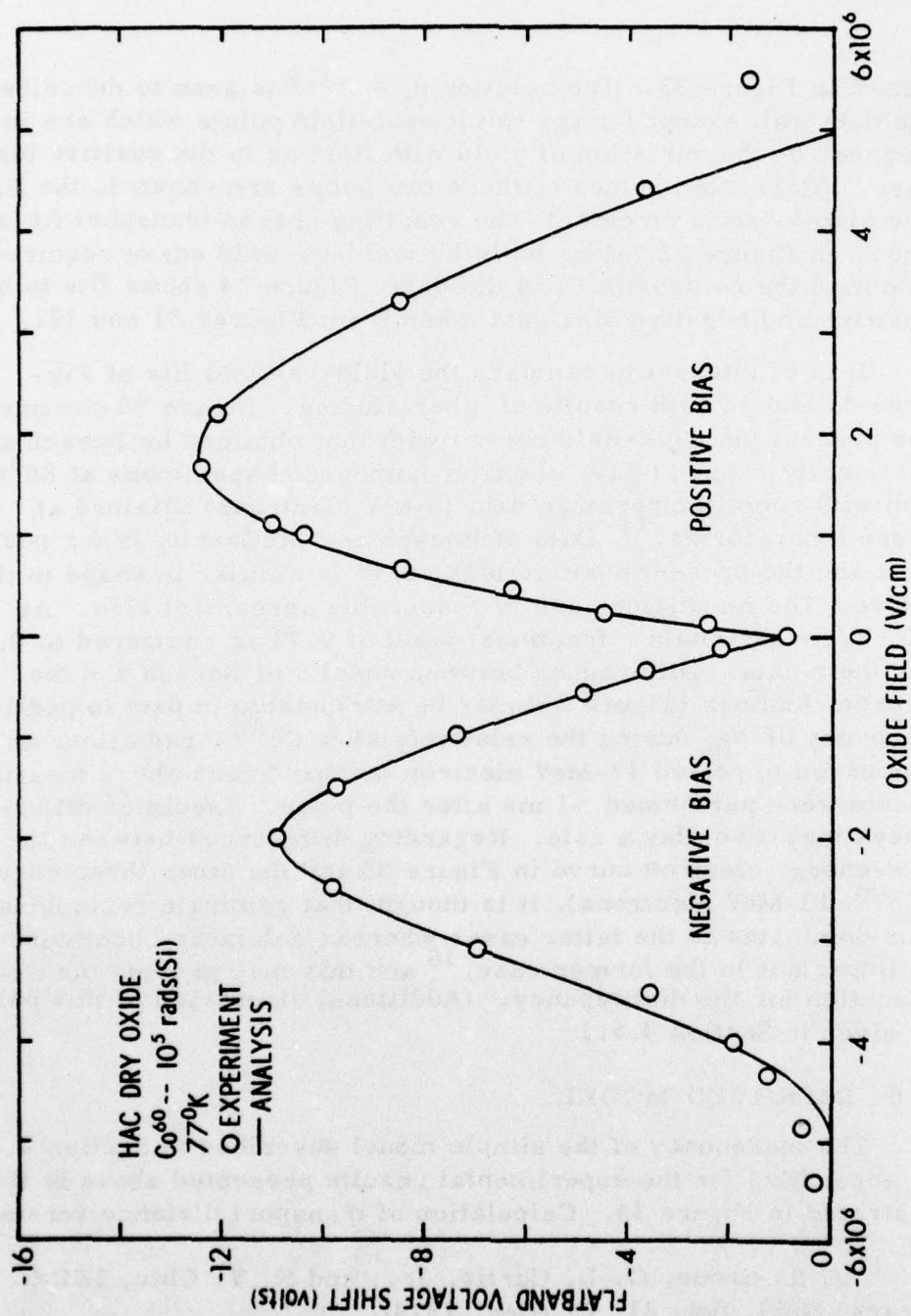


Figure 34. Overall fit to experimental data based on the fitting procedure illustrated in Figures 31 and 32.

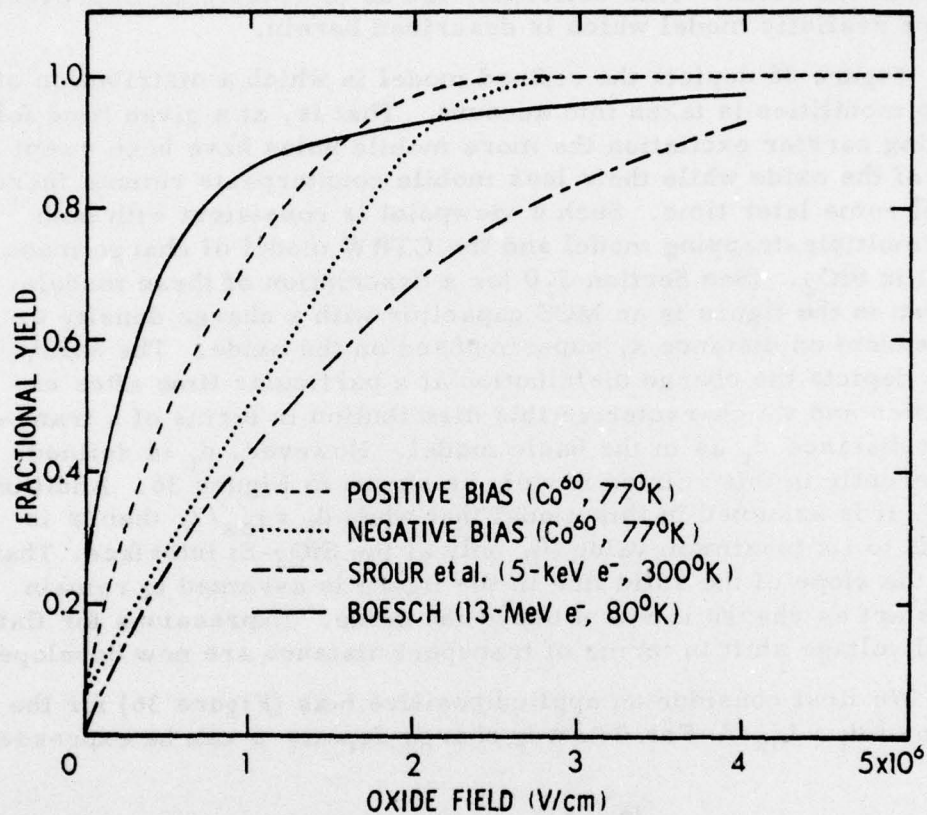


Figure 35. Fractional yield versus oxide field for the present study and for two earlier investigations. The positive and negative bias curves were taken from Figures 31 and 32, respectively.

field with this model yielded $d_t \propto E$ for positive bias whereas $d_t \propto E^{2.5}$ was obtained for negative bias. One expects the value of d_t to be independent of polarity for a given absolute value of field in the oxide. This deficiency led us to develop an improved, more realistic model which is described herein.

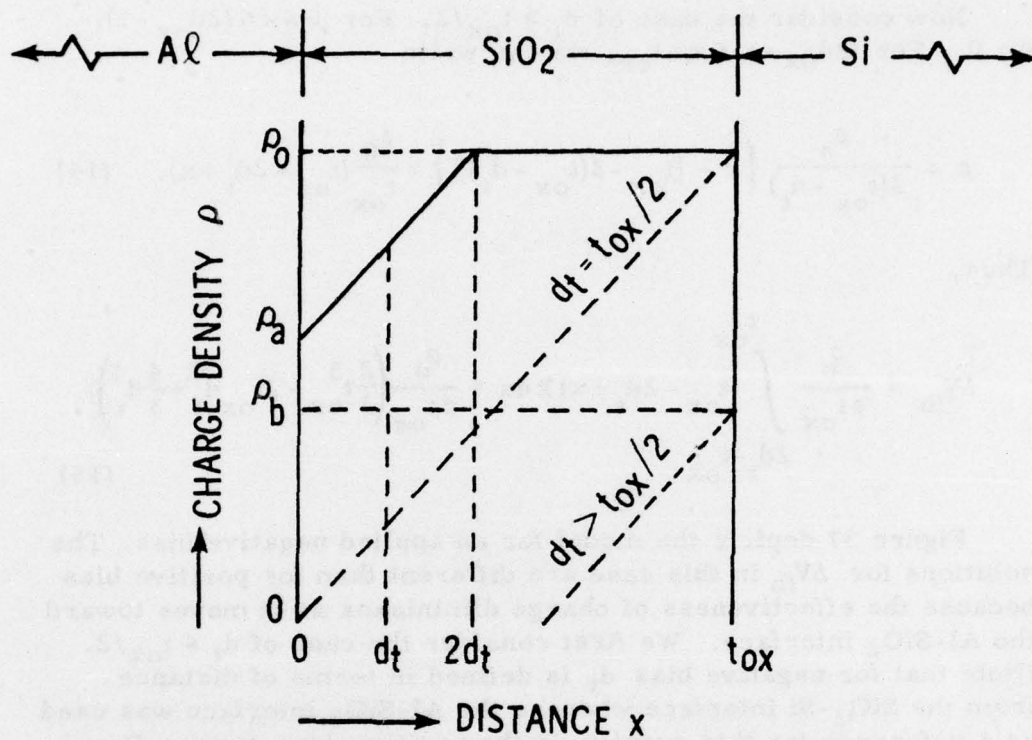
Figure 36 depicts the refined model in which a distribution of hole mobilities is taken into account. That is, at a given time following carrier excitation the more inobile holes have been swept out of the oxide while their less mobile counterparts remain there until some later time. Such a viewpoint is consistent with both the multiple-trapping model and the CTRW model of charge transport in SiO_2 . (See Section 3.0 for a description of these models.) Shown in the figure is an MOS capacitor with a charge density ρ , dependent on distance x , superimposed on the oxide. The solid line depicts the charge distribution at a particular time after excitation and we characterize this distribution in terms of a transport distance d_t as in the basic model. However, d_t is defined differently in this refined model, as shown in Figure 36. Additionally, it is assumed in this model that when $d_t = t_{\text{ox}}/2$, then ρ is equal to its maximum value ρ_0 only at the SiO_2 -Si interface. That is, the slope of the solid line in the figure is assumed to remain constant as charge is swept out of the oxide. Expressions for flat-band voltage shift in terms of transport distance are now developed.

We first consider an applied positive bias (Figure 36) for the case of $d_t \leq t_{\text{ox}}/2$. For $0 \leq x \leq d_t$, charge density ρ can be expressed as

$$\rho = \rho_a + \frac{(\rho_0 - \rho_a)}{2d_t} x = \frac{\rho_0}{t_{\text{ox}}} (t_{\text{ox}} - 2d_t + x). \quad (12)$$

For $2d_t \leq x \leq t_{\text{ox}}$, $\rho = \rho_0$. Therefore,

$$\begin{aligned} \Delta V_{\text{fb}} &= \frac{\rho_0}{\epsilon t_{\text{ox}}} \left[\int_0^{2d_t} (t_{\text{ox}} - 2d_t + x) x dx + \int_{2d_t}^{t_{\text{ox}}} t_{\text{ox}} x dx \right] \\ &= \frac{\rho_0}{\epsilon t_{\text{ox}}} \left(\frac{1}{2} t_{\text{ox}}^3 - \frac{4}{3} d_t^3 \right). \end{aligned} \quad (13)$$



POSITIVE BIAS ON ALUMINUM ELECTRODE

Figure 36. Illustration of a more realistic model for the motion of charge at high fields and low temperatures in SiO₂ (positive bias case).

Now consider the case of $d_t \geq t_{ox}/2$. For $0 \leq x \leq (2d_{ox} - t)$, $\rho = 0$. For $(2d_{ox} - t) \leq x \leq t_{ox}$, we can write

$$\rho = \frac{\rho_b}{2(t_{ox} - d_t)} \left\{ x - [t_{ox} - 2(t_{ox} - d_t)] \right\} = \frac{\rho_0}{t_{ox}} (t_{ox} - 2d_t + x). \quad (14)$$

Thus,

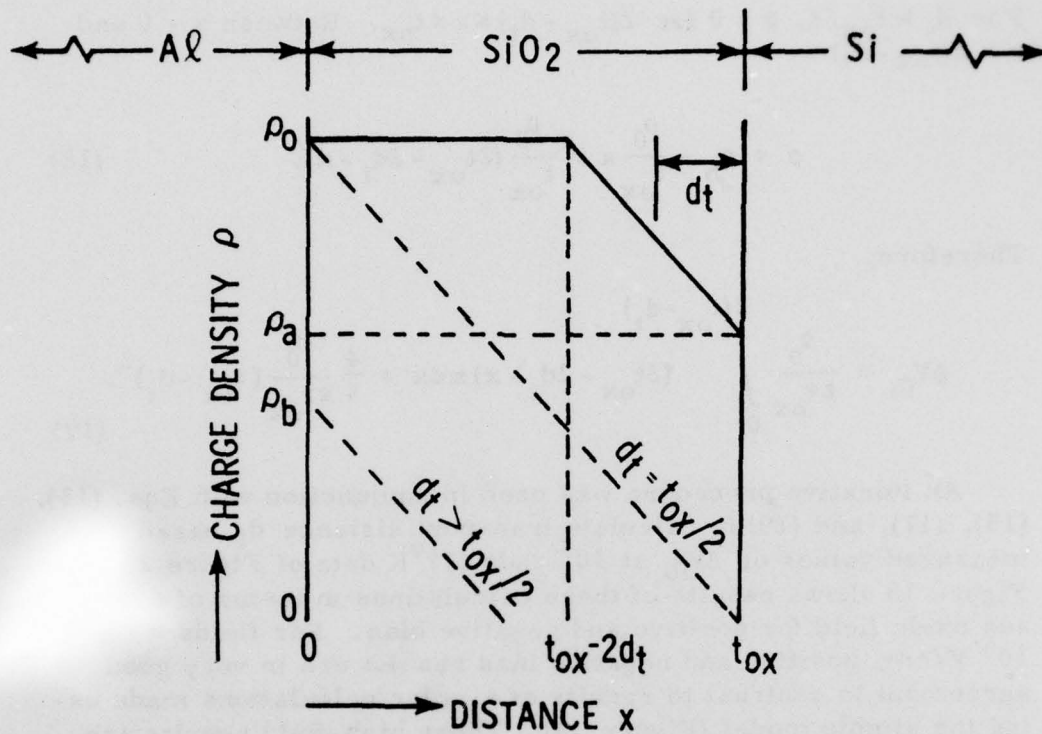
$$\Delta V_{fb} = \frac{\rho_0}{\epsilon t_{ox}} \int_{2d_t - t_{ox}}^{t_{ox}} (t_{ox} - 2d_t + x) x dx = \frac{\rho_0}{\epsilon t_{ox}} \left(\frac{2}{3} t_{ox}^3 - 2t_{ox} d_t^2 + \frac{4}{3} d_t^3 \right). \quad (15)$$

Figure 37 depicts the model for an applied negative bias. The solutions for ΔV_{fb} in this case are different than for positive bias because the effectiveness of charge diminishes as it moves toward the Al-SiO₂ interface. We first consider the case of $d_t \leq t_{ox}/2$. (Note that for negative bias d_t is defined in terms of distance from the SiO₂-Si interface whereas the Al-SiO₂ interface was used as a reference for this quantity in the positive-bias case.) For $0 \leq x \leq (t_{ox} - 2d_t)$, $\rho = \rho_0$. For $(t_{ox} - 2d_t) \leq x \leq t_{ox}$, ρ can be expressed as

$$\rho = \rho_0 - \left(\frac{\rho_0 - \rho_a}{2d_t} \right) [x - (t_{ox} - 2d_t)] = \frac{\rho_0}{t_{ox}} (2t_{ox} - 2d_t - x). \quad (16)$$

Thus,

$$\begin{aligned} \Delta V_{fb} &= \frac{\rho_0}{\epsilon} \int_0^{t_{ox} - 2d_t} x dx + \frac{\rho_0}{\epsilon t_{ox}} \int_{t_{ox} - 2d_t}^{t_{ox}} (2t_{ox} - 2d_t - x) x dx \\ &= \frac{\rho_0}{\epsilon t_{ox}} \left(\frac{4}{3} d_t^3 - 2d_t^2 t_{ox} + \frac{1}{2} t_{ox}^3 \right). \end{aligned} \quad (17)$$



NEGATIVE BIAS ON ALUMINUM ELECTRODE

Figure 37. Illustration of a more realistic model for the motion of charge at high fields and low temperatures in SiO_2 (negative bias case).

For $d_t \geq t_{ox}/2$, $\rho = 0$ for $2(t_{ox} - d_t) \leq x \leq t_{ox}$. Between $x = 0$ and $x = 2(t_{ox} - d_t)$

$$\rho = \rho_b - \frac{\rho_0}{t_{ox}} x = \frac{\rho_0}{t_{ox}} (2t_{ox} - 2d_t - x). \quad (18)$$

Therefore,

$$\Delta V_{fb} = \frac{\rho_0}{\epsilon t_{ox}} \int_0^{2(t_{ox} - d_t)} (2t_{ox} - 2d_t - x) x dx = \frac{4}{3} \frac{\rho_0}{\epsilon t_{ox}} (t_{ox} - d_t)^3. \quad (19)$$

An iterative procedure was used in conjunction with Eqs. (13), (15), (17), and (19) to calculate transport distance d_t based on measured values of ΔV_{fb} at 10^5 rads (77°K data of Figure 29). Figure 38 shows results of these calculations in terms of d_t versus oxide field for positive and negative bias. For fields $> 3 \times 10^6$ V/cm, positive and negative bias results are in very good agreement in contrast to results of similar calculations made using the simple model (Figure 33). These high-field results are fit reasonably well with a unity-slope line as shown in Figure 38. At low fields, deviation of the calculated points from this line is due to the influence of carrier yield on charge transport as was the case in Figure 33. (Note that no "corrected" points are shown in Figure 38.) The unity-slope fit yields $d_t = kE$, where $k = 1.5 \times 10^{-12} \text{ cm}^2\text{V}^{-1}$. The calculated points can also be fit with a line of nonunity slope. However, by neglecting the two highest-field points (one positive bias and one negative bias) due to the apparent onset of saturation and by neglecting points at fields $\leq 3 \times 10^6$ V/cm due to the influence of a nonsaturated yield-vs-field curve, any reasonable resulting fit has a slope near unity. Additional high-field data would be required to obtain a more accurate relation between d_t and oxide field.

The expression $d_t = kE$, with $k = 1.5 \times 10^{-12} \text{ cm}^2\text{V}^{-1}$, was then used to fit positive bias flatband shift data at 10^5 rads in the same manner as employed with the simple model described earlier. In the present case, Eqs. (13) and (15) were utilized to obtain an appropriate charge transport curve. Results are shown in Figure 39 and it is seen that an excellent fit to the data is obtained. Using the same expression for d_t and applying the same

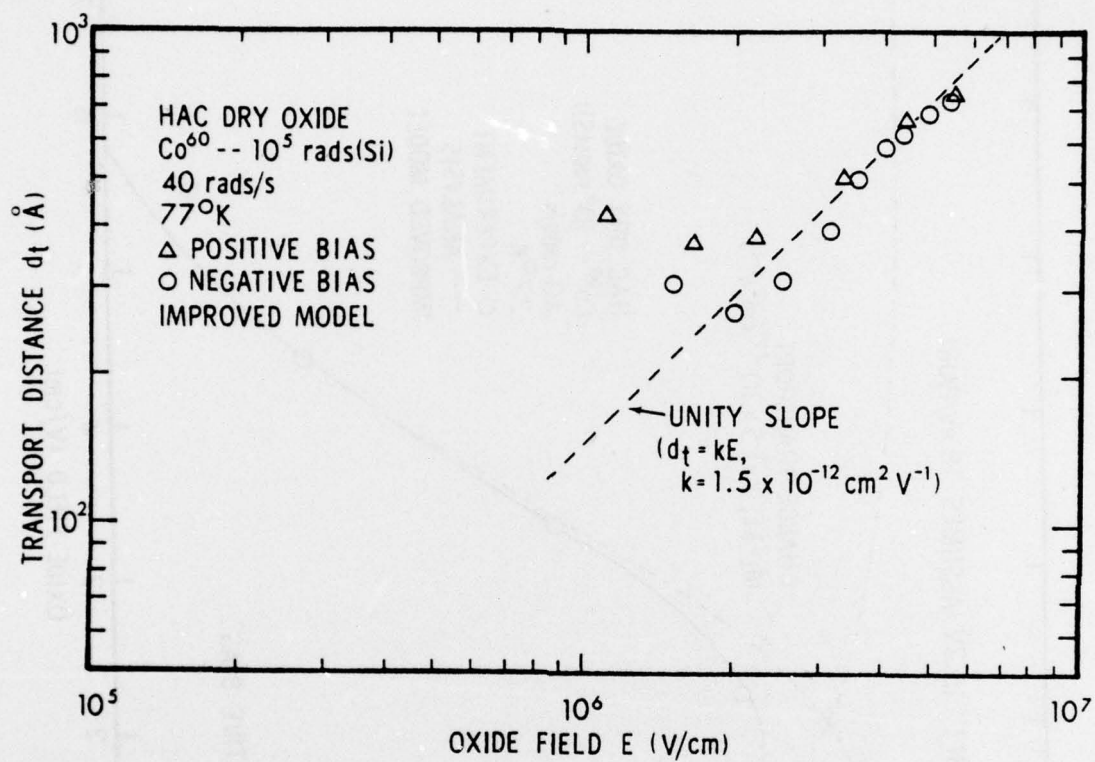


Figure 38. Transport distance versus applied field based on calculations using the improved model illustrated in Figures 36 and 37.

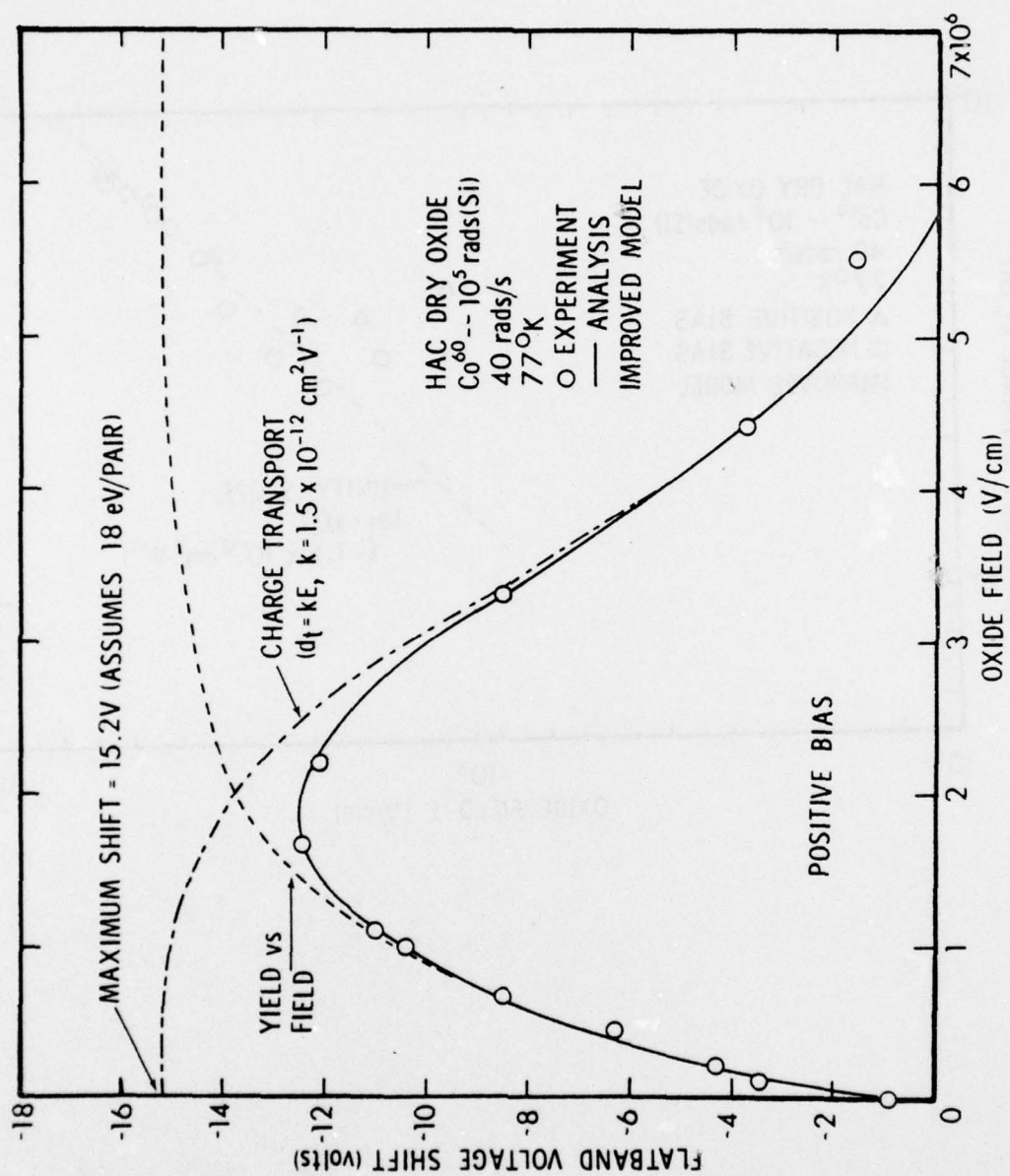


Figure 39. Flatband voltage shift at 77°K versus oxide field for the case of an applied positive bias. Results of data fitting using an improved model are shown (see text).

procedure to negative bias data was not as successful, as shown in Figure 40. The charge transport curve for $k = 1.5 \times 10^{-12}$ fits the highest-field data but deviates from data at intermediate fields. Reducing k to 1.4×10^{-12} improves the transport fit somewhat as shown in the figure. We also note that a rather severe linear yield-vs-field curve is required, in conjunction with either of the transport curves shown, to obtain a fit for data at fields $< 2 \times 10^6$ V/cm. Although the general features of the negative bias data are described by the improved modeling approach, the fit obtained is only fair compared to the positive bias case. However, the important point to note is that the improved approach has removed the $d_t \propto E$ vs $d_t \propto E^{2.5}$ discrepancy while still providing a semi-quantitative description of both positive and negative bias data.

It is of interest to compare the yield-vs-field curve in Figure 39 with previous results as was done above for the simple model. Figure 41 shows this curve along with two others which are also shown in Figure 35. The shape of the present curve and that of Boesch¹⁷ is nearly the same and excellent agreement between these curves is noted for fields $\geq 2 \times 10^6$ V/cm.

4.7 DISCUSSION

The improved model described above was much more successful in accounting for the experimental data than the simple model. However, because of the problems encountered in fitting negative bias data, a better model was sought. McLean³⁵ has calculated charge distributions in the SiO_2 layer of an MOS capacitor as a function of time after bombardment by ionizing irradiation using the CTRW model.⁶ An initially uniform charge distribution was assumed. The shapes of his calculated curves are similar to those used in the improved model employed above, but his curves are more closely approximated by the model illustrated in Figure 42. In this model, the "transport angle" θ is a variable analogous to d_t in the previous two models. For $\theta = 0$ no holes have been transported out of the oxide, and for $\theta = 90^\circ$ all holes have been swept

⁶ H. E. Boesch, Jr., F. B. McLean, J. M. McGarrity, and G. A. Ausman, Jr., IEEE Trans. Nucl. Sci. 22, 2163 (1975).

¹⁷ H. E. Boesch, Jr., and J. M. McGarrity, IEEE Trans. Nucl. Sci. 23, 1520 (1976).

³⁵ F. B. McLean, Harry Diamond Laboratories, private communication.

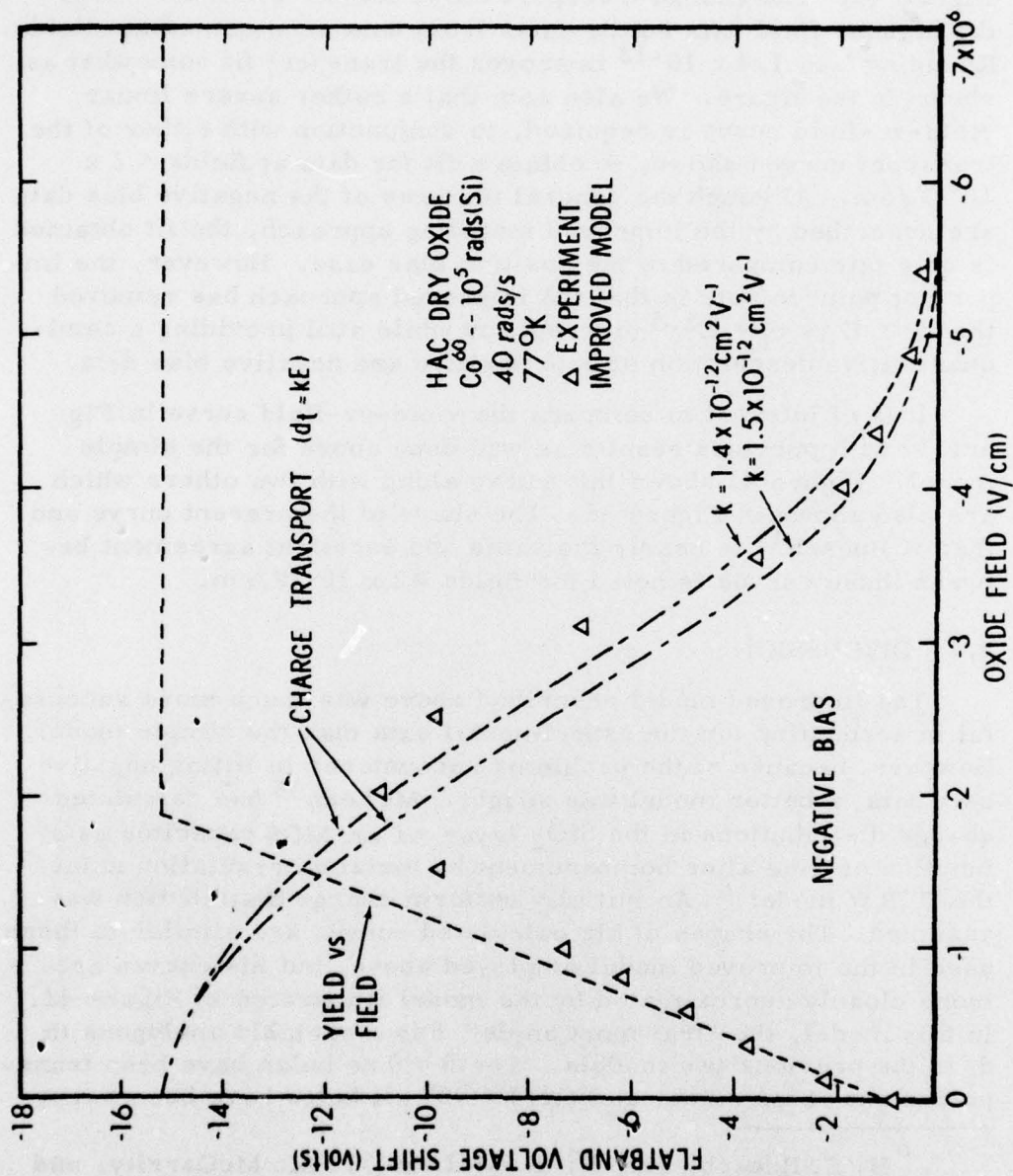


Figure 40. Flatband voltage shift at 77°K versus oxide field for the case of an applied negative bias. Results of data fitting using an improved model are shown (see text).

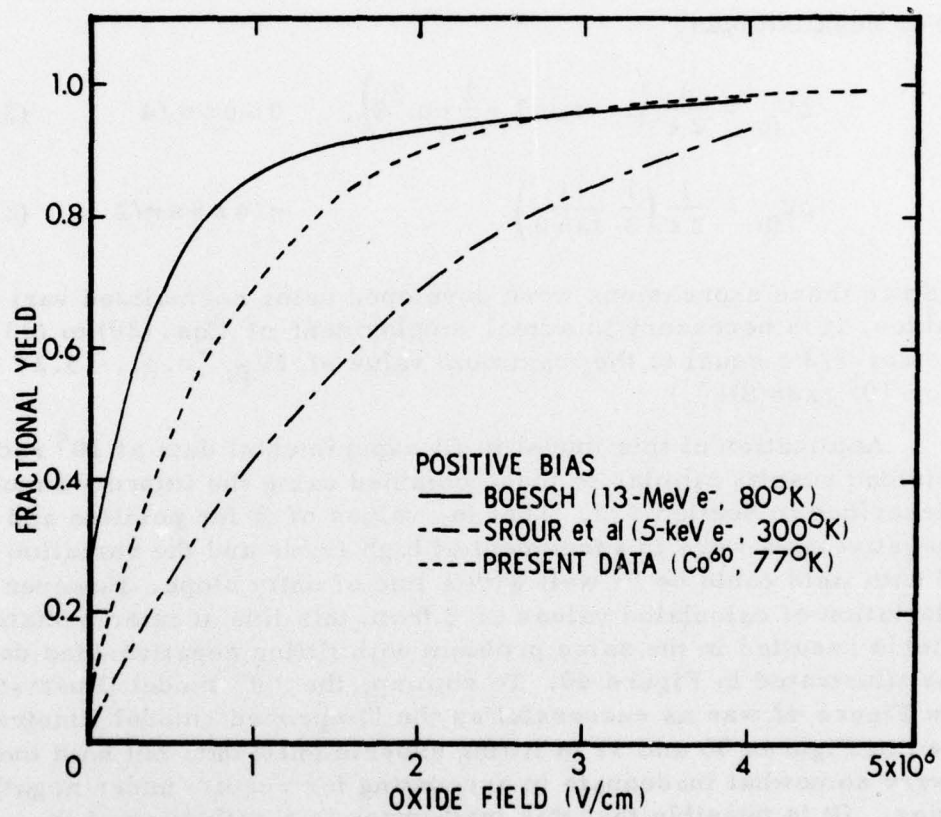


Figure 41. Fractional yield versus oxide field for the present study (from Figure 39) and for two previous investigations.

out. Expressions were developed for ΔV_{fb} in terms of θ and the following results were obtained. For positive bias,

$$\Delta V_{fb} = \frac{1}{2 \epsilon} \left(1 - \frac{1}{3} \tan^2 \theta \right), \quad 0 \leq \theta \leq \pi/4 \quad (20)$$

$$\Delta V_{fb} = \frac{1}{2 \epsilon} \left(\frac{2}{3} \frac{1}{\tan \theta} \right), \quad \pi/4 \leq \theta \leq \pi/2 \quad (21)$$

For negative bias,

$$\Delta V_{fb} = \frac{1}{2 \epsilon} \left(1 - \tan \theta + \frac{1}{3} \tan^2 \theta \right), \quad 0 \leq \theta \leq \pi/4 \quad (22)$$

$$\Delta V_{fb} = \frac{1}{2 \epsilon} \left(\frac{1}{3} \frac{1}{\tan \theta} \right), \quad \pi/4 \leq \theta \leq \pi/2 \quad (23)$$

(Since these expressions were developed using normalized variables, it is necessary in actual employment of Eqs. (20) to (23) to set $1/2 \epsilon$ equal to the maximum value of ΔV_{fb} [e.g., 15.2V for 10^5 rads(Si)].)

Application of this model to fit experimental data at 10^5 rads(Si) yielded results similar to those obtained using the improved model described in Section 4.6. That is, values of θ for positive and negative bias were in agreement at high fields and the variation of θ with field could be fit well with a line of unity slope. However, deviation of calculated values of θ from this line at intermediate fields resulted in the same problem with fitting negative-bias data as illustrated in Figure 40. To sum up, the " θ " model illustrated in Figure 42 was as successful as the "improved" model illustrated in Figures 36 and 37 in fitting experimental data but both models were somewhat inadequate in accounting for results under negative bias. (It is possible that this inadequacy is a reflection of the accuracy of the data rather than a reflection on the model employed. At high fields where ΔV_{fb} varies strongly with oxide field, it may be desirable to obtain additional data since the transport modeling procedures applied here are rather sensitive to values of ΔV_{fb} in this regime.)

We also considered the influence of an initial transport distance d_0 on the data fitting procedure for both the simple and the

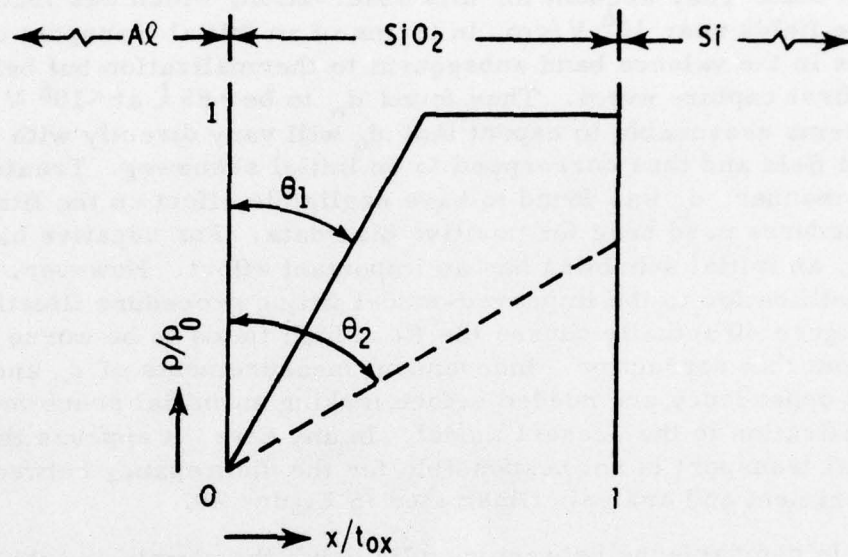


Figure 42. Illustration of a model for hole transport in SiO_2 which makes use of a variable "transport angle" θ . The Al electrode is positively biased here.

improved models. Boesch and McGarrity¹⁷ observed that initial flatband shifts (i.e., shifts at early times following pulsed irradiation) at 80°K differed slightly depending on the polarity of the applied bias. They account for this observation, which was made for oxide fields near 10^6 V/cm, in terms of an initial transport of holes in the valence band subsequent to thermalization but before the first capture event. They found d_0 to be $\sim 85 \text{ \AA}$ at $\sim 10^6$ V/cm. It seems reasonable to expect that d_0 will vary directly with applied field and thus correspond to an initial schubweg. Treated in this manner, d_0 was found to have negligible effect on the fitting procedures used here for positive bias data. For negative bias data, an initial schubweg has an important effect. However, such a modification to the improved-model fitting procedure illustrated in Figure 40 actually causes the fit at high fields to be worse than without this correction. Independent measurements of d_0 and its field dependence are needed before making an initial schubweg modification to the present model. In any case, it appears that initial transport is not responsible for the discrepancy between experiment and analysis illustrated in Figure 40.

In comparisons between results using the simple and the improved model, one feature was not mentioned above. The improved model yields a fit, for both positive and negative bias, which has a shape that conforms better to data at the highest fields than that for the simple model (compare Figures 31 and 32 with Figures 39 and 40). This is a further indication that the improved model is more appropriate for describing the data.

As mentioned earlier, it is at first surprising that d_t was found to depend linearly on field for the positive bias data of Figure 33 (simple model) and for data of both polarities in Figure 38 (improved model). Such a dependence yields an effective hole mobility that is independent of field. To calculate mobility, a characteristic time is needed first in order to obtain carrier velocity. A total dose of 10^5 rads is delivered in 41.7 min at a rate of 40 rads/s. Thus, a time of ~ 21 min can be associated with creation of the average carrier. That is, the average carrier has a transport time of ~ 21 min associated with it. In Figure 33,

¹⁷ H. E. Boesch, Jr., and J. M. McGarrity, IEEE Trans. Nucl. Sci. 23, 1520 (1976).

$d(d_t)/dE = k_1 = 1.83 \times 10^{-12} \text{ cm}^2 \text{V}^{-1}$, and we thus obtain a mobility of $1.5 \times 10^{-15} \text{ cm}^2/\text{Vsec}$. Similarly, from Figure 38 we obtain a mobility of $1.2 \times 10^{-15} \text{ cm}^2/\text{Vsec}$. These field-independent mobilities are in contrast to results presented in Sections 2.0 and 3.0 of this report in which mobility was noted to depend on $E^{3.2}$ at intermediate temperatures and on $E^{12.6}$ at low temperature (90°K). We also note that the mobilities reported here are smaller than the lowest value ($10^{-14} \text{ cm}^2/\text{Vsec}$) shown in Figure 19. However, the samples used to obtain the results in that figure were from a different batch than those used in obtaining data for the present section and agreement in absolute mobility values within an order of magnitude is perhaps reasonable.

Regarding differences in the field dependence of mobility, it is important to note that mobility was derived in a basically different manner here than in Sections 2.0 and 3.0. In the present case, a quantity related to carrier transport was measured at a fixed time following bombardment whereas in previous determinations a fixed amount of transported charge was used as the basis for evaluating mobility. We have found that evaluating field-dependent transport data by these two methods can yield significantly different results and most likely can account for observation of a field-independent μ in one case and $\mu \propto E^{3.2}$ in the other. Regarding the explanation for observing $\mu \propto E^{12.6}$ versus observing no field dependence, two factors appear important. First, as just described, the mobility evaluation methods were fundamentally different for the two cases. Second, different samples were used. This factor is important because, as reported in Sections 2.0 and 3.0, at 90°K we observed negligible hole transport at fields $< 2 \times 10^6 \text{ V/cm}$ for samples which yielded $\mu \propto E^{12.6}$ at that same temperature. On the other hand, McLean et al.²⁰ noted significant low-temperature transport at 10^6 V/cm for samples from the same wafer used to obtain data presented in this section (4.0). (See Figure 3 of Reference 20.) Thus, although a more quantitative assessment may be needed, it appears that the rather striking differences noted among observed field dependences of mobility can be accounted for on the basis of different evaluation methods and on specimen differences.

²⁰ F. B. McLean, H. E. Boesch, Jr., and J. M. McGarrity, IEEE Trans. Nucl. Sci. 23, 1506 (1976)

4.8 SUMMARY

This section has presented information regarding the low-temperature behavior of MOS devices in an ionizing radiation environment. Methods were given for alleviating the significant charge buildup that occurs at such temperatures due to the relative immobility of holes. Experimental data in the form of flat-band voltage shift versus oxide field were presented and models for describing these data were given. Positive charge buildup in irradiated MOS devices at low temperatures was explained in terms of the dependence of carrier yield on applied field and hole transport at relatively high fields.

SECTION 5.0
IONIZING RADIATION EFFECTS ON
SILICON-ON-SAPPHIRE DEVICES*

5.1 INTRODUCTION

Silicon-on-sapphire MOS devices are being developed for radiation-hardened electronic systems because they have several advantages over their MOS-on-bulk-silicon counterparts: reduced transient photoresponse; elimination of latchup; increased packing density and speed. One disadvantage of SOS devices is the occurrence of a significant ionizing-radiation-induced back-channel leakage current in n-channel transistors.³⁶⁻³⁸ This phenomenon has been attributed to the trapping of positive charge in the sapphire near the silicon-sapphire interface which induces a conducting channel in the silicon. We have performed a detailed study of ionizing radiation effects on SOS devices with emphasis being placed on examination of back-channel leakage current phenomena. Two types of radiation-hardened devices were investigated: (1) custom n-channel transistors; (2) 4007 inverters.

This section describes the results of our SOS studies, and the following topics are included: (1) comparison of threshold voltage shifts and channel mobility degradation for devices with wet and dry gate oxides; (2) radiation-induced back-channel leakage current comparison for wet and dry devices; (3) bombarding electron energy dependence of back-channel leakage current; (4) radiation-induced reduction of back-channel leakage current; (5) back-channel leakage current studies on CMOS inverters; (6) studies of the silicon-sapphire interface based on the C-V technique of Goodman^{39,40} and the transient current technique of Lehovec.⁴¹ The reader's attention is particularly directed to the

*A portion of the results presented here along with additional related findings obtained after completion of this program are contained in a paper to be published in the Dec. 1977 issue of the IEEE Transactions on Nuclear Science.

³⁶D. Neamen, W. Shedd, and B. Buchanan, IEEE Trans. Nucl. Sci. 21, 211 (Dec. 1974).

³⁷R.A. Kjar and J. Peel, IEEE Trans. Nucl. Sci. 21, 208 (Dec. 1974).

³⁸K.M. Schlesier, IEEE Trans. Nucl. Sci. 21, 152 (Dec. 1974).

³⁹A.M. Goodman, IEEE Trans. Electron Devices 21, 753 (1974).

⁴⁰A.M. Goodman, IEEE Trans. Electron Devices 22, 63 (1975).

⁴¹K. Lehovec and R. Miller, 1976 IEDM Technical Digest, p.283.

discussion of radiation-induced reduction of leakage current. This novel mechanism constitutes a potential remedy for leakage current problems in SOS devices employed in a space radiation environment.

5.2 EXPERIMENTAL CONSIDERATIONS

A variety of experiment techniques were used in this study since various quantities were measured, including threshold voltage, channel mobility, back-channel leakage current, SOS C-V curves, and current transients. Each of these techniques is described in detail below in the appropriate subsection. In the present subsection, descriptions of the radiation sources used and the SOS devices employed are given. Irradiations were performed using the Co^{60} source at Northrop Research and Technology Center and a Jeol JSM-2 scanning electron microscope. The Co^{60} dose rate was 64 rads(Si)/s in most cases but in some experiments was reduced to 4.3 rads(Si)/s. The SEM beam energy was varied over the range 7.5 to 18.5 keV for the purpose of studying the mechanisms of back channel leakage current production.

Silicon-on-sapphire devices examined in this study were obtained from various sources. Most of the information presented herein resulted from studies on custom n-channel SOS transistors fabricated at Hughes Aircraft (HAC) under the supervision of Dr. E. Harari. Sapphire wafers containing a silicon epitaxial layer (initial thickness 0.5 μm) were obtained by HAC from Union Carbide and devices containing both wet and dry gate oxides were then fabricated. All processing steps were identical for these devices except the gate oxidation. Figure 43 outlines the HAC processing sequence. Note that the wet oxide was grown at 925°C whereas the dry-oxide growth temperature was 1000°C. The gate metallization on 75% of the transistors was purposely kept thin ($750 \pm 100 \text{ \AA}$) to permit studies with a low-energy electron beam (SEM). Channel width was 8.0 mils and channel length was 0.21 ± 0.02 mil. Figure 44 schematically illustrates a custom n-channel SOS transistor with a thin gate metallization. Using the same masks, SOS capacitors were also prepared by HAC for us by implanting the channel with phosphorus, thus yielding an all-n-type silicon island.

We also investigated radiation-hardened CMOS/SOS inverters (4007) obtained from three manufacturers. Devices from five lots were examined, including two lots from each of two suppliers and

SOS PROCESSING SEQUENCE (HAC)

1. GROW OXIDE/NITRIDE LAYER TO MASK CHANNEL DURING SOURCE AND DRAIN DIFFUSION
2. SOURCE/DRAIN DIFFUSION: DRIVE-IN OF n^+ -DOPED GLASS
3. IMPLANT CHANNEL
4. GATE OXIDATION -- TWO TYPES:
 - (a) WET OXIDE (PYROGENIC, 925°C)
 - (b) DRY OXIDE (1000°C)
5. DEPOSITION OF AL FROM A HEATED CRUCIBLE
6. AL ALLOY

Figure 43. Processing sequence for custom n-channel SOS devices fabricated for NRTC by Hughes Aircraft.

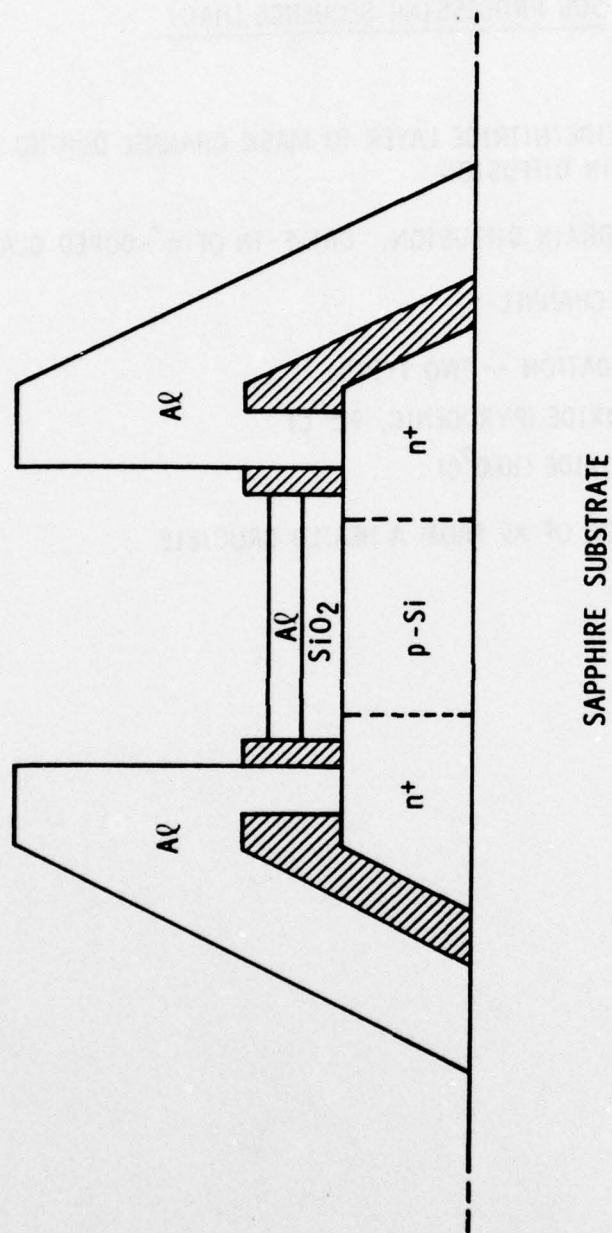


Figure 44. Schematic illustration of custom n-channel SOS transistors with a thin gate metallization (cross-hatched regions are field oxide).

one lot from the other source. Measurements on these devices were restricted primarily to radiation-induced back-channel leakage current on n-channel transistors.

5.3 THRESHOLD VOLTAGE SHIFT IN SOS TRANSISTORS

Threshold voltage V_t was measured as a function of total ionizing dose for custom n-channel SOS transistors with both wet and dry gate oxides. The experimental technique employed was the conventional one of measuring $\sqrt{I_{ds}}$ versus V_{gs} and determining threshold voltage from the intercept of the linear portion of such data with the V_{gs} axis. The circuit utilized for these measurements is described in Reference 13 and is based on the use of a current-to-voltage converter and a Bell and Howell Type 435 square-root module. Irradiations were performed using Co^{60} at a dose rate of 64 rads(Si)/s. The value of V_{ds} during irradiation and during measurement of threshold voltage was 5V. This value was chosen to be less than that for which the "kink effect" becomes evident in drain current-voltage characteristics. Data were obtained for $V_{gs} = 0$ (grounded gate) and 5V during irradiation.

Figure 45 presents threshold voltage versus dose for wet and dry oxide devices irradiated with $V_{gs} = 0$. At 10^7 rads, V_t decreased by only 0.3V for the dry case which is a remarkable degree of radiation tolerance. The wet oxide device exhibited an increase in V_t of 1V at the same dose and this increase is presumably due to the formation of negatively charged states at the SiO_2 -Si interface. McLean et al.²⁰ have reported that interface state effects are more important in wet oxide devices than in dry and the present findings are consistent with their observations.

Figure 45 also shows two data points (solid) obtained after a 72h room temperature anneal subsequent to irradiation. Annealing was conducted without bias voltages applied to the devices. The threshold voltage for the dry device recovered to its pre-irradiation value whereas ΔV_t for the wet unit increased from 1V to 1.3V. These observed changes in V_t during the annealing period can be attributed either to release of holes trapped near the SiO_2 -Si

¹³ J. R. Srour, S. Othmer, O. L. Curtis, Jr., and K. Y. Chiu, Harry Diamond Laboratories Report HDL-CR-76-161-1, June 1976.

²⁰ F. B. McLean, H. E. Boesch, Jr., and J. M. McGarrity, IEEE Trans. Nucl. Sci. 23, 1506 (1976).

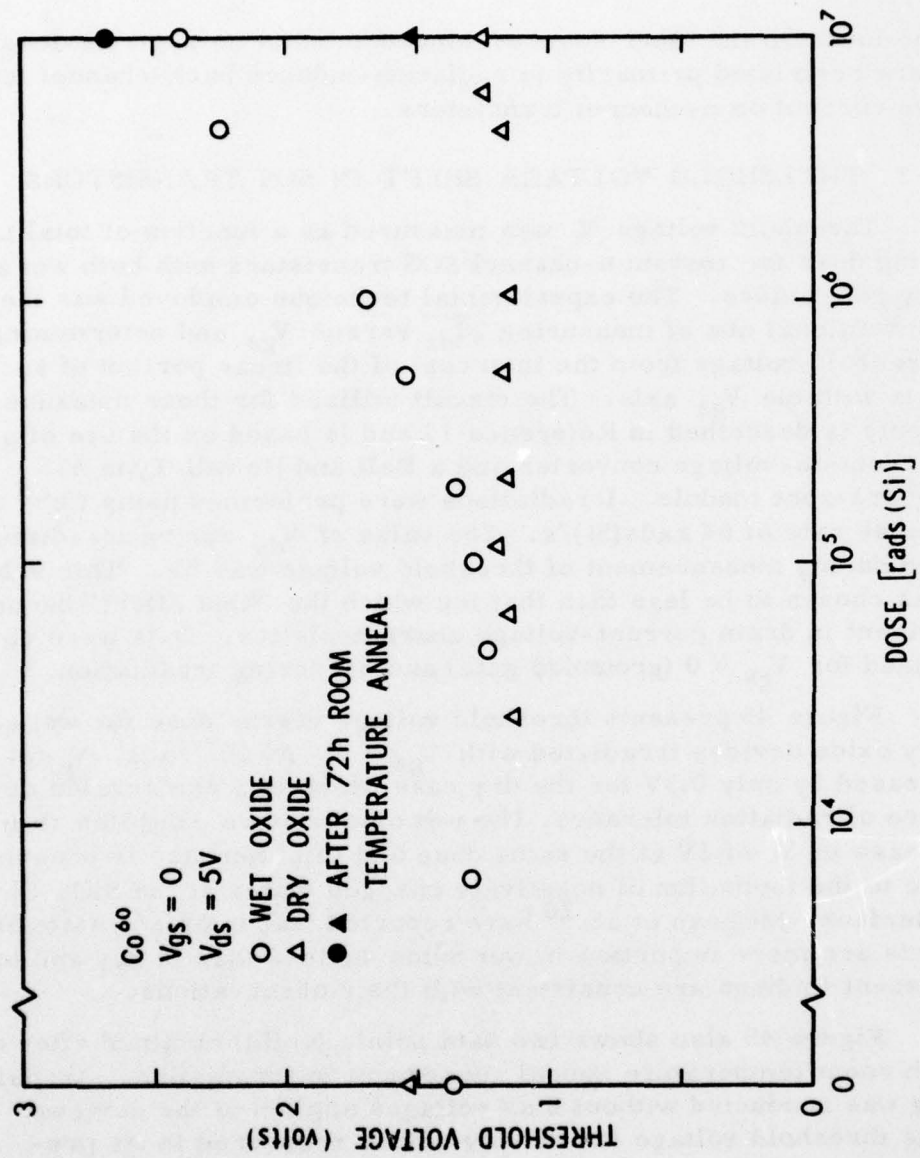


Figure 45. Threshold voltage versus dose for wet- and dry-oxide n-channel SOS transistors irradiated with $V_{gs} = 0$.

interface or to creation of additional negatively charged states at that interface. (In general, both effects may be occurring simultaneously.) Winokur et al.⁴² observed significant increases in interface state density in MOS capacitors at long times following irradiation and this phenomenon may be occurring in the present devices, particularly for the wet oxide case.

Figure 46 shows V_t versus dose for wet and dry oxide devices with $V_{gs} = 5V$ during irradiation. For the dry unit, the maximum value of ΔV_t is $-1.3V$ which is considerably larger than for the zero-bias data of Figure 45. This result is reasonable since an applied positive bias causes more holes to be transported to the SiO_2 -Si interface where a portion are trapped. For the wet transistor, V_t decreases up to about 5×10^5 rads due to positive charge buildup but increases at higher doses due to interface states. It is interesting to note that very little change in V_t occurred during the annealing period for the wet oxide device but an increase of $0.5V$ was noted for the dry unit. Additional data would be required to determine the mechanism dominating post-irradiation behavior. In conclusion, we note that both wet- and dry-oxide transistors are quite radiation tolerant. Under worst-case biasing conditions, the maximum value of ΔV_t observed up to 10^7 rads was $1.3V$.

5.4 CHANNEL MOBILITY DEGRADATION IN SOS TRANSISTORS

Carrier mobility in the inversion layer of MOS transistors can be measured in several ways. The most meaningful measurement, from a practical viewpoint, is that which yields conductance mobility μ_c . This quantity is obtained directly from measurements of the conductance between source and drain, and when the term "channel" mobility is employed here we are referring to the conductance mobility. Another measurement approach commonly employed yields field-effect mobility μ_{fe} . We have performed measurements of μ_c and μ_{fe} for wet and dry oxide n-channel SOS transistors and results are presented in this section. The approaches used to measure these quantities are described first, including a detailed description of our solution to a device-related problem in determining conductance mobility.

⁴² P. S. Winokur, J. M. McGarrity, and H. E. Boesch, Jr., IEEE Trans. Nucl. Sci. 23, 1580 (1976).

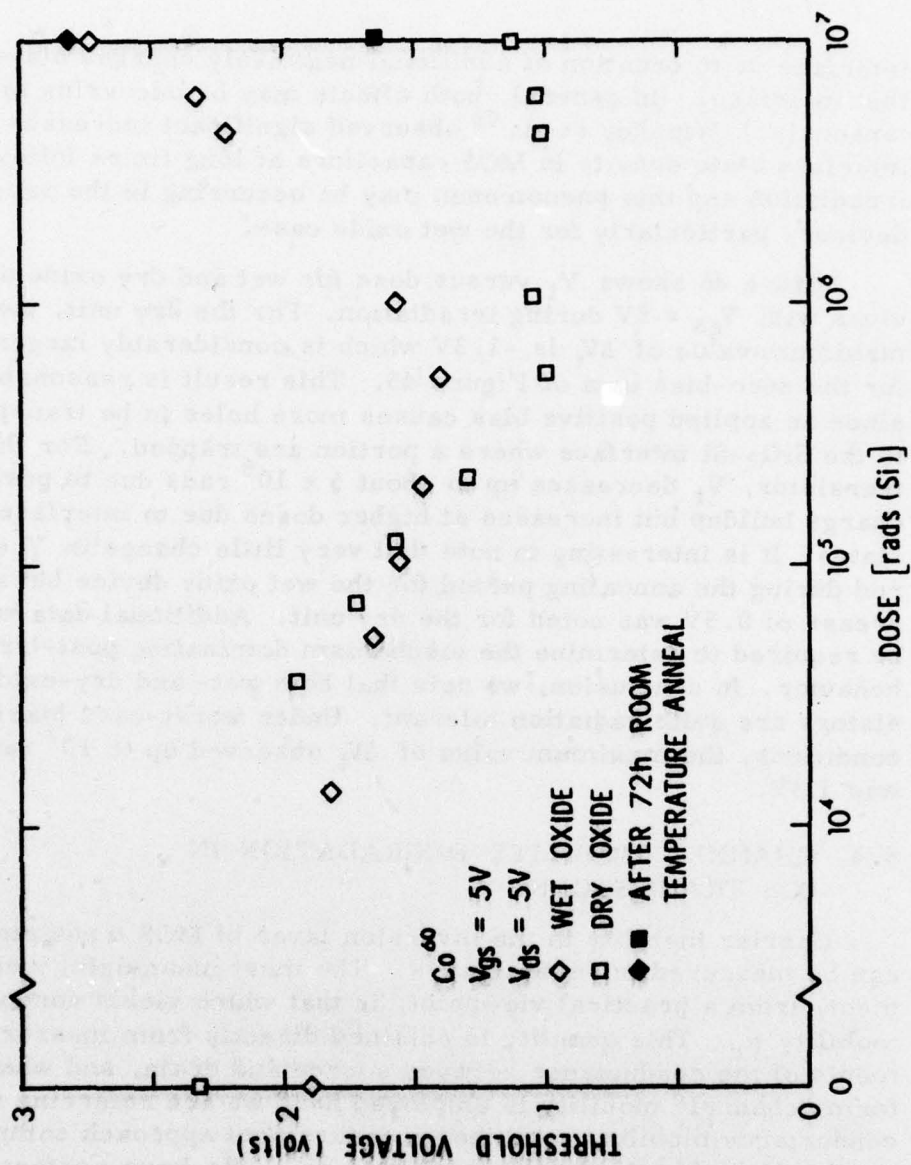


Figure 46. Threshold voltage versus dose for wet- and dry-oxide n-channel SOS transistors irradiated with $V_{gs} = 5V$.

Conductance mobility for an MOS transistor is obtained from measurements of channel conductance g_c , defined as

$$g_c = \left. \frac{\partial I_d}{\partial V_{ds}} \right|_{V_{gs}}, \quad (1)$$

where conventional notation is employed. Channel conductance and conductance mobility are related through the expression

$$\mu_c = g_c L / Q_f W, \quad (2)$$

where Q_f is the induced free charge per unit area in the channel and L and W are channel length and width, respectively. The quantities g_c , L , and W are measured and one must then determine Q_f in order to obtain mobility. Chen and Muller⁴³ have described an approach to obtaining the free charge density based on determining the interface (or surface) potential. They employed this approach in measuring conductance mobility versus inversion layer carrier concentration over a wide range. Sah et al.⁴⁴ employed the relation

$$Q_f = C_{ox} (V_{gs} - V_t) \quad (3)$$

to obtain the free charge density, where C_{ox} is oxide capacitance per unit area. This expression assumes that the additional gate voltage applied beyond the threshold voltage only induces free carriers; i.e., it assumes that the depletion region charge density and the trapped charged density at interface states remain unchanged. This assumption was made in the present work. We therefore obtain

$$\mu_c = g_c L / W C_{ox} (V_{gs} - V_t). \quad (4)$$

Equation (4) can also be obtained using the following approach. At very low values of V_{ds} , the following expression applies:

⁴³J. T. C. Chen and R. S. Muller, J. Appl. Phys. 45, 828 (1974).

⁴⁴C. T. Sah, T. H. Ning, and L. L. Tschopp, Surface Science 32, 561 (1972).

$$I_d = \frac{\mu_c W C_{ox}}{L} V_{ds} (V_{gs} - V_t). \quad (5)$$

Employing Eq. (1) in conjunction with Eq. (5) yields

$$g_c = \mu_c W C_{ox} (V_{gs} - V_t) / L, \quad (6)$$

which rearranges into Eq. (4). (In evaluating μ_c here, typical values of V_{ds} employed were on the order of 0.05V so that Eq. (5) applies.) For the linear operating regime where μ_c is determined, it is assumed that the mobility remains constant with increasing gate voltage. This can be checked by determining g_c as a function of V_{gs} , and the slope of such a plot (presumably linear) yields μ_c . Upon denoting this slope as α , Eq. (4) can be written as

$$\mu_c = \alpha L / W C_{ox}. \quad (7)$$

A practical problem was encountered in attempting to determine conductance mobility. The source and drain regions on the custom transistors studied were not doped heavily enough during fabrication with the result that Schottky barriers were present at the source and drain contacts. Thus, instead of linear I_d vs V_{ds} characteristics for low values of V_{ds} , such characteristics were nonlinear due to the superimposed reverse characteristic of the Schottky diode. In order to obtain linear I_d vs V_{ds} curves for the purpose of accurately determining μ_c , it was necessary to subtract off this diode characteristic and the following approach was employed.

Consider an applied drain bias V_{ds} . A portion (V_s) of this voltage will be dropped across the Schottky diode and the remainder (V_{d1}) of this voltage will be dropped across the channel ($V_{d1} = V_{ds} - V_s$). If V_s were known then V_{d1} could be obtained. However, the diode characteristic is not known. Figure 47 illustrates a Schottky diode characteristic and two hypothetical I_d vs V_{ds} curves for two values of V_{gs} ($V_{gs1} > V_{gs2}$). For a given value of V_{gs} , such as V_{gs1} in the figure, the goal is to determine, for some fixed drain current such as I_{da} , the corresponding value of V_{ds} which would be observed in the absence of the Schottky diode. For this example, V_{ds1} is the desired quantity. The V_{gs2} characteristic of Figure 47 serves as a reference curve in the following analysis.

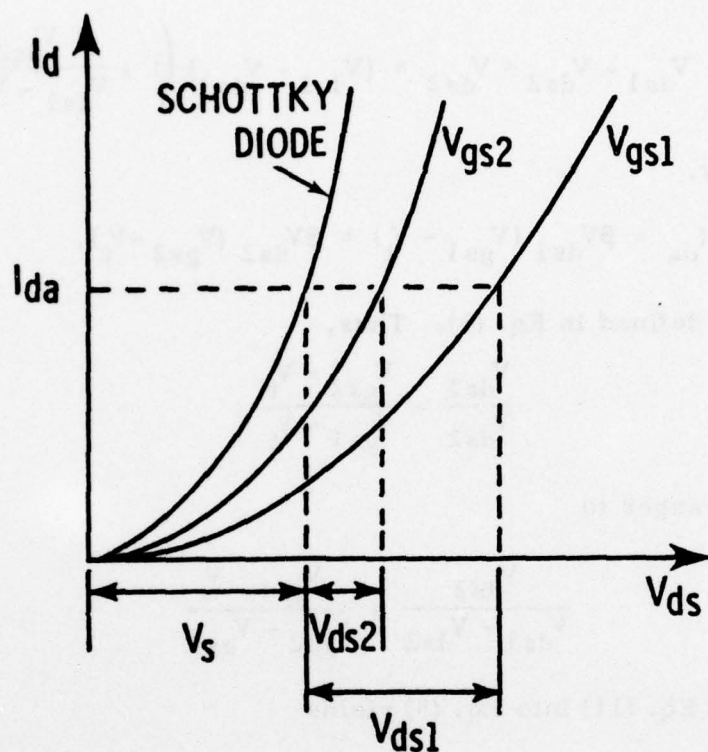


Figure 47. Illustration of a Schottky diode characteristic and two hypothetical I_d vs V_{ds} curves for two values of V_{gs} ($V_{gs1} > V_{gs2}$).

The quantity V_{ds1} can be written as

$$V_{ds1} = V_{ds1} - V_{ds2} + V_{ds2} = (V_{ds1} - V_{ds2}) \left(1 + \frac{V_{ds2}}{V_{ds1} - V_{ds2}} \right). \quad (8)$$

Additionally,

$$I_{da} = \beta V_{ds1} (V_{gs1} - V_t) = \beta V_{ds2} (V_{gs2} - V_t), \quad (9)$$

where β is defined in Eq. (5). Thus,

$$\frac{V_{ds1}}{V_{ds2}} = \frac{V_{gs2} - V_t}{V_{gs1} - V_t}, \quad (10)$$

which rearranges to

$$\frac{V_{ds2}}{V_{ds1} - V_{ds2}} = \frac{V_{gs1} - V_t}{V_{gs2} - V_{gs1}} \quad (11)$$

Substituting Eq. (11) into Eq. (8) yields

$$V_{ds1} = (V_{ds1} - V_{ds2}) \left(1 + \frac{V_{gs1} - V_t}{V_{gs2} - V_{gs1}} \right). \quad (12)$$

Equation (12) was used to obtain corrected values of V_{ds} for various values of I_d and a plot such as that illustrated in Figure 48 for a particular value of V_{gs} was obtained. (Data points are for illustration only.) This plot yields channel conductance for the chosen value of V_{gs} . Similar curves were obtained for other V_{gs} values, thus yielding a plot of g_c versus V_{gs} , as illustrated in Figure 49. As discussed above, such a plot yields conductance mobility and also reveals whether linearity is obeyed.

A frequently determined quantity for MOS transistors is field-effect mobility, μ_{fe} . This quantity is defined as

$$\mu_{fe} = \frac{d\sigma_{ds}}{dQ_s}, \quad (13)$$

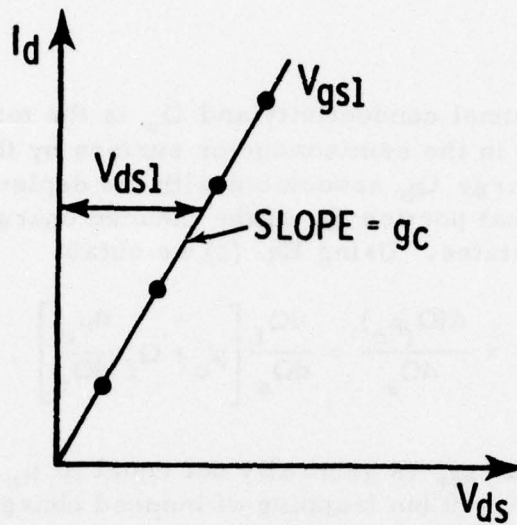


Figure 48. Illustration of an I_d versus V_{ds} curve after correcting the original characteristic (Figure 47) for the effects of the Schottky diode.

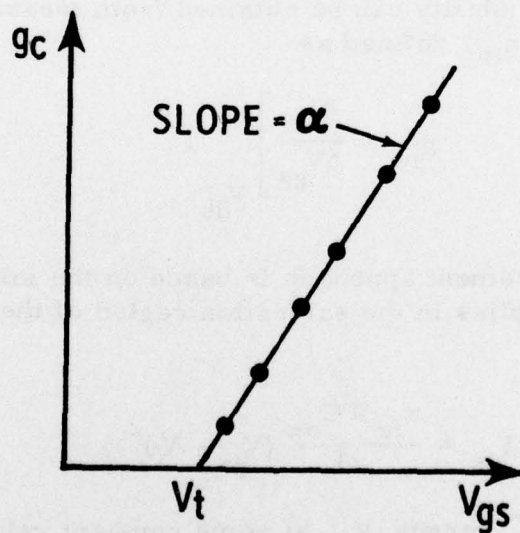


Figure 49. Illustration of a g_c versus V_{gs} curve obtained from a family of curves having the form of that shown in Figure 48.

where σ_{ds} is channel conductivity and Q_s is the total charge per unit area induced in the semiconductor surface by the applied field, including bulk charge Q_b associated with the depletion region, free charge Q_f , and that portion Q_t of the induced charge that is trapped at interface states. Using Eq. (2) we obtain

$$\mu_{fe} = \frac{d(Q_f \mu_c)}{dQ_s} = \frac{dQ_f}{dQ_s} \left[\mu_c + Q_f \frac{d\mu_c}{dQ_f} \right]. \quad (14)$$

It is thus seen that μ_{fe} is generally not equal to μ_c . For the special case of $Q_t = 0$ (no trapping of induced charge) and no incremental changes in Q_b , we obtain

$$\mu_{fe} = \mu_c + Q_f \frac{d\mu_c}{dQ_f}. \quad (15)$$

If channel mobility varies strongly with free charge density, then μ_{fe} will differ considerably from μ_c .

Field-effect mobility can be obtained from measurements of transconductance g_m , defined as

$$g_m = \left. \frac{\partial I_d}{\partial V_{gs}} \right|_{V_{ds}}. \quad (16)$$

A common measurement approach is based on the following expression which applies in the saturation region of the drain characteristics:⁴⁵

$$I_{ds} = \frac{\mu_{fe} W C_{ox}}{2L} (V_{gs} - V_t)^2. \quad (17)$$

By measuring $\sqrt{I_{ds}}$ versus V_{gs} at some constant value of V_{ds} in saturation, one obtains μ_{fe} directly from the slope of such a plot.

⁴⁵ C. T. Sah and H. C. Pao, IEEE Trans. Electron Devices 13, 393 (1966).

Sah and Pao⁴⁵ have discussed differences between μ_{fe} , which is measured in the saturation region, and μ_c , which is measured in the linear region. They presented data and analyses which show that μ_{fe} is reduced with respect to μ_c due to the effects of fixed charge in the semiconductor substrate on device characteristics. Additionally, channel mobility is a function of carrier density in the inversion layer^{46, 47} and, in general, mobility measured in the saturation region may be considerably smaller than mobility measured for very small V_{ds} . In summary, we expect μ_{fe} to be less than μ_c and this was found to be the case in the present experiments, the results of which are now described.

Table I shows measured values of conductance mobility for wet- and dry-oxide n-channel SOS transistors before and after Co^{60} -gamma irradiation. For dry devices, the change produced in μ_c by radiation was only very slight. (In two of the three cases presented, μ_c actually exhibited a small increase.) These results are consistent with the observation of negligible interface state effects in the threshold voltage studies presented above. That is, production of interface states during irradiation will increase scattering and thus reduce μ_c . For wet-oxide transistors, after 10^6 rads μ_c was reduced to 80% of its initial value for $V_{gs} = 0$. After 10^7 rads, μ_c was reduced to 38% and 47% of the initial values for $V_{gs} = 0$ and 5V, respectively. These reductions are qualitatively consistent with the interface state effects observed for wet-oxide devices in threshold voltage studies.

Figures 50 and 51 present field-effect mobility versus dose for applied values of V_{gs} during irradiation of 0 and 5V, respectively. For dry-oxide devices, only a very slight decrease in μ_{fe} is evident after 10^7 rads, which is consistent with both μ_c and V_t observations for these units. On the other hand, at that same dose μ_{fe} for wet transistors was reduced to 60% and 69% of the initial values for $V_{gs} = 0$ and 5V, respectively. These findings are, once again, in qualitative agreement with μ_c and V_t data for such devices.

⁴⁵ C. T. Sah and H. C. Pao, IEEE Trans. Electron Devices 13, 393 (1966).

⁴⁶ J. R. Brews, J. Appl. Phys. 46, 2193 (1975).

⁴⁷ J. R. Brews, J. Appl. Phys. 46, 2181 (1975).

Table I. Conductance mobility for wet- and dry-oxide n-channel
SOS transistors before and after gamma irradiation.
Bias voltages during irradiation are also shown.

	DOSE [rads(Si)]	μ_c (cm^2/Vs)	V_{ds} (V)	V_{gs} (V)
<u>WET OXIDE TRANSISTORS</u>				
HHTW2A	0	460	5	0
	10^6	370		
HNTW3A	0	380	5	0
	10^7	144		
HNTW3BD	0	316	5	5
	10^7	150		
<u>DRY OXIDE TRANSISTORS</u>				
HNTD6A	0	270	5	0
	10^6	310		
HNTD7A	0	304	5	0
	10^7	287		
HNTD7BD	0	238	5	5
	10^7	252		

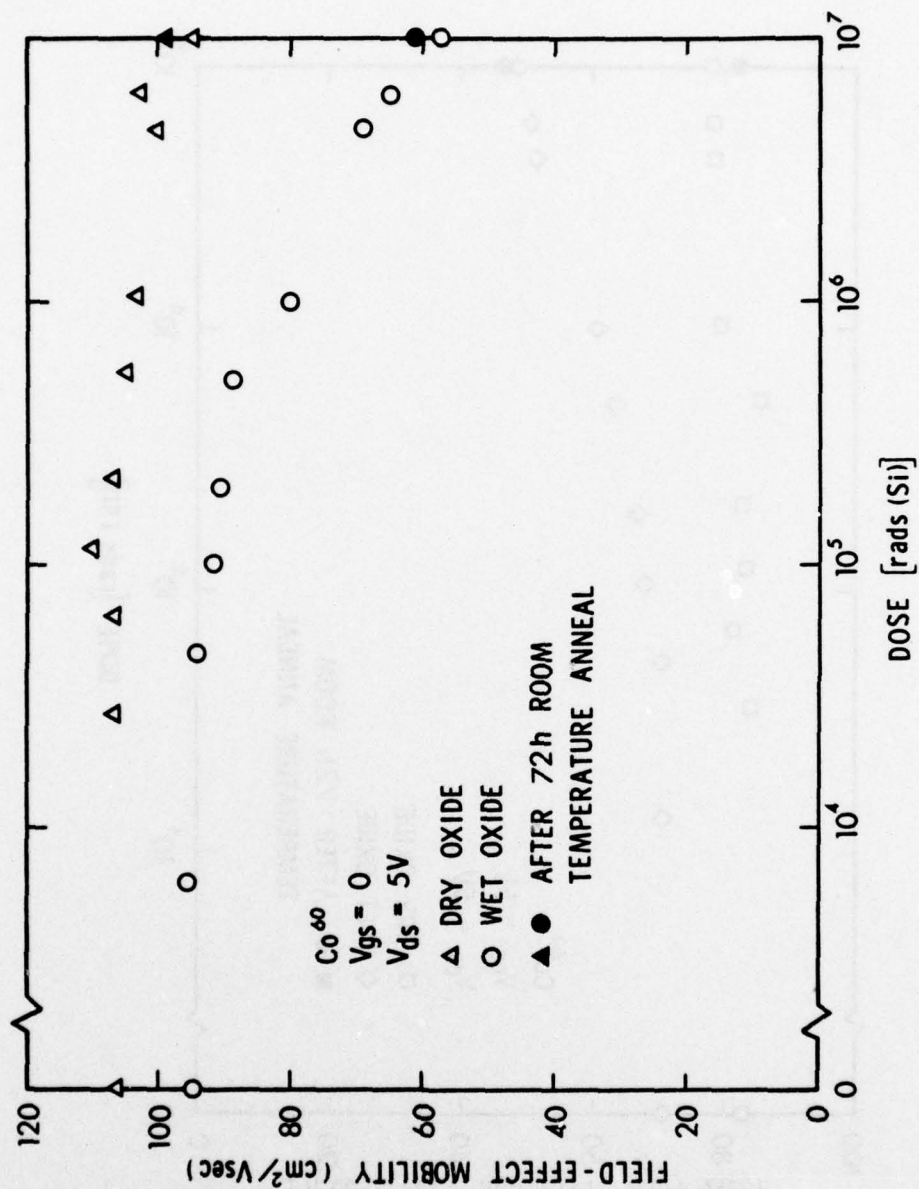


Figure 50. Field-effect mobility versus dose for wet- and dry-oxide n-channel SOS transistors irradiated with $V_{gs} = 0$.

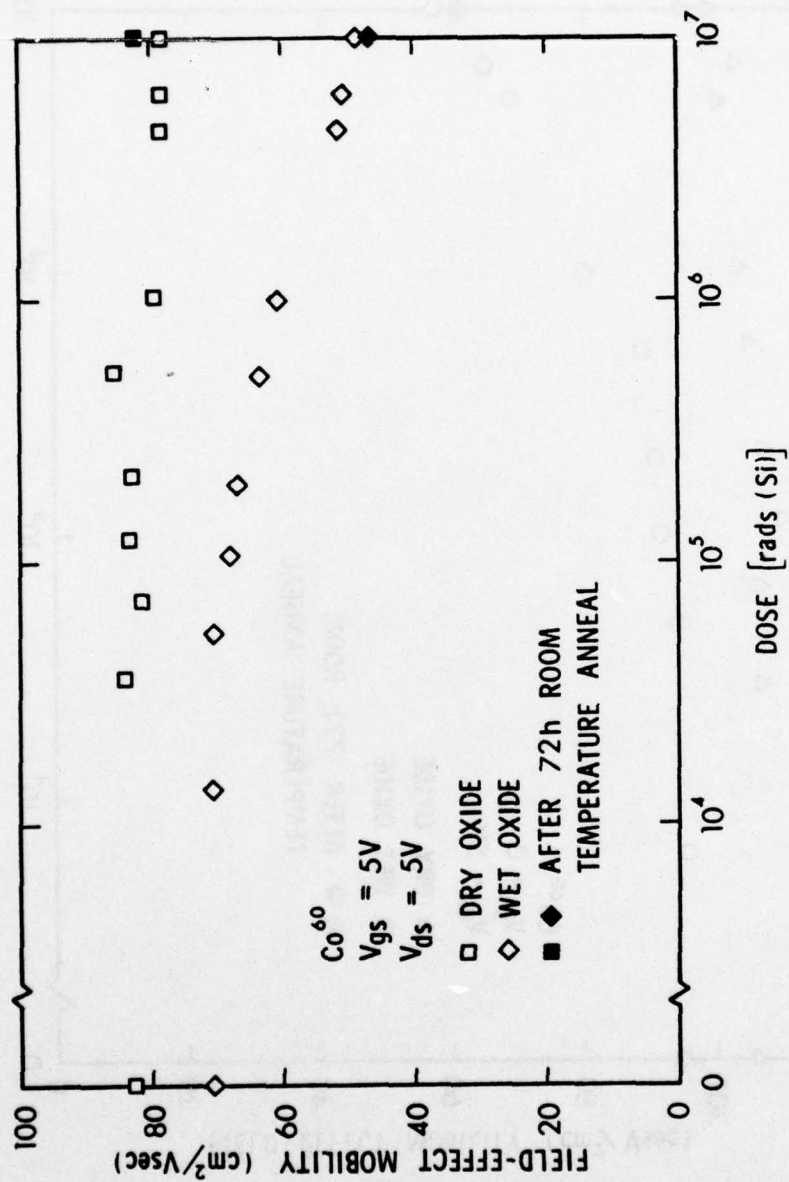


Figure 51. Field-effect mobility versus dose for wet- and dry-oxide n-channel SOS transistors irradiated with $V_{gs} = 5V$.

Two other observations should be made. First, room temperature anneals for 72h without bias resulted in nearly negligible changes in field-effect mobility as shown in Figures 50 and 51. Second, the ratio of μ_c to μ_{fe} for the data of Table I and Figures 50 and 51 is ~ 3 for dry devices and ~ 4.5 for wet units, with the ratio for both types of devices taken together being ~ 3.8 . Additional data would be required to determine whether the mobility-ratio difference between wet and dry devices is significant. We simply note here that μ_c is significantly larger than μ_{fe} , as expected.

5.5 BACK-CHANNEL LEAKAGE CURRENT STUDIES ON SOS TRANSISTORS

5.5.1 Introduction and Experimental Techniques

Studies of radiation-induced back-channel leakage current in custom n-channel SOS transistors are reported in this subsection. The two primary topics are: (1) comparison of data for wet- and dry-gate-oxide devices; (2) radiation-induced reduction of leakage current. Leakage current was obtained from measurements of drain current versus gate voltage for a constant value of V_{ds} , typically 5V. Such characteristics were recorded on an x-y plotter by applying a ramp voltage to the gate electrode and monitoring drain current by use of a current-to-voltage converter. This converter consisted of an operational amplifier (Burr Brown 3523) with a variable feedback resistor ($10^3 - 10^{11}$ ohms). In addition to obtaining I_d from $I_{ds} - I_{gs}$ characteristics, we frequently used a second method when it was necessary to minimize the time during which irradiation bias conditions were interrupted. This method involved use of a switching circuit to alter momentarily both V_{gs} and V_{ds} from fixed irradiation values to fixed measurement values. Use of this technique is discussed further below.

5.5.2 Experimental Results for Wet- and Dry-Oxide Devices

Figure 52 shows typical I_{ds} versus V_{gs} curves for a wet-oxide transistor before irradiation and after bombardment to several total doses. A plateau in I_{ds} is reached only if V_{gs} is several volts negative. The reason for this is that conduction along the front channel and at island edges must be turned off before back-channel leakage current alone is observed. One generally cannot expect to isolate I_d by measurements of drain current at $V_{gs} = 0$. In the pre-irradiation curve, as V_{gs} is increased negatively I_{ds} is observed to increase somewhat. The source of this

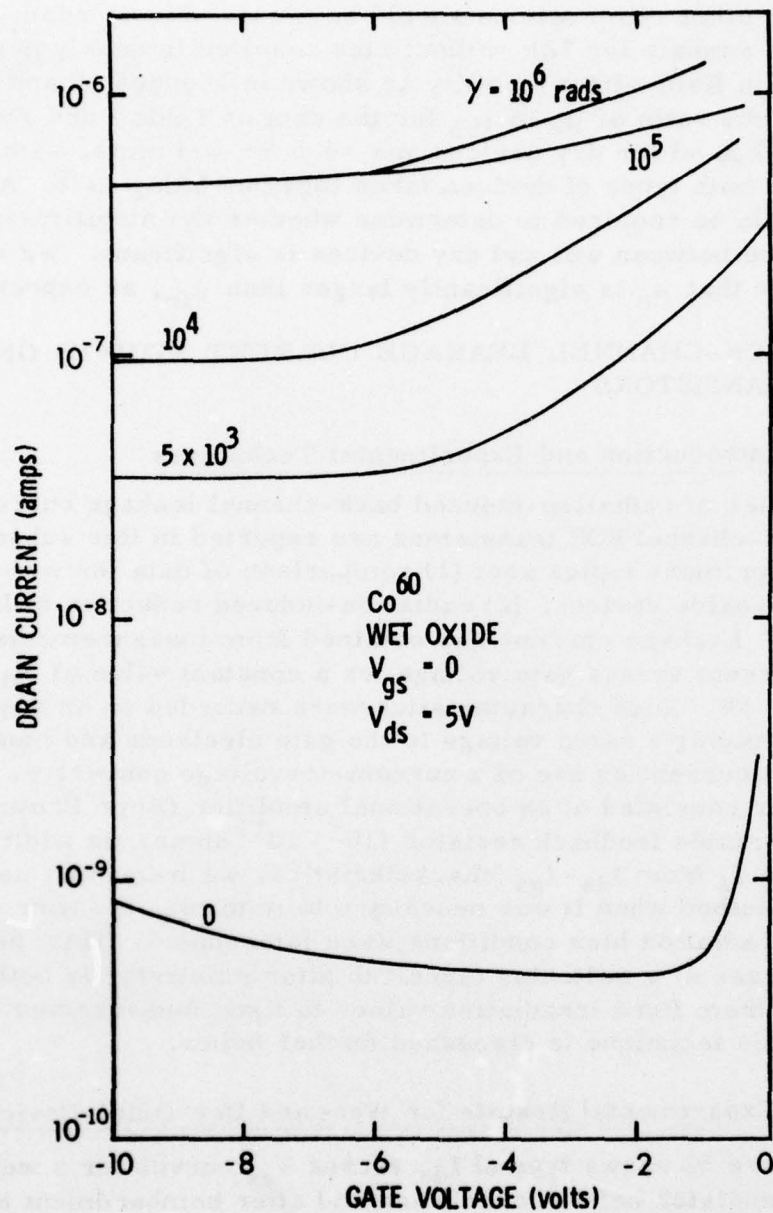


Figure 52. Typical drain current versus gate voltage characteristics with total ionizing dose as a parameter for n-channel wet-gate-oxide SOS transistors. (Irradiation conditions: $V_{gs} = 0$, $V_{ds} = 5V$.)

additional leakage component is unknown and was not observed post-radiation, as shown in Figure 52. We determined I_l from plateaus (broad minimum in the pre-irradiation case) in $I_{ds} - V_{gs}$ characteristics at negative gate bias. This plateau moves to more negative bias with increasing dose. Since the shift in threshold voltage for the front channel is nearly negligible up to 10^5 rads (Figure 45), movement of the plateau region is presumably due to a threshold shift at island edges.³⁷ That is, as the dose increases an increasingly more negative gate voltage is required to reduce island-edge leakage current to zero.

The situation for dry-oxide transistors is different from that for wet devices, as shown in Figure 53. The pre-irradiation leakage current is two orders of magnitude larger in the dry devices. Additionally, the phenomenon attributed to island edge effects in the wet case is not evident. This seems reasonable since the magnitude of the island-edge component is likely to be negligible on the current scale of Figure 53. That is, back-channel leakage current dominates. Movement of the "knee" toward positive gate bias with increasing dose can simply be attributed to intersection of I_l plateaus with different portions of the $I_{ds} - V_{gs}$ turn-on characteristic of the transistor. The envelope of the curves in Figure 53 should correspond to this characteristic.

Figure 54 shows representative I_l -versus-dose data obtained for wet and dry oxide transistors with $V_{gs} = 0$ and $V_{ds} = 5V$ during irradiation. Behavior is similar in both cases in that plateau regions are evident at low and high doses and a significant increase in I_l occurs at intermediate doses. Following irradiation to 10^6 rads, these devices were annealed under bias ($V_{gs} = 0$, $V_{ds} = 5$) at room temperature for 18h. Some recovery (i.e., reduction) in I_l was observed, as shown in the figure.

Certain relevant features of the NRTC Co⁶⁰ source need description before proceeding. A device to be irradiated is placed in the exposure room and the source is then raised up into the room. This takes approximately 5 minutes, during which time energy is being deposited in the test device at a dose rate which is time varying. The dose rate reaches a maximum when the source is completely raised ("source up") and the value of this maximum rate depends upon the location of the device with respect

³⁷ R. A. Kjar and J. Peel, IEEE Trans. Nucl. Sci. 21, 208 (1974).

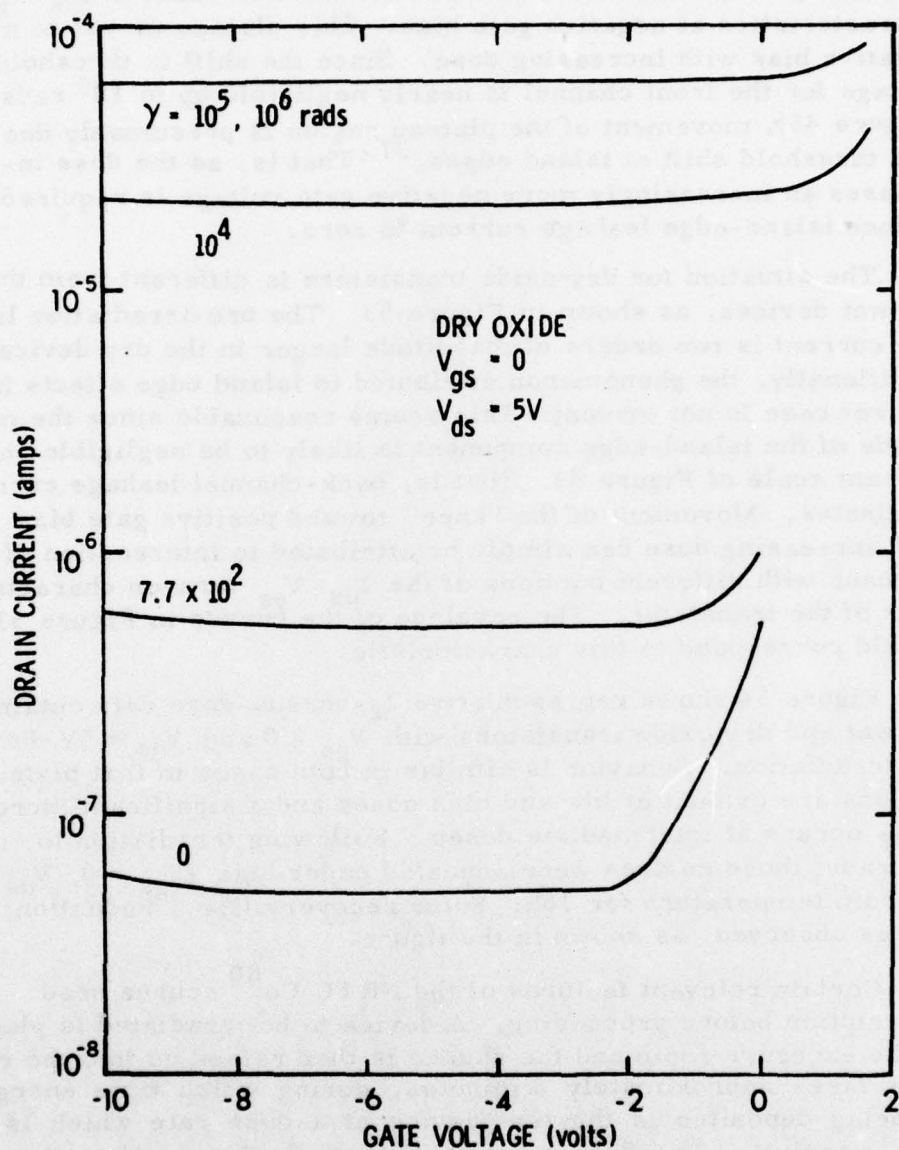


Figure 53. Typical drain current versus gate voltage characteristics with total ionizing dose as a parameter for n-channel dry-gate-oxide SOS transistors. (Irradiation conditions: $V_{gs} = 0$, $V_{ds} = 5V$.)

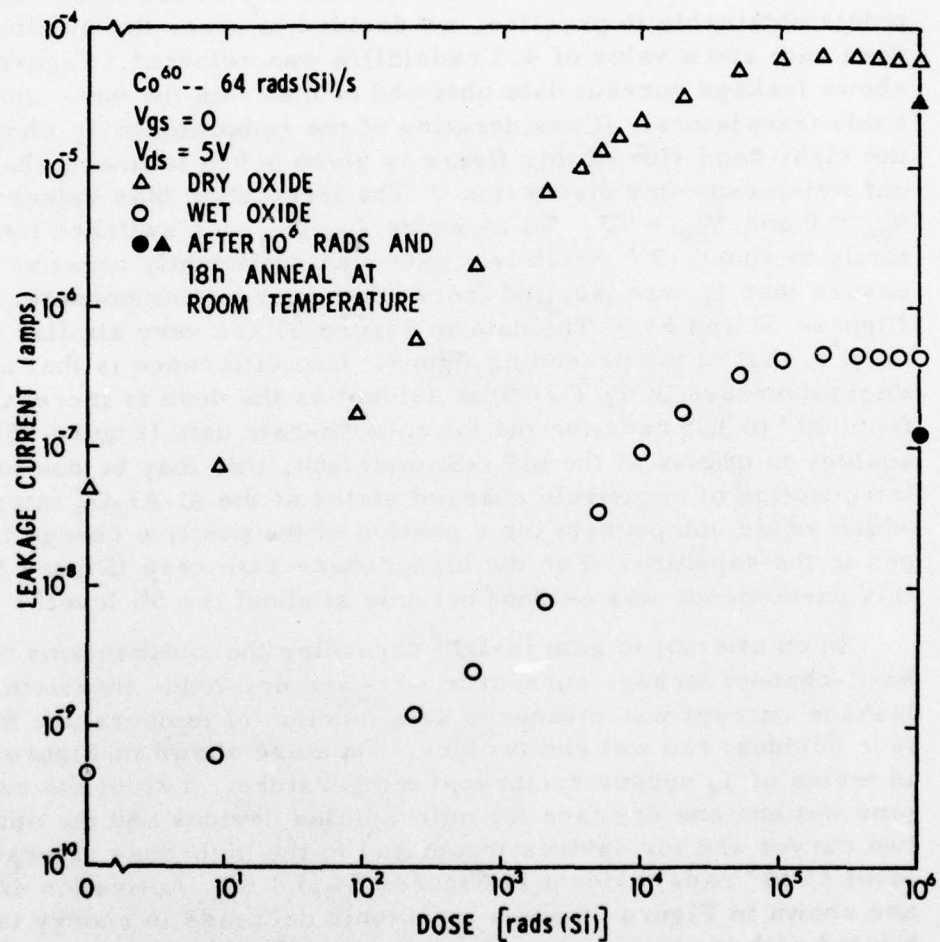


Figure 54. Back-channel leakage current versus dose for dry- and wet-oxide n-channel SOS transistors irradiated with $V_{gs} = 0$ and $V_{ds} = 5V$ at a dose rate of 64 rads(Si)/s.

to the source. Since it was desired to obtain I_L data at low total doses, detailed dosimetry was performed using CaF TLDs to characterize the source during the raising period. Upon doing so for the condition of a 64 rads(Si)/s maximum rate, data of the type shown in Figure 54 were obtained.

In order to obtain more accurate data (i.e., accurate in dose) at low doses and also to increase the number of low-dose data points obtainable in practice, we decided to lower the maximum dose rate and a value of 4.3 rads(Si)/s was selected. Figure 55 shows leakage current data obtained at that rate for wet- and dry-oxide transistors. (Consideration of the reduction in I_L shown in the right-hand side of this figure is given below following the present wet-versus-dry discussion.) The irradiation bias values were $V_{gs} = 0$ and $V_{ds} = 5V$. To measure I_L , V_{gs} was switched momentarily to about -7V which is a gate bias sufficiently negative to ensure that I_L was isolated from other current components. (See Figures 52 and 53.) The data in Figure 55 are very similar in form to that of the preceding figure. One difference is that a slight decrease in I_L (~20%) is evident as the dose is increased from 10^5 to 10^6 rads for the lower-dose-rate data (Figure 55). By analogy to effects at the SiO_2 -Si interface, this may be due to the introduction of negatively charged states at the Si- Al_2O_3 interface which would compensate for a portion of the positive charge trapped in the sapphire. For the higher-dose-rate case (Figure 54), this phenomenon was evident but only at about the 5% level.

In an attempt to gain insight regarding the mechanisms of back-channel leakage current in wet- and dry-oxide transistors, leakage current was measured as a function of temperature for four devices: two wet and two dry. Data are shown in Figure 56 in terms of I_L versus reciprocal temperature. Two of the curves (one wet and one dry) are for unirradiated devices and the other two curves are for devices irradiated to the high-dose saturation level ($>10^5$ rads) evident in Figures 54 and 55. Activation energies are shown in Figure 56 and a monotonic decrease in energy is exhibited with increasing leakage current. To examine this monotonic change further, data points at $1000/T = 3.3$ and also at temperature extremes for the four curves of Figure 56 are plotted in Figure 57 in terms of I_L versus $\Delta E/kT$. (Note that ΔE is a variable, as is temperature.) The information contained in this figure is described rather well by the empirical expression

$$I_L = 8.5 \times 10^{-3} \exp(-\Delta E/kT), \quad (18)$$

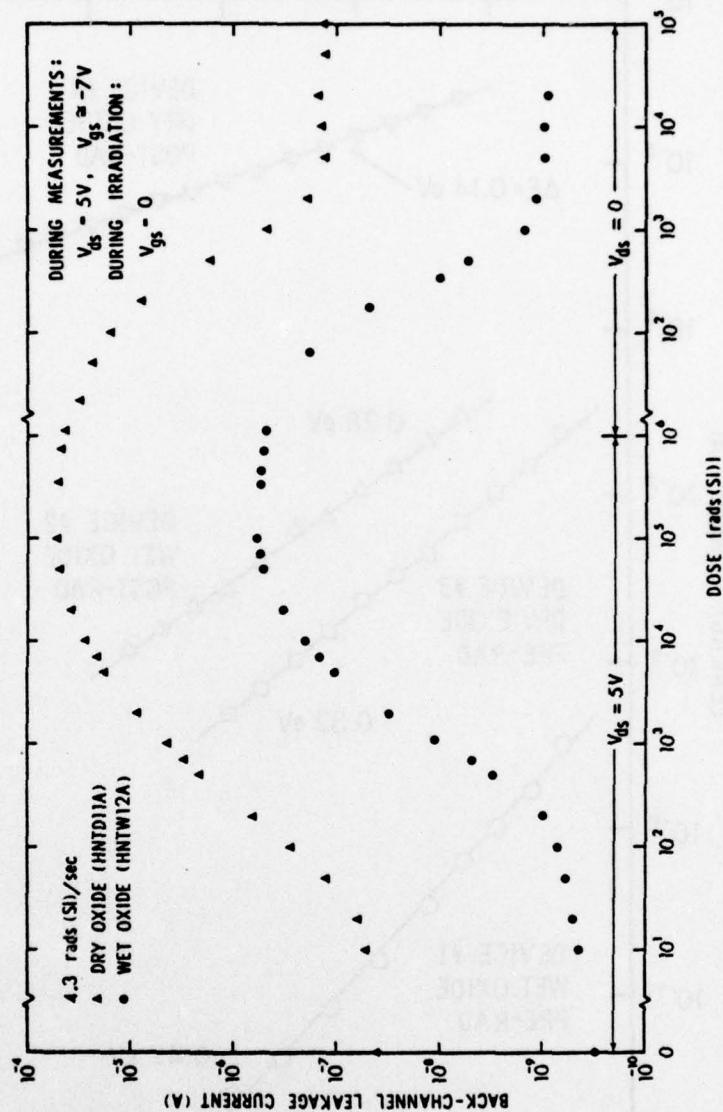


Figure 55. Back-channel leakage current versus dose for dry- and wet-oxide n-channel SOS transistors irradiated with $V_{gs} = 0$ and $V_{ds} = 5V$ at a dose rate of 4.3 rads-(Si)/s. The reduction in leakage current in the right-hand portion of this figure was accomplished by continuing to irradiate beyond 10^6 rads with $V_{ds} = V_{gs} = 0$. (Note the change in the dose scale.)

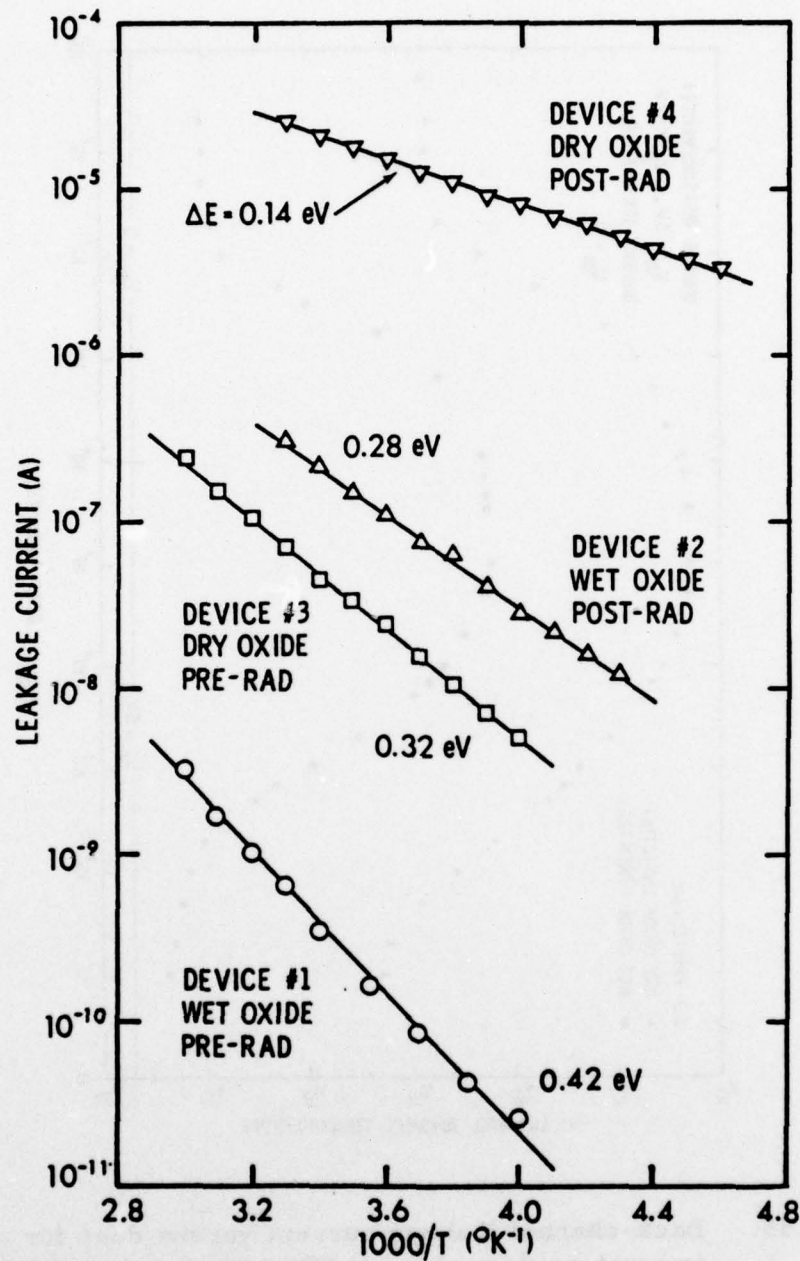


Figure 56. Leakage current versus reciprocal temperature for four n-channel SOS transistors, two with a wet oxide and two with dry. Two of the devices were not irradiated and the other two were irradiated to a level ($>10^5$ rads) sufficient to cause I_L to saturate.

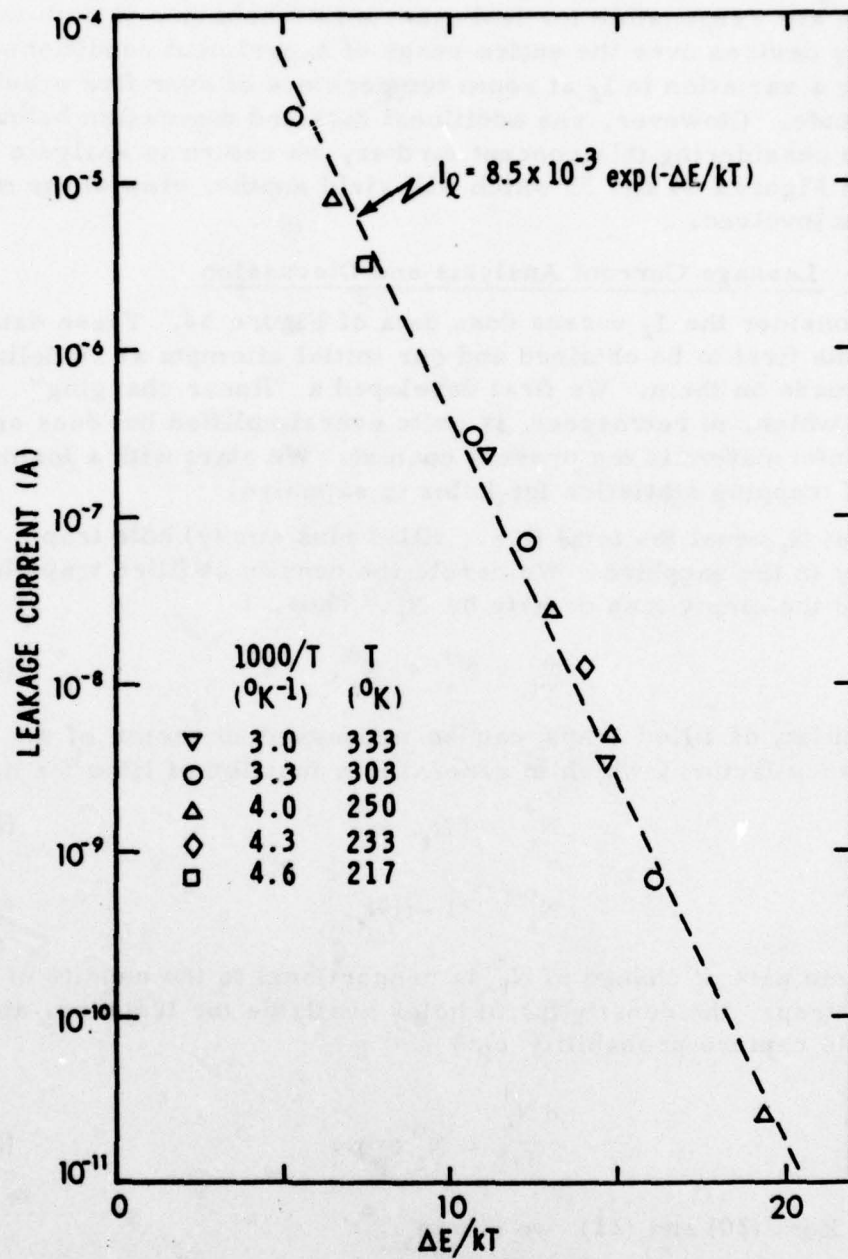


Figure 57. Leakage current versus $\Delta E/kT$. The information in this figure was derived from that in Figure 56. (Note that ΔE is a variable.)

where I_l is in amperes. Figure 57 suggests that the same mechanisms are responsible for leakage-current behavior in both wet and dry devices over the entire range of experiment conditions, including a variation in I_l at room temperature of over five orders of magnitude. (However, see additional data and discussion below.) Before considering this concept further, we return to analysis of data in Figures 54 and 55 which will yield another view of the mechanisms involved.

5.5.3 Leakage Current Analysis and Discussion

Consider the I_l versus dose data of Figure 54. These data were the first to be obtained and our initial attempts at modeling were made on them. We first developed a "linear charging" model which, in retrospect, is quite oversimplified but does serve to be informative in the present context. We start with a formulation of trapping statistics for holes in sapphire.

Let N_t equal the total (i.e., filled plus empty) hole trap density in the sapphire. We denote the density of filled traps by N_t^+ and the empty trap density by N_t^0 . Thus,

$$N_t = N_t^+ + N_t^0. \quad (19)$$

The density of filled traps can be expressed in terms of an occupancy factor f which in general is a function of time (or dose):

$$N_t^+ = f N_t, \quad (20)$$

$$N_t^0 = (1 - f) N_t. \quad (21)$$

The time rate of change of N_t^+ is proportional to the density of empty traps, the density (p) of holes available for trapping, and the hole capture probability c_p :

$$\frac{dN_t^+}{dt} = N_t^0 c_p p. \quad (22)$$

Using Eqs. (20) and (21), we obtain

$$\frac{d(fN_t)}{dt} = (1 - f) N_t c_p p, \quad (23)$$

or

$$\frac{df}{dt} = (1 - f) c_p p. \quad (24)$$

The solution to Eq. (24) is

$$f = 1 - \exp(-c_p p t). \quad (25)$$

For ^{60}Co gamma irradiation, we are concerned with total dose ϕ being delivered at a rate k_1 . At some time t , the dose is given by $k_1 t$. Thus, we can write Eq. (25) as

$$f = 1 - \exp(-c_p \phi/k_1) = 1 - \exp(-\phi/\phi_1), \quad (26)$$

where $\phi_1 = k_1/c_p$.

If we assume that a portion of the traps in the sapphire are filled prior to irradiation, giving rise to I_{l0} (the pre-irradiation back-channel leakage current), then for $\phi = 0$, $f = f_0$. Taking this assumption into account in Eq. (26) yields

$$f = f_0 + (1 - f_0) [1 - \exp(-\phi/\phi_1)]. \quad (27)$$

Upon denoting the density of filled traps for $\phi = 0$ as N_{to}^+ , we obtain (using Eq. (20))

$$N_t^+ = N_{to}^+ + (N_t - N_{to}^+) [1 - \exp(-\phi/\phi_1)]. \quad (28)$$

The basis of the linear charging model is to assume a linear relation between leakage current and the trapped charged densities of Eq. (28). That is, we assume the expression

$$I_l = I_{l0} + (I_{lm} - I_{l0}) [1 - \exp(-\phi/\phi_1)] \quad (29)$$

holds, where I_{l0} is pre-irradiation leakage current and I_{lm} is post-irradiation (saturation) leakage current. Thus, when all traps (N_t) are filled, the resulting leakage current is assumed to be I_{lm} . Equation (29) was fit to the data of Figure 54 and results are shown in Figure 58 along with values for ϕ_1 and $c_p p$, the model parameters. The fits to the data are good with the exception of the wet oxide results at low doses where some deviation is noted. The fact that model parameters for the dry device agree within a factor of two with those for the wet unit suggests that the hole trapping center responsible for charge buildup in the sapphire has the same properties (i.e., energy level position and capture probability) in both cases. Additionally, this result suggests that the reason for the difference in magnitudes

of I_L at a given dose in Figure 54 is simply the result of a considerably larger density of this same trap in dry-oxide devices than in wet transistors. However, these results must be considered tentative because of problems with the linear charging model and with the experimental data.

The main problem with the model is the assumption of a linear relation between trapped charge density and leakage current which was used to obtain Eq. (29) based on Eq. (28). In general, any unipolar current I is given by

$$I = eFAn\mu, \quad (30)$$

where e is electronic charge, F is applied field, A is cross-sectional area, n is equilibrium free-carrier density, and μ is carrier mobility. Thus, we expect I_L to be proportional to the back-channel inversion-layer carrier density n_{inv} and to the carrier mobility μ_{bc} in that channel. As N_t^+ increases, n_{inv} will increase but there will not necessarily be a linear relationship between these quantities. For example, charging of a spatial distribution of traps in the sapphire could result in N_t^+ and n_{inv} being related nonlinearly. Additionally, μ_{bc} is, in general, not a constant but varies with n_{inv} . Work of Brews,⁴⁶ Chen and Muller,⁴³ and Guzev et al.⁴⁸ has revealed that front-channel mobility in an MOS transistor increases with n_{inv} in the weak inversion regime, and their work is discussed below.

The problem with the experimental data in Figures 54 and 55 is that a small photocurrent I_{pc} of unknown origin influenced wet-oxide data at low doses, and this was not recognized initially. (See additional discussion below.) This photocurrent scaled with Co^{60} dose rate and thus had the largest effect on 64 rads/s data. Figure 58 illustrates the maximum magnitude of I_{pc} at 2000 rads which is the dose received by a device during the 5 min required to raise the source. The solid triangle is I_{pc} and the solid circle represents $I_L - I_{pc}$, which is the current that would have been measured in the absence of a photocurrent. Also shown (solid square) is the quantity $I_L - (I_{L0} + I_{pc})$,

⁴³J. T. C. Chen and R. S. Muller, J. Appl. Phys. 45, 828 (1974).

⁴⁶J. R. Brews, J. Appl. Phys. 46, 2193 (1975).

⁴⁸A. A. Guzev, G. L. Kurishev, and S. P. Sinitisa, Phys. Status Solidi A14, 41 (1972).

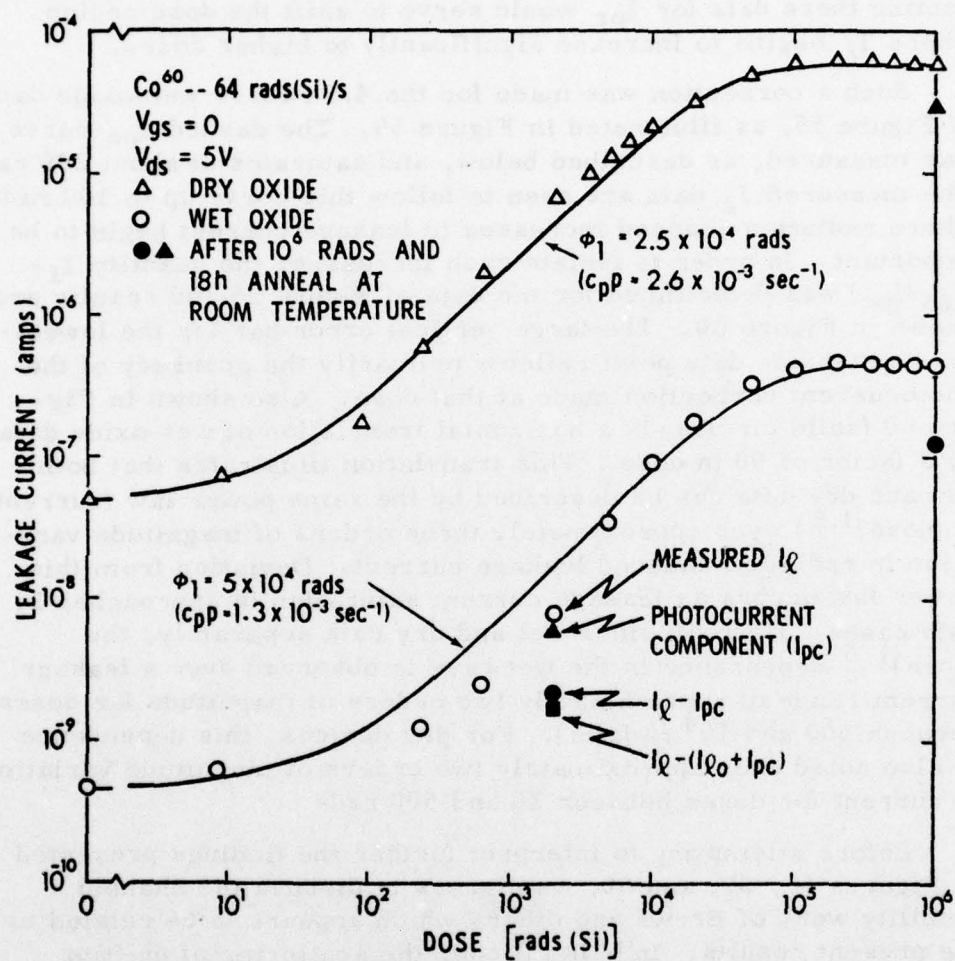


Figure 58. Results of fitting a linear charging model to the leakage current versus dose data of Figure 54.

which is the radiation-induced current component. It is clear that up to 2000 rads I_L for the wet-oxide device was dominated by I_{pc} and thus the fit to such data in Figure 58 is not meaningful. Correcting these data for I_{pc} would serve to shift the dose region where I_L begins to increase significantly to higher doses.

Such a correction was made for the 4.3 rads/s wet-oxide data of Figure 55, as illustrated in Figure 59. The dashed I_{pc} curve was measured, as described below, and saturates at about 200 rads. The measured I_L data are seen to follow this curve up to 100 rads where radiation-induced increases in leakage current begin to be important. In order to isolate such increases, the quantity $I_L - (I_{L0} + I_{pc})$ was determined for the data of Figure 55 and results are shown in Figure 60. The large vertical error bar for the lowest-dose wet-oxide data point reflects primarily the accuracy of the photocurrent correction made at that dose. Also shown in Figure 60 (solid circles) is a horizontal translation of wet-oxide data by a factor of 90 in dose. This translation illustrates that both wet and dry data can be described by the same power law (current $\propto (\text{dose})^{1.5}$) over approximately three orders of magnitude variation in radiation-induced leakage current. Deviation from this power law occurs as leakage current saturation is approached in both cases. If we consider wet and dry data separately, the $(\text{dose})^{1.5}$ dependence in the wet case is observed over a leakage current range of approximately two orders of magnitude for doses between 500 and 10^4 rads(Si). For dry devices, this dependence is also noted over approximately two orders of magnitude variation in current for doses between 20 and 500 rads.

Before attempting to interpret further the findings presented in Figures 56, 57, and 60, we digress to discuss the channel mobility work of Brews and others which appears to be related to the present results. In bulk silicon, the scattering of drifting carriers is primarily due to phonons (lattice scattering) and ionized impurities (impurity scattering), with lattice scattering dominating at 300°K. We can express the bulk drift mobility in terms of these two components as

$$\mu_{\text{bulk}}^{-1} = \mu_{\text{lattice}}^{-1} + \mu_{\text{impurity}}^{-1} \quad (31)$$

Mobile carriers in the inversion layer of an MOS transistor experience additional scattering at the oxide-semiconductor interface

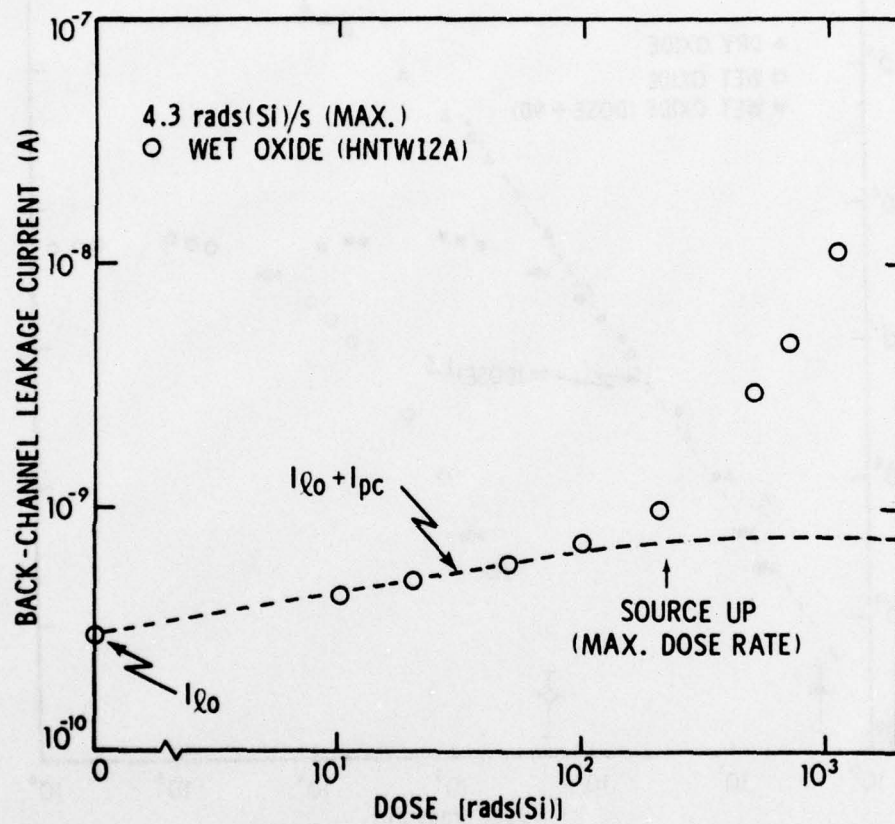


Figure 59. Illustration of a photocurrent (I_{pc}) that dominated measured leakage current at low doses for the wet-oxide data of Figure 55.

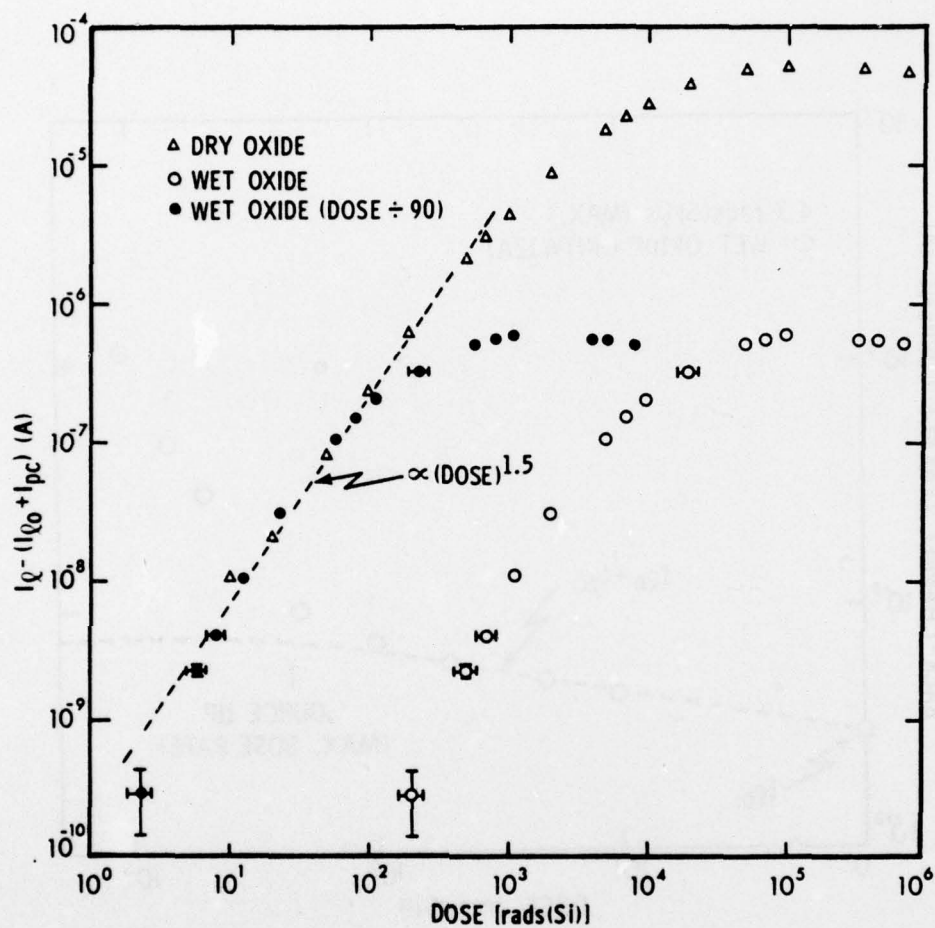


Figure 60. Radiation-induced leakage current versus dose for wet- and dry-oxide SOS transistors irradiated to a rate of 4.3 rads(Si)/s. These data were obtained by correcting the data of Figure 55 for pre-irradiation current and, in the wet-oxide case, for the photocurrent component shown in Figure 59.

while moving along the channel between source and drain. The mobility of carriers in the channel is thus described by

$$\mu_{\text{channel}}^{-1} = \mu_{\text{lattice}}^{-1} + \mu_{\text{impurity}}^{-1} + \mu_{\text{interface}}^{-1}, \quad (32)$$

with interface (or surface) scattering being the dominant term in a typical situation. (This concept and related mechanisms described below should apply for both the front channel (SiO_2 -Si interface) and the back channel (Si-sapphire interface) in an SOS transistor.)

As pointed out by Brews^{46, 47}, the above description of carrier mobility for MOS transistors is oversimplified. Eq. (32) actually applies for the microscopic channel mobility, which is determined solely by scattering processes. The measured channel mobility for a transistor can differ from the microscopic value due to the effects of channel and interface inhomogeneities. These inhomogeneities will affect the microscopic mobility through scattering but can additionally affect the measured mobility through Maxwell's equations. That is, nonuniformities can introduce modified boundary conditions and additional charge-density terms into Maxwell's equations, and thus have an effect on device current flow in addition to the microscopic scattering contribution. Either of the above-described effects of inhomogeneities will dominate depending on various conditions, as discussed by Brews, with minority-carrier density in the channel perhaps being the most important variable. Brews' analysis provides a physical framework for describing a variety of experimental MOS observations made by other workers.

Figure 61 shows the variation of channel mobility with carrier density in the inversion layer of an MOS device. This figure is based on several of the theoretical and experimental curves considered by Brews, and is employed here to describe qualitatively several important properties of conduction in inversion layers. Two example cases are shown, corresponding to low and high interface charge densities. The interface charge density includes both fixed oxide charge and interface-state charge. These inhomogeneously distributed interface charges will give rise to carrier-density

⁴⁶ J. R. Brews, J. Appl. Phys. 46, 2193 (1975).
⁴⁷ J. R. Brews, J. Appl. Phys. 46, 2181 (1975).

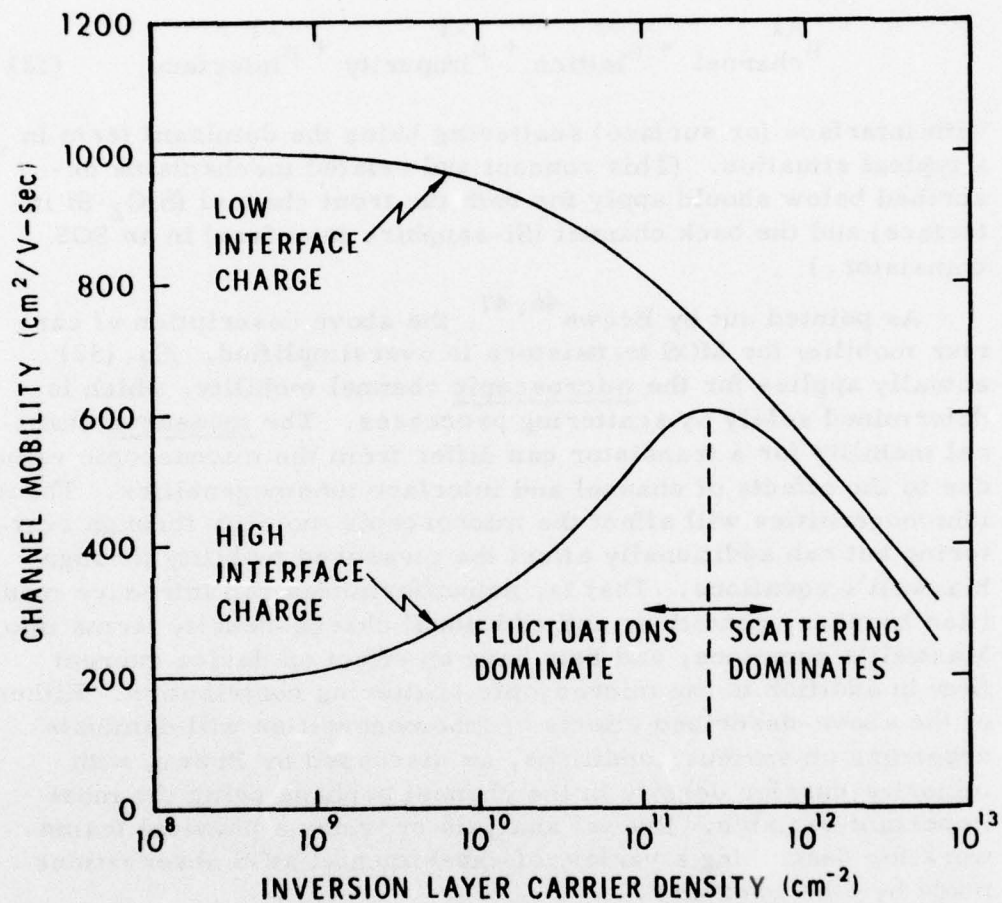


Figure 61. Channel mobility versus inversion-layer carrier density for the cases of low and high interface charge. The curves shown provide a qualitative description of several features of conduction in inversion layers. (See text for discussion.)

fluctuations in the inversion region. For the bottom curve in Figure 61, at low carrier densities these inhomogeneities dominate the channel mobility. As the gate voltage is increased, thereby increasing the inversion layer carrier density in the front channel, screening will increase with a resultant reduction in carrier-density nonuniformities. (This same statement can be made for the back channel, but in this case n_{inv} is increased by increasing the total ionizing dose deposited in an SOS device.) Hence, mobility increases. At high applied fields, channel mobility will decrease with increasing carrier density. In this regime, measured mobility will equal the microscopic mobility (i.e., scattering dominates over inhomogeneity effects). The decrease in mobility in this regime has been considered by various workers, and Cheng and Sullivan⁴⁹ point out that one must consider Coulomb scattering and surface-roughness scattering in addition to phonon scattering to account for experimental findings. For the case of low interface charge (upper curve in Figure 61), it is seen that carrier-density fluctuations do not affect channel mobility. The measured mobility will equal the microscopic, scattering-dominated mobility for this case over the entire carrier-density range.

The above qualitative discussion was based largely on the analytical work of Brews. Although further experimental work will be required to verify the predictions of his model, as mentioned above this work appears to provide a reasonable explanation for experimental observations obtained by several other researchers. In particular, Guzev et al.⁴⁸ and Chen and Muller⁴³ have obtained channel-mobility data which are well accounted for by Brews' analysis.

We now consider results in Figure 56 in light of the above discussion. Chen and Muller⁴³ observed that front-channel mobility in MOS transistors decreased with decreasing temperature and plots of such data yielded an activation energy of ~ 0.1 eV. Their findings suggest that the temperature dependence of leakage current for any one of the four cases shown in Figure 56 may be attributed to the temperature dependence of back-channel mobility.

⁴³ J. T. C. Chen and R. S. Muller, J. Appl. Phys. 45, 828 (1974).

⁴⁸ A. A. Guzev, G. L. Kurishev, and S. P. Sinitza, Phys. Status Solidi A14, 41 (1972).

⁴⁹ Y. C. Cheng and E. A. Sullivan, J. Appl. Phys. 44, 3619 (1973).

This is reasonable since leakage current is proportional to n_{inv} and μ_{bc} and, for a constant trapped hole density in the sapphire, n_{inv} should be temperature invariant. As n_{inv} increases with increasing ionizing dose, μ_{bc} will increase, according to Brews' description, and this effect is at least partially attributable to a reduction in carrier-density fluctuations due to screening. Data of Chen and Muller⁴³ and also calculations of Brews⁴⁶ reveal that in the weak inversion regime as n_{inv} increases, the spread with temperature in μ_{bc} values decreases. That is, one can expect to find an activation energy that decreases with increasing inversion-layer carrier density. The data shown in Figure 56 are consistent with this concept.

The application of the above physical concepts to the case of irradiated SOS devices is as follows. Inhomogeneities exist at the Si-Al₂O₃ interface which give rise to fluctuations in potential along the back channel, which in turn impede carrier motion. The range of radiation-induced leakage currents in the present experiments is such that the back channel was always in weak inversion. In this regime, increases in back-channel mobility occur by three mechanisms: (1) as charge builds up in the sapphire, the inversion-layer carrier density increases which reduces the effectiveness of potential fluctuations due to screening; (2) built-up charge in the sapphire also serves to "smooth out" these fluctuations, thereby causing μ_{bc} to increase; (3) increasing the temperature increases the thermal energy of carriers and thereby reduces the effectiveness of potential fluctuations. Thus, increases in leakage current can be attributed to mobility increases by the above mechanisms and to increases in inversion-layer carrier density as trapped holes build up in the sapphire. The experimental results in Figure 56 can be accounted for on the basis of both the effects of ionizing radiation on n_{inv} and μ_{bc} and the temperature dependence of μ_{bc} .

Our motivation for obtaining the temperature dependence data of Figure 56 was to gain insight regarding leakage current mechanisms before and after irradiation. In particular, we sought to evaluate the relative contribution, if any, of thermally generated carriers in the drain depletion region to observed leakage current. Appropriate expressions for the parameters of interest are presented first.

⁴³ J. T. C. Chen and R. S. Muller, J. Appl. Phys. 45, 828 (1974).

⁴⁶ J. R. Brews, J. Appl. Phys. 46, 2193 (1975).

Generation current I_g is proportional to carrier generation rate G , and for a reverse-biased pn junction⁵⁰

$$G = \frac{c_p c_n N_g n_i^2}{c_n n_1 + c_p p_1}. \quad (33)$$

This equation assumes carrier generation through a single level, and n_1 is the electron concentration that would exist if the Fermi level were located at that generation level. (A similar definition holds for p_1 .) The quantities c_p and c_n are hole and electron capture probabilities, respectively, N_g is the concentration of generation centers, and n_i is the intrinsic carrier concentration, given by

$$n_i = \sqrt{N_c N_v} \exp(-E_g / 2kT). \quad (34)$$

(The quantities N_c and N_v are effective densities of states and are each proportional to $T^{3/2}$.) In a depletion region, carrier generation occurs at a rate inversely proportional to the generation lifetime τ_g . Upon defining G in Eq. (33) as $n_i / 2\tau_g$, we find that τ_g is given by

$$\tau_g = \frac{c_p p_1 + c_n n_1}{2c_p c_n N_g n_i}. \quad (35)$$

It is frequently assumed for simplicity that the generation level is at midgap and that $c_n = c_p (= c)$. Upon making these assumptions, Eq. (33) reduces to

$$G = \frac{c N_g n_i}{2} \quad (36)$$

and Eq. (35) becomes

$$\tau_g = \frac{1}{c N_g}. \quad (37)$$

⁵⁰ J. L. Moll, Physics of Semiconductors (McGraw-Hill, New York, 1964), p. 118; A. S. Grove, Physics and Technology of Semiconductor Devices (Wiley, New York, 1967), p. 174.

The temperature dependence of I_g is then governed by those of c and n_i under the above assumptions. Over the temperature range of interest, we can closely approximate the density-of-states temperature variation in Eq. (34) as $\exp(-0.045 \text{ eV/kT})$. Thus, since E_g is 1.11 eV at room temperature, n_i is proportional to $\exp(-0.60 \text{ eV/kT})$. Caution should be exercised when attempting to attribute the temperature dependence of measured current to thermal generation by simply comparing the experimental activation energy with that for n_i . Even in the simplified expression for generation rate (Eq. (36)) a capture probability term appears which is, in general, temperature dependent. For recombination centers, it is not unusual to find capture-probability temperature dependences as strong as $\exp(\pm 0.1 \text{ eV/kT})$. Additionally, although it is a good approximation that the dominant generation level is at mid-gap, it is not generally true that c_p and c_n will be equal in magnitude and in temperature dependence. In the absence of such detailed information, it is difficult to conclude definitely on the basis of temperature dependence data that a measured current is due solely to thermal generation in a depletion region.

The data in Figure 56 for an unirradiated wet-oxide transistor yield an activation energy of 0.42 eV. On the basis of this relatively strong temperature dependence, one might be tempted to conclude that pre-irradiation I_g is dominated by thermal generation for this case. However, the above discussion should make one hesitate before doing so. In addition, one must consider all of the data in Figure 56. It is accepted that post-irradiation behavior is due to formation of a back channel by built-up positive charge in the sapphire. However, the activation energy of 0.28 eV for this case (Device #2 in Figure 56) is still relatively large. In addition, the information presented in Figure 57 suggests that the same mechanism is important in determining leakage current behavior for all conditions examined, including wet and dry oxides, irradiated and unirradiated devices, and behavior as a function of temperature. As discussed above, this mechanism is postulated here to be the dependence of n_{inv} and μ_{bc} on ionizing dose and the temperature dependence of μ_{bc} . If thermal generation was the only contributor to pre-irradiation I_g for wet-oxide devices, while the above mechanism determined behavior for all other conditions in Figure 56 (including dry oxide data), then one would not expect the continuous behavior exhibited in Figure 57. That is, the mechanisms determining ΔE in the thermal generation case are very

much different from the mechanisms determining ΔE in the second situation, so that fitting of all data by a single, relatively simple expression as in Figure 57 would be an unlikely occurrence.

One problem with the above interpretation is that it appears to be in conflict with findings of Harari and McGreivy.⁵¹ They performed extensive experiments on irradiated and unirradiated n-channel SOS transistors and obtained convincing evidence that pre-irradiation leakage current in wet oxide devices very similar to those studied here is attributable to thermal generation. To reconcile their viewpoint with ours is likely to require more data and analyses. For the present, we postulate the following reconciliation. The thermal generation process is rather strongly temperature activated, as discussed above. The leakage current mechanism described in the present work also appears to have a strong temperature dependence. It is conceivable that the temperature dependences for these two processes are comparable and that both are effective here in determining pre-irradiation behavior for wet-oxide devices. A second possibility is that this behavior is dominated by the mobility mechanism at room temperature but at a somewhat elevated temperature the thermal generation mechanism would become important. Alternatively, if the room-temperature I_L was somewhat lower than that observed here (accomplished perhaps by processing changes), then thermal generation would dominate. To investigate the above possibilities, additional studies over a wider temperature range than that in Figure 56 are needed.

During the final stages of preparing this report, we performed one such experiment and results and a preliminary interpretation are given here. Measurement of pre-irradiation leakage current in a wet-oxide transistor was made over the range 204 - 435°K and data are shown in Figure 61a. These data reveal that the temperature range for the corresponding data in Figure 56 (250 - 333°K) was indeed too narrow since two regimes are clearly evident in Figure 61a. At high temperatures, an activation energy of 0.57 eV is apparent which is suggestive of a thermal generation mechanism. At low temperatures, a considerably shallower slope is evident, corresponding to $\Delta E \approx 0.28$ eV. Over the $1000/T$ range from 3.0 to 4.0°K⁻¹, it is clear that one could extract an intermediate

⁵¹ E. Harari and D. J. McGreivy, to be published in IEEE Trans. Electron Devices.

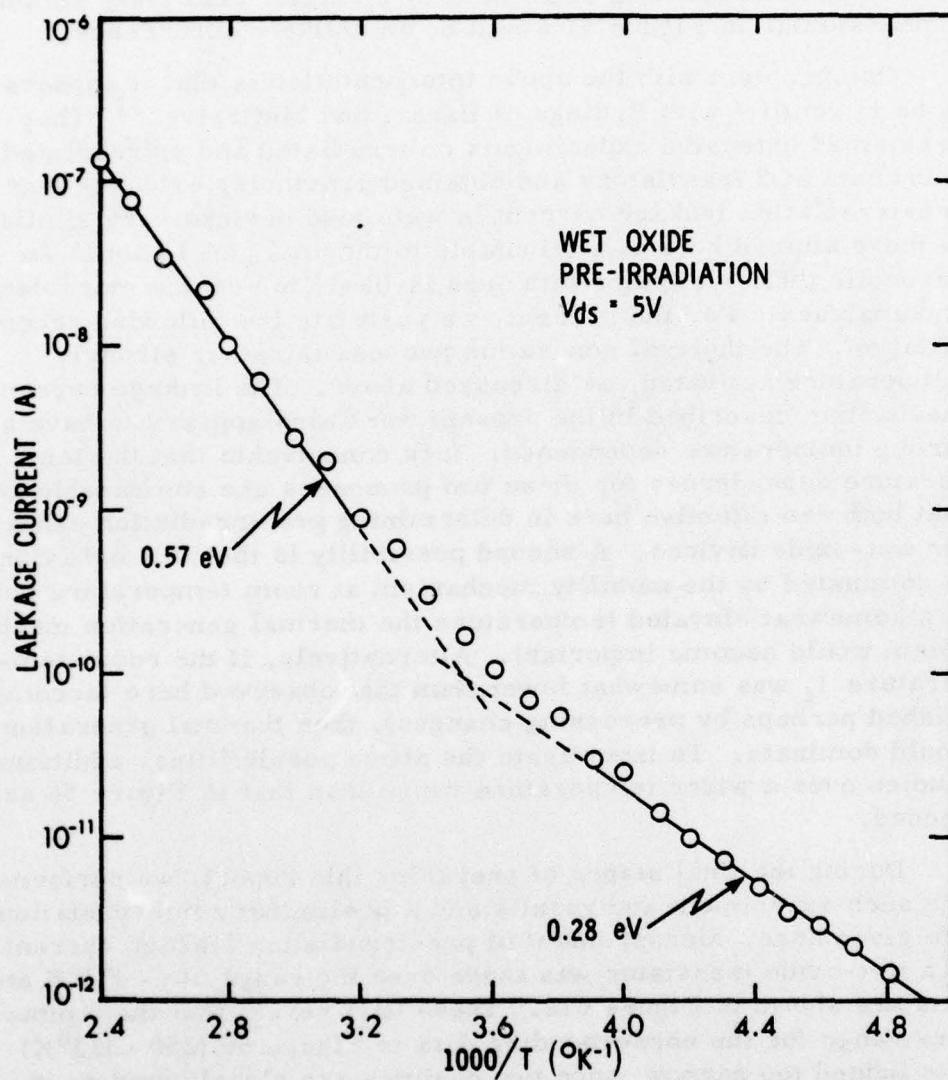


Figure 61a. Leakage current versus reciprocal temperature for an unirradiated wet-oxide n-channel SOS transistor.

value of ΔE from limited data. The transition from the 0.57 eV regime to the 0.28 eV regime occurs over this range, giving rise to data which are influenced by two mechanisms at and near room temperature. We attribute low-temperature behavior to the mobility mechanism discussed above and at high temperatures thermal generation presumably dominates.

It was suggested above that to reconcile data of Harari and McGreivy⁵¹ with the present findings, one could postulate the importance of both thermal generation and the mobility mechanism for unirradiated wet-oxide transistors. Figure 61a indicates that this is the case at room temperature. However, these recent data also force us to reconsider our interpretation of Figures 56 and 57. It seems clear that as one irradiates a wet-oxide device, and thereby increases I_L , a point will quickly be reached where thermal generation is no longer important at room temperature. However, it is not presently clear how the activation energy for the mobility mechanism will vary with dose. Measurements of I_L versus temperature with dose as a parameter are planned which should clarify this situation.*

Interpretation of the room-temperature data of Figure 60 is now given. The same functional dependence of radiation-induced leakage current on ionizing dose is exhibited for wet- and dry-oxide devices, which suggests that the same physical processes are occurring in both cases. Information presented in Figure 57 also indicates that this is the case (but this may be fortuitous, as discussed above). One needs then to account for the factor-of-ninety displacement in dose exhibited in Figure 60. At some constant value of radiation-induced leakage current in the non-saturation regime we can state, based on Eq. (30), that the product of mobility and carrier density in the back channel for the dry-oxide case must be equal to that for wet oxide. (In this discussion, we are considering the open symbols in Figure 60.) Such a comparison can be made for leakage currents ranging from $\sim 10^{-8}$ to $\sim 3 \times 10^{-7}$ A and for doses ranging from ~ 10 to ~ 200 rads

* For more recent data, see paper by the present authors which will appear in the Dec. 1977 issue of the IEEE Transactions on Nuclear Science.

⁵¹ E. Harari and D. J. McGreivy, to be published in IEEE Trans. Electron Devices.

for dry oxide and from $\sim 10^3$ to $\sim 2 \times 10^4$ rads for wet oxide. Based on the interpretation of data in Figures 56 and 57, a mobility mechanism is assumed to be important, and thus we are assuming that as n_{inv} increases, μ_{bc} will also increase. Since the rate at which the mobility-carrier density product increases with dose is the same for wet and dry devices, one is tempted to conclude that at a given value of leakage current mobilities are equal and carrier densities are equal for the two transistor types. The displacement in dose exhibited in Figure 60 would then be attributed to a larger density of traps in dry-oxide devices than in their wet-oxide counterparts. The fact that leakage-current saturation occurs at approximately the same dose also suggests that the same trap is responsible for observed behavior in both cases. Acceptance of a significantly larger trap density in dry-oxide devices then suggests that in the wet case only a very small fraction of the holes generated in the Al_2O_3 per unit dose are trapped there, and the rest recombine.

An alternative to the above explanation is that identical traps and trap densities exist in the sapphire for wet and dry devices. At a given value of leakage current, it would then be required that μ_{bc} (dry) be greater than μ_{bc} (wet) and that n_{inv} (dry) be less than n_{inv} (wet), or vice-versa. Otherwise, one would be unable to account for the enormous (~ 3 orders of magnitude) difference in dry and wet leakage currents at a fixed dose in the non-saturation regime, assuming that the trapped charge density is the same in both cases. For equal trapped charge densities, it seems reasonable to assume that n_{inv} would be comparable for the two device types. However, this would then require that μ_{bc} (dry) be a factor on the order of 10^3 larger than μ_{bc} (wet). This requirement is unreasonable and we judge the alternative explanation given here to be much less attractive than the unequal-trap-density model suggested above.

In order to determine the dry-to-wet trap-density ratio responsible for the factor-of-ninety displacement in Figure 60, one would need to relate N_t^+ (or dose) quantitatively to n_{inv} and μ_{bc} . The present data do not yield these relations. It is interesting to note in Figure 60 that the dry-to-wet I_g ratio in saturation is also 90. However, this is probably fortuitous since, as shown in Figure 56 (Devices 2 and 4), the saturation ratio varies with temperature due to the temperature dependence of μ_{bc} . On the other hand, the displacement ratio is expected to be temperature invariant since it depends only on the trap density ratio (assuming μ_{bc} (dry) = μ_{bc} (wet) for a constant leakage current).

It is useful to review the relations among quantities considered up to this point. Back-channel leakage current I_l can be expressed in terms of a pre-irradiation value I_{l0} and a radiation-induced component I_{lr} :

$$I_l = I_{l0} + I_{lr}. \quad (38)$$

The inversion-layer carrier density n_{inv} in the back channel can also, in general, be thought of in terms of two components, with the radiation-induced part being due to holes generated by radiation and trapped in the sapphire. Back-channel mobility μ_{bc} increases with ionizing radiation under the present description. Using Eq. (30), we can write,

$$I_l = e F A n_{inv} \mu_{bc}. \quad (39)$$

From Figure 57, we obtained the empirical expression

$$I_l = 8.5 \times 10^{-3} \exp(-\Delta E/kT), \quad (40)$$

where ΔE is dose dependent. For doses below leakage-current saturation at room temperature, we have found (Figure 60) that

$$I_{lr} = k_a \phi^{1.5}, \quad (41)$$

where the constant k_a depends on whether wet-oxide or dry-oxide findings are considered.

Equation (38) is general. Equation (39) holds unless I_{l0} is a generation current, in which case Eq. (39) only applies to I_{lr} . Some of the present data suggest that Eq. (40) is a general relation for the devices studied under all conditions (i.e., different temperatures, wet and dry oxide, pre- and post-irradiation). (However, in view of data in Figure 61a and the corresponding discussion given above, further study will be required to examine the validity of this point.) Comparing Eqs. (39) and (40) illustrates that ΔE depends on n_{inv} and μ_{bc} which, in turn, are both dose dependent. Equation (41) is quite specific, as noted above. Based on data in Figure 56, it is expected that the 1.5 exponent in this expression will vary with temperature.

5.5.4 Radiation-Induced Reduction of Back-Channel Leakage Current

The right portion of Figure 55 illustrates a phenomenon we have observed involving radiation-induced reduction of back-channel leakage current. Reducing V_{ds} to zero after radiation-induced increases in I_l have been observed causes I_l to decrease dramatically to near its pre-irradiation value if irradiation is continued in this bias condition. To obtain the recovery data of Figure 55 (note break in dose axis just beyond 10^6 rads), V_{ds} was reduced to zero after 10^6 rads and irradiation continued. To measure leakage current at a given dose, V_{ds} was momentarily switched to 5V and V_{gs} to -7V (typically). This measurement took 2-3 sec and then V_{gs} and V_{ds} were returned to zero. If the measurement is not made rapidly, then I_l will increase significantly during the measurement period. In Figure 55, it is shown that a few thousand rads is sufficient to reduce I_l to a saturation level.

The I_l reduction process can be repeated as evidenced by data in Figure 62. This figure shows findings for a wet-oxide transistor irradiated with $V_{ds} = 5V$ to a dose of 10^3 rads, at which point V_{ds} was reduced to zero and irradiation continued. Substantial recovery is evident. This process was repeated for four more cycles as shown. Upon completion of this cycling experiment, the Co^{60} source was lowered (dose rate = 0 -- "source down" condition in Figure 62), with a resulting decrease in I_l to within 25% of the pre-irradiation value. The source was raised again (with $V_{ds} = 0$) and I_l increased, and we attribute this increase to a photocurrent as mentioned in Section 5.5.3. (Note that the photocurrent saturates when the source is completely up. This process is repeatable.) The recovery phenomenon observed here suggests that periodic reduction of V_{ds} to zero to cause a reduction in I_l is a potential remedy for leakage current problems in SOS devices employed in a space radiation environment.

It should be noted that no observable photocurrent is expected for dry-oxide devices (although no measurements were made) because I_l is orders of magnitude larger than I_{pc} . In Figure 55, the post-recovery value of I_l for the dry-oxide transistor is a factor of three larger than I_{l0} and we attribute this effect to radiation-induced increases in I_l that occur under zero bias as noted by Kjar³⁷ and others. This effects appears to be unimportant in the

³⁷R.A. Kjar and J. Peel, IEEE Trans. Nucl. Sci. 21, 208 (Dec. 1974).

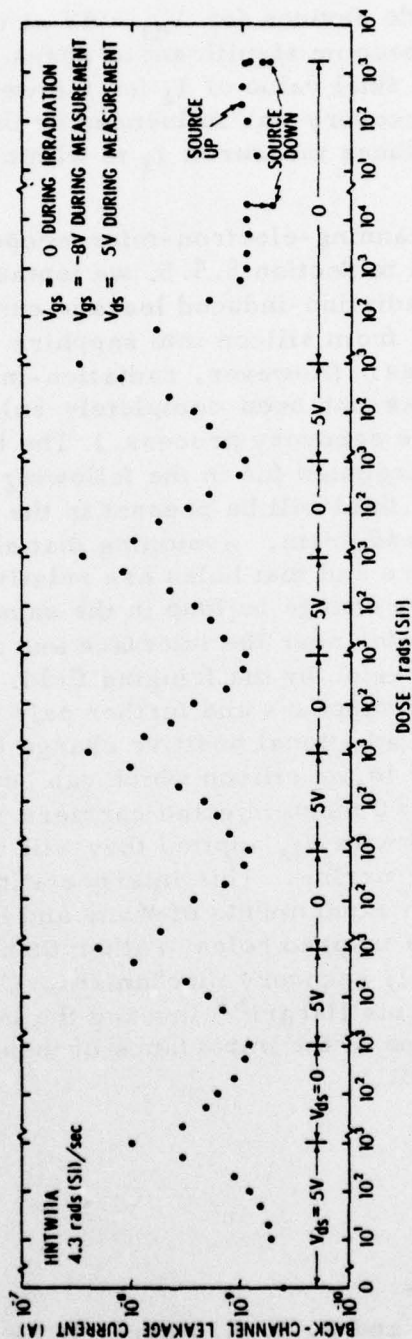


Figure 62. Leakage current versus dose for a wet-oxide n-channel MOS transistor. The effect of irradiating with $V_{ds} = 5V$ and $V_{gs} = 0$ is illustrated.

present wet-oxide devices for $V_{ds} = 5V$ at the total doses considered here but might become significant at doses $\gg 10^6$ rads. (Note that in Figure 55 the final value of I_L for the wet device following radiation-induced recovery was influenced by the photocurrent. Subtracting I_{pc} reduces measured I_L to within 50% of its pre-irradiation value.)

Based on scanning-electron-microscope studies which are described in detail in Section 5.5.5, we tentatively conclude that the mechanism of radiation-induced leakage current recovery is injection of electrons from silicon into sapphire where they recombine with trapped holes. (However, radiation-induced depopulation of trapped holes has not been completely ruled out as an important mechanism in the recovery process.) The bias dependence of recovery can be accounted for in the following manner. With V_{ds} applied, a fringing field will be present in the sapphire in the region between source and drain. Assuming that electrons are quite mobile in sapphire and that holes are relatively immobile (readily trapped), positive charge buildup in the sapphire will occur due to the trapping of holes near the interface and a sweeping out of electrons from this region by the fringing field. If V_{ds} is reduced to zero, this field disappears and further pair generation by radiation will not result in additional positive charge buildup. Radiation excites electrons in the silicon which can be injected into the sapphire. With $V_{ds} = 0$ these injected carriers can recombine with trapped holes but with V_{ds} applied they will be swept out without recombination occurring. This interpretation is in contrast to the photodepopulation experiments of Wang and Royce⁵² in which optical release of trapped holes, rather than electron injection, was given as the I_L recovery mechanism. On the other hand, in similar experiments Harari⁵³ invoked the latter mechanism. Further discussion of the importance of these processes is given in Section 5.5.5.3.

⁵² S. T. Wang and B. S. H. Royce, IEEE Trans. Nucl. Sci. 23, 1586 (1976).

⁵³ E. Harari, Appl. Phys. Letters 29, 25 (1976).

5.5.5 Scanning Electron Microscope Studies

5.5.5.1 Introduction

The scanning electron microscope is a useful tool for investigating, with high spatial localization, ionizing radiation effects on devices. We have applied this technique here in order to investigate the mechanisms of both back-channel leakage current production and radiation-induced reduction of this current. Both dry- and wet-oxide devices were studied. Experimental methods and results obtained in studies of leakage current production and leakage current reduction as a function of beam energy are described. A brief discussion of island edge effects in wet and dry devices is also given. The mechanisms of leakage current production and reduction were found to be rather complicated and it is clear that further experiments using electron-beam excitation are required to verify certain aspects of the interpretation given here.*

5.5.5.2 Experimental Design and Procedure

A scanning electron microscope is in many ways an ideal source of localized ionizing radiation. The radiation dose may be limited not only in area but also in depth by choice of beam energy. Direct observation of the sample under irradiation is possible, the radiation source can be turned off abruptly (in contrast to Co^{60}) to permit immediate measurement, and a wide range of dose rates is available. For the present purposes, the only localization of interest is in terms of depth into the sample in order to probe the source of carriers which are trapped in the Al_2O_3 and give rise to back-channel leakage current, and the source of neutralizing carriers which result in reduction of leakage current. The energy deposition profile has been studied in detail for low-energy electrons in low-Z material, most recently and comprehensively by Everhart and Hoff¹⁵ who derived a generalized depth-dose curve valid for the range of 5 - 25 keV in beam energy. Energy deposition profiles appropriate for the present devices were derived from their formulation and are shown in Figure 63. The different materials are treated identically except that their thickness is given in terms of an equivalent thickness of SiO_2 by means of density ratios. The Everhart-Hoff treatment does not reveal in detail the nature

* After completion of the work described in this section, additional data were obtained using an SEM which elaborate on the preliminary findings reported here. These later results will appear in a paper in the Dec. 1977 issue of the IEEE Trans. Nucl. Sci.

¹⁵ T.E. Everhart and P.H. Hoff, J. Appl. Phys. 42, 5837 (1971).

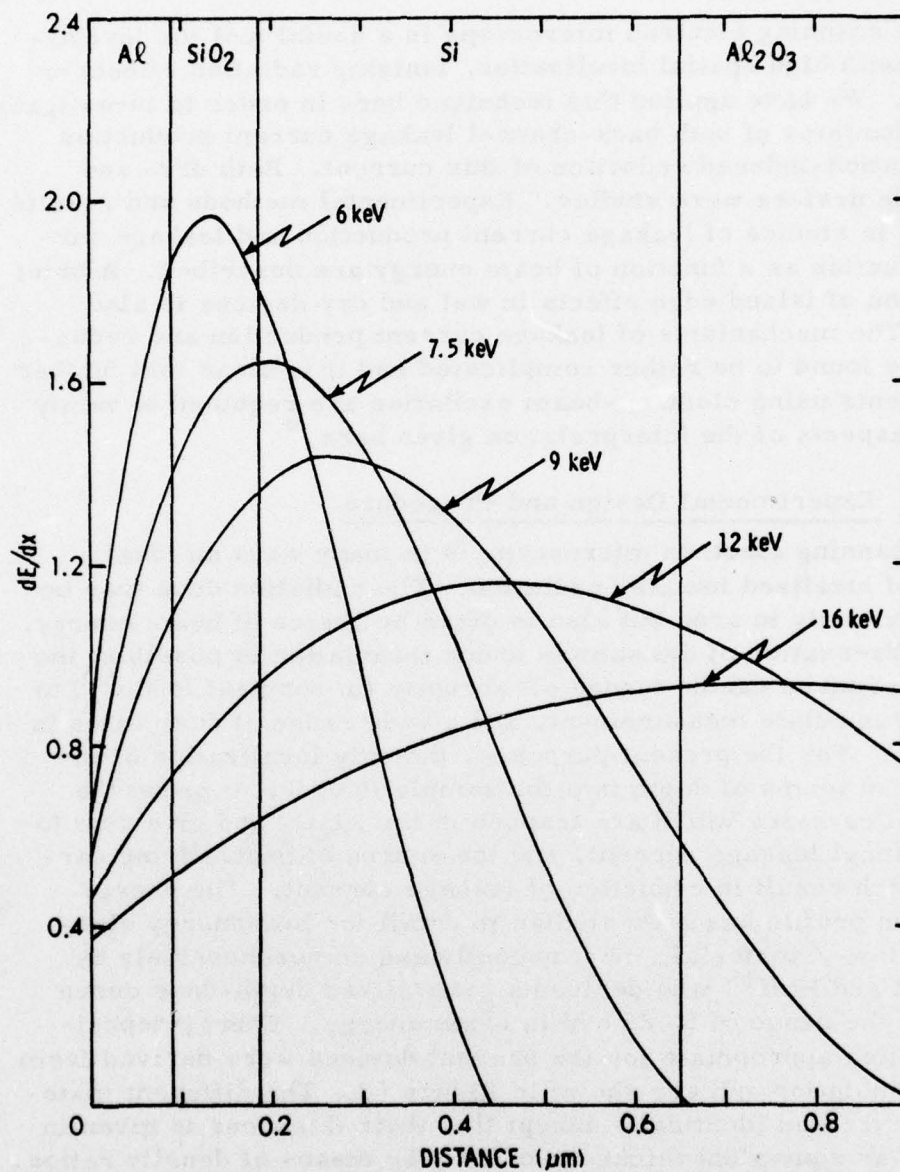


Figure 63. Energy deposition profiles for the present SOS structures bombarded by low energy electrons. Profiles were calculated based on the work of Everhart and Hoff.¹⁵

of the "tail" in the dose-depth curve, but it can be argued on physical grounds that the profile must end rather abruptly, as shown. The resulting dose deposition is not uniform but is well confined dimensionally.

In principle, it would be desirable to confine the incident radiation to the actual dimensions of the gate electrode. That was found to be impractical for the SEM utilized here. In the present instance, this was of no consequence since the samples were provided with thick metallization except for the gate region. Beam incidence on the bare sapphire surrounding the silicon islands was deemed to be harmless. In practice, irradiation took place over a square area by means of a raster scan. Determination of the dose delivered to the sample required knowledge of the beam current, the dose profile over the region of interest, the raster area, the magnification factor, and the rastering rate. Of these, only the beam current requires comment. It was determined by means of a Faraday cup mounted on the sample holder. Currents were measured by means of a current-to-voltage converter, an electrometer operational amplifier (Burr-Brown 3523) in inverting configuration. For the small currents employed (3 - 10 pA), the requisite measurement accuracy was obtained by scanning the beam over the aperture of the Faraday cup and performing ac measurements of the cup current on a scope under conditions of limited signal bandwidth (about 100 Hz).

The raster employs from 125 to 500 lines per scan, and the question of lateral uniformity of dose deposition may be raised. With a well-focused scanning beam, the shape of the deposition profile may be likened to a teardrop with a width on the order of one-half the range at that energy. At the point of impact, focusing may be to 100 Å or so. To achieve uniformity in dose, it is appropriate to defocus the beam slightly until the resolution observed in the secondary electron mode drops below the line spacing. This does not affect the magnification factor.

The magnification factor and focusing conditions both depend on beam energy. Determination of dose therefore needs to be made for each energy employed. In practice, the magnified area scanned was kept constant at 10 cm^2 , so that the actual sample area scanned varied as $1/(\text{magnification factor})^2$. An approximate desired dose was chosen, and on this basis the appropriate number of

raster scans selected. For the higher doses, where exposure times exceeded 1 - 2 minutes, the magnification was increased. The beam current was shut off from the sample before and after exposure by means of deflection plates inserted in a drift space below the anode of the SEM gun, to which several hundred volts were applied, which is sufficient to deflect the beam onto an intervening aperture. With the beam off, the active area could be moved away and the beam allowed to strike the Faraday cup quiescently while measurements were made on the sample in situ. Since both the Faraday cup aperture and the sample active area need to be found "blind", the pointing accuracy of the beam is restricted to the mechanical resettability of the sample mount, and this is the reason it is impractical to restrict irradiation to the actual gate area in the scanning microscope utilized.

5.5.5.3 Experimental Results

The first experimental objective was to confirm unambiguously that the observed radiation-induced leakage current is exclusively a back-channel phenomenon. To this end, comparison was made of the rate of leakage current production using a 7.5-keV beam and an 18.5-keV beam. It is seen in Figure 63 that the 7.5-keV profile peaks at the front channel for the present samples, while depositing a negligible fraction of energy at the sapphire interface. The 18.5-keV profile (not shown) is reasonably flat at the sapphire interface, while contributing relatively less at the front channel (<5% of the total dose goes into the SiO₂). Results of measurements at these two energies on one wet-oxide transistor as a function of dose are shown in Figure 64. The first experiment on this device was measurement of I_L versus dose up to $\sim 10^6$ rads for the 7.5-keV case, where the dose employed was that deposited in the SiO₂. Next, irradiation was continued to an additional 2×10^6 rads using 18.5-keV electrons (open circles in Figure 64). (Dose in this case is defined as that received at the Si-Al₂O₃ interface.) Next, the device was annealed at room temperature under bias for 1h and a slight reduction in I_L was observed. Following this, the device was irradiated with $V_{ds} = V_{gs} = 0$ by 18.5-keV electrons to an additional total dose of ~ 2000 rads and a two-order-of-magnitude reduction in I_L was noted. Such behavior is consistent with the Co⁶⁰ data discussed in Section 5.5.4.

Data in Figure 64 demonstrate that in order to observe significant radiation-induced increases in leakage current one must deposit energy in the sapphire. The nonpenetrating 7.5-keV beam is seen to

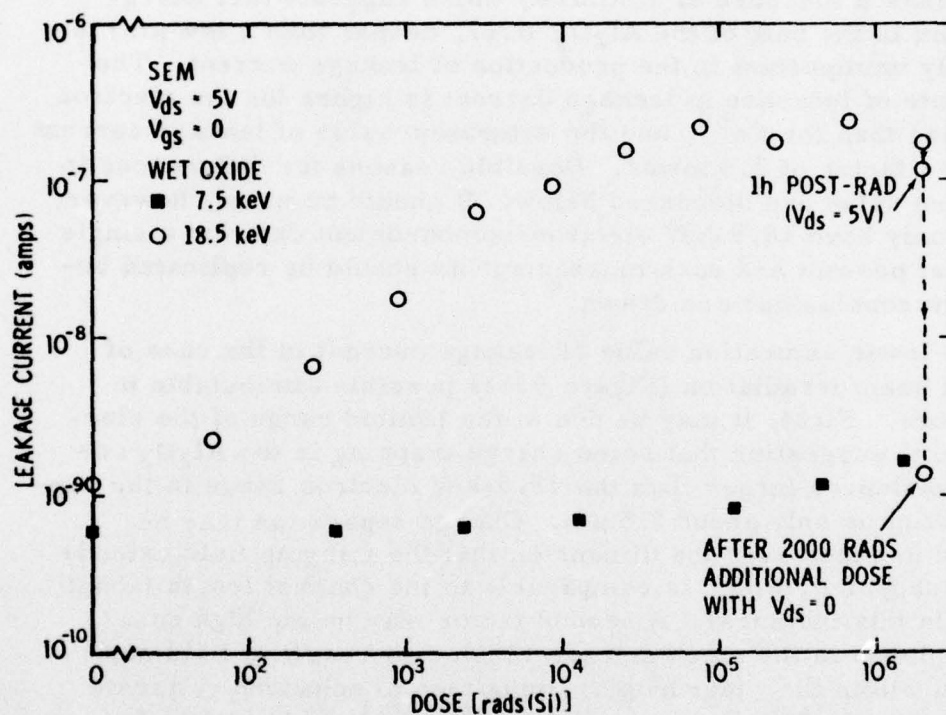


Figure 64. Back-channel leakage current versus dose for 7.5-keV and 18.5-keV electron bombardment of a wet-oxide n-channel SOS transistor. Also shown is radiation-induced reduction of leakage current by 18.5-keV bombardment with $V_{ds} = 0$. (For 7.5 keV, the dose given is that deposited in the SiO_2 whereas for 18.5 keV it is that received at the $Si-Al_2O_3$ interface.)

be relatively ineffective in leakage current production. There is some increase in I_L at that energy at the highest doses which may be due to a slight amount of energy deposition in the sapphire due to the tail of the deposition profile, which just reaches the Si-Al₂O₃ interface (Figure 63).

Comparison of the 18.5-keV data of Figure 64 with data observed for Co⁶⁰ bombardment (Figure 60) is made in Figure 65 where the pre-irradiation current has been subtracted out in both cases. The curves show a measure of similarity which suggests that energy deposition in the bulk of the Al₂O₃ (i.e., deeper than a few μm) is relatively unimportant in the production of leakage current. The initial rate of increase in leakage current is higher for the electron beam case than for Co⁶⁰, and the saturation value of leakage current is about a factor of 2.5 lower. Possible reasons for differences in saturation value are discussed below. It should be noted, however, that we only have 18.5-keV electron-bombardment data for a single sample at present and such measurements should be replicated before firm conclusions are drawn.*

The lower saturation value of leakage current in the case of electron beam irradiation (Figure 65) is possibly attributable to two factors. First, it may be due to the limited range of the electron beam, suggesting that some charge trapping in the Al₂O₃ occurs at distances larger than the 18.5-keV electron range in the sapphire, which is only about 1.5 μm . Charge separation may be expected to occur over the dimension that the fringing field extends into the sapphire, which is comparable to the channel length (about 5.5 μm in this instance). A second factor may be the high dose rate employed in the electron case which may result in field suppression within the "teardrop", giving rise to enhanced geminate recombination. The dose rate is indeed considerably higher for electron bombardment than for Co⁶⁰ since irradiation times differ by a factor of 300 - 6000, only a fraction of the irradiation time in the e-beam case results in exposure of the active area, and only a fraction of the active area is exposed at any one time (depending on the amount of defocusing employed, which was not quantified). A dose-rate ratio of $10^4 - 10^6$ rads(Si)/s is estimated. Since charge separation leading to trapped holes in the Al₂O₃ presumably requires the presence of the fringing field, suppression of the field due to the electron beam could easily be responsible for the reduction in saturated leakage current. This hypothesis need not be inconsistent with the low-dose data which show a high rate of increase

* See IEEE Trans. Nucl. Sci., Dec. 1977, for more recent data.

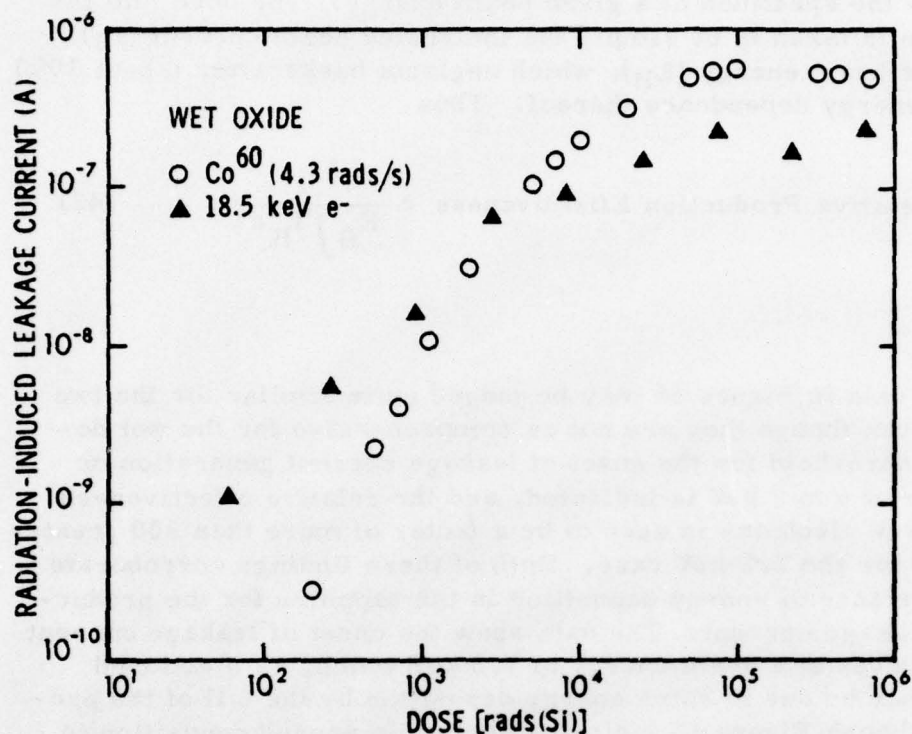


Figure 65. Radiation-induced leakage current versus dose for wet-oxide n-channel SOS transistors bombarded by Co^{60} gamma rays (from Figure 60) and by 18.5-keV electrons (derived from Figure 64).

of leakage current since the dose rate employed there was considerably lower than for the higher dose data points.

It is clear that complementary data using electron-beam excitation at lower dose rates, and also at more penetrating beam energies, are required before a more detailed understanding can be achieved. The points of difference in the data just discussed should not, however, obscure the basic finding of a similarity in behavior of penetrating Co^{60} irradiation and for 18.5-keV electron-beam bombardment which penetrates only about $1.5 \mu\text{m}$ into the sapphire. More explicit demonstration of the dependence of leakage current production on dose deposited near the Si- Al_2O_3 interface may be obtained by measuring the effectiveness in inducing leakage current as a function of beam energy. Such data are shown in Figure 66 for a dry and a wet device. In this plot, "relative production effectiveness" is defined as the change in leakage current induced by unit

dose into the specimen at a given beam energy. The dose into the specimen is taken to be simply the integrated beam current (I_B) times the beam energy (E_B), which neglects backscatter (about 10%) and the energy dependence thereof. Thus

$$\text{Relative Production Effectiveness} = \frac{\Delta I_L}{E_B \int I_B dt} . \quad (42)$$

The data in Figure 66 may be judged quite similar for the two cases, even though they are not as comprehensive for the wet device. A threshold for the onset of leakage current generation on the order of 6 to 7 keV is indicated, and the relative effectiveness of 18.5-keV electrons is seen to be a factor of more than 200 greater than that for the 7.5-keV case. Both of these findings corroborate the importance of energy deposition in the sapphire for the production of leakage current. The data show the onset of leakage current increase even at a beam energy of 7.5 keV which, as mentioned above, may be due to some energy deposition by the tail of the profile. Although Figure 63 indicates negligible energy deposition in the sapphire at 7.5 keV, a slight error in the silicon thickness assumed in profile calculations could account for the experimental observations.

The data in Figure 66 were taken at successively higher beam energies, with the increments in leakage current such that saturation was approached at 12.3 keV, resulting in a slight suppression of that data point. Beyond 12.3 keV, radiation-induced recovery of I_L was employed so that pre- and post-irradiation values of leakage current were comparable for each of the data points shown. The nonlinearity of the I_L -versus-dose curve observed in the case of Co^{60} irradiation (the 1.5 power law illustrated in Figure 60) was not taken into account in the treatment of the data.

In an attempt to demonstrate the dependence of leakage current production on deposited energy in the sapphire more quantitatively, the relative effectiveness data of Figure 66 for the dry oxide may be expressed in terms of the fraction of the total dose which is deposited in the sapphire, according to the Everhart and Hoff energy deposition curves. We therefore define an absolute production effectiveness as

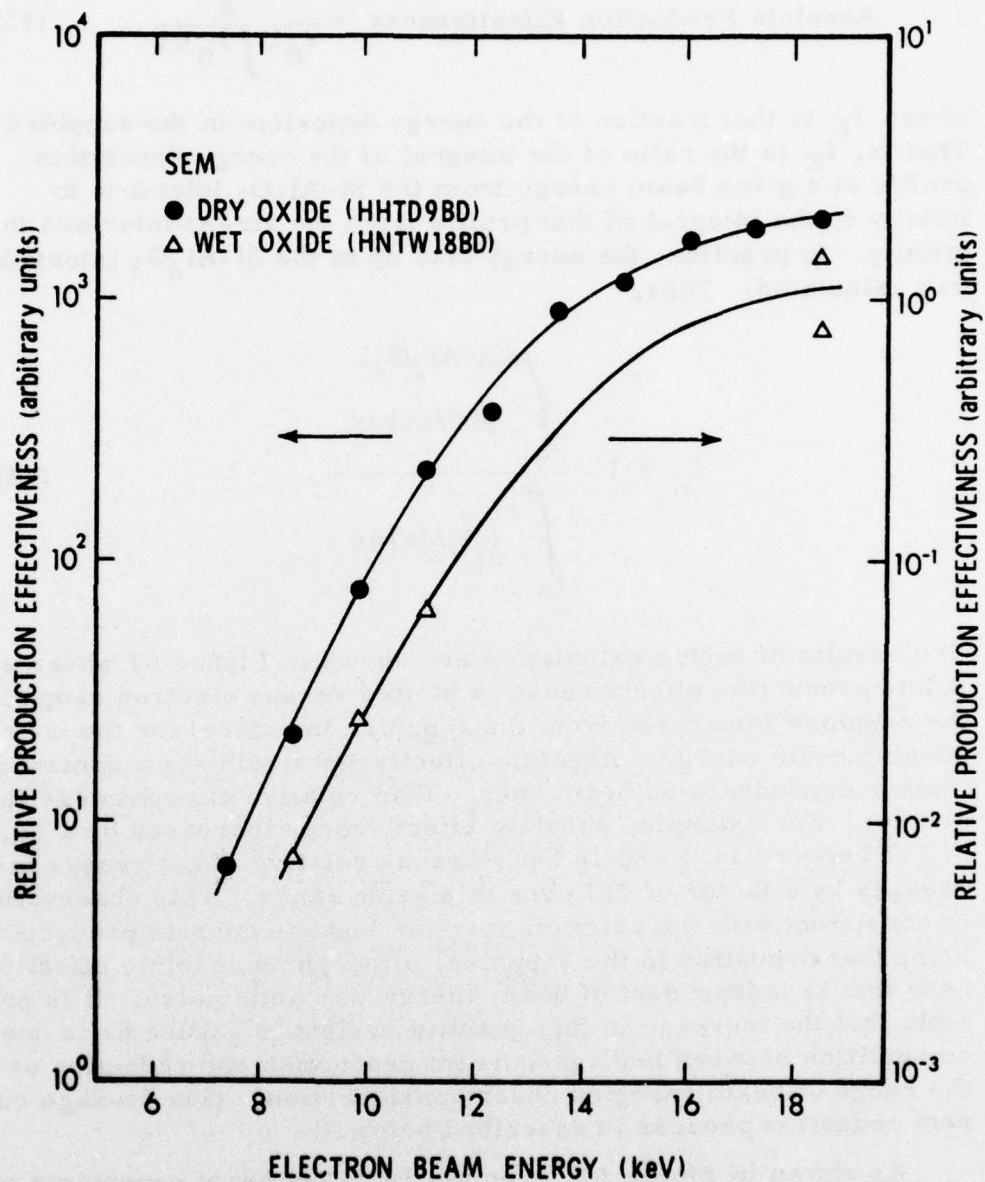


Figure 66. Relative effectiveness in producing leakage current vs. bombarding electron beam energy for dry- and wet-oxide transistors. (Relative production effectiveness is defined by Eq. (42) in the text.)

$$\text{Absolute Production Effectiveness} = \frac{\Delta I_A}{f_E \int I_B dt}, \quad (43)$$

where f_E is that fraction of the energy deposited in the sapphire. That is, f_E is the ratio of the integral of the energy deposition profile at a given beam energy from the Si-Al₂O₃ interface to infinity to the integral of that profile from the air-Al interface to infinity. In practice, the energy loss up to the Si-Al₂O₃ interface was calculated. Thus,

$$f_E = 1 - \frac{\int_0^{x(\text{Si-Al}_2\text{O}_3)} (dE/dx) dx}{\int_0^{\infty} (dE/dx) dx}. \quad (44)$$

The results of such a calculation are shown in Figure 67 where absolute production effectiveness is plotted versus electron range in the sapphire (measured from the sapphire interface) for the corresponding beam energy. Absolute effectiveness exhibits a somewhat weaker dependence on beam energy than relative effectiveness (Figure 66). For example, absolute effectiveness increases by a factor of 3.7 between 11.1 and 16 keV whereas relative effectiveness increases by a factor of 7.7 over this same range. This observation is consistent with the relevant dose for leakage current production being that deposited in the sapphire, although an absolute effectiveness that is independent of beam energy was anticipated. It is possible that the increase in this quantity evident in Figure 67 is due to competition between leakage-current production and reduction over the range of beam energies under consideration. (The leakage current reduction process is described below.)

As shown in Figure 67, even the 18.5-keV beam penetrates only about 1.5 μm into the sapphire. One expects that the depth into the sapphire which potentially contributes to leakage current is on the order of the channel length, which in this case is about 5 μm . This is because the fringing field due to V_{ds} , which presumably is required for the production of leakage current, extends into the sapphire a distance comparable to the channel length, and also because any trapped charge within that compass would yield an image charge

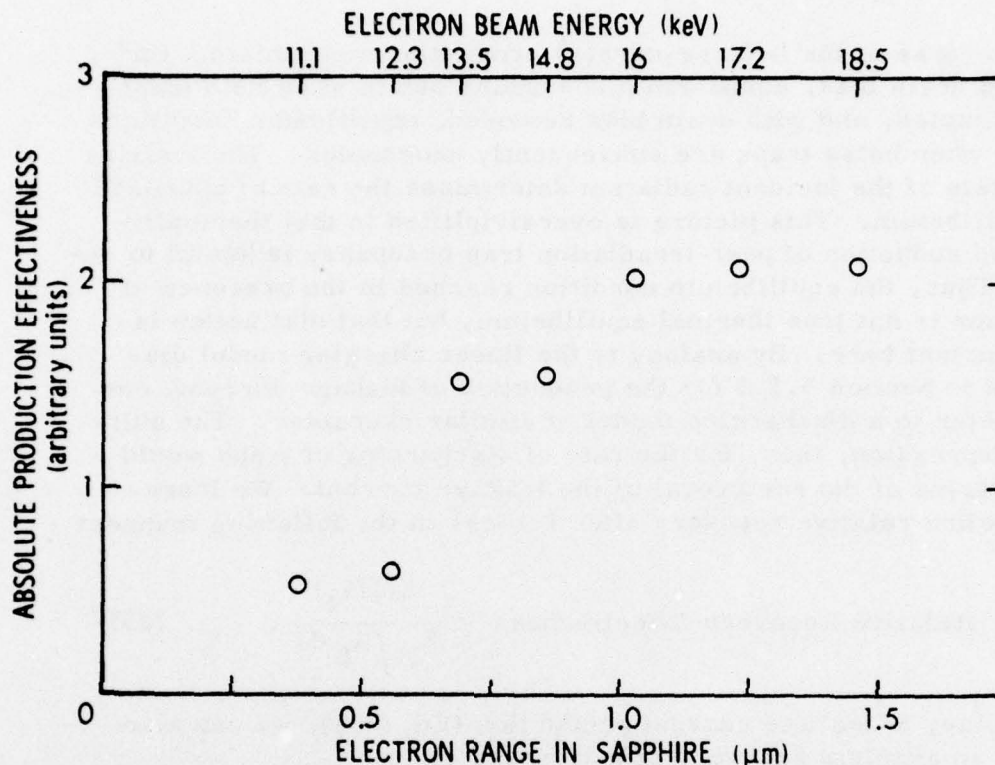


Figure 67. Absolute production effectiveness versus electron range in sapphire for a dry-oxide n-channel SOS transistor (based on data in Figure 66).

predominantly within the channel region. It would be of interest to determine the absolute production effectiveness for higher beam energies in order to map out the spatial dependence of the effectiveness with which leakage current is produced.* A significant decrease in absolute effectiveness is expected for electron ranges on the order of 5 μm or larger, and such ranges are obtainable with our SEM, which has a beam voltage capability up to 45 keV.

The phenomenon of radiation-induced reduction of leakage current by means of irradiation under conditions of $V_{ds} = 0$ has been discussed above. It was occasionally employed in SEM experiments in order to permit more extensive studies of leakage current production on a particular sample. Experiments were also performed to shed light on the recovery mechanism. It is of interest to determine the relative effectiveness of electron-beam irradiation for inducing recovery, and for this purpose a suitable criterion needs to be adopted. We assume that the reduction process is

* See IEEE Trans. Nucl. Sci., Dec. 1977.

the converse of the leakage-current production mechanism. Under applied drain bias, equilibrium conditions obtain when hole traps are occupied, and with drain bias removed, equilibrium conditions obtain when holes traps are subsequently unoccupied. The ionizing dose rate of the incident radiation determines the rate of approach to equilibrium. This picture is oversimplified in that thermally-induced reduction of post-irradiation trap occupancy is known to occur. Thus, the equilibrium condition reached in the presence of radiation is not true thermal equilibrium, but that distinction is unimportant here. By analogy to the linear charging model discussed in Section 5.5.3 for the production of leakage current, one may refer to a discharging model of similar character. The suitable expression, then, for the rate of discharging of traps would be in terms of the reciprocal of the leakage current. We therefore define relative recovery effectiveness in the following manner:

$$\text{Relative Recovery Effectiveness} = \frac{\Delta(1/I_l)}{E_B \int I_B dt} \quad (45)$$

By analogy to leakage current production (Eq. (43)), we can also define an absolute recovery effectiveness as

$$\text{Absolute Recovery Effectiveness} = \frac{\Delta(1/I_l)}{f_E E_B \int I_B dt} \quad (46)$$

Recovery data in terms of relative effectiveness for several beam energies are presented in Figure 68 for a dry- and a wet-oxide transistor. The previously discussed curve for leakage current production effectiveness for a dry transistor (similar to wet) is also shown (taken from Figure 66). It is apparent that the strong energy dependence of the relative effectiveness for producing leakage current is not observed in the recovery process. Data for the wet-oxide transistor were only obtained at two beam voltages, but these were taken concurrently with the leakage-current production effectiveness values shown in Figure 66. These wet data were judged to provide a more accurate basis for comparison of the effectiveness for recovery with the effectiveness for production of leakage current because behavior for dry transistors was found to be more complicated, as discussed below.

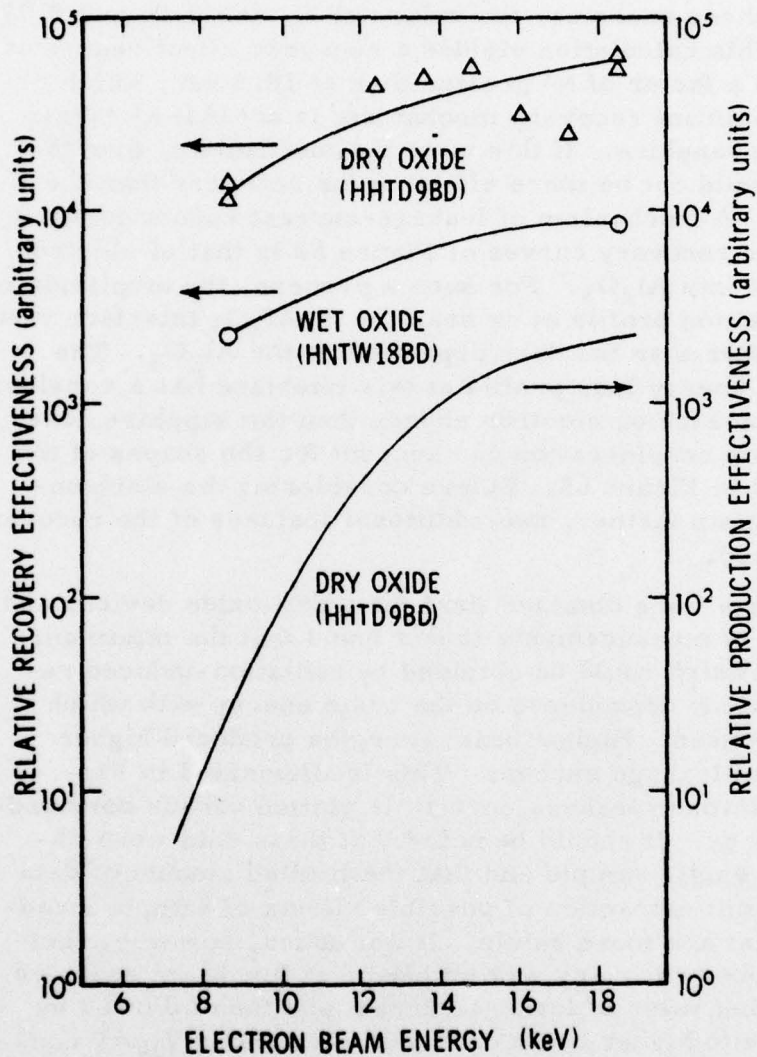


Figure 68. Relative recovery (or reduction) effectiveness vs. bombarding electron beam energy for leakage currents in dry- and wet-oxide n-channel SOS transistors. Also shown is a curve taken from Figure 66 (dry oxide) illustrating relative production effectiveness versus energy. (The two recovery effectiveness curves are shown on the same scale for convenience only.)

Equation (46) was used to calculate absolute recovery effectiveness for the wet-oxide transistor at beam energies of 8.6 keV and 18.5 keV. For these energies, the values of f_E are 0.06 and 0.77, respectively. This calculation yielded a recovery effectiveness at 8.6 keV that was a factor of ~ 4 greater than at 18.5 keV, which reveals that the dominant recovery mechanism is not that of energy deposition in the sapphire. If this were the mechanism, then the 8.6-keV beam would not be more effective for recovery than the 18.5-keV beam. A mechanism of leakage-current reduction which would explain the recovery curves of Figure 68 is that of electron injection from Si into Al_2O_3 . For such a process, the amplitude of the energy deposition profile at or near the Si- Al_2O_3 interface would be important rather than the dose deposited in the Al_2O_3 . The amplitude of the energy loss profile at this interface has a considerably softer dependence on electron energy than the sapphire dose. Qualitatively, this consideration can account for the shapes of the recovery curves in Figure 68. Before considering the electron-injection mechanism further, two additional features of the recovery data are described.

Recovery data were obtained first for a dry-oxide device, and over the course of measurements it was found that the minimum leakage current which could be obtained by radiation-induced recovery showed some dependence on the beam energy with which recovery was induced. Higher beam energies produced higher limiting values of leakage current. This is illustrated in Figure 69 where minimum leakage current is plotted versus bombarding electron energy. It should be noted that these data were obtained only on a single sample and that the limited amount of data taken do not permit extraction of possible effects of sample irradiation history that are more subtle. It was found, however, that if radiation-induced recovery was employed at low beam energies to reach a limiting value of leakage current and then followed by further exposure to higher beam energies (also under $V_{ds} = 0$ conditions), an increase in leakage current was noted. Such increases were in accordance with Figure 69 in that they occurred up to current levels appropriate to the particular beam energy employed. The implications of this finding have not yet been fully discerned, but it is mentioned here because of its potential effect on recovery data shown in Figure 68 for the dry device. This phenomenon was not evident for the wet-oxide transistor in the limited experiments performed. It is noteworthy that the radiation-induced recovery curves (wet and dry) appear to be similar despite this difference.

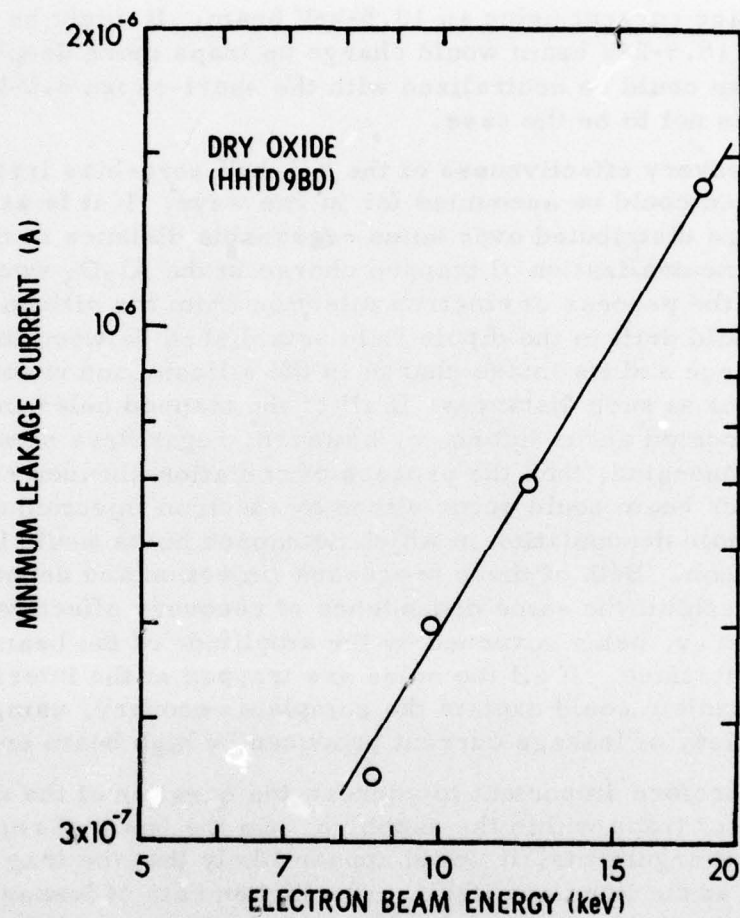


Figure 69. Minimum back-channel leakage current in a dry-oxide transistor versus the bombarding electron beam energy used to reduce leakage current to a particular minimum value by irradiation with $V_{ds} = 0$.

The second feature of the data which should be mentioned is that in the case of the wet device the radiation-induced recovery data of Figure 69 were obtained at both 8.6 and 18.5 keV following production of leakage current using an 18.5-keV beam. It might be expected that the 18.5-keV beam would charge up traps more deeply in the sapphire than could be neutralized with the short-range 8.6-keV beam. This appears not to be the case.

The recovery effectiveness of the 8.6-keV zero-bias irradiation just described could be accounted for in two ways. If it is assumed that traps are distributed over some reasonable distance in the sapphire, then neutralization of trapped charge in the Al_2O_3 would have to occur by the process of electron injection from the silicon. These carriers would drift in the dipole field established between the fixed positive charge and its image charge in the silicon, and recombine with the holes at such distances. If all of the trapped holes in the Al_2O_3 are located at the interface, however, regardless of where they were generated, then the process of radiation-induced recovery by an 8.6-keV beam could occur either by electron injection or by the process of hole depopulation in which detrapped holes would be injected into the silicon. Both of these processes (injection and depopulation) would exhibit the same dependence of recovery effectiveness on beam energy, being governed by the amplitude of the beam profile at the interface. If all the holes are trapped at the interface, either mechanism could explain the complete recovery, using low beam energies, of leakage current produced by high beam energies.

It is therefore important to address the question of the spatial distribution of traps within the sapphire. On the basis of reasonable physical arguments, it would appear likely that the trap sites are located at the interface itself. The higher rate of leakage current production in the case of the dry oxide has been ascribed to a greater trap density, which must be processing-related. It is likely that such processing effects extend over quite limited range into the sapphire, perhaps the distance over which stoichiometry is affected or over which stress prevails. Such distances are expected to be small compared to the 1.5- μm range of an 18.5-keV beam in the sapphire. If it can be argued that the traps occur at the interface in the case of the dry oxide, then it is likely that the same holds for the wet oxide since the observed energy dependence of the recovery effectiveness is so similar in the two cases. The possibility of a spatial distribution of trapping sites into the sapphire cannot be ruled out a priori, however.

Electron-beam experiments are capable of shedding light on this question. If all the trapping sites occur at the interface, then we would not expect the saturation leakage current to be different for the case of electron-beam bombardment than for Co^{60} irradiation, contrary to our (limited) observation (Figure 65). A more comprehensive determination of the dependence of saturation leakage current on electron energy would permit a determination of the location of trapping sites. If such an experiment is to be unambiguous, however, the alternative hypothesis for the saturation leakage current difference should be kept in mind. This hypothesis holds that the electron-beam-induced saturated leakage current may be lower because of a dose-rate dependence of leakage current production via field suppression at the interface in the presence of the electron beam. If, as a result of such studies, the traps are indeed found to be broadly distributed, then a choice in favor of the mechanism of electron injection is clearly indicated. In the event that traps are found to be strongly localized at the interface, however, as is likely, then electron-beam experiments may not be able to discriminate between electron injection and hole depopulation.

As discussed in Section 5.5.4, Harari⁵³ and Wang and Royce⁵² performed experiments in which leakage current reduction was achieved by optical excitation. Harari postulated an electron injection mechanism whereas Wang and Royce explained their findings in terms of photodepopulation of trapped holes, with the assumption that the temporarily mobile holes move away from the interface under influence of their mutual repulsion. Drawing general conclusions on the basis of these other studies for the present work is difficult since the experimental conditions are so different in the two cases. More detailed SEM studies may be helpful in establishing the dominant leakage-current recovery mechanism in a specific situation.

An additional study undertaken with the SEM concerned the radiation susceptibility of island edges on SOS transistors. These $\langle 111 \rangle$ faces exhibit different threshold shifts with dose than for the oxide in the channel region, where the silicon is of $\langle 100 \rangle$ orientation. The SEM technique is particularly suitable to such

⁵² S. T. Wang and B. S. H. Royce, IEEE Trans. Nucl. Sci. 23, 1586 (1976).

⁵³ E. Harari, Appl. Phys. Letters 29, 25 (1976).

an investigation in that the beam energy can be chosen to maximize the dose into the silicon dioxide with respect to the dose received by the sapphire. Additionally, whatever leakage current is produced upon irradiation may be eliminated by radiation-induced recovery, so that the only net change effected in drain characteristics is due to the increased conductivity attributable to the island edge. Since the conductance of the island edges is observed to be small, it is seen only when the front channel is weakly inverted.

The island edge effect was studied in both wet- and dry-oxide transistors, with emphasis placed on dry devices where the effect is more easily masked by the high back-channel leakage current and where the additional sensitivity of the SEM technique is particularly advantageous. Transistors were used in this study which were fabricated with uniform metallization thickness, so that the front-channel region was not preferentially irradiated. The metallization thickness was in excess of $1\text{ }\mu\text{m}$, thus requiring rather higher electron-beam energies to penetrate to the silicon dioxide than in the case of the thin gate metallization. A threshold for increase in island edge conductance was observed at about 9 keV and for production of back-channel leakage current at about 10 keV. These studies yielded no profound new insights and therefore no presentation of specific experimental results is made here.

5.5.6 Non-Ohmic Contact Effects on Leakage Current Measurements

It was mentioned in Section 5.4 that the custom SOS transistors used in this study had source and drain regions which were not doped heavily enough to yield ohmic contacts. The resulting non-ohmic source and drain contacts (Schottky barriers) were carefully taken into account in channel mobility measurements, as described in that section. We also made an assessment of the possible effects of these contacts on measurements of back-channel leakage current and our findings are discussed here.

The main effect addressed was determination of that portion of the applied drain-to-source voltage V_{ds} which was dropped across the two non-ohmic contacts (one forward biased and the other reverse biased). To do this, we made use of SOS capacitors fabricated simultaneously with SOS transistors. As described in Section 5.2, these devices were identical to the transistors except that the channel was implanted with phosphorus. Thus, measurements on such structures, each of which consists of a resistor with non-ohmic contacts on each end, permit Schottky-barrier effects to be isolated.

Current-voltage characteristics were determined for SOS capacitors with wet and dry oxides at room temperature and the resulting curves were identical. In addition, current-voltage characteristics were determined for a wet-oxide unit over the temperature range shown for data in Figure 56. For wet oxides at room temperature, the leakage current range covered in measurements on transistors as a function of dose (Figure 55) was from $\sim 4 \times 10^{-10}$ to $\sim 6 \times 10^{-7}$ A. From SOS capacitor measurements we found that the total voltage drop across the two non-ohmic contacts for these two cases was ~ 0 and ~ 0.5 V, respectively. This means that for $V_{ds} = 5$ V the percentage of V_{ds} that was dropped across the channel during irradiation of a wet-oxide transistor ranged from 100% pre-irradiation to $\sim 90\%$ for irradiation to a dose $\geq 10^5$ rads. This means that the increasing voltage drop across the non-ohmic contacts with increasing dose caused the measured I_L to be slightly less than it would have been if the contacts had been ohmic. Below room temperature, I_L is smaller and this effect is reduced. On data plots such as those shown in Figures 54 - 56, the correction of wet-oxide data for contact effects is negligible.

For the larger leakage currents of dry-oxide transistors, contact effects are also enhanced. At room temperature, I_L varied from $\sim 4 \times 10^{-8}$ to $\sim 5 \times 10^{-5}$ A in exposures up to 10^6 rads. The pre-irradiation contact voltage drop is ~ 0.1 V whereas post-irradiation this drop is ~ 1.4 V. Thus, for $V_{ds} = 5$ V the correction for contact effects in dry-oxide transistors ranges from negligible pre-irradiation to $\sim 30\%$ post-irradiation. At lower temperatures, I_L is smaller and the correction is smaller. For example, at $1000/T = 4.0$ in Figure 56, the post-irradiation I_L for a dry-oxide transistor is $\sim 9 \times 10^{-6}$ A. Current-voltage characteristics for an SOS capacitor at that temperature yielded a voltage drop of ~ 1 V for that current, which is a 20% contact effect. Dry-oxide data in Figures 54 - 56 (and other figures) were not corrected for contact effects. However, doing so would not have an important effect on the analysis and conclusions made in previous sections.

5.6 BACK-CHANNEL LEAKAGE CURRENT STUDIES ON CMOS/SOS INVERTERS

Studies of radiation-induced back-channel leakage current were made on radiation-hardened CMOS/SOS inverters (4007) obtained from three manufacturers. As mentioned in Section 5.2, devices from five lots were examined, including two lots from each of two manufacturers and one from the third supplier. Quantities were quite small (two devices from each lot in most cases), so we emphasized investigation of only one phenomenon: radiation-induced reduction of leakage current. Our purpose was to determine whether the findings for specific custom n-channel SOS transistors reported in Section 5.5.4 were general. Irradiations were performed using Co^{60} at a dose rate, in most cases, of 64 rads(Si)/s. Measurements of leakage current were typically made at $V_{gs} = 0$; input protection circuits prevented us from using a more negative gate bias. Individual n-channel transistors on the 4007 chips were investigated.

Large variations in radiation response were observed from lot to lot. However, the radiation-induced recovery phenomenon was evident for all devices examined, including units from all three manufacturers. We thus conclude that this effect is general and not specific to the custom transistors studied in detail. Rather than present a number of graphs showing radiation-induced increases and reduction of I_{ℓ} for various devices obtained under a variety of conditions, we instead summarize key observations in tabular form for example cases (Table II). In all cases shown, pre-irradiation I_{ℓ} is relatively small. In three of the four cases, post-irradiation I_{ℓ} is at least an order of magnitude larger than before irradiation (nearly four orders of magnitude larger in two cases). Reduction of I_{ℓ} was accomplished by continuing the irradiations with $V_{ds} = V_{gs} = 0$, as discussed in Section 5.5.4. Recovery was significant in all four cases. In fact, for three cases the post-recovery value of I_{ℓ} is smaller than the pre-irradiation value (an order of magnitude smaller in one case -- Manufacturer #2, lot #1). (We also observed this effect for other devices not listed in Table II.) This finding suggests a method by which SOS manufacturers could, in some cases, reduce pre-irradiation I_{ℓ} : irradiate devices to a moderate level ($\sim 10^4$ rads) with all the leads shorted.

Table II. Leakage current information for irradiated n-channel transistors in CMOS/SOS inverters from three manufacturers. Ionizing doses for irradiation under bias and irradiation with $V_{ds} = 0$ are shown in parentheses.

Device Source	I_L (A) Pre-Rad	I_L (A) Post-Rad	I_L (A) Post-Recovery	Comments
Manufacturer #1	7.2×10^{-9} ($V_{ds} = 10V$)	6.8×10^{-5} (10^4 rads)	4.0×10^{-9} (2×10^4 rads)	Irradiation: $V_{ds} = 10V$ $V_{gs} = 0$ Recovery: $V_{ds} = V_{gs} = 0$
Manufacturer #2 (lot #1)	7.5×10^{-8} ($V_{ds} = 5V$)	1.3×10^{-6} (2×10^5 rads)	7.0×10^{-9} (2×10^5 rads)	Irradiation: $V_{ds} = 5V$ $V_{gs} = 0$ Recovery: $V_{ds} = V_{gs} = 0$
Manufacturer #2 (lot #2)	3.6×10^{-10} ($V_{ds} = 5V$)	2.6×10^{-6} (10^6 rads)	6.6×10^{-10} (4×10^6 rads)	Irradiation: $V_{ds} = 5V$ $V_{gs} = 0$ Recovery: $V_{ds} = V_{gs} = 0$
Manufacturer #3	1.7×10^{-8} ($V_{ds} = 15V$)	3.8×10^{-8} (2×10^5 rads)	1.0×10^{-8} (2×10^4 rads)	Irradiation: $V_{ds} = 15V$ $V_{gs} = 0$ Recovery: $V_{ds} = V_{gs} = 0$ The two devices in this lot exhibited excellent resistance to increases in I_L by radiation.

The above observation suggests that positive charge is trapped in the Al_2O_3 for some as-manufactured CMOS inverters which gives rise to leakage current. The fact that we were able to reduce I_{g} by a zero-bias irradiation is in contrast to the work of Harari and McGreivy.⁵¹ They were unable to reduce I_{g} in unirradiated devices by photodepopulation. On the other hand, in the present studies on custom SOS transistors (discussed in earlier sections) we never observed a post-recovery leakage current that was less than the pre-irradiation value, which is in agreement with Harari's observations.

5.7 STUDIES OF THE SILICON-SAPPHIRE INTERFACE USING CAPACITANCE-VOLTAGE MEASUREMENTS

A modified capacitance-voltage measurement technique has recently been developed^{39, 40} to characterize the silicon-sapphire interface in terms of fixed charge, interface density, silicon doping concentration, bias-temperature stress effects, and radiation tolerance. In this measurement, bias is applied across the sapphire wafer to sweep the surface potential at the silicon-sapphire interface. An experimental facility has been built at Northrop to perform such measurements on state-of-the-art hardened SOS wafers, and suitable test wafers were obtained. However, these wafers did not arrive before the end of the program, so testing was confined to older Inselek wafers for the purpose of verifying performance of the test apparatus. In this section the experimental method and our implementation will be described.

Application of the conventional C-V measurement technique to the case of an MIS structure employing a thick insulator presents several difficulties. First, the total capacitance change induced by depleting the silicon is very small since it is in series with a small insulator capacitance. Secondly, a large bias voltage swing is required to sweep the space-charge capacitance over the range of interest. The modification of the conventional C-V technique which facilitates measurements under these conditions consists of

³⁹ A. M. Goodman, IEEE Trans. Electron Devices 21, 753 (1974).

⁴⁰ A. M. Goodman, IEEE Trans. Electron Devices 22, 63 (1975).

⁵¹ E. Harari and D. J. McGreivy, to be published in IEEE Trans. Electron Devices.

bucking out the bulk of the capacitance signal by means of an opposite-phase signal derived from the same ac-excitation source. This method of baseline subtraction reduces sensitivity to source intensity fluctuations and to drift in the detection circuitry. In its application to this particular problem, the method has been exploited primarily by Goodman^{39, 40} who has also performed an analysis of sources of error.

The experimental design to be described differs somewhat from that of Goodman, and may offer some advantages of simplicity. The circuit is illustrated schematically in Figure 70. A dc bias and ac-modulation in the range of 10 to 10^5 Hz are applied to the epitaxial silicon layer, and the ac sample current is recovered by means of a current-to-voltage converter. The capacitive feedback employed with the converter results in direct calibration in terms of capacitance, independent of excitation frequency. The 10^9 - Ω resistor in the feedback loop prevents saturation of the amplifier, but is irrelevant to the calibration at frequencies of interest. The ac-modulation voltage is applied to the sample through a 20 kV, 0.01 μ F oil-filled glass capacitor. The dc bias is applied through a 20 M Ω resistor, which limits the current from the filter capacitor in the event of dielectric failure of the sample. The bias level was derived from a manually-controlled high-voltage power supply (Universal Voltronics BAL-16-50). High-voltage transients resulted in saturation of the lock-in, requiring the use of low-pass filters in the dc bias circuit. Subsequently, it was found desirable to sweep the dc bias in a more controlled fashion, and to this end a 200-sec risetime RC circuit was incorporated into the circuit. The dc bias was monitored by means of a voltage divider and follower amplifier to eliminate loading of the divider by the X-Y recorder.

The ac-modulation signal is inverted in the bucking circuit and, with suitable phase trim, impressed upon a variable capacitance used as the principal amplitude control of the bucking signal. Since the overall gain of the inverter is about 1/2, the approximate setting of the variable capacitance is twice the sample capacitance. A final amplitude trim is provided at the input of the inverter amplifier.

³⁹ A. M. Goodman, IEEE Trans. Electron Devices 21, 753 (1974).

⁴⁰ A. M. Goodman, IEEE Trans. Electron Devices 22, 63 (1975).

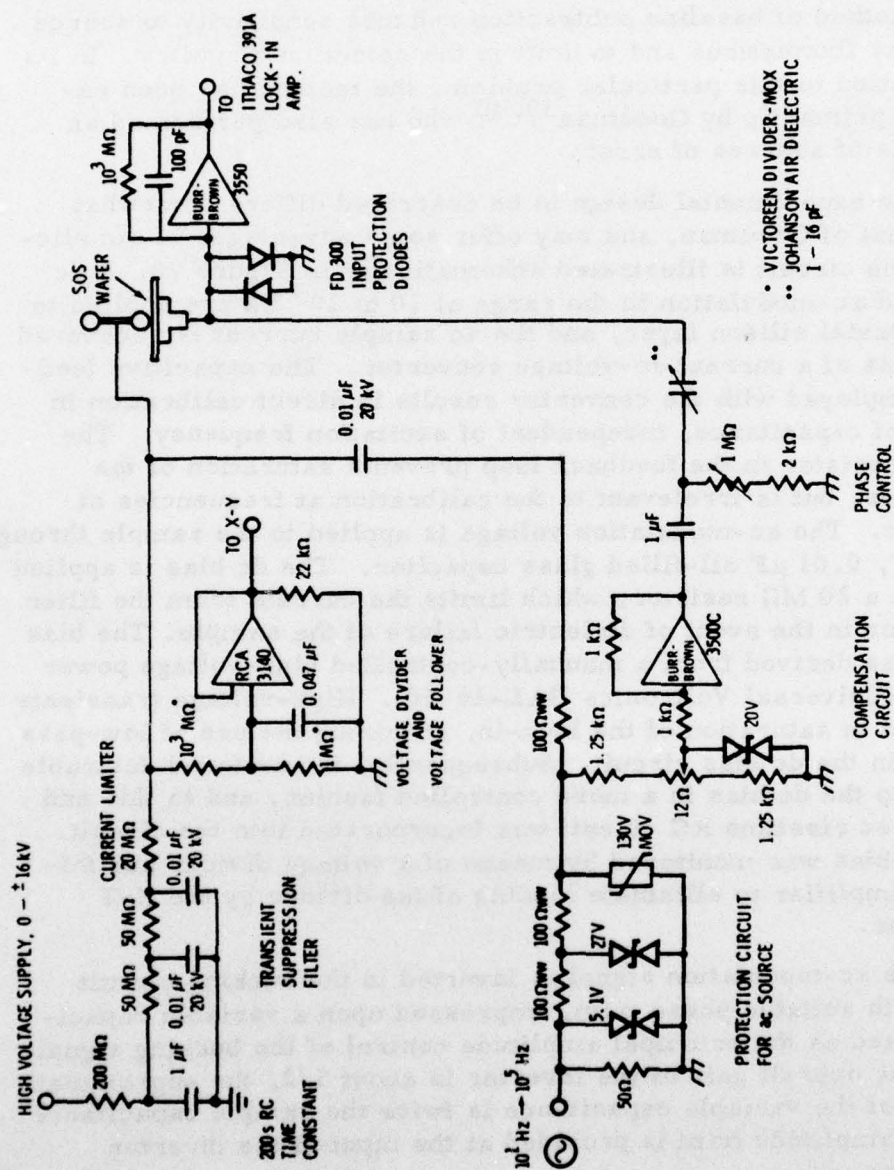


Figure 70. Schematic of experimental technique developed to measure C-V characteristics for SOS structures.

In preliminary testing of the circuit using Inselek SOS wafers obtained several years ago, dielectric failure of one test device was experienced, and the output stage of the ac-modulation source was sacrificed. Subsequently, a protection circuit was installed for both the ac source and the inverter amplifier. The current-to-voltage converter is protected, somewhat marginally, by means of low-leakage diodes. These do affect the dc performance of the amplifiers, giving rise to some 20 pA of offset, but this is not of consequence. More trustworthy input protection for the amplifier would be desirable, but has been resisted because of the effects on circuit function. The current-to-voltage converter is probably somewhat at risk in the event of dielectric failure, even though it has survived so far.

The experimental limitation of the modified C-V system in the determination of space charge capacitance is essentially the noise level of the measurement. Referring to the input and output ac amplitudes, respectively, as V_{in} and V_{out} , the measurement yields, with bucking signal applied

$$\frac{V_{out}}{V_{in}} = \frac{\Delta C}{100 \text{ pF}} \quad (47)$$

Under typical conditions, the noise level corresponds to $\Delta C = 3 \times 10^{-17} \text{ F}$. It is of interest to ascertain the sensitivity this affords in the determination of the space-charge capacitance, C_{SC} , when in series combination with a small, say 10 pF, insulating layer capacitance, C_I . For the case of relatively large C_{SC} , the approximation

$$C_{SC} = \frac{C_I^2}{\Delta C} \quad (48)$$

may be employed. Using the above values, a space-charge capacitance as large as $3 \times 10^{-7} \text{ F}$ may be detected with 10:1 S/N ratio. Put slightly differently, the ratio C_{SC}/C_I corresponding to 10:1 S/N

ratio is 3×10^4 . According to the error analysis performed by Goodman,³⁹ for a high C_{SC}/C_I ratio the error in the determination of C_{SC} , using compensation, ranges up to two to three times the error prevailing in the determination of C_I using the conventional measurement, depending on assumptions.

In practice, it was found that several conditions limited performance of the equipment to somewhat less than the limit imposed by the noise level. First of all, it was found that overload of the lock-in amplifier resulting from transients as the high voltage power supply was being manually swept were difficult to avoid, despite the use of the long RC time constant and the transient filter. Even when the range of voltage change was kept low enough to avoid overloading, some hysteresis in the curves was observed. This may, of course, have been due to real physical effects such as slow interface states; however, it could also have been due to residual effects of the bias sweep since the lock-in is sensitive to the Fourier component of the ramp at the test frequency. In order to eliminate any residual error due to the second of these possibilities, an additional compensation circuit was incorporated to buck out the displacement current resulting from the high voltage transient at the input of the current-to-voltage converter. (This circuit has been tested successfully, but has not been included in Figure 70.)

Secondly, we have observed the effects of small coronas at elevated voltages which make measurements difficult even before the point of dielectric failure of the device is reached. The discharges depend on sign and magnitude of the sweep rate, rather than merely on the absolute voltage level, which suggests that they may arise from redistribution of surface charge on dielectric components of the high-voltage circuitry, or on the sample itself. Careful cleaning of all such parts was found to yield significant, though temporary, improvement. The method of contacting the sample was changed to the use of a large (0.5-in. diameter) ball, minimizing radii of curvature to avoid coronas from this source. The ball makes contact with the aluminum metallization on the sample by force of gravity. Another likely source of coronas is either the periphery of the circular metallization pattern, or the periphery of the silicon. The solution to that problem might

³⁹ A. M. Goodman, IEEE Trans. Electron Devices 21, 753 (1974).

be the use of a field plate to reduce the concentration of field lines at these peripheries. To reduce the incidence of these coronas, the sample holder was provided with desiccant and dry nitrogen (obtained from a liquid nitrogen dewar and heated) was passed through the sample chamber continuously. The problem nevertheless remains to some extent.

The preferable solution to the above experimental difficulties is to employ samples with thinner than conventional substrates, thus reducing the bias voltage range required. We have consequently obtained SOS wafers from Union Carbide fabricated on 5-mil and 9-mil substrates. The former will reduce the required voltage range to the order of 6 kV, which should be quite manageable. The wafers were not received in time to be tested.

In summary, an experimental facility has been described for performing C-V measurements to characterize the silicon-sapphire interface and to test for radiation susceptibility. The facility extends the range of applicability of C-V measurements by some three orders of magnitude in the ratio C_{SC}/C_I , while offering relative simplicity in the achievement of this objective. Experimental difficulties have been largely eliminated using test wafers. Wafers of technological interest have been received, but not in sufficient time for testing under the present program.

5.8 STUDIES OF THE SILICON-SAPPHIRE INTERFACE USING TRANSIENT CURRENT MEASUREMENTS

An adaptation of the conventional capacitance-voltage technique to the particular case of the silicon-sapphire interface was described in Section 5.7. This method, however, has limitations with regard to determination of interface-state density distributions in energy within the forbidden gap. The C-V method is limited in the energy range over which interface-state parameters may be determined, and places a high demand on the precision of the experimental data. This latter condition is particularly difficult to meet in the case of the silicon-sapphire interface. Alternatives to the C-V method, or methods, have been successfully employed to derive the interface state density in MOS devices fabricated on bulk silicon. In contrast to ac-modulation techniques, these quasi-dc techniques permit a relatively straightforward determination of interface state density functions under certain simplifying assumptions.

Consider a bulk MOS capacitor biased into accumulation. In equilibrium, interface states are filled up to the Fermi level at the interface. If a voltage step is then impressed upon the device, taking it into deep depletion, the Fermi level will approach the new equilibrium as interface states empty. By the nature of the Fermi function, the interface states which predominate at any instant in time following the pulse are those which lie close to the instantaneous Fermi level. The current-versus-time waveform, therefore, is a sort of mapping of the interface state density function over the range that the Fermi level is being swept. Simmons et al.^{54,55} have analyzed this problem and have determined that under some idealizing assumptions the quantity (current times time) is proportional to the trap density at the quasi-Fermi level, and that the latter, measured with respect to the conduction band edge in the case of the electron emission process in the upper half of the gap, is proportional to the logarithm of time. A similar analysis is valid for the generation process in the lower half of the gap, with the current-time product yielding the interface trap density at the quasi-Fermi level which, when measured with respect to the valence band edge, exhibits a logarithmic time dependence.

The case of the silicon-sapphire interface is somewhat more complex. Consider an MOS capacitor on sapphire in which the silicon layer is thin enough and sufficiently lightly doped such that the whole layer is depleted in the inversion regime. Then the charge equilibration process following a depleting pulse involves generation at the sapphire interface throughout the recovery transient. If the sapphire-silicon interface has a high density of generation centers, then it will in fact dominate the recovery process. Lehovec and Miller have treated this problem theoretically and obtained fits to experimental data on such a structure.⁴¹

In view of the relative simplicity of the experimental technique involved and because of uncertainty as to whether we would be successful in implementing ac-modulation techniques, the transient recovery method was attempted and applied to SOS capacitors

⁴¹ K. Lehovec and R. Miller, 1976 IEDM Technical Digest, p. 283.

⁵⁴ J. G. Simmons and L. S. Wei, Solid-State Electronics 17, 117 (1974).

⁵⁵ J. G. Simmons and H. A. Mar, Solid-State Electronics 19, 369 (1974).

AD-A046 169

NORTHROP RESEARCH AND TECHNOLOGY CENTER HAWTHORNE CALIF F/6 18/6
IONIZING RADIATION EFFECTS ON SILICON-ON-SAPPHIRE DEVICES AND S--ETC(U)
AUG 77 J R SROUR, S OTHMER, O L CURTIS DAA639-76-C-0090
NRTC-77-28R HDL-CR-77-090-1 NL

UNCLASSIFIED

3 OF 3

AD
A046169



END

DATE
FILMED

12-77

DDC

in order to determine the sensitivity of the interface state density to gamma irradiation. The experimental method utilized is illustrated schematically in Figure 71. It provides for the application of a transient to the capacitor for the measurement of the sample current over wide dynamic range and for compensation of the transient resulting from the expulsion of majority carriers from the silicon layer. This transient would result in saturation of the amplifier, with possible consequences to the transient recovery waveform. The bucking circuit keeps operation in the linear range of the amplifier. To facilitate this, some control over the rise-time of the pulse is provided. The amplifier settling characteristics obtained with the transient compensation circuit are illustrated in Figure 72 for an 18V pulse applied to an 8 pF porcelain capacitor employed as a surrogate sample. With an actual device such close compensation is not possible since the sample capacitance is not time-independent. It is sufficient, however, to keep amplifier operation linear.

Preliminary data were taken on a wet-oxide capacitor, despite the fact that the doping concentration was so high in these samples (on the order of 10^{16} cm^{-3}) that the depletion width did not extend to the sapphire interface in the equilibrium inversion condition. The silicon film thickness here is $0.46 \mu\text{m}$ and the depletion depth only about $0.3 \mu\text{m}$. Initially, data were taken as a function of final depleting voltage, with a constant quiescent bias of 3V in accumulation. Results are shown in Figure 73. One expects to see, and indeed one observes, an increase in the generation current component with increasing bias in inversion over a certain range. However, theory suggests a well-defined region in which generation current declines only moderately with time until the free carrier concentration at the sapphire interface increases sufficiently so that recombination becomes significant and net generation declines rapidly (see insert in Figure 73). This behavior was not observed. It was also found that the data showed some change over time and considerable variation among samples. It was therefore with only moderate enthusiasm that we proceeded to test for the effect of ionizing radiation on the generation current waveform. The results for 10^6 rads(Si) (Co^{60}) are shown in Figure 74. The amplifier settling response under the prevailing conditions of the experiment is also indicated. No profound effects are noted.

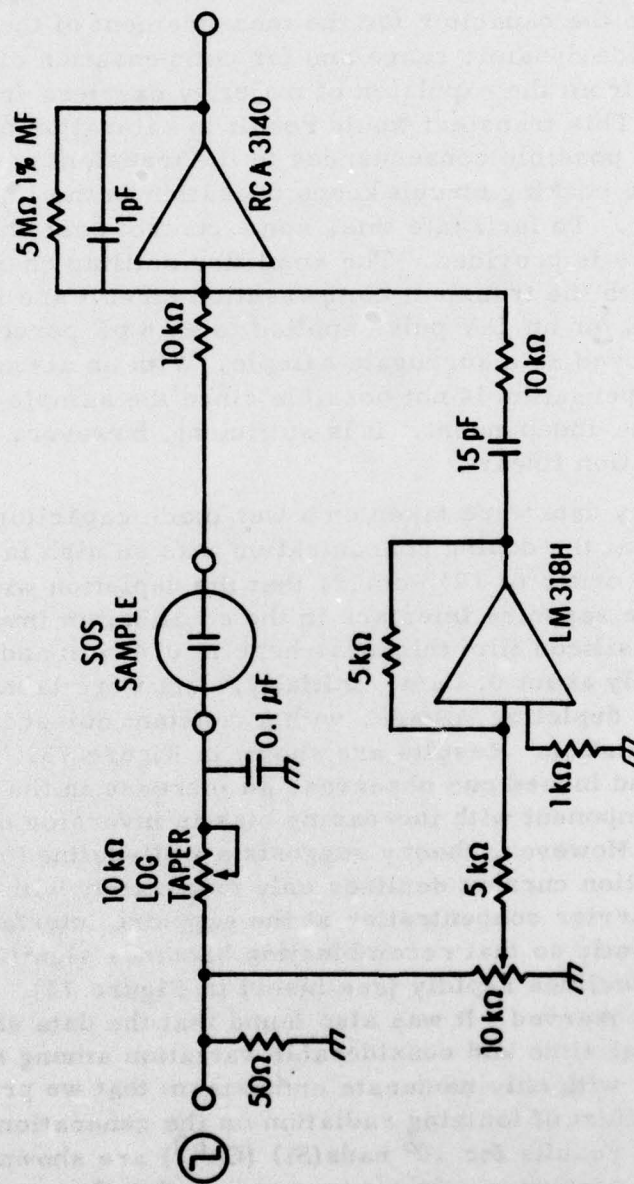


Figure 71. Schematic of circuit employed to measure transient currents in SOS capacitors.

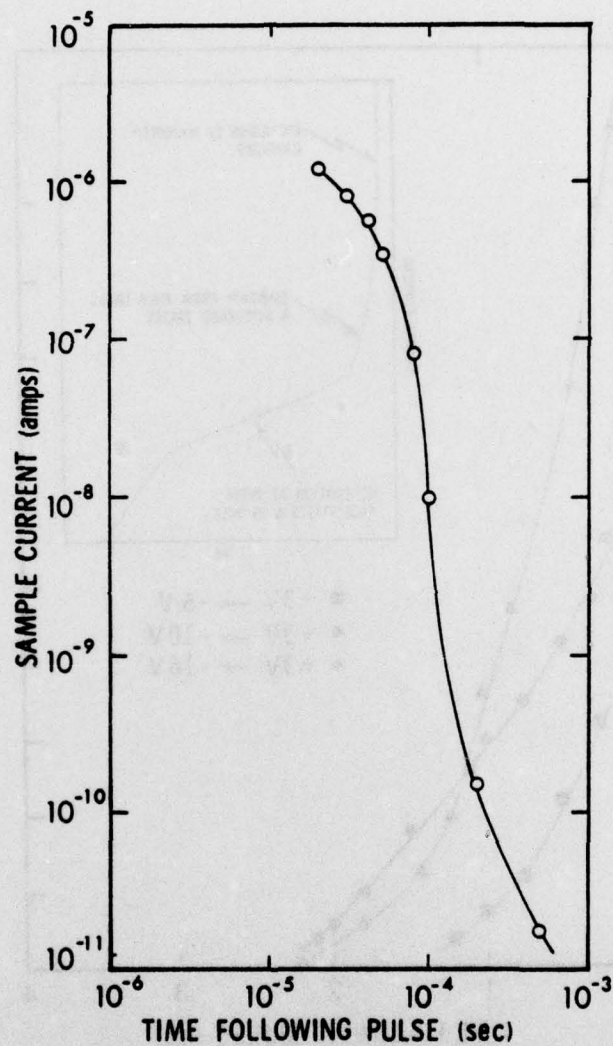


Figure 72. Current settling waveform for transient recovery circuit incorporating transient compensation.

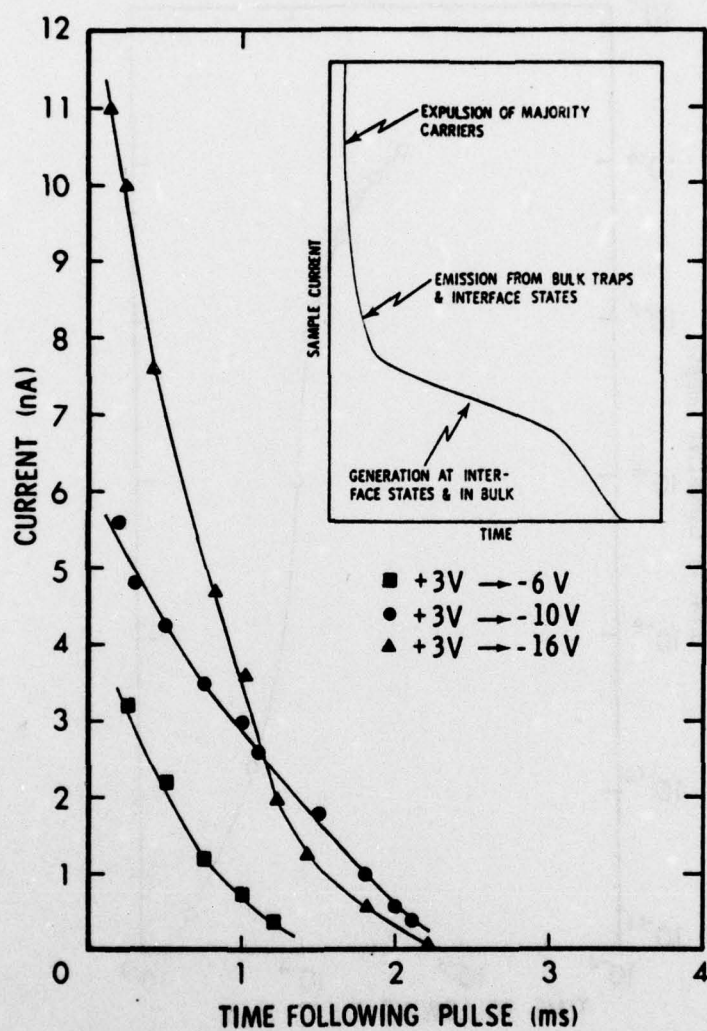


Figure 73. Transient current following depleting pulse from accumulation to inversion for three final voltages in inversion.

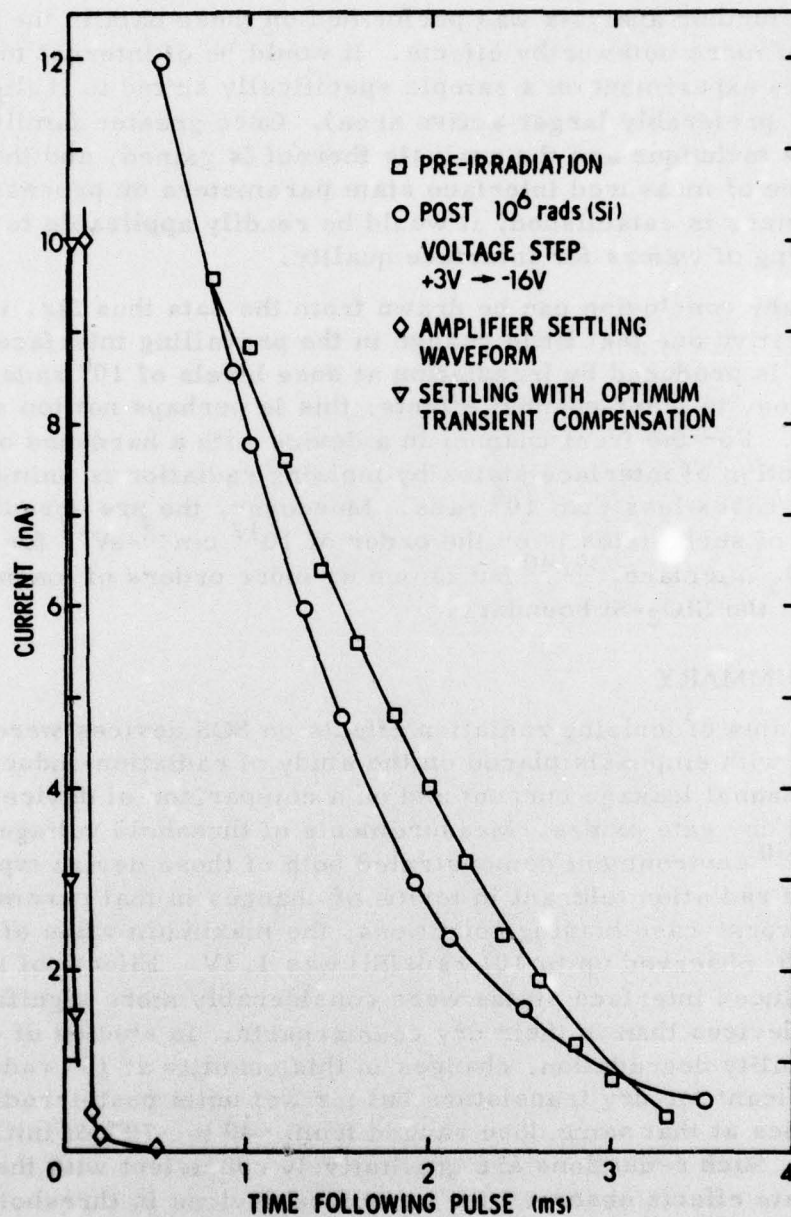


Figure 74. Current transient before and after irradiation with 10^6 rad(Si) Co^{60} gammas. The corresponding amplifier settling waveform is also shown, as well as one achieved with optimum transient compensation.

No further analysis was performed on these data in the absence of more noteworthy effects. It would be of interest to perform the experiment on a sample specifically suited to it (lighter doping, preferably larger active area). Once greater familiarity with the technique and the analysis thereof is gained, and the dependence of measured interface state parameters on processing parameters is established, it would be readily applicable to the screening of wafers for interface quality.

If any conclusion can be drawn from the data thus far, it is the tentative one that little change in the prevailing interface state density is produced by irradiation at dose levels of 10^6 rads(Si). By analogy to front-channel effects, this is perhaps not too surprising. For the front channel in a device with a hardened oxide, introduction of interface states by ionizing radiation is unimportant for doses less than 10^6 rads. Moreover, the pre-irradiation density of such states is on the order of $10^{12} \text{ cm}^{-2}\text{-eV}^{-1}$ for the Si-Al₂O₃ interface,^{39, 40} but is one or more orders of magnitude lower at the SiO₂-Si boundary.

5.9 SUMMARY

Studies of ionizing radiation effects on SOS devices were performed with emphasis placed on the study of radiation-induced back-channel leakage current and on a comparison of devices with wet and dry gate oxides. Measurements of threshold voltage shift in a Co⁶⁰ environment demonstrated both of these device types to be quite radiation tolerant in terms of changes in that parameter. Under worst-case biasing conditions, the maximum value of threshold shift observed up to 10^7 rads(Si) was 1.3V. Effects of radiation-induced interface states were considerably more significant in wet devices than in their dry counterparts. In studies of channel mobility degradation, changes in this quantity at 10^7 rads were insignificant for dry transistors but for wet units post-irradiation mobilities at that same dose ranged from ~40 to ~70% of initial values. Such reductions are qualitatively consistent with the interface state effects observed for wet-oxide devices in threshold voltage studies.

³⁹ A. M. Goodman, IEEE Trans. Electron Devices 21, 753 (1974).

⁴⁰ A. M. Goodman, IEEE Trans. Electron Devices 22, 63 (1975).

In back-channel leakage current studies, several significant observations were made. Leakage currents in the dry-oxide transistors investigated are approximately two orders of magnitude larger than in wet devices both before and after irradiation. These findings are interpreted in terms of differing densities of identical traps in the two device types. At room temperature, radiation-induced leakage current varies as (dose)^{1.5} for wet and dry devices at doses less than that for which leakage current saturation is observed. The variation of leakage current with temperature in both irradiated and unirradiated devices is attributed to the dependence of back-channel mobility on both temperature and inversion-layer carrier density. For an unirradiated wet-oxide transistor at room temperature, in addition to this back-channel "mobility mechanism", thermal generation in the drain depletion region also appeared to be important in giving rise to leakage current. A process of radiation-induced reduction of back-channel leakage current was observed. This reduction of I_L to near its pre-irradiation value is accomplished by irradiating a device with $V_{ds} = 0$. A cycling experiment showed that this process can be repeated, which suggests that periodic reduction of V_{ds} to zero to cause a reduction in I_L is a potential remedy for leakage current problems in SOS devices employed in a space radiation environment.

Scanning-electron-microscope studies indicate that injection of electrons from Si into Al_2O_3 where they recombine with trapped holes is the mechanism of radiation-induced recovery. However, if all trapped holes are located at the Si- Al_2O_3 interface and are not distributed spatially into the sapphire, then we cannot rule out radiation-induced hole depopulation as the dominant mechanism. SEM studies as a function of beam energy also demonstrate that energy must be deposited in the sapphire before significant increases in back-channel leakage current will be observed. In addition, such studies indicate that energy deposition deep in the sapphire bulk is relatively unimportant in producing leakage current. The process of radiation-induced reduction of I_L was also observed in measurements on radiation-hardened CMOS inverters obtained from three manufacturers. In fact, post-recovery leakage currents were often observed to be less than pre-irradiation values. Studies of the Si- Al_2O_3 interface based on C-V measurements and transient current techniques have also been performed and preliminary findings were described.

LITERATURE CITED

1. A. J. Steckl, R. D. Nelson, B. T. French, R. A. Gudmundsen, and D. Schechter, Proc. IEEE 63, (1975).
2. K. Nummedal, J. C. Fraser, S. C. Su, R. Baron, and R. M. Finnilla, in "Proceedings of 1975 International Conference on the Application of Charge-Coupled Devices," p. 19.
3. R. L. Nielsen and D. K. Nichols, IEEE Trans. Nucl. Sci. 20, 319 (Dec. 1973).
4. E. Harari, S. Wang, and B. S. H. Royce, J. Appl. Phys. 46, 1310 (1975).
5. H. H. Sander and B. L. Gregory, IEEE Trans. Nucl. Sci. 22, 2157 (1975).
6. H. E. Boesch, Jr., F. B. McLean, J. M. McGarrity, and G. A. Ausman, Jr., IEEE Trans. Nucl. Sci. 22, 2163 (1975).
7. R. C. Hughes, E. P. EerNisse, and H. J. Stein, IEEE Trans. Nucl. Sci. 22, 2227 (1975).
8. H. Scher and E. W. Montroll, Phys. Rev. B12, 2455 (1975).
9. F. B. McLean, G. A. Ausman, Jr., H. E. Boesch, Jr., and J. M. McGarrity, J. Appl. Phys. 47, 1529 (1976).
10. K. G. Aubuchon, IEEE Trans. Nucl. Sci. 18, 117 (Dec. 1971).
11. J. R. Srour, O. L. Curtis, Jr., and K. Y. Chiu, IEEE Trans. Nucl. Sci. 21, 73 (Dec. 1974).
12. O. L. Curtis, Jr., J. R. Srour, and K. Y. Chiu, IEEE Trans. Nucl. Sci. 22, 2174 (1975).
13. J. R. Srour, S. Othmer, O. L. Curtis, Jr., and K. Y. Chiu, Harry Diamond Laboratories Report HDL-CR-76-161-1, June 1976.
14. O. L. Curtis, Jr., J. R. Srour, and K. Y. Chiu, J. Appl. Phys. 45, 4506 (1974).
15. T. E. Everhart and P. H. Hoff, J. Appl. Phys. 42, 5837 (1971).

16. G. A. Ausman and F. B. McLean, Appl. Phys. Lett. 26, 173 (1975).
17. H. E. Boesch, Jr., and J. M. McGarrity, IEEE Trans. Nucl. Sci. 23, 1520 (1976).
18. R. M. Hill, Phil. Mag. 23, 59 (1971).
19. N. F. Mott and R. W. Gurney, Electronic Processes in Ionic Crystals, 2d. Ed. (Dover, New York, 1964), p. 160.
20. F. B. McLean, H. E. Boesch, Jr., and J. M. McGarrity, IEEE Trans. Nucl. Sci. 23, 1506 (1976).
21. J. R. Srour, S. Othmer, O. L. Curtis, Jr., and K. Y. Chiu, IEEE Trans. Nucl. Sci. 23, 1513 (1976).
22. R. C. Hughes, Phys. Rev. Lett. 30, 1333 (1973).
23. R. C. Hughes, Appl. Phys. Lett. 26, 436 (1976).
24. R. C. Hughes, Phys. Rev. B15, 2012 (1977).
25. S. K. Bahl and K. L. Chopra, J. Appl. Phys. 40, 4940 (1969).
26. K. J. Siemsen and E. W. Fenton, Phys. Rev. 161, 632 (1967).
27. K. Kosek and J. Tauc, Czech. J. Phys. B20, 94 (1970).
28. J. J. O'Dwyer, The Theory of Electrical Conduction and Breakdown in Solid Dielectrics (Clarendon Press, Oxford, 1973), p. 137.
29. J. G. Simmons, Phys. Rev. 155, 657 (1967).
30. E. Harari, personal communication.
31. A. Servini and A. K. Jonscher, Thin Solid Films 3, 341 (1969).
32. M. Silver and L. Cohen, paper submitted for publication.
33. H. E. Boesch, Harry Diamond Laboratories, private communication.
34. G. F. Derbenwick and B. L. Gregory, IEEE Trans. Nucl. Sci. 22, 2151 (1975).
35. F. B. McLean, Harry Diamond Laboratories, private communication.

36. D. Neamen, W. Shedd, and B. Buchanan, IEEE Trans. Nucl. Sci. 21, 211 (Dec. 1974).
37. R. A. Kjar and J. Peel, IEEE Trans. Nucl. Sci. 21, 208 (Dec. 1974).
38. K. M. Schlesier, IEEE Trans. Nucl. Sci. 21, 152 (Dec. 1974).
39. A. M. Goodman, IEEE Trans. Electron Devices 21, 753 (1974).
40. A. M. Goodman, IEEE Trans. Electron Devices 22, 63 (1975).
41. K. Lehovec and R. Miller, 1976 IEDM Technical Digest, p. 283.
42. P. S. Winokur, J. M. McGarrity, and H. E. Boesch, Jr., IEEE Trans. Nucl. Sci. 23, 1580 (1976).
43. J. T. C. Chen and R. S. Muller, J. Appl. Phys. 45, 828 (1974).
44. C. T. Sah, T. H. Ning, and L. L. Tschopp, Surface Science 32, 561 (1972).
45. C. T. Sah and H. C. Pao, IEEE Trans. Electron Devices 13, 393 (1966).
46. J. R. Brews, J. Appl. Phys. 46, 2193 (1975).
47. J. R. Brews, J. Appl. Phys. 46, 2181 (1975).
48. A. A. Guzev, G. L. Kurishev, and S. P. Sinita, Phys. Status Solidi A14, 41 (1972).
49. Y. C. Cheng and E. A. Sullivan, J. Appl. Phys. 44, 3619 (1973).
50. J. L. Moll, Physics of Semiconductors (McGraw-Hill, New York, 1964), p. 118; A. S. Grove, Physics and Technology of Semiconductor Devices (Wiley, New York, 1967), p. 174.
51. E. Harari and D. J. McGreivy, to be published in IEEE Trans. Electron Devices
52. S. T. Wang and B. S. H. Royce, IEEE Trans. Nucl. Sci. 23, 1586 (1976).
53. E. Harari, Appl. Phys. Letters 29, 25 (1976).

54. J. G. Simmons and L. S. Wei, Solid-State Electronics 17, 117 (1974).
55. J. G. Simmons and H. A. Mar, Solid-State Electronics 19, 369 (1974).

DISTRIBUTION LIST

Director
Defense Communications Agency
Washington, DC 20305
Attn: Code 930 M.I. Burgett

Defense Documentation Center
Cameron Station
Alexandria, VA 22314
Attn: TC

Director
Defense Intelligence Agency
Washington, DC 20301
Attn: DS-4A2

Director
Defense Nuclear Agency
Washington, DC 20305
Attn: DDST
TITL Tech Library
RAEV
RATN
STVL

Director of Defense Rsch & Engr
Department of Defense
Washington, DC 20301
Attn: S&SS (OS)

Commander
Field Command
Defense Nuclear Agency
Kirtland AFB, NM 87115
Attn: FCPRL

Director
Interservice Nuclear Weapons Sch.
Kirtland AFB, NM 87115
Attn: Document Control

Director, Joint Strat Tgt
Planning Staff JCS
Offutt AFB, Omaha, NE 68113
Attn: JLTW-2

Chief
Livermore Div. Fld Command DNA
Lawrence Livermore Laboratory
P.O. Box 808
Livermore, CA 94550
Attn: FCPRL

Director
National Security Agency
Ft. George G. Meade, MD 20755
Attn: R-425
TDL

Project Manager
Army Tactical Data Systems
U.S. Army Electronics Command
Fort Monmouth, NJ 07703
Attn: Dwaine B. Huewe
DRCPPN-TDS-SD

Commander
BMD System Command
P.O. Box 1500
Huntsville, AL 35807
Attn: BDMSC-TEN

Commander
Frankford Arsenal
Bridge & Tacony Streets
Philadelphia, PA 19137
Attn: SARFA-FCD

Commander
Harry Diamond Laboratories
2800 Powder Mill Road
Adelphi, MD 20783
Attn: J. Halpin
J. McGarrity
DRXDO-TI Tech Lib
DRXDO-RCC (2)
DRXDO-NP
DRXDO-RC
DRXDO-EM
DRXDO-RBH

Commander
Picatinny Arsenal
Dover, NJ 07801
Attn: SMUPA-ND-W
SMUPA-ND-N-E
SARPA-ND-C-E
SARPA-FR-E
SARPA-ND-N

Commander
Redstone Scientific Information Ctr
U.S. Army Missile Command
Redstone Arsenal, AL 35809
Attn: Chief, Documents

Secretary of the Army
Washington, DC 20310
Attn: ODUSA or Daniel Willard

Director
TRASANA
White Sands Missile Range
New Mexico 88002
Attn: ATAA-EAC

Director
U.S. Army Ballistic Research Labs
Aberdeen Proving Ground,
Maryland 21005
Attn: DRXBR-AM
DRXBR-X
DRXRD-BVL

Chief, U.S. Army
Communications Systems Agency
Fort Monmouth, NJ 07703
Attn: SCCM-AD-SV Library

Commander
U.S. Army Electronics Command
Ft. Monmouth, NJ 07703
Attn: DRSEL-TL-MD
DRSEL-TL-EN (2)
DRSEL-CT-HDK
DRSEL-GG-TD
DRSEL-TL-IR
DRSEL-TL-ND
DRSEL-PL-ENV

Commander-in-Chief
U.S. Army and Seventh Army
APO New York 09403 (Heidelberg)
Attn: ODCSE-E AEAGE-PI

Commander
U.S. Army Missile Command
Redstone Arsenal, AL 35809
Attn: DRSMI-RGD
DRCPM-LCEX
DRSMI-RGP
DRSMI-RRR
DRCPM-PF-FA

Commander
U.S. Army Mobility Equip R&D Ctr
Fort Belvoir, VA 22060
Attn: STSFB-MW

Chief
U.S. Army Nuc & Chemical Surety Gp
Bldg. 2073, North Area
Ft. Belvoir, VA 22060
Attn: MOSG-ND

Commander
U.S. Army Nuclear Agency
7500 Backlick Road, Bldg. 2073
Springfield, VA 22150
Attn: ATCN-W

Commander
U.S. Army Test & Evaluation Comd
Aberdeen Proving Ground, MD 21005
Attn: DRSTE-EL
DRSTE-NB

Chief of Naval Research
Navy Department
Arlington, VA 22217
Attn: Code 421
Code 427

Commander
Naval Electronic Systems Command
Naval Electronic Systems Cmd Hqs
Washington, DC 20360
Attn: PME 117-21
Code 504510
ELEX 05323

Commanding Officer
Naval Intelligence Support Ctr
4301 Suitland Road, Bldg. 5
Washington, DC 20390
Attn: P. Alexander

Director Naval Research Laboratory Washington, DC 20375 Attn: Code 6631 Code 5216 Code 7701 Code 6440 Code 601 Code 4004 Code 5210	AF Institute of Technology, AU Wright-Patterson AFB, OH 45433 Attn: ENP Charles J. Bridgman	SAMSO/MN Norton AFB, CA 92409 (Minuteman) Attn: MNNG MNNH
Commander Naval Sea Systems Command Navy Department Washington, DC 20362 Attn: SEA-9931 (2)	AF Materials Laboratory, AFSC Wright-Patterson AFB, OH 45433 Attn: LTE	SAMSO/SR Post Office Box 92960 Worldway Postal Center Los Angeles, CA 90009 (Reentry Systems) Attn: RSSE RSMG
Commander Naval Ship Engineering Center Department of the Navy Washington, DC 20362 (Hyattsville) Attn: Code 6174D2	AF Weapons Laboratory, AFSC Kirtland AFB, NM 87117 Attn: ELS ELA DES NTS ELP SAB	SAMSO/SZ Post Office Box 92960 Worldway Postal Center Los Angeles, CA 90009 (Space Defense Systems) Attn: SZJ
Officer-in-Charge Naval Surface Weapons Center White Oak, Silver Spring, MD 20910 Attn: Code WA52 Code WA50 Code WA501 Navy Nuc Prgms Off.	AFTAC Patrick AFB, FL 32925 Attn: TAE TFS	Commander-in-Chief Strategic Air Command Offutt AFB, NE 68113 Attn: NRI-STINFO Library XPES
Commander Naval Surface Weapons Center Dahlgren Laboratory Dahlgren, VA 22448 Attn: William H. Holt	Air Force Avionics Laboratory, AFSC Wright-Patterson AFB, OH 45433 Attn: AAT Mason Friar DH LTC McKenzie DHE H J Hennecke	University of California Lawrence Livermore Laboratory P. O. Box 808 Livermore, CA 94550 Attn: Tech Info Dept L-3 Ronald L. Ott L-531 J. E. Keller, Jr. L-125 H. Kruger L-96 L. Cleland L-156 F. R. Kovar L-31 D. J. Meeker L-545
Commander Naval Weapons Center China Lake, CA 93555 Attn: Code 533 Tech Lib	Commander, ASD Wright-Patterson AFB, OH 45433 Attn: ENACC Robert I. Fish	Los Alamos Scientific Laboratory P. O. Box 1663 Los Alamos, NM 87545 Attn: DOC CON/Bruce W. Noel DOC CON/J. Arthur Freed DOC CON/Marvin M. Hoffman
Commanding Officer Naval Weapons Support Center Crane, IN 47522 Attn: Code 7024 Code 70242	Headquarters Electronic Systems Division/YS Hanscom AFB, MA 01731 Attn: YSEV	Sandia Laboratories Livermore Laboratory P. O. Box 969, Livermore, CA 94550 Attn: DOC CON/Theodore A. Dellin
Commanding Officer Nuclear Weapons Training Center Pacific Naval Air Station, North Island San Diego, CA 92135 Attn: Code 50	Commander Foreign Technology Division, AFSC Wright-Patterson AFB, OH 45433 Attn: FTDF	Sandia Laboratories P.O. Box 5800 Albuquerque, NM 87115 Attn: DOC CON/Org. 2110, J.A. Hood DOC CON/3141 Sandia Rpt Coll Div. 5231 James H. Renken DOC CON/Org 1933 F.N. Coppage DOC CON/Org 2140 B.L. Gregory DOC CON/Org 5220 J.V. Walker
Director Strategic Systems Project Office Navy Department Washington, DC 20376 Attn: NSP-2342	Commander Rome Air Development Center, AFSC Griffiss AFB, NY 13440 Attn: RBRP	U.S. Energy Resch & Dev Admin Albuquerque Operations Office P.O. Box 5400 Albuquerque, NM 87115 Attn: DOC CON/WSSB
AF Geophysics Laboratory, AFSC Hanscom AFB, MA 01731 Attn: J. Emery Cormier LQR Edward A. Burke	Commander RADC, AFSC Hanscom AFB, MA 01731 Attn: FTS R Dolan FT B Buchanan	
	SAMSO/YE Post Office Box 92960 Worldway Postal Center Los Angeles, CA 90009 (Technology) Attn: YEE	
	SAMSO/IN Post Office Box 92960 Worldway Postal Center Los Angeles, CA 90009 (Intelligence) Attn: IND I.J. Judy	

Central Intelligence Agency
Attn: RD/SI Rm. 5G48 Hq Bldg
Washington, DC 20505
Attn: Alice A. Padgett

Department of Commerce
National Bureau of Standards
Washington, DC 20234
Attn: Security Officer for
Appl Rad Div R.C. Placious
Judson C. French

Aerojet Electro-Systems Co
Div of Aerojet-General Corp
P.O. Box 296
Azusa, CA 91702
Attn: Thomas D. Hanscome

Aerospace Corporation
P.O. Box 92957
Los Angeles, CA 90009
Attn: William W. Willis
Irving M. Garfunkel
L. W. Aukerman
Library
Julian Reinheimer

Avco Research & Systems Group
201 Lowell St.
Wilmington, MA 01887
Attn: Research Lib A830, Rm 7201

The BDM Corporation
7915 Jones Branch Drive
McLean, VA 22101
Attn: T. H. Neighbors

The BDM Corporation
P.O. Box 9274
Albuquerque International
Albuquerque, NM 87119
Attn: D.R. Alexander

The Bendix Corporation
Communication Division
East Joppa Road
Baltimore, MD 21204
Attn: Document Control

The Bendix Corporation
Research Laboratories Division
Bendix Center
Southfield, MI 48075
Attn: Mgr Prog Dev D.J. Niehaus

The Boeing Company
P.O. Box 3707
Seattle, WA 98124
Attn: Aerospace Library
C. Rosenberg 2R-00
Itsu Arimura 2R-00
H.W. Wicklein MS 17-11
Robt. S. Caldwell 2R-00

Booz-Allen and Hamilton, Inc.
106 Apple St.
Tinton Falls, NJ 07724
Attn: Raymond J. Chrisner

California Institute of Technology
Jet Propulsion Laboratory
4800 Oak Grive Drive
Pasadena, CA 91103
Attn: J. Bryden
A.G. Stanley

Charles Stark Draper
Laboratory Inc
555 Technology Square
Cambridge, MA 02139
Attn: Richard G. Halmmaier
Paul R. Kelly
Kenneth Fertig

Computer Sciences Corporation
201 La Veta Drive N.E.
Albuquerque, NM 87108
Attn: Richard H. Dickhaut

Control Data Corporation
P.O. Box O
Minneapolis, MN 55440
Attn: Jack Meehan

Cutler-Hammer, Inc.
AIL Division
Comac Road
Deer Park, NY 11729
Attn: Central Tech Files A. Anthony

Dikewood Industries, Inc.
1009 Bradbury Drive, S.E.
Albuquerque, NM 87106
Attn: L. Wayne Davis

F-Systems, Inc.
Greenville Division
P.O. Box 1056
Greenville, TX 75401
Attn: Library 8-50100

Effects Technology, Inc.
5383 Hollister Avenue
Santa Barbara, CA 93111
Attn: Edward John Steele

Exp & Math Physics Consultants
P.O. Box 66331
Los Angeles, CA 90066
Attn: Thomas M. Jordan

Fairchild Camera & Instrument Co.
464 Ellis St.
Mountain View, CA 94040
Attn: Sec Dept/2-233 D.K. Myers
Fairchild Industries, Inc.
Sherman Fairchild Tech Center
20301 Century Blvd.
Germantown, MD 20767
Attn: Mgr Config Data & Stndrds

University of Florida
Attn: Patricia B. Rambo
P.O. Box 284
Gainesville, FL 32601
Attn: D. P. Kennedy

Ford Aerospace & Communications
3939 Fabian Way
Palo Alto, CA 94303
Attn: Samuel R. Crawford MS531
Donald R. McMorro MS G30

Ford Aerospace & Comm Operations
Ford & Jamboree Roads
Newport Beach, CA 92663
Attn: Tech Info Section
Ken C. Attinger

The Franklin Institute
20th Street & Parkway
Philadelphia, PA 19103
Attn: Ramie H. Thompson

General Dyamics Corp.
Electronics Div. Orlando Operations
P.O. Box 2566
Orlando, FL 32802
Attn: D.W. Coleman

General Electric Company, Space
Division, Valley Forge Space Center
P.O. Box 8555
Philadelphia, PA 19101
Attn: J. C. Peden VFSC. Rm 4230M
John L. Andrews
Larry I. Chasen

General Electric Company, Re-Entry
& Environmental Systems Div
P.O. Box 7722
Philadelphia, PA 19101
Attn: Robert V. Benedict
John W. Palchefskey Jr.

General Electric Company
Ordnance Systems
100 Plastics Avenue
Pittsfield, MA 01201
Attn: Joseph J. Reidl

General Electric Company
Tempo-Center for Advanced Studies
P.O. Drawer QQ
Santa Barbara, CA 93102
Attn: Royden R. Rutherford
DASLAC
M. Espig

General Electric Company
Aircraft Engine Business Group
Evendale Plant Int. Hwy. 75 S
Cincinnati, OH 45215
Attn: John A. Ellerhorst E 2

General Electric Company
Aerospace Electronics Systems
French Road
Utica, NY 13503
Attn: W. J. Patterson DROP 233

General Electric Company
P.O. Box 5000
Binghamton, NY 13902
Attn: David W. Pepin DROP 160

General Electric Company-Tempo
Attn: DASLAC
c/o Defense Nuclear Agency
Washington, DC 20305
Attn: William Alfente

General Research Corporation
P.O. Box 3587
Santa Barbara, CA 93105
Attn: Robert D. Hill

Georgia Institute of Technology
Georgia Tech Research Institute
Atlanta, GA 30332
Attn: R. Curry

Grumman Aerospace Corporation
South Oyster Bay Road
Bethpage, NY 11714
Attn: Jerry Rogers, Dept. 533

GTE Sylvania, Inc., Electronics
Systems Grp - Eastern Division
77 "A" Street
Needham, MA 02194
Attn: Leonard L. Blaisdell
C. A. Thornhill, Librarian
James A. Waldon

GTE Sylvania, Inc.
189 "B" Street
Needham Heights, MA 02194
Attn: Charles H. Ramsbottom
Herbert A. Ullman
Paul B. Fredrickson
H&V Group

Harris Corporation
Harris Semiconductor Division
P.O. Box 883
Melbourne, FL 32901
Attn: Carl F. Davis, MS17-220
T. L. Clark, MS 4040
Wayne E. Abare, MS16-111

Hazeltine Corporation
Pulaski Road
Greenlawn, NY 11740
Attn: Tech Info Ctr, M. Waite

Honeywell Incorporated
Avionics Division
2600 Ridgeway Parkway
Minneapolis, MN 55413
Attn: Ronald R. Johnson A1622

Honeywell, Incorporated
Avionic Division
13350 U.S. Highway 19 North
St. Petersburg, FL 33733
Attn: MS 725-J, Stacey H. Graff

Honeywell Incorporated
Radiation Center
2 Forbes Road
Lexington, MA 02173
Attn: Technical Library

Hughes Aircraft Company
Centinela & Teale
Culver City, CA 90230
Attn: B.W. Campbell MS6-E-110
K.R. Walker MS D157
Dan Binder MS 6-D147

Hughes Aircraft Company
El Segundo Site
P.O. Box 92919
Los Angeles, CA 90009
Attn: E.C. Smith MS A620
W.W. Scott MS A1080

IBM Corporation
Route 17C
Owego, NY 13827
Attn: Frank Frankovsky

Ion Physics Corporation
South Bedrod Street
Burlington, MA 01803
Attn: Robert D. Evans

IRT Corporation
P.O. Box 81087
San Diego, CA 92187
Attn: R. L. Mertz
MDC
James A. Naber
Ralph H. Stahl

Jaycor
205 S. Whiting St., Suite 500
Alexandria, VA 22304
Attn: Catherine Turesko
Robert Sullivan

Kaman Sciences Corporation
P.O. Box 7463
Colorado Springs, CO 80933
Attn: Albert P. Bridges
Jerry I. Lubell
Donald H. Bryce
Walter F. Ware

Litton Systems, Inc.
Guidance & Control Systems Div
5500 Canoga Avenue
Woodland Hills, CA 91364
Attn: V.J. Ashby MS67
J.P. Retzler

Lockheed Missiles & Space Co Inc
P.O. Box 504
Sunnyvale, CA 94088
Attn: L. Rossi Dept. 81-64
B.T. Kimura Dept. 81-14
E.A. Smith Dept. 85-85
G.F. Heath Dept. 81-14
P.J. Hart Dept. 81-14
S.I. Taimuty Dept. 85-85

Lockheed Missiles & Space Co Inc
3251 Hanover St.
Palo Alto, CA 94304
Attn: Tech Info Ctr D/Coll
M.I.T. Lincoln Library
P.O. Box 73
Lexington, MA 02173
Attn: Leona Loughlin Librarian A-082

Martin Marietta Aerospace
Orlando Division
P.O. Box 5837
Orlando, FL 32805
Attn: William W. Mras MP-413
Mona C. Griffith Lib. MP-30

Martin Marietta Corporation
Denver Division
P.O. Box 179
Denver, CO 80201
Attn: Ben T. Graham MS PO-454
Research Lib 6617 J.R. McKee
J.E. Goodwin MS 0452 (U)

McDonnell Douglas Corporation
P.O. Box 516
St. Louis, MO 63166
Attn: Technical Library

McDonnell Douglas Corporation
5301 Bolsa Avenue
Huntington Beach, CA 92647
Attn: Stanley Schneider

Mission Research Corporation
735 State Street
Santa Barbara, CA 93101
Attn: William C. Hart

Mission Research Corporation
P.O. Box 1209
La Jolla, CA 92038
Attn: J.P. Raymond
V.A.J. van Lint

National Academy of Sciences
National Materials Advisory Board
2101 Constitution Ave, NW
Washington, DC 20418
Attn: R.S. Shane Nat Mat Advay

University of New Mexico
Dept/Campus Security & Police
1821 Roma N.E.
Albuquerque, NM 87106
Attn: W.W. Grannemann

University of New Mexico
Elec. Engr. & Computer Sci. Dept.
Albuquerque, NM 87131
Attn: Harold Southward

Northrop Corporation
Electronics Division
2301 West 120th St.
Hawthorne, CA 90250
Attn: Boyce T. Ahlport
George H. Towner
Vincent R. DeMartino

Northrop Corporation
Research and Technology Center
3401 West Broadway
Hawthorne, CA 90250
Attn: David N. Pocock
J.R. Srour

Physics International Company
2700 Merced Street
San Leandro, CA 94577
Attn: DOC CON/Chas. H. Stallings
DOC CON/John H. Huntington

R & D Associates
P.O. Box 9695
Marina del Rey, CA 90291
Attn: S. Clay Rogers

Raytheon Company
Hartwell Road
Bedford, MA 01730
Attn: G.H. Josht, Radar Sys Lab

RCA Corporation
Government Systems Division
Astro Electronics
P.O. Box 800, Locust Corner
East Windsor Township
Princeton, NJ 08540
Attn: George J. Brucker

RCA Corporation
David Sarnoff Research Center
P.O. Box 432
Princeton, NJ 08540
Attn: K.H. Zaininger

Rensselaer Polytechnic Institute
P.O. Box 965
Troy, NY 12181
Attn: Ronald J. Gutmann (U)

Research Triangle Institute
P.O. Box 12194
Research Triangle Park, NC 27709
Attn: Sec Off/Eng Div,
M. Simons, Jr.

Rockwell International Corporation
P.O. Box 3105
Anaheim, CA 92803
Attn: James F. Bell HA10
Geo. C. Messenger FB61
Donald J. Stevens FA70
K.F. Hull
N.J. Rudie FA53

Rockwell International Corporation
Collins Divisions
400 Collins Rd NE
Cedar Rapids, IA 52406
Attn: Dennis Sutherland

Sanders Associates, Inc.
95 Canal Street
Nashua, NH 03060
Attn: Moe L. Aitel NCA1-3236

Science Applications Inc.
P.O. Box 2351
La Jolla, CA 92038
Attn: Larry Scott
J. Robert Beyster

Science Applications, Inc.
Huntsville Division
2109 W. Clinton Ave., Suite 700
Huntsville, AL 35805
Attn: Noel R. Byrn

Science Applications, Inc.
2680 Hanover Street
Palo Alto, CA 94303
Attn: Charles Stevens

Science Applications, Inc.
8400 Westpark Drive
McLean, VA 22101
Attn: William L. Chadsey

Simulation Physics, Inc.
P.O. Box D
Bedford, MA 01730
Attn: Roger G. Little

The Singer Company (Data Sys)
150 Totowa Rd.
Wayne, NJ 07470
Attn: Tech Info Center

The Singer Company
Security Manager
1150 McBride Avenue
Little Falls, NJ 07424
Attn: I. Goldman, Eng. Mgmt.

Sperry Rand Corporation
Sperry Division
Marcus Avenue
Greak Neck, NY 11020
Attn: Charles L. Craig EV
Paul Maraffino

Stanford Research Institute
333 Ravenswood Avenue
Menlo Park, CA 94025
Attn: Philip J. Dolan

Stanford Research Institute
306 Wynn Drive, NW
Huntsville, AL 35805
Attn: MacPherson Morgan

Sunstrand Corporation
4751 Harrison Avenue
Rockford, IL 61101
Attn: Curtis B. White

Texas Instruments, Inc.
P.O. Box 6015
Dallas, TX 75222
Attn: D.J. Marus MS 72

TRW Defense & Space Sys Group
One Space Park
Redondo Beach, CA 90278
Attn: O.E. Adams R1-1144
Tech Info Center/S-1930
R.M. Webb R1-2410
R.K. Plebuch R1-2078
H.H. Holloway R1-2036

TRW Defense & Space Sys Group
P.O. Box 1310
San Bernardino, CA 92402
Attn: R. Kitter
F.B. Fay
Earl W. Allen 520/141

Vought Corporation
P.O. Box 5907
Dallas, TX 75222
Attn: Technical Data Center

Westinghouse Electric Corporation
Defense & Electronics Systems Ctr
P.O. Box 1693
Baltimore-Washington Intl Airport
Baltimore, MD 21203
Attn: Henry P. Kalapaca MS 3525